# Laser Spectroscopic and Theoretical Studies of Silicon and Germanium-Containing Species

Thesis submitted for the degree of
Doctor of Philosophy
At the University of Leicester

by

Matthew Richard Dover, BSc (Leicester), MRSC
Department of Chemistry
University of Leicester

September 2008

This thesis is dedicated to Sophia

# STATEMENT OF ORIGINALITY

The work in this thesis was conducted by the author in the Department of Chemistry at the University of Leicester during the period between October 2004 and October 2007 and is original unless otherwise acknowledged in the text or references.

None of the work has been submitted for another degree at this or any other university.

Signed_____          Date_____

# *Abstract*

A detailed examination of both the ground ( $\tilde{X}\,^1A'$ ) and first excited ( $\tilde{A}\,^1A''$ ) singlet states of HSiNC and HSiNCO have been carried out through analysis of the 520-420 nm and 490-450 nm band systems, respectively. HSiNC and HSiNCO have been generated by electric discharge through $(CH_3)_3SiCN$ and $(CH_3)_3SiNCO$ vapour in argon, respectively. The pulsed electrical discharge jet coupled with laser induced fluorescence (LIF) and dispersed fluorescence (DF) techniques were employed to investigate these species. Previous theoretical and microwave studies were used for comparison with the HSiNC species. Rotational analysis of the $0_0^0$ band yielded a new set of rotational constants for both the ground and excited states of both species. Eleven vibrational bands have been tentatively assigned for both species in their excited states. DF spectroscopy has also been applied to both species.

As there have been no previous studies on HSiNCO, a detailed *ab initio* study has been carried out on the possible [H, Si, N, C, O] isomers, with particular attention paid to the HSiNCO species, for use as comparison with the aforementioned experimental study. Different levels of theory have been applied to the seven lowest lying isomers and the transition states connecting them have also been determined. The stability of the isomers has also been checked by carrying out thermodynamic calculations. Finally, as a continuation of the silicon work, a detailed *ab initio* study has been carried out on the previously unstudied [H, Ge, N, C, O] isomers. Different levels of theory have been applied to the five lowest lying isomers, and their stability has been checked by carrying out thermodynamic calculations.

## *Acknowledgements*

# Table of Contents

## *List of Tables*

## List of Figures

# Chapter One

*Introduction*

## 1.1    Introduction

This work involves laser spectroscopy and theoretical studies of small silicon- and germanium-containing free radicals, and a detailed theoretical study of an analogous germanium containing species. A combination of experimental and theoretical methods has allowed the detailed investigation of the properties of these species. This introduction of the subject is followed by chapters which detail the methodology and theory used and then goes on to a discussion of the spectra and analysis.

## 1.2    Importance of Silicon-Containing Species

### 1.2.1   Reactive Intermediates

Reactive intermediates are, by definition, transient in their existence, and as a result this type of molecule is generally highly reactive. Typically, these types of species will not exist for any appreciable amount of time, due to their extremely high reactivity.

Reactive intermediates are present in a variety of chemical systems where detection of the species, and an understanding of its chemical properties, would aid in the understanding of the overall chemical system. If one can pin down the geometry and energy levels of the reactive intermediate species, then a rationalisation of the reaction mechanism is possible. For example, knowledge of the equilibrium structure of a molecule can provide important clues as to its reaction pathway – at which position in a molecule a reaction is most likely to take place, and at what stage any structural rearrangement of the intermediate species is likely to occur.

Spectroscopic information can also be used in the deduction of thermodynamic parameters for reaction intermediates and therefore, ultimately for specific elementary reactions involving these intermediates. Finally, spectroscopic data also provides a method for probing chemical intermediates *in situ*, e.g., in kinetic studies.

### 1.2.2   Chemical Vapour Deposition

The current desire for faster and more elaborate electronic and optoelectronic devices has generated enormous interest in developing new conducting, semiconducting and insulating materials for various functions. Most modern electronic devices are based on the transistor, an electronic component made from semiconducting materials.[1]

Silicon is the most commonly used semiconductor substrate in electronics, partly because of its high naturally occurring abundance on Earth. Recently there has been a great deal of research going on in the area of group 13-15 semiconductors, which include both silicon and germanium containing species. These sorts of semiconductors are used in some special, high speed electronics applications, such as wireless communications and optoelectronic devices.

In many electronic devices it is necessary to prepare these semiconductor materials as thin even films. Preparation of these films is typically carried out using chemical vapour deposition (CVD).[2] CVD is a process in which gas-phase precursors are decomposed in some way (usually via photolysis or pyrolysis) to leave behind a thin layer of solid material. The decomposition of the precursor, as with many chemical reactions, often occurs via reactive intermediates which can be studied by techniques similar to those used in this work. Monitoring these intermediates in the CVD process may reveal important information on the deposition mechanisms which are still not well understood. This, in turn, could lead to improvements in the CVD process.

One of the potential future directions of the work contained in this thesis is the possibility of producing some novel group 14 semiconductor materials (germanium and possibly tin containing) as well as looking at the potential of the silicon-containing species discussed in Chapters 4, 5 and 6.

### 1.2.3 Presence of Silicon-Containing Species in Space

Many silicon-containing free radicals have a potentially significant effect on the chemistry in space. Ten silicon-bearing molecules have been discovered in interstellar clouds or circumstellar shells, including the diatomics SiO [3] and SiS,[4] the carbon chain $SiC_4$,[5] and two rings, $SiC_2$ [6] and $SiC_3$.[7]

Interstellar clouds are of interest to astronomers as they are often the site of star and planet formation. Various carbon, hydrogen, nitrogen and silicon-containing species have been identified in well studied stars such as IRC +10216 (located 500 light years from Earth in the constellation Leo).[3,8-10] The conditions in interstellar regions, such as very low densities of species and very low temperatures, give rise to

relatively collision free environments. This means that various radicals are able to form and have extremely long lifetimes.

With the abundance of silicon in space (fifth most abundant element cosmically), as well as an abundance of carbon, nitrogen and hydrogen, there are potentially many other cyanosilicon molecules that will be formed and can be observed. Obvious examples might include species such as HSiCN, HSiNC, HSiNCO and many others. Of these species, new work on the isocyanosilylene (HSiNC) and isocyanatosilylene (HSiNCO) radical species are reported in Chapters 4 and 6, respectively.

## *1.3    Importance of Germanium-Containing Species*

Germanium containing chemistry in the laboratory has attracted continuing interest from various fields. A number of germanium containing free radicals and ions may act as basic building blocks in organogermanium chemistry, and thus play an important role in modern organometallic chemistry.[11-13]

More recently there has been a renewed interest in germanium containing species from the perspective of the semiconductor industry. It has been shown that the mobility of carriers in germanium is greater than in carbon and silicon, making them particularly attractive for the design of high performance logic devices.[11] As with the silicon containing species discussed above, it has been found that germanium containing radicals are an important part of the CVD process in the development of semiconductor films. As such, the structures and isomerisation processes occurring in germanium molecular systems is of fundamental significance to understand the interaction mechanism of the deposition process. Compared with silicon, there has been relatively little work carried out on germanium containing species. However, the recent interest coming from the electronics industry has spurred on recent experimental and theoretical studies in the area.[14-20]

Finally, it is worth mentioning the potential interest of germanium containing species in space. Unlike, silicon, germanium is not known to be particularly abundant in the interstellar medium. However, very recently, atomic germanium has been detected in space. In 2002, a transition belonging to Ge III (1088.46 nm) was detected and measured for the first time in the planetary nebulae (PNe) SwSt 1, BD + 30°3639, NGC 3132 and IC 4593.[21] As with the silicon containing species it is expected that as

more and better laboratory data is collected on germanium-containing species such as GeO, GeC, $GeC_2$, GeCN and GeNC, it is just a matter of time before germanium-containing species are discovered in space. However, up to now no such gas-phase molecular species have been found in either the stellar or interstellar medium.

The work on germanium in this thesis is covered in Chapter 7, detailing an analogous study to that in Chapter 5. This looks at the various isomers of the [H, Ge, N, C, O] system, looking at the relative stability and possible isomerisation processes which may occur.

## 1.4 Experimental and Theoretical Methods

### 1.4.1 Laser Spectroscopy

Spectroscopy has become an essential tool in the understanding of virtually all compounds, from early measurements of the electronic structure of hydrogen atoms, through to the NMR spectra of complex biological molecules.

An important development in spectroscopy in recent decades has been the introduction of the laser.[22] The most important properties of laser radiation are the high intensity they can afford, monochromaticity, low beam divergence and coherence that this radiation source produces. These properties have been used to great effect, making many new techniques possible, and increasing the applications of existing ones. The high intensity of a laser as a light source in spectroscopy makes it possible to detect trace amounts of a species with high sensitivity. For example, the laser induced fluorescence (LIF) spectroscopy technique used in this work relies upon the high intensity of the laser to provide electronic spectra with very high detection sensitivity.

Despite the development of new techniques, most notably cavity ringdown absorption spectroscopy (CRDS),[23] LIF is still an extremely important technique in the investigation of short-lived species such as free radicals.

The high resolution gained by using lasers in spectroscopy can provide a great deal of information on molecules. Electronic, vibrational, rotational and, occasionally, even nuclear hyperfine structure can be observed. This can then be linked to the geometry and bonding in the molecule being studied.

Another significant experimental development in the study of chemical intermediates is the use of supersonic jet expansion.[24] Supersonic jet expansions provide a virtually collisionless, and extremely low temperature environment. This environment is ideal for the study of highly reactive species, such as free radicals, and has been exploited in this work. The low sample concentrations obtained in a supersonic jet means that the highly sensitive techniques of laser spectroscopy are particularly suited to the detection of species in this environment. A more detailed description of the techniques used can be found in Chapter 2.

### 1.4.2 Theoretical Studies of Molecules

An understanding of the principles of quantum mechanics has yielded a number of theoretical methods for predicting the molecular properties of various systems. The Schrödinger wave equation, along with many of the fundamental concepts of quantum mechanics, was introduced in the 1920s. This equation describes the properties of molecular structure in quantum mechanical terms, providing the foundation for many methods of electronic structure calculations.

Modern quantum mechanical methods, both *ab initio* and semi-empirical, are commonly used in the interpretation of physical observations. *Ab initio* (meaning 'from first principles') calculations attempt to describe molecular structure using only quantum mechanical principles and a few fundamental physical constants, whereas semi-empirical techniques, while still retaining a quantum mechanical picture, make assumptions based on experimental data, which simplify calculations.[25] Being able to accurately model molecular structures and reactions in chemistry can help describe many physically unobservable phenomena as well as resolve ambiguity in experimental results. With the capabilities of modern computers, accurate simulations of almost any molecule or reaction type are becoming a very real prospect, even for large systems such as biological molecules.

Both *ab initio* calculations and semi-empirical techniques have been used in this work to predict the structure and properties of the molecules observed in the experimental work. As well as providing a guide for the experimental results, the calculations provide an insight into the quality of the particular theoretical methods

employed. Details of the theoretical methods used in this work are discussed in more detail in Chapter 3.

## *1.5    Aims and Thesis Content*

To date there have been no spectroscopic studies on pseudohalosilylene species with the exception of  a microwave study of HSiCN and HSiNC,[26] and an infrared matrix isolation study of some [H, Si, C, N] isomers.[27] As a result, there is a lack of spectroscopic studies on these species which could be used to yield excited state parameters. Therefore, the first aim of this project was to establish whether or not it is possible to carry out laser induced fluorescence (LIF) studies on any such species and to extract useful data on both the ground and excited states. Briefly, the generation of these species was attempted by subjecting various precursors to a high voltage discharge before being supersonically expanded into a vacuum chamber through which a tuneable dye laser was passed. At the point of intersection between the supersonic jet and the dye laser beam, any species present were electronically excited and the resulting fluorescence was detected as a function of the laser wavelength to produce a LIF spectrum. The results of these efforts were successful in allowing the observation of the LIF spectrum of HSiNC for the first time. As an extension to this work, the LIF spectrum of the analogous HSiNCO species was also observed together with a detailed theoretical study of the possible [H, Si, N, C, O] isomers, constituting the first ever study of its kind. Finally a similar theoretical study has been carried out on the possible [H, Ge, N, C, O] isomers to aid in the future possible spectroscopic studies of such species.

The content of the remainder of this thesis is as follows. In Chapter 2, the experimental procedure is described in detail, along with some important aspects of the spectroscopic background theory relevant to the work discussed in this thesis. Chapter 3 covers the theory behind the theoretical methods employed in this work. Chapter 4 details the previous work on halo- and pseudohalosilylene species as well as the LIF and dispersed fluorescence (DF) spectroscopic study of the isocyanosilylene (HSiNC) radical species. Also discussed in Chapter 4 are details of theoretical studies conducted previously,[28,29] together with more high-level calculations conducted by the author of this thesis for use as comparison data with the experimental data collected. Chapter 5 gives details of the results of the high-level theoretical study on the possible [H, Si, N, C, O] isomers. Chapter 6 focuses on

the LIF and DF spectroscopic investigation of isocyanatosilylene (HSiNCO) radical species. Finally, Chapter 7 focuses on a theoretical study, analogous to that described in Chapter 5, on the possible [H, Ge, N, C, O] isomers. Each of the results chapters (4, 5, 6 and 7) contains a summary of the findings and conclusions drawn, as well as a discussion of the scope for further work in the area.

## 1.6    REFERENCES FOR CHAPTER 1

(1)     Whitaker, J. C. *The Electronics Handbook*; CRC Press and IEEE Press: Cleveland, **1996**.

(2)     Hitchman, M. L.; Jenson, K. F. *Chemical Vapour Deposition: Principles and Applications*; Academic Press: London, **1993**.

(3)     Wilson, R. W.; Penzias, A. A.; Jefferts, K. B.; Kutner, M.; Thaddeus, P. *Astrophys. J.* **1971**, *167*, L97.

(4)     Morris, M.; Gilmore, W.; Palmer, P.; Turner, B. E.; Zuckerman, B. *Astrophys. J.* **1975**, *199*, L47.

(5)     Ohishi, M.; Kaifu, N.; Kawaguchi, K.; Murakami, A.; Saito, S.; Yamamoto, S.; Ishikawa, S.; Fujita, Y.; Shiratori, Y.; Irvine, W. M. *Astrophys. J.* **1989**, *345*, L83.

(6)     Butenhoff, T. J.; Rohlfing, E. A. *J. Chem. Phys.* **1991**, *95*, 1.

(7)     Apponi, A. J.; McCarthy, M. C.; Gottlieb, C. A.; Thaddeus, P. *Astrophys. J.* **1999**, *516*, L103.

(8)     Guelin, M.; Cernicharo, J.; Kahane, C.; Gomezgonzalez, J. *Astron. Astrophys.* **1986**, *157*, L17.

(9)     Lucas, R.; Guelin, M.; Kahane, C.; Audinos, P.; Cernicharo, J. *Astrophys. Space Sci.* **1995**, *224*, 293.

(10)    Thaddeus, P.; Cummins, S. E.; Linke, R. A. *Astrophys. J.* **1984**, *283*, L45.

(11)    Barrau, J.; Escudie, J.; Satge, J. *Chem. Rev.* **1990**, *90*, 283.

(12)    Pola, J.; Taylor, R. *J. Organomet. Chem.* **1992**, *437*, 271.

(13)    Riveros, J. M. *Int. J. Mass Spectrom.* **2002**, *221*, 177.

(14)    Harper, W. W.; Clouthier, D. J. *J. Chem. Phys.* **1998**, *108*, 416.

(15)    Harper, W. W.; Klusek, C. M.; Clouthier, D. J. *J. Chem. Phys.* **1998**, *109*, 9300.

(16)    Pang, W. X.; Wang, M. S.; Yang, C. L.; Zhang, Y. F. *J. Chem. Phys.* **2007**, *126*, 194301.

(17)    Saito, K.; Obi, K. *Chem. Phys. Lett.* **1993**, *215*, 193.

(18)    Wang, Q.; Ding, Y.; Sun, C. *J. Chem. Phys.* **2005**, *122*.

(19)    Wang, Q.; Ding, Y. H.; Xie, H. B.; Sun, C. C. *J. Comput. Chem.* **2006**, *27*, 505.

(20)    Sari, L.; Yamaguchi, Y.; Schaefer, H. F. *J. Chem. Phys.* **2001**, *115*, 5932.

(21)    Sterling, N. C.; Dinerstein, H. L.; Bowers, C. W. *Astrophys. J.* **2002**, *578*, L55.

(22)    Andrews, D. L.; Demiov, A. A. *An Introduction to Laser Spectroscopy*; Plenum Press: New York, **1995**.

(23)    Wheeler, M. D.; Newman, S. M.; Orr-Ewing, A. J.; Ashfold, M. N. R. *Journal of the Chemical Society-Faraday Transactions* **1998**, *94*, 337.

(24)    Engelking, P. C. *Chem. Rev.* **1991**, *91*, 399.

(25)    Levine, I. N. *Quantum Chemistry*, 4th ed.; Prentice Hall: New Jersey, **1991**.

(26)    Sanz, M. E.; McCarthy, M. C.; Thaddeus, P. *Astrophys. J.* **2002**, *577*, L71.

(27)    Maier, G.; Reisenauer, H. P.; Egenolf, H.; Glatthaar, J. *Eur. J. Org. Chem.* **1998**, 1307.

(28)    Flores, J. R.; Perez-Juste, I.; Carballeira, L. *Chem. Phys.* **2005**, *313*, 1.

(29)    Wang, Q.; Ding, Y. H.; Sun, C. C. *Chem. Phys.* **2006**, *323*, 413.

# Chapter Two

*Experimental Design and*

*Spectroscopic Background*

## 2.1  Introduction

This chapter describes the main experimental aspects involved in the production and observation of the species investigated in this work. After a general overview of the experimental set-up, more detailed descriptions of certain features of the experiment are given. After this there is a reasonably lengthy discussion of the background theory of the spectroscopic techniques employed in the work contained in this thesis including: general spectroscopic theory of asymmetric tops, selection rules, fitting procedures.

## 2.2  Overview of Experiment

Figure 2.1 shows a diagram of the overall laboratory arrangement for the laser-induced fluorescence (LIF) experiments carried out in this work. Below is a brief description of a typical experiment that will make the central features of the diagram clear.

An inert carrier gas (typically argon) at a pressure of approximately 2 bar is flowed through the pick-up cell which contains a small amount of the precursor sample. The sample then enters the vacuum chamber through a pulsed valve. As the gas mixture exits the pulsed valve it passes between two ring electrodes across which a pulsed electric discharge is created. This discharge produces radical species which are then supersonically cooled as they travel into the centre of the vacuum chamber.

The method used to probe the short-lived species produced in the discharge is LIF spectroscopy. In this method a tuneable dye laser crosses the supersonic jet causing electronic transitions in the molecular species. Fluorescence from the decay of the electronically excited molecules is monitored with a photomultiplier tube (PMT). The signals produced are collected as a function of the probe laser wavelength to give an excitation spectrum. The laser wavelength is calibrated by means of an optogalvanic cell (Section 2.6.2) coupled with an etalon and photodiode to allow accurate wavelength determination.

## 2.3  Vacuum System

The LIF vacuum chamber (designed by Dr. M. D. Wheeler and built in the University of Leicester Chemistry Department workshop) is shown in Figures 2.2, 2.3 and 2.4. It consists of a hollow stainless steel cylinder, 300 mm high and 261 mm

in diameter with various ports labelled **A-G**. Port **A** is a viewport, which allows laser alignment when the system is under vacuum, and can be covered when running LIF experiments to prevent any ambient light entering the chamber. Alternatively, to achieve maximum fluorescence collection, a concave spherical mirror may be mounted in port **A** with a suitable effective focal length to be imaged on to the PMT mounted on the opposite side (port **B**). This method was of particular use when recording the dispersed fluorescence spectra. Figure 2.5 shows a photograph of a typical setup for the collection optics in such an experiment.

Port **B** is where the PMT is mounted in such a way that it is perpendicular to the laser beam. Ports **C** and **D** provide entrance and exit windows for the probe laser via long baffle arms as shown in Figure 2.3. The turbo pump (Leybold Turbovac T 1600) is positioned at port **G** on the underside of the chamber, backed by a roots blower (Edwards EH250) and rotary pump (Edwards E2M40). This vacuum system is capable of producing a base pressure of ~$10^{-7}$ torr, measured on a vacuum gauge (Edwards, Penning) on an opening on top of the flange on port **F**. The backing pressure of the system is also monitored by means of another vacuum gauge (Leybold, THERMOVAC) mounted in between the backing pumps and the turbo molecular pump.

The main experimental flange (port **F**) is used to introduce samples through a pulsed valve (General Valve Co., series 9) mounted on the end of a length of 0.25 ″ diameter stainless steel tubing. This tubing passes through the centre of a flange with various electrical feedthroughs mounted on top of the vacuum chamber, via a 0.25 ″ Cajon Ultratorr fitting.
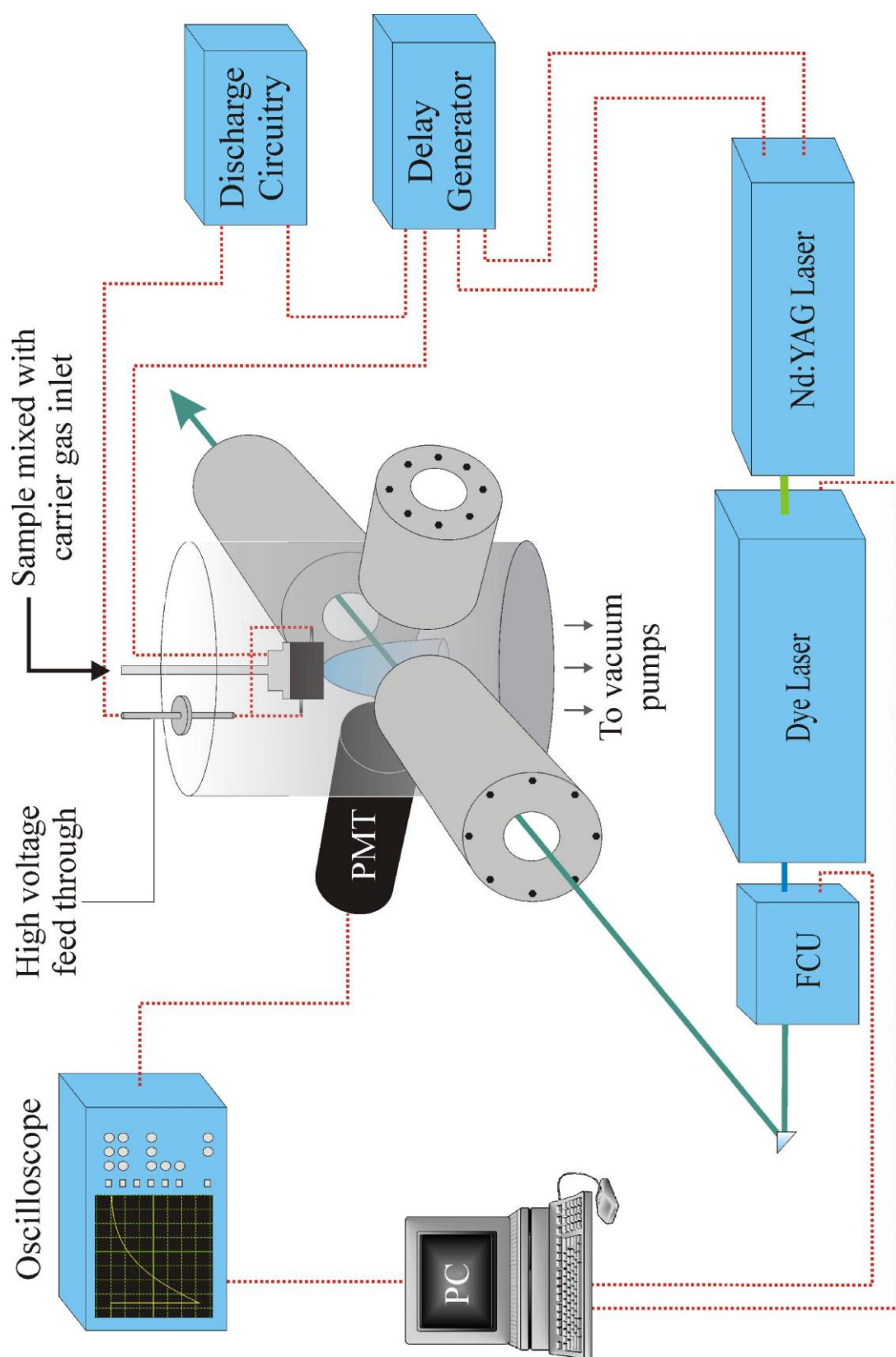
Figure 2.1: Experimental arrangement for a LIF excitation experiment
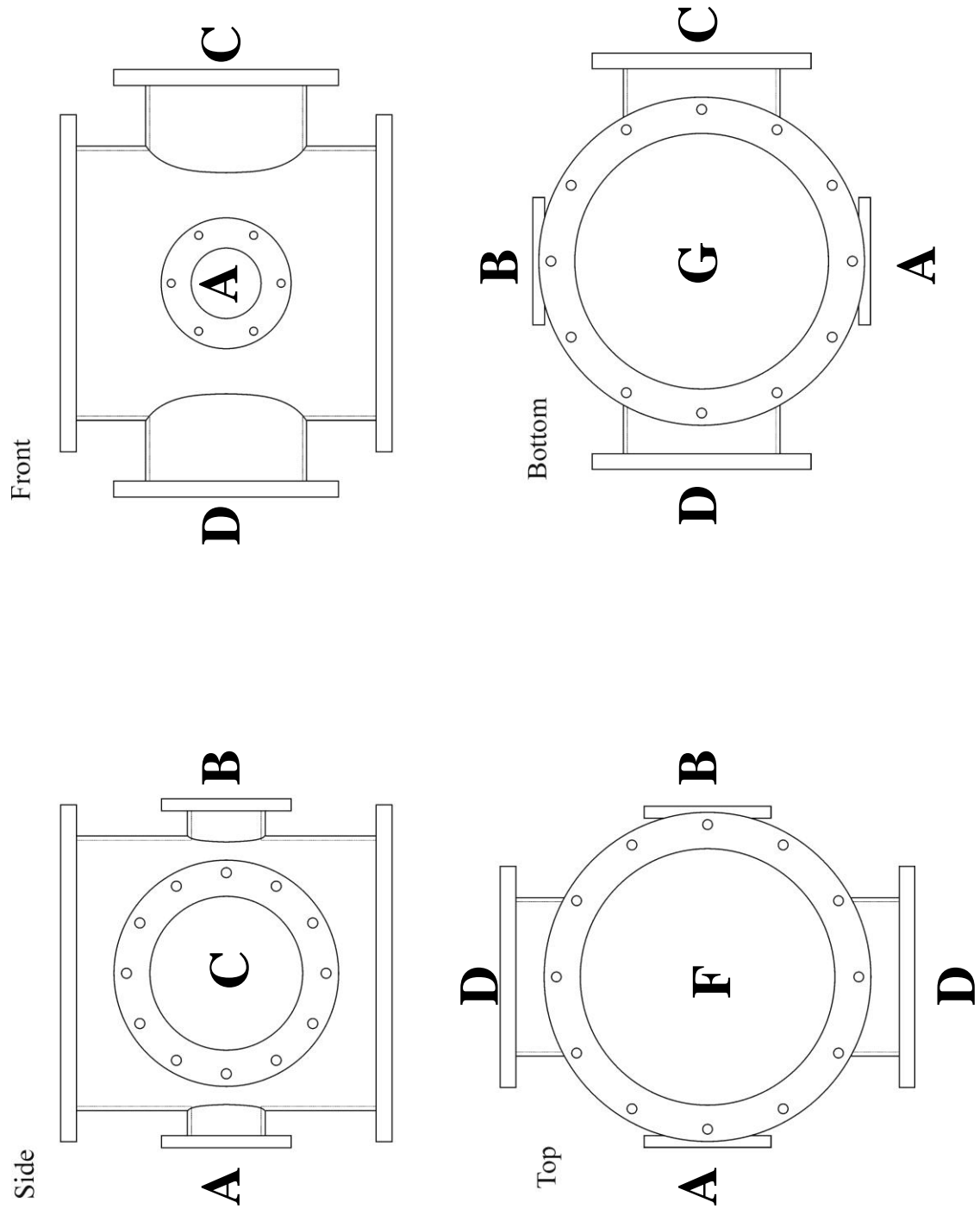
Figure 2.2: Diagram showing projection views of the LIF vacuum chamber
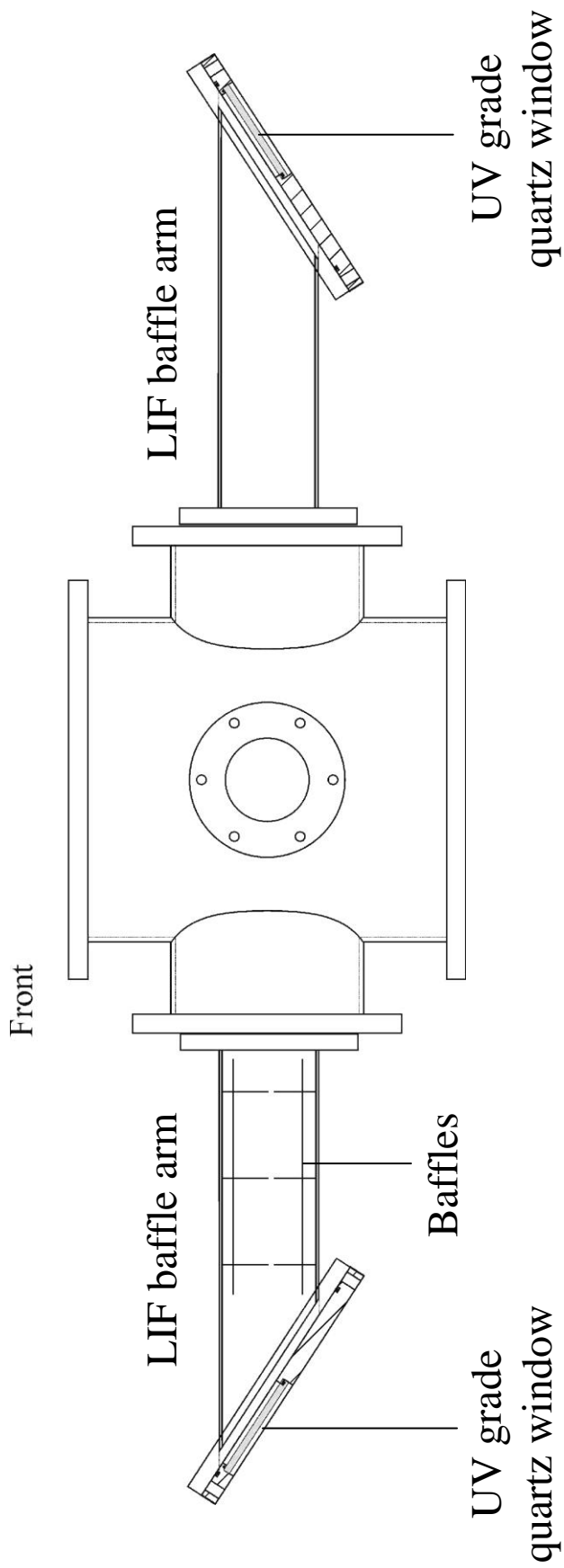
Figure 2.3: Diagram showing a front view of the vacuum chamber including the baffle arms
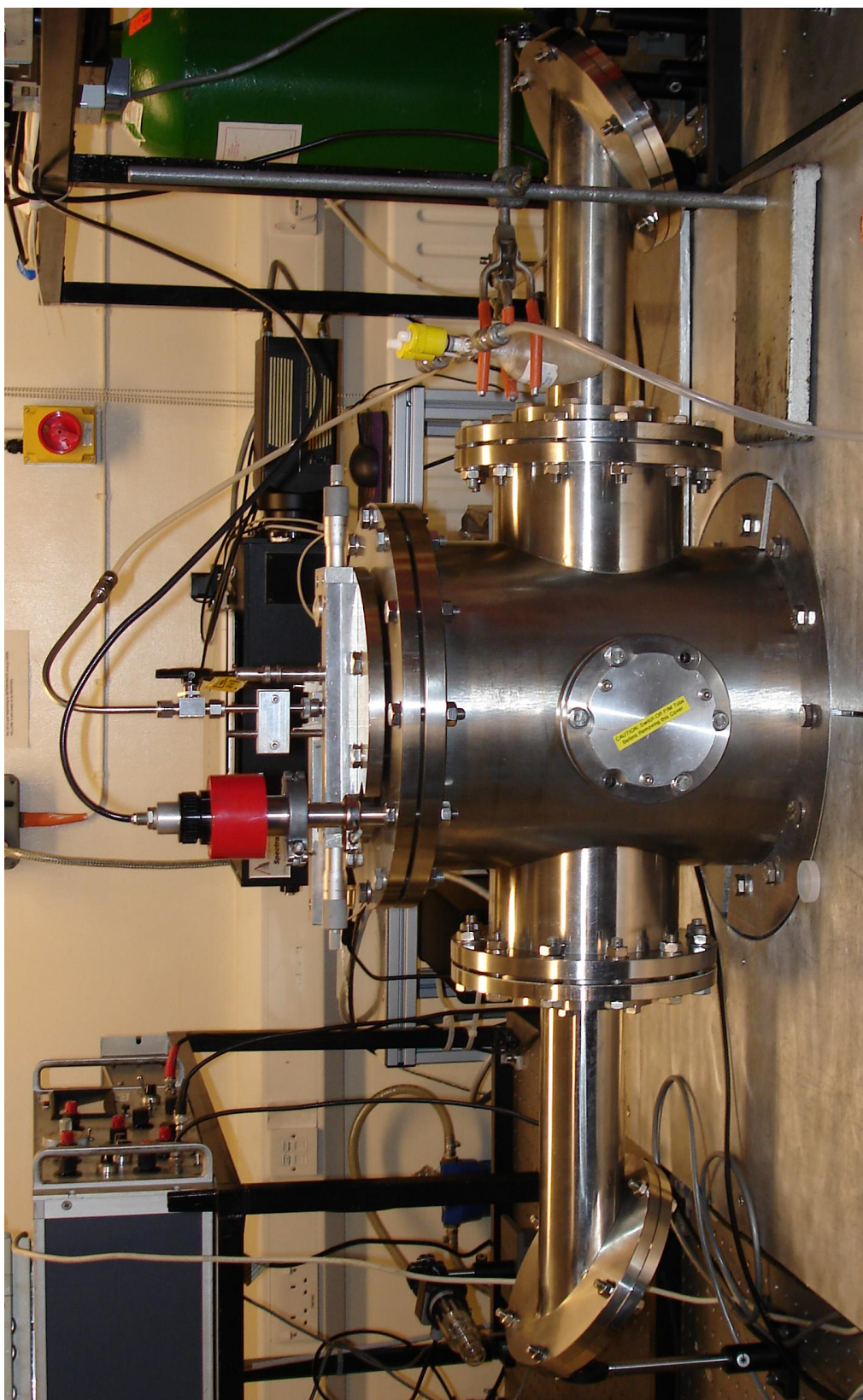
Figure 2.4: Photograph of the vacuum chamber
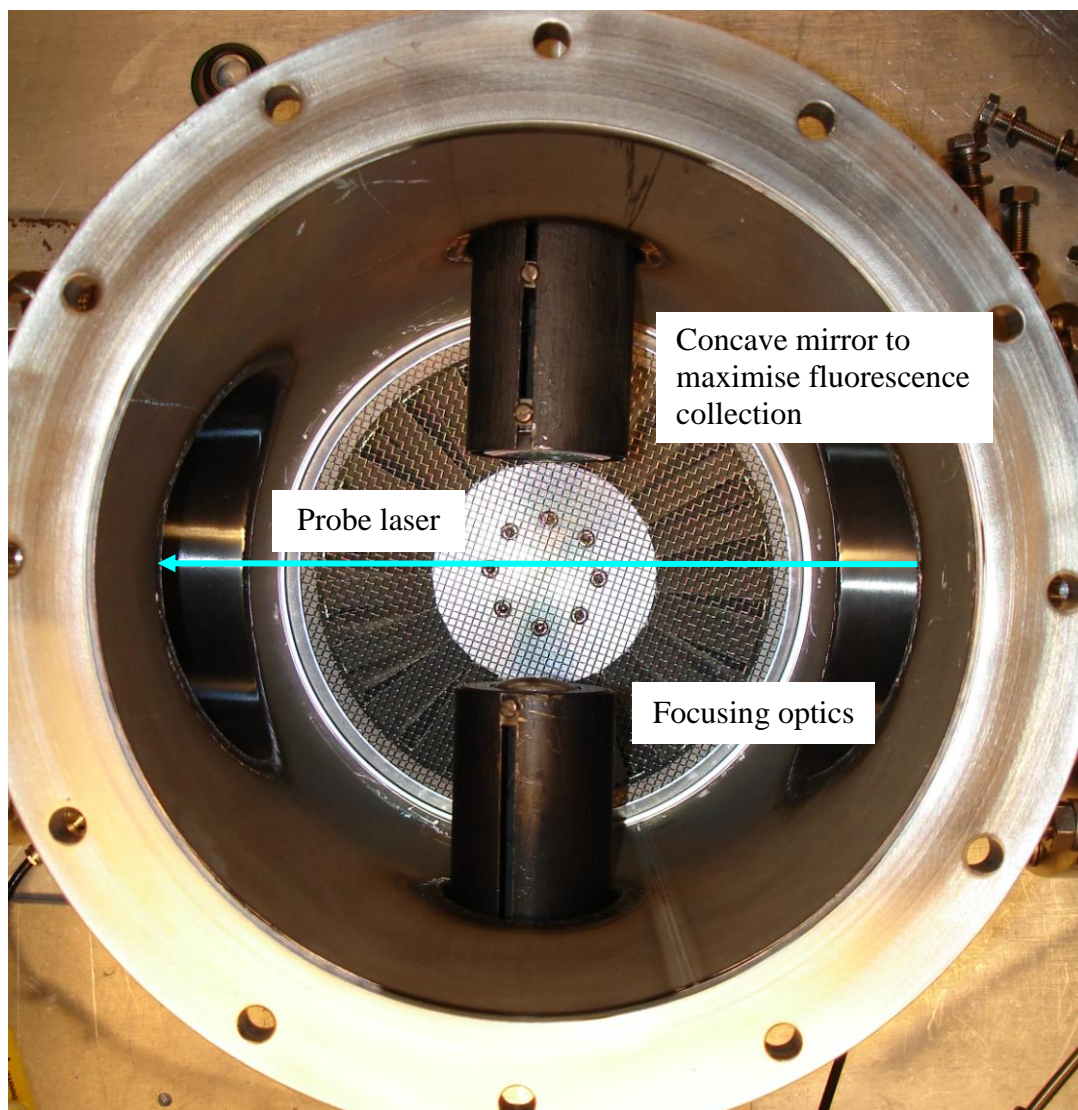
Figure 2.5: Photograph showing the position of the collection optics in place in the vacuum chamber.

## 2.4    Laser Systems

Laser systems are ideal light sources for spectroscopic investigations due to their high intensity, monochromicity and collimated beam profiles. Many different types of laser have been utilised in this work, and what follows is a brief description of each. Further, comprehensive details of lasers in chemistry and laser systems may be found elsewhere.[2-4]

### 2.4.1    Nd:YAG Pump Laser

The dye laser used in this work is optically pumped by a neodymium-YAG (Nd:YAG) laser. The Nd:YAG laser has a strong emission at a wavelength of 1064 nm which can be efficiently frequency doubled or tripled using KDP (potassium

dihydrogen phosphate) crystals to produce laser light with a wavelength of 532 or 355 nm.

Nd:YAG laser operation involves transitions of the inner shell $4f$ electrons of $Nd^{3+}$ ions seeded into a solid matrix of yttrium aluminium garnet ($Y_2Al_5O_{12}$) crystal, or YAG. The $^4F_{3/2}$ and $^4I_{11/2}$ states of $Nd^{3+}$ are split into several components by the YAG's crystal field effect resulting in a strong laser transition at 1064 nm. The laser action follows a four-level system, the population inversion being benefited by depopulation of the lower state and rapid filling of the upper state of the transition by collisional relaxation of the energy levels. In the Spectron SL805G-10 series Nd:YAG laser used in this work, a pair of flashlamps (oscillator and amplifier) are used to optically pump the Nd:YAG rods within the laser cavity.

The upper state of the lasing transition has a reasonably long lifetime so that the Nd:YAG laser can be operated with Q-switching. This produces very short (10 ns) powerful laser pulses. A high peak power increases the efficiency of the frequency doubling and tripling of the laser light mentioned above.

### 2.4.2   Dye Laser

A feature of many lasers is their ability to lase at one or just a few wavelengths depending on the laser medium. Dye lasers offer broad tuneability from near-ultraviolet to near infrared wavelengths making them excellent for use as a light source in electronic spectroscopy. This is facilitated by the variety of organic dye solutions available for use in the active medium of the laser, usually optically pumped by another laser.

The lasing transition in the dyes involves the two lowest singlet electronic states. Vibrational and rotational levels within these electronic states are broadened due to the collisional broadening in the liquid leading to a continuum of levels. Rapid collisional relaxation of molecules in these singlet states depopulates the upper levels while populating the lower levels of the states, producing a population inversion between the upper levels of the ground electronic state and lower levels of the excited electronic state. This allows the possibility of laser action over a broad wavelength range. The upper state of the dye is populated by optical pumping using a Nd:YAG laser (see above).

### 2.4.3    High Resolution OPO

High resolution spectra were recorded using a pulsed optical parametric oscillator (OPO) laser system in the laboratory of Dr C. M. Western at the University of Bristol. What follows here is a brief description of the OPO laser system used, as its design and performance has been well documented elsewhere.[1,5]

Figure 2.6 shows a schematic of the OPO cavity. Two BBO crystals are mounted in a four mirror planar cavity in a walk-off compensation arrangement.[6] The BBO crystals are pumped through one of the cavity mirrors with a portion of the 355 nm output of an injection seeded Spectra-Physics PRO 190-10 long-pulse Nd:YAG laser. The OPO seeds on the idler wave with an external cavity diode laser (EOSI ECU-2010). The diode module used in this work lases between 890 and 930 nm, which corresponds to a tuning range of the signal wave of 480 and 504 nm. One of the cavity mirrors is mounted on a piezoelectric (PZT) driven mount. The cavity was locked to the seed laser by modulating the PZT driven mirror at approximately 3 kHz. The leakage of continuous wave (cw) light through one of the cavity mirrors was monitored with a photodiode and the component of this light modulated at 3 kHz was detected with a lock-in amplifier. The error signal thus produced was monitored using a computer program which in turn controlled the offset of the PZT driven mirror using a simple feedback algorithm. The computer program allowed simple detection and discrimination of the diode saturation in the presence of the pump pulse and resetting of the cavity once the end of the PZT adjustment range had been reached. The signal wave was separated from the idler using two dielectric mirrors. The light was then doubled in a KDP crystal before being steered into the vacuum chamber. The overall linewidth achieved for the OPO was 0.015 cm$^{-1}$. Fluorescence from the intersection of the laser and molecular beams was imaged onto an adjustable slit placed in front of a photomultiplier tube (PMT). The slit was set so that only light from the central core of the jet was collected, to minimize Doppler broadening of the spectra. The signal from the PMT was recorded via a digital oscilloscope onto a computer. To calibrate the spectra, a portion of the signal wave was directed to a high resolution wavemeter (Cluster LM-007 Lambdameter), which measured the absolute signal wavelength; this was recorded simultaneously with the spectrum on the computer.
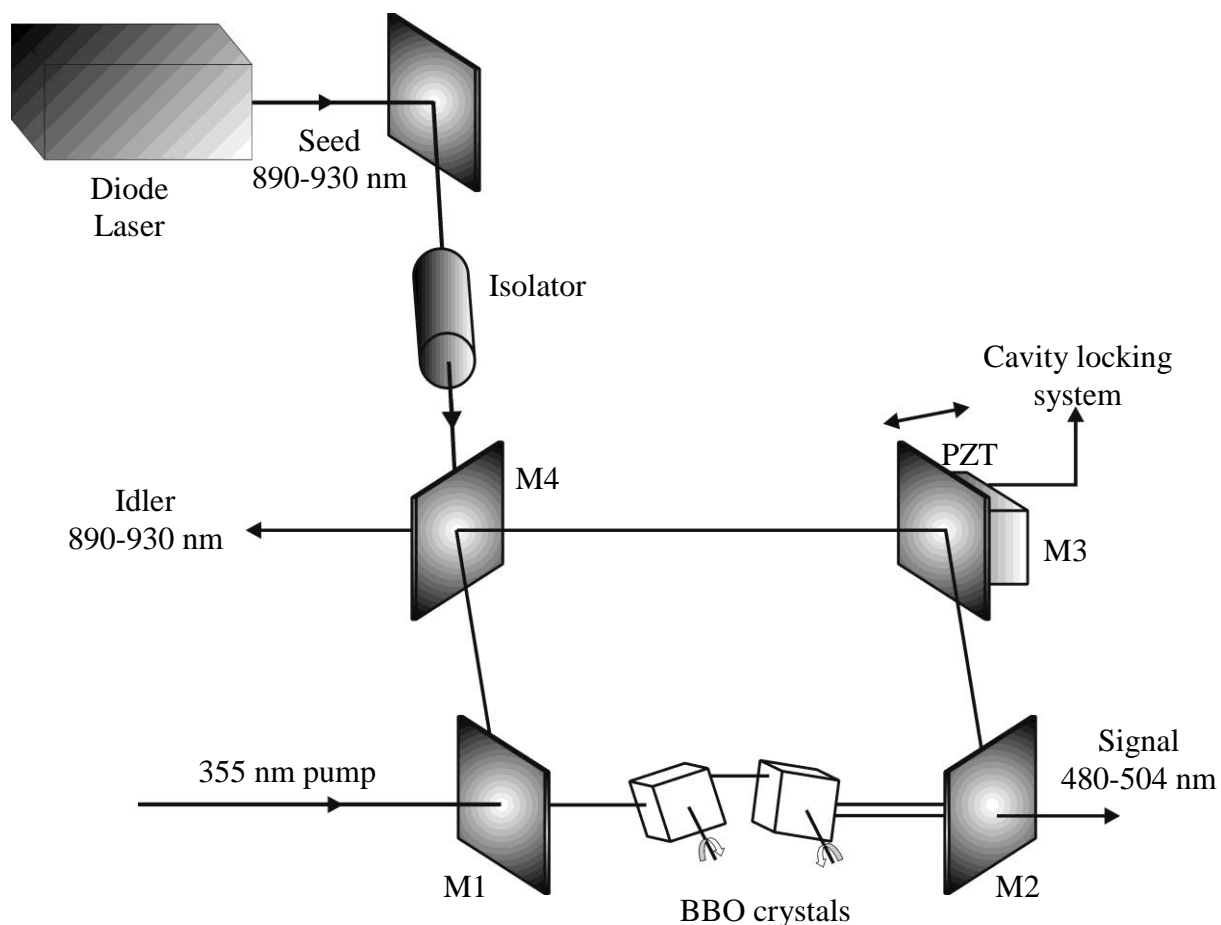
Figure 2.6: Schematic of the OPO cavity. The ring cavity is formed by four plane mirrors (M1-M4) which reflect the idler wavelengths and transmit the signal and pump wavelengths. Active cavity length control is provided by a piezo mounted mirror, M3 (PZT) connected to computer controlled electronics, which include a photodiode and lock-in amplifier. The UV pump beam is introduced through cavity mirror M1 and is separated from the signal beam by an additional dichroic after the cavity. The arrows by the BBO crystals indicate their axes of rotation. Figure modified from Chekhlov et al. 1

## 2.5 Radical Production

### 2.5.1 Pulsed Electric Discharge

The circuitry which creates the high voltage pulses consists of two electric coils: a small Tesla coil and a larger motor car ignition coil. A switch allows selection of one of these coils to obtain an optimum discharge. The Tesla coil is capable of creating an output of up to ~10 kV, and the motor car ignition coil is capable of producing an output of up to ~15 kV. For this work it was found that the Tesla coil gave the most stable discharge. The duration of the discharge was ~ 2 μs.

The pulsed valve opens typically for ~200-250 μs, releasing a small amount of relatively high pressure gas into the chamber. Attached to the end of the pulsed valve is a 24 mm discharge block made out of Delrin$^{TM}$. Housed inside the block are two stainless steel ring electrodes separated by a homemade polytetrafluoroethene (PTFE) spacer (1 mm). Figure 2.7 shows a photograph of the components of the discharge apparatus. A high voltage electric feedthrough allows the electrodes to be connected to the pulsed high voltage source. By allowing the sample jet to pass through the discharge the reactive species is created with little disturbance to the flow of the supersonic jet.

A photograph of the pulsed valve/discharge apparatus is shown in Figure 2.8. The discharge block is attached to the pulsed valve, behind which the carrier gas/precursor mixture is introduced. A 5 mm diameter flow channel passes through the discharge block, which is 30 mm in length, from the pulsed valve to the vacuum chamber. 10 mm downstream from the pulsed valve are the pair of ring electrodes separated by the 1 mm thick PTFE spacer. After the discharge process, the reactive species pass out of the end of the discharge fixture, and are supersonically expanded into the vacuum chamber.

### 2.5.2 Sample Preparation

The precursor used depends on the species under investigation e.g., trimethylsilylcyanide is used to produce the HSiNC radicals described in Chapter 4. A stainless steel 0.25 ″ diameter tubing leads from the regulated inert gas supply to the sample container. 0.25 ″ stainless steel Cajon Ultratorr fittings connected to 0.25 ″ Teflon hose pass the carrier gas into the vacuum chamber via the sample container. The carrier gas used is normally argon at a typical pressure of 1-3 bar.

The carrier gas is passed through a pick up cell (a glass u-tube or bubbler) containing a small amount (~ 5 ml) of the liquid sample (of known vapour pressure), so that the precursor mixes with the carrier gas before it reaches the pulsed valve. Changing the absolute carrier gas pressure or the temperature of the sample used can vary the percentage of precursor in the mixture.

The gas mixture then passes to the experiment via stainless steel tubing connected to the pulsed valve inside the vacuum chamber.
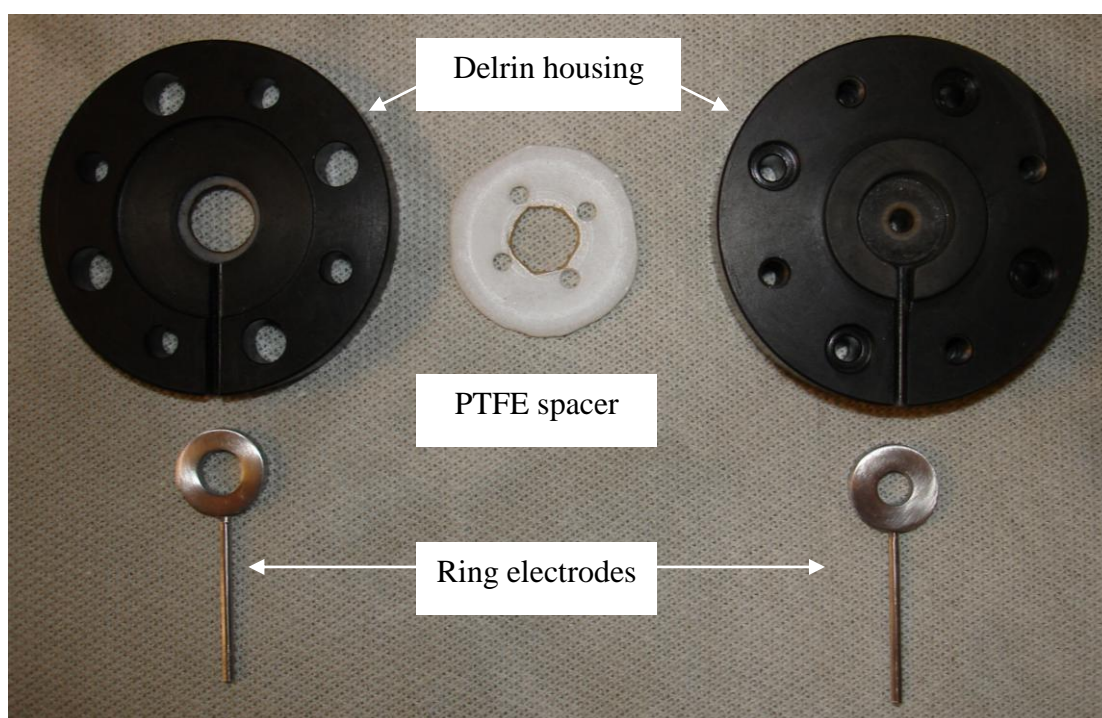


Figure 2.7: Photograph showing the components of the discharge block.
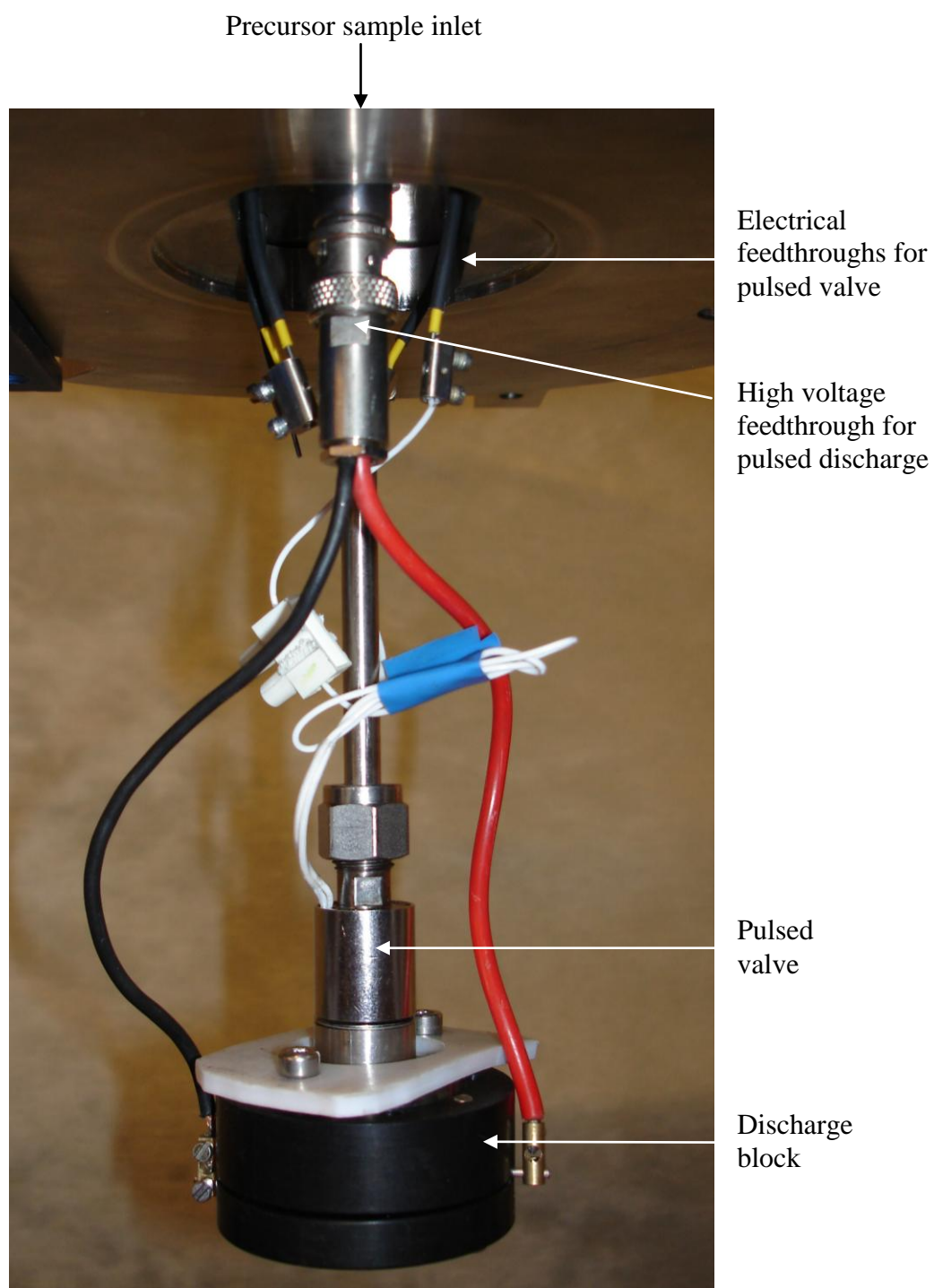
Figure 2.8: Photograph showing the pulsed valve with the high voltage feedthrough and discharge assembly attached.

### 2.5.3 Supersonic Jet Expansion

Supersonic jets have been widely used in spectroscopy for studying species such as radicals, ions and van der Waals complexes. Molecules in a supersonic expansion are relatively simple to produce and can aid spectroscopic studies, as described below.

A supersonic (free) jet expansion can be produced as a gas at relatively high pressure passes through a small orifice (typically tens to hundreds of μm) to a vacuum. If the nozzle diameter is much larger than the mean free path of the molecules then collisions occurring in and just outside the nozzle convert random motion of particles to a highly directional flow with a narrow range of velocities. The result of this is, firstly, downstream of the nozzle virtually collisionless conditions are reached, and secondly, a very low translational temperature, potentially lower than 1 K, can be achieved.

Figure 2.9 is a schematic diagram of a free jet expansion showing the atoms/molecules' have random translational motion and a Maxwellian distribution of speeds before supersonic expansion. On passing into a vacuum through the pinhole, velocity ordering occurs, and the Maxwellian distribution in the region of relatively high pressure has instead been replaced by a much narrower distribution of velocities. This corresponds to translational cooling in the diverging jet. The local speed of sound is dependent on the translational temperature of the jet, and proportional to the square root of the temperature. As the temperature is extremely low, very high Mach numbers may be reached, hence the term *supersonic* jet.

The translational cooling affects the rotational and vibrational temperatures in the jet through energy transfer during collisions, but as the quantised rotational and vibrational energy levels are much further apart than translational energy levels this cooling is less efficient. Typical temperatures of 10 and 100 K are achieved for the rotational and vibrational degrees of freedom, respectively.

High Pressure

Vacuum

Decreasing temperature and
molecular collisions

Number of molecules

Speed

Number of molecules

Speed
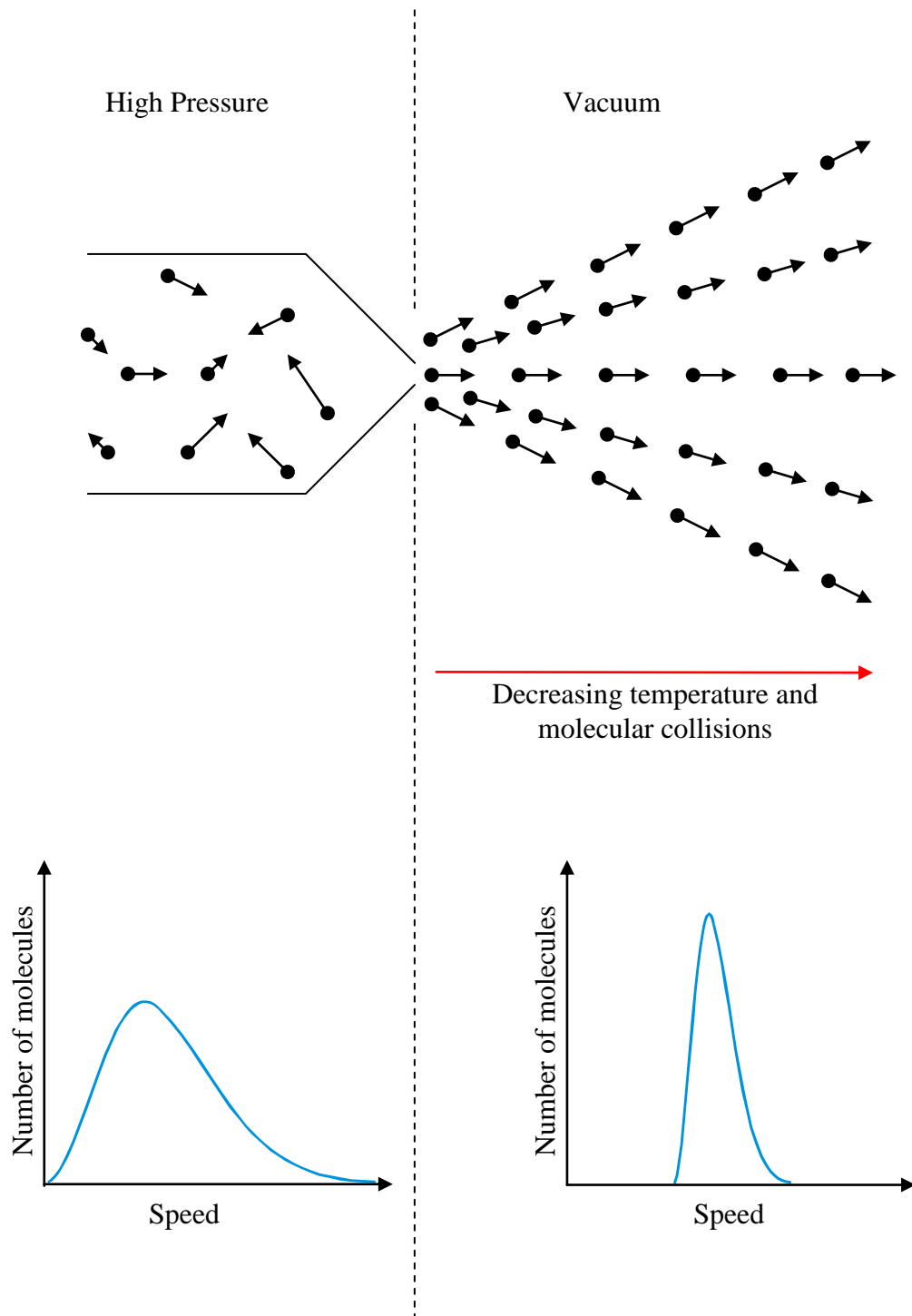
Figure 2.9: Schematic diagram of molecular cooling in a supersonic jet expansion. Arrows indicate the velocity vector of individual gas molecules.

The collision free environment is ideal for the study of highly reactive species such as free radicals. The cooling effect of the jet has many beneficial effects. Firstly, the jet cooling allows the formation of very labile species by removing energy from the degrees of freedom that may lead to dissociation of the molecule such as vibrations and rotations. This makes it possible to observe weakly bound species such as van der Waals complexes. Jet-cooling also leads to great simplification of spectra as fewer quantum levels in the ground electronic state are occupied. Typically transitions are only seen out of the ground vibrational level and just a few rotational levels. As well as reducing the number of rotational lines observed in each vibronic band, there is an increase in the transition intensity out of the more heavily populated (lower energy) rotational levels. Consequently, clearer assignments can be made as vibrational hot bands are suppressed and rotational structure is simplified. Several good reviews on supersonic jets are available for further reading.[7,8]

## 2.6 Spectroscopic Observation

### 2.6.1 Laser Induced Fluorescence (LIF)

LIF is a widely used spectroscopic technique. Its simplicity combined with high sensitivity make it an excellent method for measuring electronic spectra of molecules in supersonic jets, where the sample concentration is usually very low. In fact the technique can achieve successful detection of samples with number densities as low as $10^5$ molecules cm$^{-3}$. Figure 2.10 shows a Jablonski type diagram indicating the different processes that may occur in a spectroscopic experiment.

In our laboratory the tuneable dye laser beam perpendicularly crosses the supersonic jet approximately 20 mm downstream of the discharge fixture. If the frequency of the laser matches a transition frequency of the sample then a photon of the laser light will be absorbed to produce an excited species. This excited species can decay to a lower energy by emitting a photon, *i.e.*, by fluorescing. Fluorescence is collected by a lens ($f$=10 cm) and focused directly on to a photomultiplier tube (PMT) (Electron Tubes B2F/RFI), as shown in Figure 2.11.

The horizontal dye laser beam is perpendicular to the optical axis of the PMT to prevent laser light, as well as light from outside the chamber, reaching the PMT. This allows fluorescence to be detected on a nominally zero background, giving rise to the sensitivity of the technique. In practice some scattered light from the laser will reach

the PMT, but this is minimised by careful laser alignment, and the use of cut-off filters. Scattered light is also minimised by the use of a set of baffles through which the dye laser beam enters the vacuum chamber. Baffles are also available for use on exiting the vacuum chamber, but it has been found that the inclusion of these leads to an increase in scattered light so were not used in the work detailed in this thesis. The windows mounted on each arm of the vacuum chamber are 10 mm thick UV grade quartz windows, which are placed at Brewster's angle (~56°) to maximise the transmission of the polarised laser beam.

In order to observe a transition by LIF, it must have a non-zero transition probability, and the excited state must decay by fluorescing appreciably. This second point is the major limitation of LIF compared with other techniques, as processes other than photon emission can occur by non-radiative relaxation processes, such as internal conversion, collisional relaxation and predissociation. To investigate excited state species, which do not decay by fluorescence, other techniques must be used such as cavity ringdown spectroscopy (CRDS)[9] or resonance enhanced multi-photon ionisation (REMPI).[10]
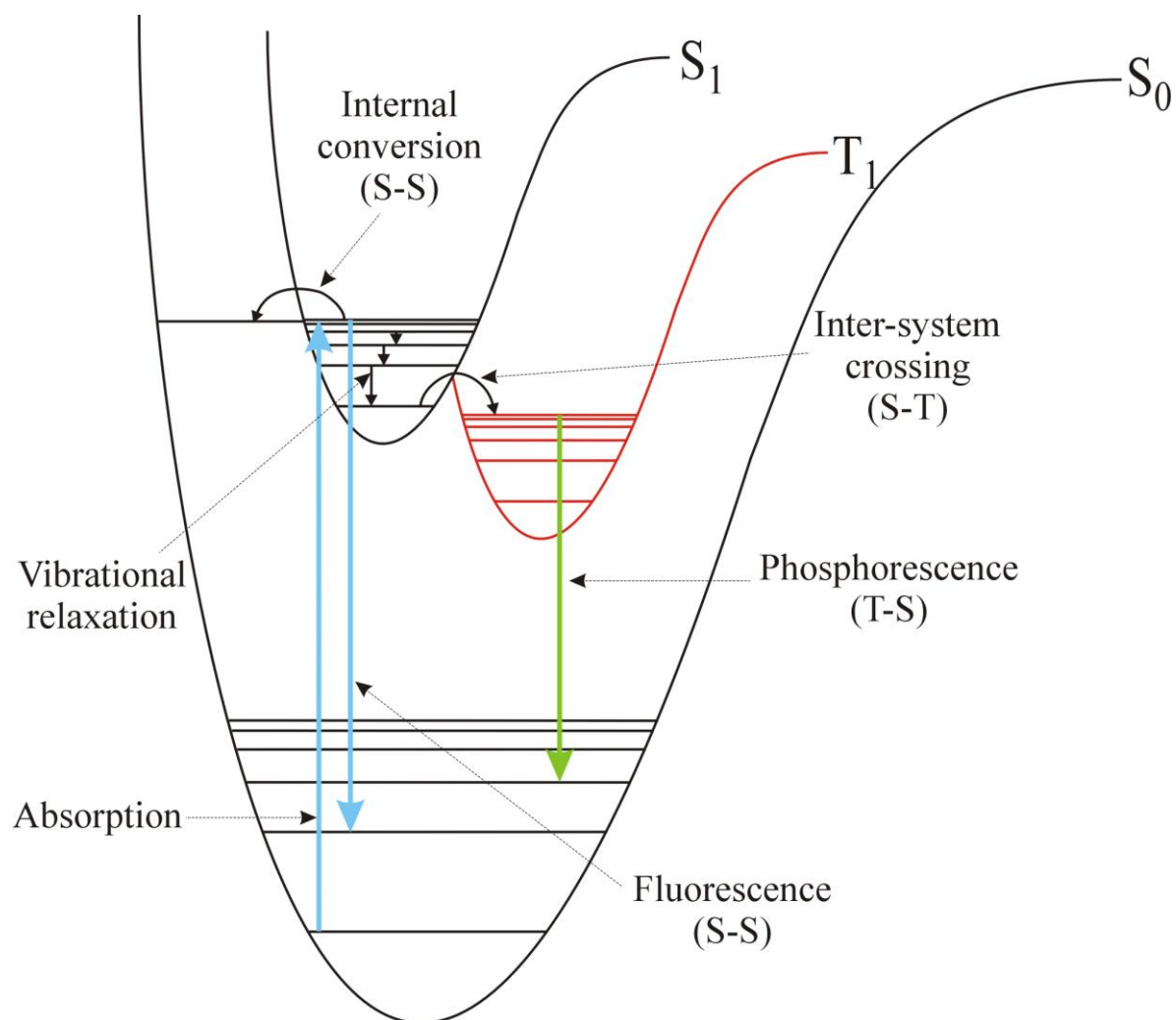
Figure 2.10: Jablonski type diagram indicating the different processes that may occur in a spectroscopic experiment
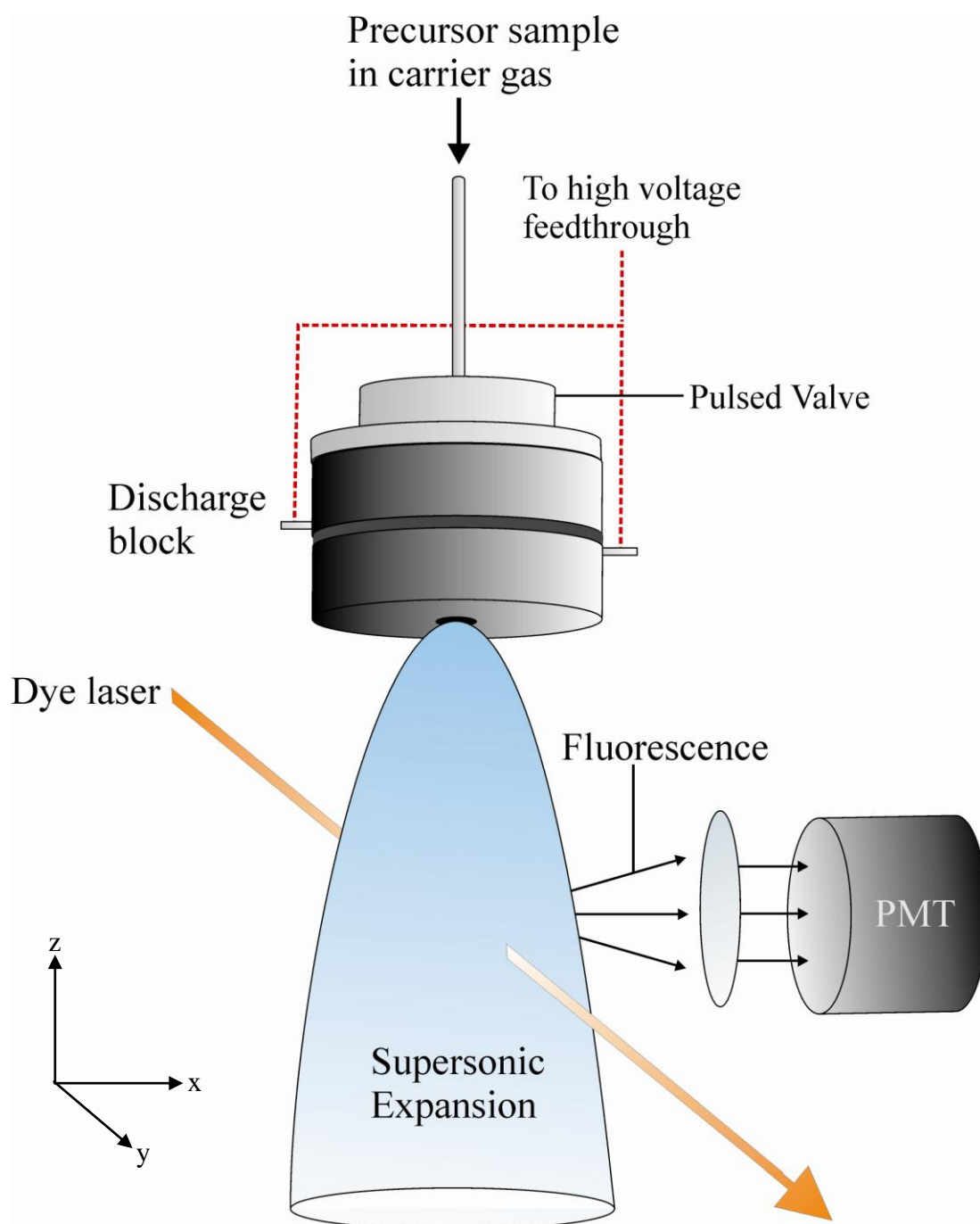
Figure 2.11: Diagram showing the set-up for a LIF experiment

### 2.6.2 Dispersed Fluorescence (DF) Spectroscopy

By wavelength-resolving the fluorescence from electronically excited molecules information about the lower states of the molecules can be gained. This is the essence of dispersed fluorescence (DF) spectroscopy. The DF process is illustrated in the energy level diagram in Figure 2.12. Like LIF, DF spectroscopy is a zero-background technique allowing for high sensitivity.

DF measurements differ from excitation spectroscopy (e.g., LIF) as the dye laser is tuned to, and fixed at, the wavelength of a particular resonance transition. The emission from the chosen excited state is collected and focused onto the entrance slit of a 0.50 m path length scanning monochromator (Acton Research SpectraPro 2500i) fitted with a 1800 lines/mm grating blazed at 500 nm situated at the exit of port **B** in Figure 2.2. The rotatable diffraction grating in the monochromator then disperses the fluorescence and a Peltier cooled CCD camera (PI-MAX system), amplified with a gain of 255 after the exit slits measures the intensity. The spectrum is obtained by scanning the diffraction grating over the desired wavelength range under computer control using the supplied software (WinSpec32). The monochromator scan was calibrated to an estimated accuracy of $\pm 10$ cm$^{-1}$ using known emission lines from a mercury lamp. However, the system used to record the DF spectra in this work was found to drift significantly over very short time periods which explains the relatively high error associated with the measurements.

By dispersing the fluorescence into its component wavelengths some sensitivity is lost when compared to excitation spectroscopy as the light intensity may be spread over a wide spectral range. The slit width on the monochromator may be adjusted to compensate for the typically weaker signals, allowing as much light as possible through. However, there is an inverse relationship between the slit width and the resolution of the spectrum, so by increasing the slit width there is a reduction in the achieved resolution of the spectrum. Even with the narrowest of slit widths the highest achievable resolution is ~10 cm$^{-1}$.
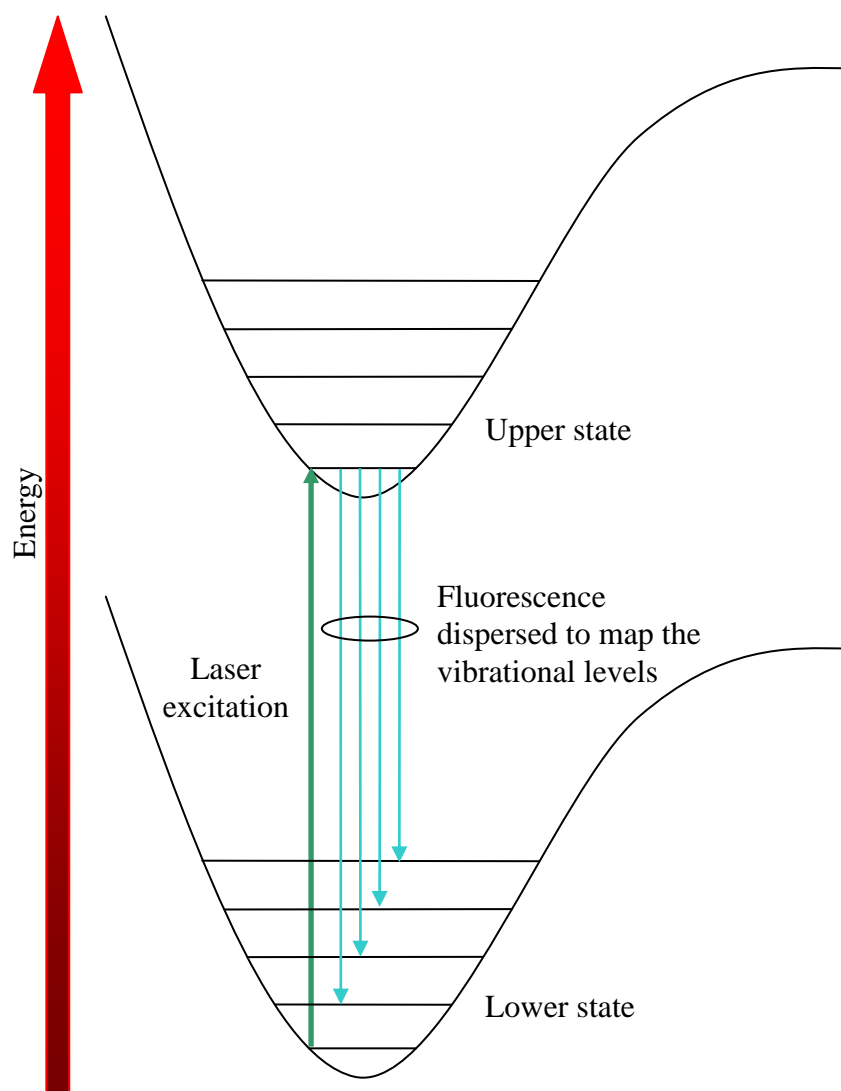
Figure 2.12: Energy level diagram showing how dispersed fluorescence spectroscopy is used to gain information (typically vibrational) on states lying below that initially excited by the pump laser.

### 2.6.3   Laser Calibration by an Optogalvanic Cell

In optogalvanic (OG) spectroscopy, the current passing through a gas discharge is monitored as a laser light source is tuned through the frequencies of allowed transitions for excited atoms in the discharge. When the laser resonantly excites an atom from a low lying state to an excited state, it is excited to a less bound state, thereby increasing the probability that the atom will be ionized by discharge collisions and may contribute to an increase in the discharge current. This small change in discharge current can be detected with great sensitivity if the laser beam is pulsed and the periodic variation of the discharge current at the frequency is detected by a lock-in amplifier. It should be emphasized that OG spectroscopy does not require a photomultiplier tube or photodiode detector to obtain atomic transition spectra, because the gas discharge itself serves as a resonant photodetector. There are many subtleties concerning the OG effect that will not be discussed here, as detailed reviews of the OG effect in high resolution spectroscopy are available elsewhere.[11,12] To obtain an accurate calibration one cannot rely only on the OG cell, as it will obviously only provide spectral lines at specific wavelengths. Therefore, it is usual to combine the OG cell with an etalon of known free spectral range (FSR) to fill in the spaces between the OG lines and allow calibration of suitable accuracy. In this work the optogalvanic signals from a neon filled hollow cathode lamp were detected using a boxcar integrator (Princeton Applied Research, Model 160) and monitored using the computer program, together with the signal from a photodiode picking up the fringes from an etalon with a FSR of 1 cm$^{-1}$.

Wavelength calibration of tunable lasers is a very important part of experimental spectroscopy. For the region between 500 and 675 nm (~ 20000-15000 cm$^{-1}$), an iodine absorption cell may be used, as a good atlas exists. However, in the blue and near UV regions of the electromagnetic spectrum, there is a shortage of suitable species for laser calibration. OG spectroscopy offers a solution to this problem as the OG lines from a hollow cathode offer a means of precise wavelength calibration of tunable lasers. Further information and experimental details of the OG wavelength calibration used in this work may be found elsewhere.[12]

### 2.6.4 Data Collection

Fluorescence signals from the PMT can be optimised in real-time on a digital oscilloscope (LeCroy Waverunner LT342), and captured by a PC using home written software. The software controlling the data collection was written in LabVIEW[TM] [13] by Dr. M. D. Wheeler, with later modifications made by the author. The real-time profile of the signal allows the user to gate a portion of the signal to be integrated during wavelength scans. The signal is sampled over several shots (typically 10-30) for averaging before the program instructs the dye laser to move its grating to the next wavelength position.

### 2.6.5 Pulse Synchronisation

The opening of the pulsed valve must be appropriately synchronised with the discharge firing and the laser pulse. Figure 2.13 shows a diagram indicating the synchronisation in the LIF experiments. The pulse generator (BNC 555 series) is triggered by the opening of the pulsed valve. The pulsed valve opening time is typically 200 μs. The discharge circuitry is triggered 600 μs after the opening of the pulsed valve for a period of 20 μs. The flashlamps of the Nd:YAG pump laser are triggered 530 μs after the opening of the pulsed valve, for a period of 40 μs. The delay between the firing of the flashlamps and Q-switching is 150 μs (so the Q-switch is triggered 680 μs after the opening of the pulsed valve), and the width of this pulse is also 40 μs. The resulting fluorescence signal is collected by the PMT and the signal sent to the oscilloscope before data processing on the PC.
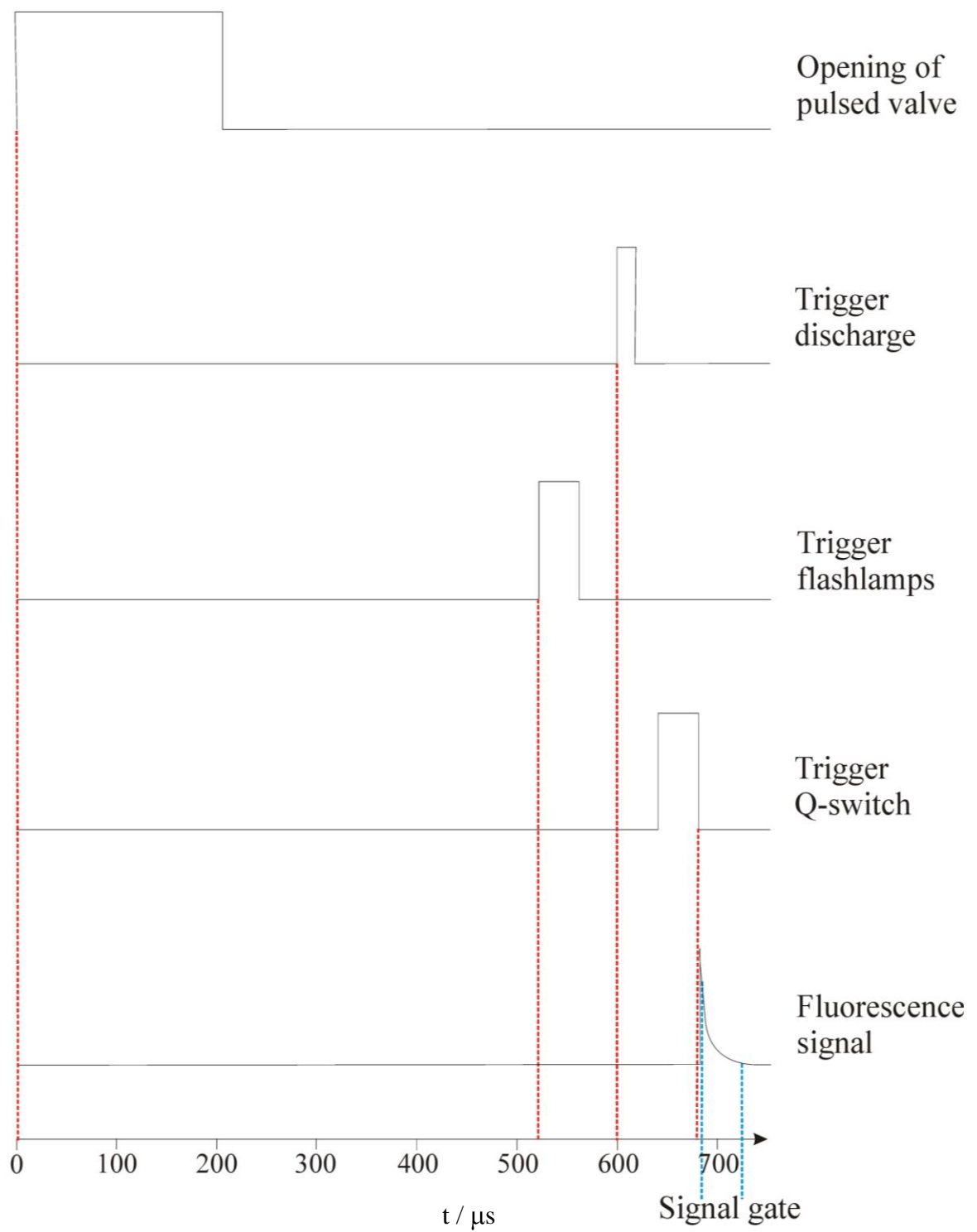
Figure 2.13: Diagram sequence of events in a typical experiment. The Dashed lines in red show which edge of the TTL pulses are active.

## 2.7    Spectroscopic Background Theory

### 2.7.1   Introduction

The general theories of spectroscopy have been reviewed many times, from many different points of view. Notable examples of reference sources are the texts by Bernath,[14] King,[15] Gordy and Cook[16] and Hollas.[4] In this section a brief description of asymmetric tops is given including the relevant points which must be considered for the work contained in this thesis.

### 2.7.2   Asymmetric Tops

As the species under investigation in this thesis belong to the group of species known as asymmetric top molecules, it is pertinent at this point to discuss the general spectroscopic background associated with these species. What follows is a brief description of these species together with the general spectroscopic rules and conventions associated with them.

The majority of polyatomic molecules fall into the asymmetric top category. For an asymmetric top, all three of the principle moments of inertia are different ($I_a \neq I_b \neq I_c$). As a result, in this case, it is not possible to rearrange the Hamiltonian such that it is comprised only of square of the total angular momentum ($\mathbf{R}^2$) and one component of the total rotational angular momentum ($\mathbf{R}_a$, $\mathbf{R}_b$ or $\mathbf{R}_c$). this means that we cannot describe the rotational motion in terms of a conserved motion about a particular axis. This property is best imagined on a macroscopic scale, where asymmetric objects 'tumble' through space in no particular orientation. Compare this with symmetric objects, which will spin about a particular axis.

To solve this problem, one must first determine the 'level of asymmetry' contained within the molecule. This is defined by Ray's asymmetry parameter, $\kappa$, and is defined as:

$$\kappa = \frac{(2B - A - C)}{(A - C)} \qquad [2.1]$$

The value of $\kappa$ ranges from $-1$, representing the prolate symmetric rotor limit, to $+1$, representing the oblate symmetric rotor limit. As with symmetric top molecules, where it was important to be able to distinguish between a prolate top ($I_a < I_b = I_c$) and an oblate top ($I_a = I_b < I_c$), because of the quite different energy level patterns, so

it is important to distinguish between the three possibilities for asymmetric tops. These are: near-prolate ($\kappa \sim -1$), near-oblate ($\kappa \sim +1$) and very asymmetric ($\kappa \sim 0$).

### 2.7.3   Selection Rules

The rotational state is defined by two quantum numbers $J$ and $K$. $J$ is total angular momentum quantum number and $K$ is the quantum number of the projection of the angular momentum on the rotating axis.

The selection rules governing the transitions between rotational energy levels in $J$ for an asymmetric top are:

$$\Delta J = 0, \ \pm 1 \qquad\qquad [2.2]$$

Transitions where $\Delta J = 0$ are called $Q$-branch transitions, and transitions where $\Delta J = -1$ and $+1$ are called $P$-branch and $R$-branch transitions, respectively. The selection rules that replace the $\Delta K = 0$ rule in symmetric rotors are more complex. They involve the parity (*i.e.*, the evenness or oddness) of $K_a$ and $K_c$, and also the direction of the permanent dipole moment of the molecule, which must be non-zero. Consider a system where the dipole moment is along the $a$-axis: The parity of either $K_a$ or $K_c$ must change during the transition. If we label the rotational energy levels *ee*, *eo*, *oe* or *oo*, the selection rules are those given in Table 2.1 for an $a$-axis dipole moment. In this case, the allowed transitions are referred to as $A$-type transitions. The *ee*, *eo*, *oe* and *oo* labels refer to the parity of $K_a$ and $K_c$, *e* refers to an even value and *o* refers to an odd value. Table 2.1 summarises these selection rules for asymmetric top transitions with dipoles along each of the three inertial axes.

Table 2.1: Selection rules for an asymmetric rotor. The direction of the dipole moment determines whether an $A$-, $B$- or $C$-type transition is observed.

| Direction of dipole moment | Selection rules | | | Parity considerations[a] |
|---|---|---|---|---|
| $a$-axis | $\Delta J = 0, \pm 1$ | $\Delta K_a = 0, \pm 2$ | $\Delta K_c = \pm 1, \pm 3$ | *ee* $\leftrightarrow$ *eo* <br> *oe* $\leftrightarrow$ *oo* |
| $b$-axis | $\Delta J = 0, \pm 1$ | $\Delta K_a = \pm 1, \pm 3$ | $\Delta K_c = \pm 1, \pm 3$ | *ee* $\leftrightarrow$ *oo* <br> *oe* $\leftrightarrow$ *eo* |
| $c$-axis | $\Delta J = 0, \pm 1$ | $\Delta K_a = \pm 1, \pm 3$ | $\Delta K_c = 0, \pm 2$ | *ee* $\leftrightarrow$ *oe* <br> *eo* $\leftrightarrow$ *oo* |

[a] The double arrow ($\leftrightarrow$) indicates that the transition may occur in either direction

### 2.7.4 Rotational Analysis of Asymmetric Top Molecules

The fitting of rotationally resolved asymmetric top molecules is non-trivial. This is because for an asymmetric top, with three unequal rotational constants, there is no general formula for the energy levels as there is for simpler cases of linear molecules or symmetric tops. Therefore, the necessary diagonalisation of the Hamiltonian matrix must be performed numerically for any given case by means of a computer program.

When only very low $J$ values are considered the problem can be simplified as centrifugal distortion terms may be minimised and, therefore, essentially neglected. Indeed, in the early days of spectroscopy many microwave studies were conducted with measurement of only a few lines with very low angular momentum for exactly this reason. As computer technology evolved such that it became possible to fit higher order terms, much new work and effort went into simplifying the complex problem of fitting spectra with higher $J$ values, particularly with the inclusion of an accurate description of centrifugal distortion effects.

Today, the standard Hamiltonian operator used for fitting asymmetric top molecules is one of two forms developed by Watson.[17] In the work by Watson, the complexity of the Hamiltonian was reduced significantly with five fourth degree terms, seven sixth degree terms, and in general (n+1) nth degree terms.

Watson's $A$ reduction of the asymmetric top rotational Hamiltonian takes the form of Equation [2.3] in the $I^r$ representation (see below). The definition of $F_1$ is given in Equation [2.5]:

$$E_{k,k} = \left\langle J,k \left| \hat{H}_{rot}^{(A)} \right| J,k \right\rangle = \left[ \frac{1}{2}(B^{(A)} + C^{(A)})J(J+1) \right] + \left[ A^{(A)} - \frac{1}{2}(B^{(A)} + C^{(A)})J(J+1) \right]k^2$$
$$- \Delta_J J^2(J+1)^2 - \Delta_{JK} J(J+1)k^2 - \Delta_K k^4 + ... \qquad [2.3]$$

$$E_{k\pm2,k} = \left\langle J,k\pm2 \left| \hat{H}_{rot}^{(A)} \right| J,k \right\rangle = \left[ \frac{1}{4}(B^{(A)} - C^{(A)}) - \delta_J J(J+1) - \frac{1}{2}\delta_K \left[ (k\pm2)^2 + k^2 \right] + ... \right]$$
$$\times F_1$$

37

Watson's *S* reduction of the asymmetric top rotational Hamiltonian takes the form of Equation [2.4] in the $I^r$ representation (see below). The terms $F_1$, $F_2$ and $F_3$ are defined in Equation [2.5]:

$$E_{k,k} = \left\langle J,k \left| \hat{H}_{rot}^{(S)} \right| J,k \right\rangle = \left[ \frac{1}{2}(B^{(S)} + C^{(S)})J(J+1) \right] + \left[ A^{(S)} - \frac{1}{2}(B^{(S)} + C^{(S)}) \right] k^2$$
$$- D_J J^2 (J+1)^2 - D_{JK} J(J+1)k^2 - D_K k^4 + ...$$

$$E_{k\pm2,k} = \left\langle J,k\pm2 \left| \hat{H}_{rot}^{(S)} \right| J,k \right\rangle = \left[ \frac{1}{4}(B^{(S)} - C^{(S)}) + d_J J + ... \right] \times F_1$$

[2.4]

$$E_{k\pm4,k} = \left\langle J,k\pm4 \left| \hat{H}_{rot}^{(S)} \right| J,k \right\rangle = \left[ h_k + ... \right] \left[ (J+1) - k(k\pm1) \right] F_2 \times F_3$$

Where:

$$F_1 = \left\{ \left[ (J+1) - k(k\pm1) \right] \left[ (J+1) - (k\pm1)(k\pm2) \right] \right\}^{1/2}$$

$$F_2 = \left[ J(J+1)) - (k\pm1)(k\pm2) \right] \left[ (J+1) - (k\pm2)(k\pm3) \right]^{-}$$

[2.5]

$$F_3 = \left\{ \left[ J(J+1)) - (k\pm3)(k\pm4) \right] \right\}^{1/2}$$

In the work contained in this thesis, the inclusion of distortion terms of higher order than quartic was not necessary in order to achieve a good fit of the data. However, it is important to note that the above expressions could also be extended to show sextic (and beyond) centrifugal distortion constants, but for the sake of brevity these have not been shown.

It is usual when fitting a spectrum to assess the fit by trying both the *A* and *S* reductions and then deciding which reduction has given the best fit. If there is no significant difference then it is conventional to use the slightly simpler *A* reduction, although with today's computers it doesn't matter which reduction is chosen as they can be easily handled.

The choice of the representation of the Watson *A* or *S* reduction is important in order to achieve a good fit of data. These representations govern the ordering of the *a*, *b* and *c* inertial axes in relation to the *x*, *y* and *z* Cartesian axes. As will be seen in later chapters, the molecules under consideration in the work contained in this thesis are

concerned with near prolate asymmetric top molecules (*i.e.*, have $\kappa \sim -1$). Therefore, the $I^r$ representation of Watson's *A* reduction is used in these cases. For near oblate asymmetric top molecules the $III^l$ representation should be used. There are various different representations which may be used for those molecules which are in between these two extremities and these are summarised in Table 2.2.

Table 2.2: The ordering of the inertial axes *a*, *b*, *c* with *x*, *y*, *z* for the various different representations of the Hamiltonian operator for asymmetric top molecules.

| | Representation | | | | | |
|---|---|---|---|---|---|---|
| | $I^r$ | $II^r$ | $III^r$ | $I^l$ | $II^l$ | $III^l$ |
| *x* | *b* | *c* | *a* | *c* | *a* | *b* |
| *y* | *c* | *a* | *b* | *b* | *c* | *a* |
| *z* | *a* | *b* | *c* | *a* | *b* | *c* |

As mentioned in the above text, nowadays the fitting of these complex rotational Hamiltonians are carried out by computer programs. There are many available programs designed for this purpose, and in this thesis three have been used; PGOHPER, SPFIT and Jet Beam 95 (jb95).[18-20] Other home-written programs have also been used during the course of the work conducted for this thesis, and these have all been written in MATLAB®.[21] These programs will be mentioned where relevant in the text.

### 2.7.5 Combination Differences

Ground state combination differences (GSCD) is a technique used by spectroscopists to confirm the identity of a spectral carrier. To carry out GSCD, the following data is required: a rotationally resolved spectrum of the species in question, and some form of comparison data. The comparison data is comprised of the ground state rotational constants, which may come from previous experimental studies or from theoretical calculations.

By examining two transitions with the same excited energy level but different ground energy level, the GSCD may be calculated. Figure 2.14 shows an example of how a GSCD is determined in the form of an energy level diagram. The value of the GSCD may then be compared with a fitted value determined from the comparison data. If

the two determined values are in good agreement with each other, then the identity of the spectral carrier is confirmed, and another estimate for the rotational parameters is produced.

An analogous procedure may be used to determine excited state combination differences (ESCD). In this case, the two transitions share a common ground energy level but different excited energy level. An important advantage of using combination differences in the determination of rotational constants is that it affords ground or excited state data without reliance on the other state.
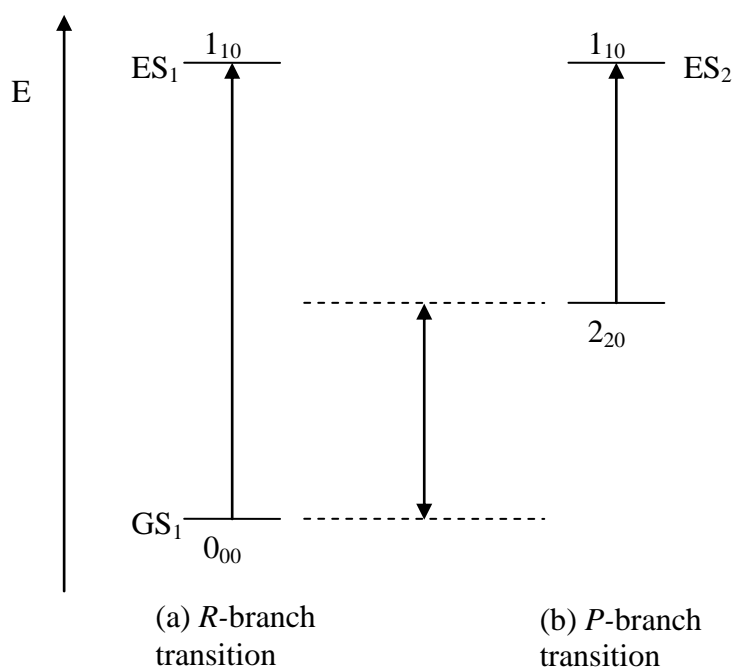


Figure 2.14: Energy level diagram showing how GSCD may be determined from experimentally observed data. (a) shows an $R$-branch transition and (b) shows a $P$-branch transition.

## 2.8    REFERENCES FOR CHAPTER 2

(1)     Chekhlov, O. V.; Fitzpatrick, J. A. J.; Rosser, K. N.; Western, C. M.; Ashworth, S. H. *J. Mod. Opt.* **2002**, *49*, 865.

(2)     Andrews, D. L. *Lasers in Chemistry*; Springer: New York, **1997**.

(3)     Andrews, D. L.; Demiov, A. A. *An Introduction to Laser Spectroscopy*; Plenum Press: New York, **1995**.

(4)     Hollas, J. M. *High resolution spectroscopy*, 2 ed.; Butterworths: Chichester, **1998**.

(5)     Ashworth, S. H.; Elks, J. M. F.; Western, C. M. *Chem. Phys. Lett.* **2000**, *328*, 197.

(6)     Bosenberg, W. R.; Pelouch, W. S.; Tang, C. L. *Appl. Phys. Lett.* **1989**, *55*, 1952.

(7)     Engelking, P. C. *Chem. Rev.* **1991**, *91*, 399.

(8)     Miller, T. A. *Science* **1984**, *223*, 545.

(9)     Wheeler, M. D.; Newman, S. M.; Orr-Ewing, A. J.; Ashfold, M. N. R. *J. Chem. Soc Faraday T.* **1998**, *94*, 337.

(10)    Butler, L. J.; Neumark, D. M. *J. Phys. Chem.* **1996**, *100*, 12801.

(11)    Barbieri, B.; Beverini, N.; Sasso, A. *Rev. Mod. Phys.* **1990**, *62*, 603.

(12)    Zhu, X. M.; Nur, A. H.; Misra, P. *J. Quant. Spectrosc. Radiat. Transfer* **1994**, *52*, 167.

(13)    LabVIEW; 7.0 ed.; National Instruments, **2003**.

(14)    Bernath, P.F. *Spectra of Atoms and Molecules*; Oxford University Press: New York, **1995**.

(15)    King, G. W. *Spectroscopy and Molecular Structure*; Holt, Reinhardt and Winston: New York, **1964**.

(16)    Gordy, W.; Cook, R. L. *Microwave Molecular Spectra*; Wiley: New York, **1984**.

(17)    Durig, J. R. *Vibrational spectra and structure : a series of advances. Vol.6*; Elsevier: Amsterdam ; Oxford, **1977**.

(18)    Pickett, H. M. SPFIT; a linear least squares fitting program, **1990**.

(19)    Western, C. PGOPHER; 5.2.343 ed.; Bristol laser group: Bristol, **2005**; A program for simulating rotational structure; http://pgopher.chm.bris.ac.uk.

(20)    Plusquellic, D. F. Jb95 Spectral Fitting Program, (verison 2.05.1); http://physics.nist.gov/jb95 **2002**.

(21)    MATLAB; 7.4.0.287 (R2007a) ed.; The MathWorks, Inc., **2007**.

# Chapter Three

*Background to Theoretical*

*Methods*

## 3.1 Introduction

The underlying principle of computational chemistry is the elucidation of physically meaningful information from the solution of the time-independent Schrödinger Wave Equation (SWE).

Current advances in computer technology have lead to rapid changes in state of the art computational systems, with molecular systems of increasing size and complexity being routinely studied using high-level methodologies combined with increasingly large basis sets. There are two distinct approaches to quantum chemical calculations: *ab initio* techniques and semi-empirical methods.

*Ab initio* calculations are based solely on the solution of the SWE, and do not rely on any empirical parameters; indeed the term *ab initio* is derived from the Latin phrase "from the beginning" and may be interpreted as meaning "from first principles". Conversely, semi-empirical methods rely on parameterisation, typically to experimental data, in order to fit calculated results to experimental results. Density Functional Theory (DFT) is a popular example of this type of approach. DFT is based around the calculation of the total electron density, and uses sets of mathematical functionals that are tailored to accurately describe a variety of different properties of chemical importance using as few parameters as possible.

## 3.2 The Schrödinger Wave Equation

The Schrödinger Wave Equation (SWE) as shown in Equation [3.1] forms the basis of all quantum chemistry and its solution underpins our understanding of molecular properties. The Hamiltonian operator, $\hat{H}$, consists of terms to describe the electron-nuclei interactions and the electron-electron interactions and is constructed from kinetic and potential energy terms.[1]

$$\hat{H}\,\psi = E\psi \qquad\qquad [3.1]$$

The Born-Oppenheimer approximation, which assumes the nuclei to be effectively stationary relative to the motion of electrons, may be used to simplify the Hamiltonian by separating out the nuclear kinetic energy terms. Applying the Born-Oppenheimer approximation, the form of the Electronic Hamiltonian used in most quantum chemical calculations is

$$\hat{H} = \sum_{i=1}^{n} h_i + \sum_{i=1}^{n}\sum_{j>i} g_{ij} + \sum_{a}\sum_{a>b} \frac{Z_a Z_b}{|R_a - R_b|} \qquad [3.2]$$

In Equation [3.2] $\hat{H}$ is the Hamiltonian operator, $h_i$ and $g_{ij}$ are the one- and two-electron terms, describing the motion of individual electrons in a static electric field (from the nuclei) and the repulsion between electrons, respectively, $Z$ represents a nuclear charge and $R$ the electron-nucleus distance. Note that the wavefunction is thus a function of $3N$ coordinates, where $N$ is the total number of particles. From Equation [3.2] it is clear that the nuclear repulsion term is independent of the electron coordinates, and for any given nuclear geometry will remain constant regardless of the numerical values of the electronic terms. The forms of $h_i$ and $g_{ij}$ are given in full as

$$h_i = -\frac{1}{2}\nabla_i^2 - \sum_{a} \frac{Z_a}{|R_a - r_i|} = \hat{T} + \hat{V}_{Ne} \qquad [3.3]$$

$$g_{ij} = \frac{1}{|r_i - r_j|} = \hat{V}_{ee} \qquad [3.4]$$

where $Z$ represents a nuclear charge, $r$ the electron-electron distance, $R$ the electron-nucleus distance and $\nabla^2$ is the standard Laplacian operator.[2]

Following construction of a suitable wavefunction ($\psi$), which satisfies the SWE, one may use an appropriate operator to generate eigenvalues of almost any desired observable. It is clear from the SWE that the energy of a system is dependent upon the wavefunction, although generation of a wavefunction requires some knowledge of the energy. Thus, iterative procedures must be employed to optimise a wavefunction with respect to the energy.

Initially, a guess wavefunction is constructed, based upon a set of nuclear coordinates. The energy is then minimised for these coordinates by optimisation of the wavefunction in an iterative process. At this point, one may continue using this wavefunction, assuming that the initial guess geometry was of sufficiently good quality, or continue the process by minimising the energy with respect to changes in the nuclear coordinates where at each step the wavefunction is optimised with

respect to energy. This iterative procedure continues until changes to the nuclear coordinates no longer improve the energy of the wavefunction. At this point, the geometry is considered to be optimised. Generally, this procedure is adopted to be sure that the nuclear coordinates are representative of minima or stationary points on the potential energy surface.

Verification that a particular optimised geometry lies at a stationary point is made by calculating gradients and performing harmonic frequency calculations. Location of a true minimum will be revealed by a complete set of real (positive) frequencies. Imaginary (negative) frequencies are indicative of a saddle-point, in which a local maximum is located along the coordinate describing the normal mode whose frequency is negative. The distinction between local and global minima and $n$th order saddle points is shown in Figure 3.1.

The possibility of locating saddle points is of particular significance for molecular systems in which several possible conformations might exist. In order to correctly identify the global minimum in such cases, one must identify all of the likely conformations and characterise them in terms of their relative energies, and their status as true minima.
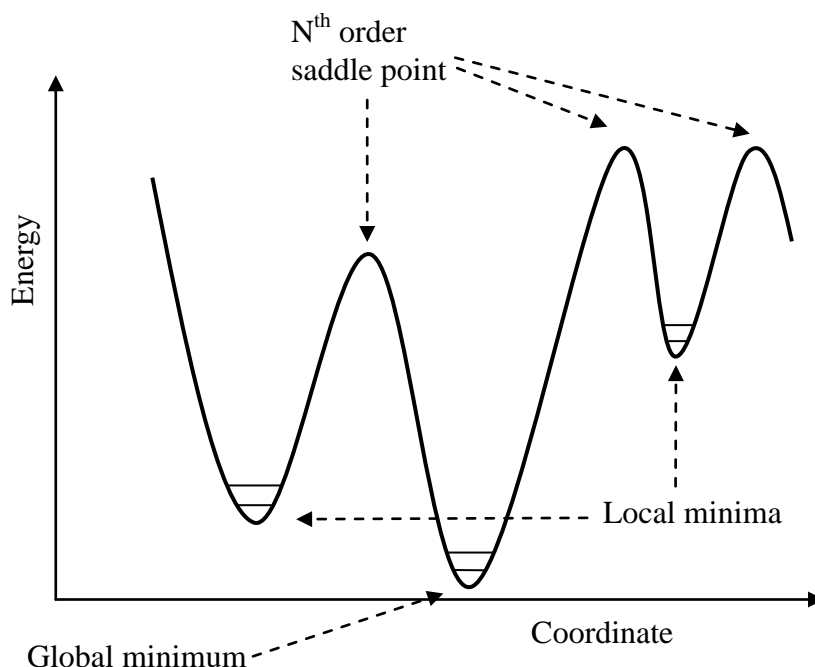


Figure 3.1: Schematic of a potential energy surface, showing the difference between saddle points, local minima and global minimum.

## 3.3    Levels of Theory

### 3.3.1    Hartree-Fock Theory

The Schrödinger Wave Equation is only exactly solvable for one-electron systems (such as H and $H_2^+$), and so in order to extend its application to polyelectronic systems some approximations must be made. Solution of the SWE for an one-electron system results in a set of one-electron atomic or molecular orbitals, each with a well-defined set of quantum numbers ($n$, $l$, $m_l$).[3] An important point to note is that each orbital generated as a solution is a one-electron orbital, and does not take into account the Pauli principle. To satisfy the Pauli exclusion principle, *i.e. a many-electron wavefunction must be antisymmetric with respect to the interchange of the coordinates of any two electrons,* each electron must be described by its spatial coordinates, *r*, as well as its spin, *ω*. Therefore, the electronic wavefunction is constructed from the product of one-electron orbital wavefunctions and spin functions, termed spin-orbitals.[4]

The simplest approximation used to solve the SWE is the Hartree-Fock (HF) approximation, and forms the basis of all *ab initio* calculations. In this method, the wavefunction is formed from a single Slater determinant, which is a finite set of atomic spin-orbitals (or atomic basis functions) that constitute a basis set. The general form of the Slater determinant is shown in Equation [3.5] and explicitly accounts for asymmetry with respect to particle exchange.

$$\psi_{SD} = \frac{1}{\sqrt{n!}} \begin{vmatrix} \phi_1(1) & \phi_2(1) & \cdots & \phi_n(1) \\ \phi_1(2) & \phi_2(2) & \cdots & \phi_n(2) \\ \vdots & \vdots & \ddots & \vdots \\ \phi_1(n) & \phi_2(n) & \cdots & \phi_n(n) \end{vmatrix} \qquad [3.5]$$

Each spin-orbital is represented by a function, $\phi_i(n)$, where *n* is the electron index, *i* is the orbital index, and $1/\sqrt{n!}$ is a normalization constant. Each spin-orbit is orthonormal, such that Equation [3.6] is satisfied (where $\delta_{ij}$ is the Kronecker delta).

$$\langle \phi_i | \phi_j \rangle = \delta_{ij} \qquad [3.6]$$

The Slater determinant can be used to describe the ground state wavefunction of any atom or molecule. HF theory uses a wavefunction of the form given in Equation [3.5] as a trial wavefunction in a variational of Equation [3.1]. By minimising the energy with respect to variations in the spin-orbital gives the so-called HF equations,

$$\hat{F}_i \phi_i = \varepsilon_i \phi_i \qquad [3.7]$$

where $\varepsilon_i$ is the energy of electron $i$ and $\hat{F}_i$ is the corresponding Fock operator given by

$$\hat{F}_i = \frac{1}{2}\nabla_i^2 - \sum_{A=1}^{M} \frac{Z_A}{r_{iA}} + v^{HF}(i) \qquad [3.8]$$

$v^{HF}$ is known as the HF potential, and represents the mean field potential experienced by the $i^{th}$ electron due to the presence of all other electrons. It is dependent on the spin-orbitals of the other electrons in the system, such that the Fock operator is dependent on its own eigenfunctions. As a result, the problem of solving the HF equations is cyclic. These cyclic problems may not be solved analytically, so instead an iterative, numerical approach is undertaken where an initial guess is used to provide the first approximation of the spin-orbitals. The mean field, $v^{HF}$, that each electron is subjected to is then calculated using these approximate functions, which may then be used to solve the eigenvalue Equation [3.7]. The resulting eigenfunctions from this process are then used to generate a new set of spin-orbitals and the process repeated. This continues until there is no further change in the mean field, $v^{HF}$, or the optimisation criteria are met. At this point, the wavefunction is deemed to be optimised, the energy should be minimised, and self-consistency is said to have been reached. Hence, the overall method is known as the self-consistent-field (SCF) method.

It is important to note that each element of the Fock matrix is composed of some combination of basis functions, with unknown coefficients. This combination of functions determines each orbital within the Slater determinant. The result is a series of simultaneous equations which must be solved to determine the coefficients of each function within the orbital description.

An unfortunate shortcoming of the HF method is the mean field approximation. Rather than explicitly treating each two-electron integral and summing over each

electron coordinate, the two-electron integrals are treated in an averaged manner. That is to say, each electron is assumed to interact with the averaged charge from the sum of all other electrons distributed within fixed molecular orbitals. The Coulomb and Exchange integrals do not explicitly evaluate the electron-electron repulsion; rather they evaluate the repulsion between an individual electron and the average charge arising from all other electrons orbiting the positively charged nucleus. To improve the accuracy of an electronic structure calculation some method of accounting for this electron correlation must be included.

### 3.3.2 Post Hartree-Fock Methodologies

Physically, electron correlation can be described as an increase in the electron-electron distance, relative to that obtained from the HF wavefunction, due to the fact that the HF formalism does not correctly describe the dynamic interaction between two or more electrons in the same or nearby orbitals. This is due to the increased instantaneous repulsion that an electron feels as it interacts with other electrons in its vicinity. Often, it is extremely important to include a significant proportion of the electron correlation since this is typically the effect which is important in determining the chemistry of a system. For example, electron correlation is of particular importance when van der Waals species are investigated, because they often rely on instantaneous dispersion interactions to bind two neutral, non-polar fragments together. It is essentially impossible to treat this type of interaction correctly using the HF methodology, and this is deemed the major shortcoming of the HF methodology.

The only way in which the HF approach can be used to treat dispersive interactions is to use an extensive basis set for which the HF wavefunction will account for up to 99% of the correlation energy.[5] However, the larger the basis set, the higher the computational expense and so other methods are required to recover as much of the electron correlation as possible within practical time and computational constraints.

There are a number of methods which may be used for the recovery of electron correlation, although the HF wavefunction forms the basis reference state for the majority of advanced quantum chemistry methods. These advanced methods broadly fall into two categories: perturbation methods and configuration interaction methods.

*3.3.2.1 Perturbation Theory*

Following the construction of a suitable HF wavefunction, electron correlation may be included through the introduction of some small perturbation to the Hamiltonian. Assuming that this perturbation is independent of time, the energy of the system may then be recomputed to include the effects of the perturbation. Perturbation theory assumes that the perturbation to the Hamiltonian is small relative to the unperturbed system. This implies that the results of operating with the perturbed Hamiltonian may be interpreted in terms of the unperturbed zero-order HF wavefunction to maintain a well understood, simple description of the perturbed system.

A popular routine, based on perturbation theory, that adequately incorporates the effects of electron correlation is Møller-Plesset Perturbation theory.[6] This method takes the zero-order HF Hamiltonian and incorporates a small perturbation, devised to model the effects of electron correlation, in the form of a Taylor expansion added to the unperturbed Hamiltonian and is shown in Equation [3.9]. In this equation, $\lambda$ is some coefficient, which describes the extent of the perturbation ($\lambda=0$ describes the unperturbed system, while $\lambda=1$ invokes the full perturbation).

$$\hat{H}_{Pert} = \hat{H}_0 + \sum_{n=1}^{\infty} \lambda^n \hat{H}_n \qquad [3.9]$$

The corrections are referred to as first-, second-, third-order corrections, and can extend up to $i^{th}$-order. The effects of this perturbation to the energy of the HF wavefunction may then be assessed. When one operates on a wavefunction using the perturbed operator, the result will be a series of expectation values that are related to the expectation values obtained from the Fock operator – these values are shown in Equation [3.10].

$$\hat{H}_0 \psi = E_{MP0} \psi = \sum_{i=1}^{n} \varepsilon_i \psi,$$

$$\hat{H}_1 \psi = E_{MP1} \psi = -\langle V_{ee} \rangle \psi, \qquad [3.10]$$

$$\hat{H}_0 \psi = E_{MP2} \psi \ldots$$

Naturally, the operation from the unperturbed operator results in a series of eigenvalues which represent the orbital energies, $\varepsilon_i$, for each occupied orbital

included in the HF wavefunction – this result is unsurprising since the unperturbed Hamiltonian is simply composed of the sum of one-electron Fock-operators used to generate the Fock matrix. The first-order correction results in an expectation value which describes the (averaged) electron-electron repulsion. Since the perturbation takes the form of a summation and the first-order correction takes the form of the averaged electron-electron repulsion, adding the first- and second-order terms will result in the HF energy.

Thus, the first real correction in this scheme is the second-order correction (MP2), and the method is known as Møller-Plesset $n$ (MP$n$) Perturbation Theory where $n$ is the index of the correction. The explicit form of the MP2 correction is given in Equation [3.11] and represents excitation of two electrons from occupied orbitals labelled $i$ and $j$ into virtual orbitals labelled $a$ and $b$.

$$E_{MP2} = \sum_{i<j}^{occ} \sum_{a<b}^{vir} \frac{\left[ \langle \phi_i \phi_j | \phi_a \phi_b \rangle - \langle \phi_i \phi_j | \phi_b \phi_a \rangle \right]^2}{\varepsilon_i + \varepsilon_j - \varepsilon_a - \varepsilon_b} \qquad [3.11]$$

This formalism describes the energy contribution (as a result of electron correlation) from doubly excited determinants; that is to say, excitation of a pair of electrons from a single occupied orbital to a single virtual orbital, and accounts for up to 80% of the correlation energy.[5] Effectively, this second-order correction describes the interaction between pairs of electrons.

One must justify the necessity of further corrections (*i.e.*, the use of MP3, MP4 and further corrections) based on their computational cost. This scales with the sixth power (or more) of the number of electrons for large molecular systems. Therefore, it is generally unfeasible to carry out such calculations, as it will not recover significantly large correlation contributions to make them worthwhile. Typically, it is not worth the computational expense of using higher MP methods for what is only a relatively small increase in accuracy. Recent research in this area suggests there are far more efficient methods of obtaining high accuracy at significantly lower computational cost than using higher order MP methods, such as extrapolation methods combined with high order correlation techniques.[7]

*3.3.2.2 Configuration Interaction Methods*

An alternative to the Møller-Plesset method of electron correlation energy recovery is the Configuration Interaction (CI) method. The basic premise of a CI calculation is to take a *configuration* of Slater determinants, formed by a linear combination of single determinant sets, and allow them to *interact* by means of cross terms which correspond to single, double, triple and so forth excitations. Unfortunately, such an approach carries with it a huge computational cost and in practice is limited to single excitations (CIS) for all but the most simple systems.[8] In some cases, it is possible to include some, but not all of the possible double excitations (CIS(D)).

In this scenario, one must not only determine the orbital contributions to the wavefunction, but the coefficients within a linear combination of Slater determinants. Clearly, there is some similarity between the physical meaning of the excitation terms included in the CIS calculation and the MP2 calculation, although the mathematical formalism used to generate the expressions differ somewhat. The manner in which the determinants are constructed and allowed to interact makes CIS calculations one of the cheaper, albeit relatively inaccurate, methods for calculation of an excited state wavefunction. The main shortcoming of the CIS/CIS(D) methods is that it is only possible to calculate different electronic states with the same symmetry. Therefore, if the system under study has different symmetries for different electronic states, it is not possible to implement the method without introducing inconsistency between the ground and excited states. To overcome this problem Pople and co-workers introduced the quadratic configuration interaction method including single and double excitations (QCISD), and the slightly more sophisticated version with inclusion of a perturbative correction for contributions from unlinked triple excitations (QCISD(T)).[9] This method provides an elegant solution to the problems associated with CIS/CISD calculations allowing calculation of ground and excited states with different symmetry. A full description of these methods is beyond the scope of this thesis but a full description may be found in computational chemistry textbooks.[5,10] The main shortcomings of the QCISD and QCISD(T) methods is that the time taken for the enhanced accuracy given by the electron correlation treatment obtained is often prohibitive, and the theory often breaks down when attempting to predict bond dissociation energies through an exaggeration of T effects in those cases where triple excitations are important.[11]

*3.3.2.3 Multireference Methods*

Other schemes based on excitations into virtual orbitals include Complete Active Space Self Consistent Field (CASSCF)[12] and Restricted Active Space Self Consistent Field (RASSCF) calculations, which allow excitations of all electrons into all configurations of a set of so-called active orbitals (generally chosen to reflect the chemistry exhibited by a system) and restricted excitations into the selected set of active orbitals respectively. While relatively good at recovering large amounts of electron correlation within the active space these calculations are not simple procedures, and meaningful results rely on the correct choice of active space which requires a species-specific understanding of the chemical problem at hand.

The CASSCF methodology falls into a category of calculations known as multireference methods − the reference states are the occupied orbitals from which excitations are allowed to occur. Since excitations are not restricted to the highest most occupied orbitals, there are multiple reference states. The limit of a CASSCF calculation involves the excitation of all electrons, in all possible combinations, into all the virtual orbitals. This is equivalent to a full CI calculation, and is unfeasible for all but the smallest of systems.

*3.3.2.4 Symmetry Adapted Cluster Configuration Interaction Method*

Given the shortcomings of the CIS method and the difficulties associated with multireference methods, an excellent alternative is the symmetry adapted cluster/configuration interaction (SAC/SAC-CI) method developed by Nakatsuji and co-workers.[13] The main advantage of this method lies in its applicability to different electronic states with the same level of accuracy. The SAC method is used to calculate singlet closed shell states (*i.e.*, ground states) and the SAC-CI method is then used to calculate one of a number of different excited states allowed by the code. This is shown schematically in Figure 3.2.

SAC    Singlet closed shell (ground state)

SAC-CI

　　　—— Singlet excited states
　　　—— Triplet ground and excited states
　　　—— Ionised states (doublet ground and excited states)
　　　—— Electron attached states (doublet ground and excited states)
　　　—— Quartet to septet states (ground and excited states)
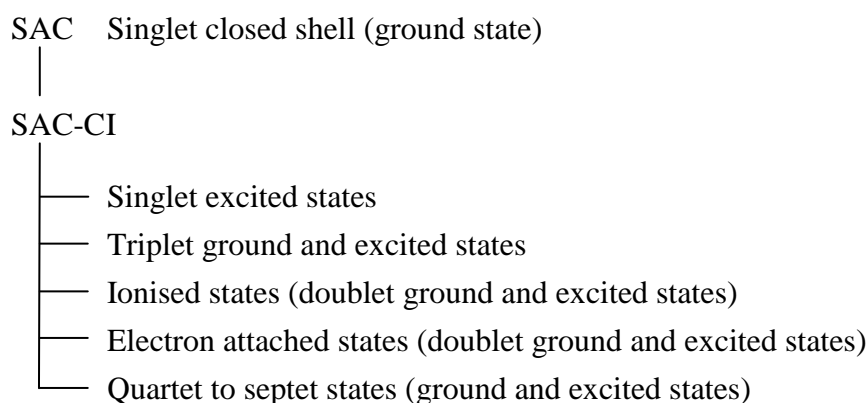
Figure 3.2: Schematic showing the electronic states currently accessible by the SAC/SAC-CI codes. Figure adapted from Ref [13].

### 3.3.3   Density Functional Theory

Density functional theory (DFT)[14] provides an alternative to HF calculations and can recover some of the electron correlation. Whereas the HF method aims to solve the Schrödinger equation using a wavefunction approach, DFT focuses on the electron density. By describing the interacting system of electrons via its first-order ground state density, $\rho(r)$, the complexity of the calculation is reduced to three spatial coordinates rather than $3N$ interacting electrons.

The foundation of DFT methods is the Hohenberg-Kohn theorem which states that "the exact ground state energy of a molecular system is a function only of the electron density and the fixed positions of the nuclei".[15] The ground state of the system in this theorem is defined as the electron density distribution that minimises the total energy. As the electron density in three-dimensional space is sufficient to construct the full electronic Hamiltonian, it is possible to solve the Schrödinger equation and obtain any ground state property for a particular set of nuclear coordinates. Therefore, any ground state property may be described by a functional of the density, $\rho(r)$. This makes DFT a very attractive option for theoreticians as the complexity of the calculations are significantly reduced.

Unfortunately, Hohenberg-Kohn theory only proves the existence of a functional that relates the ground state electron density to an observable; it does not provide the functional itself. A modification to Hohenberg-Kohn theory by Kohn and Sham[16] made significant improvements on previous methods and has revolutionised DFT calculations. The key principle in Kohn-Sham DFT is describing the ground state

electron density with an electronic energy functional which consists of several terms. The known terms in the functional may be solved iteratively as a set of one-particle Schrödinger type equations in a similar fashion to the HF method. The unknown parts of the density functional, often referred to as the exchange-correlation energy functional, include the electron-electron interactions. Therefore, approximate exchange-correlation energy functionals must be carefully chosen to correct the single-particle energies as a result of the various contributions owing to electron-electron interactions.

Over the past three decades, there have been a number of significant developments in the design of the exchange-correlation part of the energy functional. Although the precise functionals cannot be calculated, getting as close as possible is the intent of many theoreticians to gain the highest accuracy from the Kohn-Sham method. These include the local density approximation (LDA), where other high level *ab initio* calculations are carried out on a uniform electron gas and then used to construct a functional. However, a molecular system deviate considerably from that of an ideal electron gas described above and the method only accounts for electron kinetic energy and Coulomb energy. Consequently, DFT results using the LDA approximation are not especially accurate. A modification to the LDA approach is the Becke (B-88) functional, which includes the LDA approximation, as well as exchange energies for rare gases to improve the accuracy.[17]

Lee, Yang and Par (LYP) avoided the uniform electron gas as a base to their functional and instead used the helium atom.[18] When combined with the B-88 functional, this new functional, termed BLYP, was found to predict energies comparable to that of MP2 calculations, but in quicker computational time. A further modification to BLYP includes the gradient corrected Perdew-Wang 91 functional,[19] a modified version of the B-88 functional, to produce the hybrid B3LYP functional. B3LYP is now probably the most applied functional in modern DFT, capable of accurately predicting structures and frequencies of molecules containing first, second and third row elements.[20]

As mentioned above, the main advantage of using DFT methods is that there is a significant reduction in the cost of the calculation with little loss to the accuracy. This increase in computational efficiency is derived from the fact that DFT methods utilise the electron density of a chemical system rather than explicitly treating each

particle on its own. This is a double-edged sword, as it also leads to the main shortcoming of DFT methodology. DFT methods are poor at describing the physical properties of chemically non-bonded complexes (e.g., hydrogen-bonding, dispersion forces). These problems may be overcome, to a degree, by employing diffuse functions in the basis set. As the development of new functionals occurs the problems mentioned above may be overcome in the future.

### 3.3.4   Open and Closed Shell Species

For closed shell molecules, a useful additional approximation is to restrict electrons of $\alpha$ and $\beta$ spin to the same spatial orbital. Consequently, HF or MP2 calculations that employ this approximation are known as restricted Hartree-Fock (RHF) or restricted Møller-Plesset (RMP2) calculations. For molecules containing an unpaired electron (e.g., for an electronically excited state), such an approximation is no longer valid and we must then apply unrestricted methodologies where the $\alpha$ and $\beta$ spin-orbitals are no longer restricted to the same spatial region and may be independently optimised. Unrestricted HF or unrestricted MP2 calculations are thus known as UHF or UMP2.

One significant potential shortcoming of unrestricted methodologies is the introduction of spin contamination. Spin contamination is the introduction of higher lying triplet and quintet states into the lowest energy singlet state or of higher lying quartet and sextet states into a doublet state due to the independent optimisation of the $\alpha$ and $\beta$ spin-orbitals.

It is possible to remove spin contamination in a UHF wavefunction either during the SCF procedure,[21] directly after SCF convergence[22] or following correction for electron correlation.[23] A widely used method to remove spin contamination is using a spin projection operator, which removes contributions to the determinant that result from higher spin states. Generally, it is sufficient to remove the first unwanted spin state. Projection of the spin states during the SCF procedure results in a set of equations for which it is extremely difficult to include electron correlation; projecting spin states onto a converged SCF wavefunction may result in distortion of the potential energy surface,[24] and it is, therefore, generally accepted that projection following the inclusion of electron correlation has the most favourable result.

## 3.4    Basis Sets

A basis set is a series of mathematical functions chosen to approximate atomic orbitals. A Linear Combination of Atomic Orbitals (LCAO) (or basis functions) is then used to construct the molecular orbitals. This is described by Equation [3.12], where $\psi_{mol}$ is the molecular orbital, $\phi_a$ are the functions contained within the basis and $c_{ia}$ are the atomic orbital coefficients.

$$\psi_{mol} = \sum_{i=1}^{n} c_{ia}\phi_a \qquad\qquad [3.12]$$

Basis sets range from simple combinations of Gaussian functions to more complex functions that can better describe diffuse and/or high angular momentum orbitals. Each basis set is tailored such that it describes various physical properties so the choice of a basis set requires some intuitive chemical knowledge as well as an understanding of the capabilities of each set. The type of atomic orbital like functions used in the LCAO approximation fall into two categories: Slater Type Orbitals (STO) and Gaussian Type Orbitals (GTO).

### 3.4.1    Slater Type Orbitals

The general form of the STO[25] is shown in Equation [3.13] (using spherical polar coordinates).

$$\chi_{\zeta nml}(r,\theta,\phi) = NY_{lm}(\theta,\phi)r^{n-1}e^{-\zeta r} \qquad\qquad [3.13]$$

$N$ is a normalization constant, $Y_{lm}$ are spherical harmonics, $r$ is the electron-nucleus distance and $\zeta$ is a parameter that describes the spatial extent of the orbital. The orbital exponent, $\zeta$, is chosen so that the electron-nucleus distance is exactly that found in the hydrogen atom orbitals (the one-electron orbits found to be solutions of the SWE).

Unfortunately radial nodes are not described by a single STO, and must be included using linear combinations. Although the exponential dependence ensures a good description of atomic one-electron orbitals, analytical calculation of two-electron (and higher order) integrals is not possible. The STO, and its linear combinations, are only feasible for use with extremely small systems where high accuracy is required or in semi-empirical calculations where it is not necessary to include higher-order integrals. In addition, orbitals of different principal quantum number, $n$, but identical values of $l$ and $m_l$, are not orthogonal, leading to some problems in the formulation of

the Slater determinant. A particular advantage of the STO is their description of the discontinuous derivative, or 'cusp', in the region of the atomic nucleus. This 'cusp' is a physically meaningful discontinuation as it represents the inability of an electron to penetrate the nucleus and results in a reasonably accurate description of electron behaviour in this region.

### 3.4.2 Gaussian Type Orbitals

GTOs[26] have the general form shown in Equation [3.14] using Cartesian coordinates.

$$\chi_{\zeta,l_x,l_y,l_z,}(x,y,z) = N x^{l_x} y^{l_y} z^{l_z} e^{-\zeta r^2} \qquad [3.14]$$

In functions of this form, the sum of $l_x$, $l_y$ and $l_z$ determines the angular momentum characteristics of the orbital. An alternative form of the GTO, using spherical polar coordinates is shown in Equation [3.15].

$$\chi_{\zeta,n,l,m}(r,\theta,\phi) = N Y_{l,m}(\theta,\phi) r^{(2n-2-l)} e^{-\zeta r^2} \qquad [3.15]$$

Unfortunately, the $r^2$ dependence of the exponential function results in poor behaviour of the wavefunction in the region of the nucleus, and rapid fall off of the wavefunction at large distances from the nucleus. Generally the number of GTOs required to reproduce a result found using STOs will be significantly larger. Despite these limitations, GTOs are generally chosen to build a basis set due to the relative ease in evaluating their two electron integrals. In addition to using isolated GTOs, pre-optimised combinations of GTOs (referred to as contracted functions) may be used to model the STOs (such that the electron behaviour in the region of the nucleus is better described) further improving their usefulness in quantum chemistry despite their shortcomings.

### 3.4.3 Basis Set Construction and Size

A minimal basis set simply includes sufficient functions to describe all of the electrons of each neutral atom in a calculation. In this scenario, first row elements will be represented by two *s*-orbitals (*1s* and *2s*) and one set of *p*-orbitals (*2p_x, 2p_y* and *2p_z*). These orbitals may comprise either a single STO, or a linear combination of Gaussian functions to model the STO. While this is a physically accurate description

of an atomic system, it is not sufficient to accurately describe the chemistry of a molecular system, and requires the addition of further functions.

Thus, for example, each atomic orbital for first row elements can be described using two functions *1s, 1s´, 2s, 2s´, 2p* and *2p´* and any basis set that uses such functions is referred to as a split-basis set. The differentiation between the *1s* and *1s´* function arises due to the use of different orbital exponent values, $\zeta$; a split-basis set which uses two functions to describe each atomic orbital is referred to as a double-zeta (DZ) basis. Similarly the basis may be further split to extend to triple-, quadruple-zeta and beyond.

Chemical bonding is an excellent example of the importance of the split basis set. If one considers a double bond, the $\sigma$-bond is formed through overlap of an atomic *s*-orbital and an atomic *p*-orbital directed along a defined axis (or indeed two *p*-orbitals directed along the same axis), say *z,* while the $\pi$-bond is formed through overlap of two atomic *p*-orbitals orientated perpendicular to the $\sigma$-bond, say two $p_x$-orbitals. Should a single exponent be used to describe the *p*-orbitals involved in both $\sigma$- and $\pi$-bonding then the $\pi$-bond will not be adequately described relative to the spatial extent of the $\sigma$-bond. If one uses a split valence basis set to describe this bonding situation, then the different exponents are employed to describe the $\sigma$- and $\pi$-bonds. The $\pi$-bond, which is more diffuse than the $\sigma$-bond, is formed from *p*-orbitals with a smaller orbital exponent than the *p*-orbital used to form the $\sigma$-bond. It is this flexibility of the basis sets which is the key to accurately describing the molecular wavefunction. When higher levels of theory are used to better describe electron correlation this becomes more important.

In a real chemical system, it is not generally necessary to represent all of the orbitals using a split basis. The core orbitals do not generally contribute anything like the same extent as valence orbitals to the chemical and structural characteristics of the system and to save computational cost these orbitals can be represented by single functions with only one orbital exponent and only the valence orbitals are represented using multiple functions with different exponents. This type of basis set is referred to as a split valence basis set and comprises of two main types as developed by Pople[27] (e.g., 6-31G(d) and 6-31G(d,p)) and Dunning[28] (e.g., cc-pVDZ and cc-pVTZ).

It is often important to include some functions in the basis set which describe the higher angular momentum orbitals *d-, f-* and higher. These functions, known as polarization functions, allow for the non-spherical distribution of electrons about the nucleus. Adding a *p*-function to the hydrogen 1*s* orbital, for example, allows it to become polarised such that the electron distribution parallel and perpendicular to any bonds formed will be allowed to vary.

One additional modification to a basis set is the addition of diffuse functions, which can correct for the poor behaviour of the wavefunction at large distances from the nucleus. These functions are of particular importance in describing weakly bound species such as van der Waals complexes, and weakly bound electrons such as those in anions[29] and excited state species.[30]

The Pople basis sets are constructed by the fitting, rather than optimisation, of Gaussian orbitals to Slater Type Orbitals. Six Gaussian functions (6G) are generally used for each AO, and the basis is enlarged by the addition of split valence functions (6-31G) and diffuse functions (6-31+G) and polarization functions (6-31G(d)). Clearly, as the number of Gaussian functions summed to approximate the Slater functions increases, there will be an improved representation of the wavefunction, if only as a result of an increased number of optimisable parameters. An unfortunate property of this family of basis sets is their representation of functions of different orbital angular momentum; *s-* and *p*-functions are represented by the same orbital exponent although this has the advantage of minimizing computational expense.

In contrast to the Pople basis sets, the Dunning basis sets employ variable exponents to represent *s-* and *p*-functions. While this leads to greater flexibility in the wavefunction, there is a corresponding increase in computational cost since each exponent must be individually optimised. Effects not included in the HF method may be partially accounted for through the addition of polarization functions. If these functions are only added to the valence shell, the size of the basis set is reduced and the calculation becomes significantly more manageable. The design and implementation of the Dunning basis sets has been such that they are consistent with the effects of electron correlation. This property of the Dunning basis sets is reflected in their names; cc-pVDZ refers to a correlation consistent basis, formed using a

doubly split valence exponent with polarization functions. Further augmentations have been applied to these basis sets by Dunning *et al.*[31] and these basis sets (given the abbreviation aug-cc-pV*X*Z with *X*=2,3,4,etc.) are now commonly used in high-level theoretical studies.

One common theme of all basis sets is the relationship between their size and the degree to which a particular calculation of an observable, such as energy, approaches the true value. As the physical description of the molecular system becomes more and more complete with the addition of further functions, the observables should all tend to their experimentally determined values. By performing a series of calculations, while systematically increasing the size of the basis set (for example cc-pVDZ, cc-pVTZ, cc-pVQZ), one may extrapolate any value to obtain the value in the basis set limit. It is important to note that while progressive increases in basis set size for any given level of theory will result in smaller differences between the computed and true values of a particular observable, this will not be monotonic and eventually the basis set will become saturated with no further changes being observed.

## 3.5 Quantum Chemistry Composite Methods

The Gaussian-*X* (*X*=1,2,3,4) methods (G*X*) are composite techniques which comprise of a sequence of well defined *ab initio* molecular orbital calculations allowing derivation of the total energy of a given molecular species, and have been developed by Curtiss *et al.*[32,33] These very accurate energies may then be used to compute thermochemical properties, such as enthalpies of formation, ionization potentials, electron affinities, proton affinities, etc. In the work carried out in this thesis modified versions of the G2 and G3 methods have been employed, namely, the G2MP2, G3MP2 and G3B3 methods.[34,35] What follows is a brief description of the general formulation of these methods.

The G2 and G3 methods comprise a series of six calculations:

1) An initial equilibrium structure is dertermined at the HF/6-31G(d) level together with suitably scaled harmonic frequencies used for evaluation of zero point energy and thermal effects.

2) The equilibrium geometry is refined at the MP2(full)/6-31G(d) level. This geometry is then implemented in all the higher level single-point calculations in step 3, unless otherwise indicated.

3) A single-point energy calculation is carried out at the MP4/6-31G(d) level. The energy calculated is then modified by a series of corrections:

   a) A correction for correlation effects beyond fourth order perturbation theory using the quadratic configuration interaction

   b) A correction for diffuse functions

   c) A correction for higher polarisation functions

   d) A correction for larger basis set effects using the "G3Large" basis set

4) Spin-orbit corrections are included for atomic species, taken from experimental results where available or from accurate theoretical calculations in other cases

5) A higher level correction is added to take into account remaining deficiencies in the energy calculations

6) Finally the total energy is obtained by collecting all the corrections together in an additive manner.

A more detailed description of these calculations together with a description of how the modified methods work may be found in papers published by Curtiss *et al.*[32-35]

The G2 and G3 methods have been rigorously tested by comparing computed enthalpies of formation at 298 K of approximately 100 species with well established values determined via experiment.

The G3MP2 and G3B3 methods have been implemented in determination of accurate energies and formation enthalpies of various ground state [H, Si, N, C, O] isomers detailed in Chapter 5 of this thesis. The G2MP2 method has been used for determination of accurate energies and formation enthalpies of various ground state [H, Ge, N, C, O] isomers detailed in Chapter 7 of this thesis.

## 3.6 Natural Bond Analysis

Natural bond analysis (NBA) provides a means by which the molecular electrostatic potential is analysed to provide information on the degree of hybridisation of the molecular orbitals and hence give information on the bond order between the nuclei of a given molecular system.

The NBA program used in the work contained in this thesis was the NBO version 3 as implemented in Gaussian 03.[36] This program works by performing analysis of a many-electron molecular wavefunction in terms of localised electron-pair bonding units. Firstly, the program carries out the determination of natural atomic orbitals (NAOs), natural hybrid orbitals (NHOs), natural bond orbitals (NBOs), and natural localised molecular orbitals (NLMOs). These are then used to perform natural population analysis (NPA), NBO energetic analysis, and other tasks related to localised analysis of wavefunction properties. The NBO method makes use of only the first-order reduced density matrix of the wavefunction, and hence is applicable to wavefunctions of general mathematical form; in the open-shell (*i.e.*, excited state) case, analysis is performed in terms of different NBOs for different spins, based on distinct density matrices for $\alpha$ and $\beta$ spin.

NBO analysis is based on a method for optimally transforming a given wavefunction into localised form, corresponding to the one centre (lone pair) and two centre (bond) elements of the Lewis structure picture. The NBOs are referred to as 'natural' in the sense of having optimal convergence properties for describing the electron density. The set of high occupancy NBOs, each taken to be doubly occupied, is said to represent the natural Lewis structure of the molecule. Delocalisation effects appear as weak departures from this idealised localised picture. The result of the population analysis provides great insight into the hybridisation of the molecular orbitals, from which the bond order between the nuclei may be inferred. Also the location and degree of hybridisation of any lone pairs of electrons which may reside in the molecular system are determined.

## 3.7   *Geometry Optimisation*

An important procedure in theoretical calculations which must be undertaken to obtain accurate energies is geometry optimisation. The principle behind the geometry optimisation is to calculate the energy of a molecular system with user defined nuclear coordinates using the desired level of theory and basis set. The positions of the nuclei are then moved according to the optimisation algorithm, and the energy of the system recalculated. This procedure continues until a stationary point on the potential energy surface is found and the energy is minimised. The structure located

is then assumed to be the same as the equilibrium structure of the actual gas phase molecule.

Geometry optimisations are generally the most troublesome aspect of theoretical calculations to conduct. For instance, locating the equilibrium geometry for a diatomic is straight forward, as only one coordinate is varied. However, for larger molecules, more degrees of freedom increase the dimensionality of the optimisation thus making the location of minima more time consuming. Furthermore, as discussed previously, larger molecules may have several local minima or saddle points which the optimisation procedure may locate, rather than the global minimum. Therefore, it is crucial that the initial nuclear optimisation parameters are carefully selected to ensure the optimisation procedure converges and finds the true global minimum. These include the starting geometry, the molecular coordinate system, the convergence criteria and the optimisation method. These parameters are also highly dependant upon the nature of the chemical system to be studied, e.g., van der Waals clusters in comparison to covalently bonded systems.

## 3.8    *Vibrational Frequency Analysis*

Following the identification of a stationary point on a potential energy surface (regardless of the theory and basis set used to compute the geometry) it is necessary to have some means to distinguish between potential energy minima and saddle points. Neglecting, for a moment, the multi-dimensional potential energy surface and instead focussing on a simple function of only one variable (with multiple minima, maxima and saddle points), it is relatively simple to distinguish between these stationary points through computation of the second derivative of the potential.

Similarly, to distinguish between minima and saddle points on a potential energy surface which involves multiple degrees of freedom also requires that the second derivative of the potential energy function (or Hessian matrix) of a system with respect to the nuclear coordinates at their equilibrium positions. The Hessian can be used to calculate the harmonic vibrational frequencies of a molecule. This computation takes the form of a harmonic vibrational frequency analysis.

The first step in any such procedure is the identification, and isolation, of each vibrational degree of freedom. For a non-linear polyatomic molecule there will be 3N-6 degrees of freedom which equate to the fundamental molecular vibrations and coordinates. In a normal mode of vibration, each atom reaches the turning points of motion simultaneously, with identical frequency, and the motion is in phase.[37]

Broadly speaking, there are two methods of frequency determination; analytical and numerical methods. Analytical methods rely on the algebraic formulation of the Hessian matrix while numerical solution requires the computation of numerical differences between gradients at a number of points about the atomic displacement for each vibration; these must be individually assessed for a large number of numerical points for each matrix element of the Hessian matrix. When available, analytical methods are preferred as they are systematic, computationally more accurate and somewhat less expensive. Following its initial construction, the Hessian matrix is converted to a force constant matrix, $k_{i,j}$, through diagonalisation. The force constant matrix yields a set of eigenvalues for each vibration, which may be converted to vibrational frequencies by multiplication by $1/2\pi c$.

Following the computation of each normal mode of vibration it is simple to distinguish between potential energy minima and saddle points. A potential energy minimum represents a point along which all variables are minimised and the molecular structure is bound along all coordinates, for which each vibrational frequency will be positive. If a computed geometry represents a saddle point, at least one coordinate is no longer bound and is represented by a maximum turning point. In this case, there will be the presence of an imaginary (negative) frequency representative of each unbound coordinate. Therefore, a third order saddle point would give three imaginary vibrational frequencies, each one representative of an unbound coordinate.

Generally, in the investigation of any molecular system containing more than two atoms, there exists the possibility of multiple structural conformations; this highlights the need for the confirmation that a stationary point is a potential energy minimum rather than some transition structure between conformers and should be combined with energy calculations to identify local and global minima.

The major shortcoming of harmonic frequency calculations is that, by definition, the effects of vibrational anharmonicity are neglected. Since the calculated frequencies are most commonly compared with fundamental vibrational frequencies, the tendency is for the calculated values to be substantially larger than the experimental fundamental frequencies. This overestimation can vary from one method to another, by 5-10 % range. Consequently, one possible solution is to use a scaling factor to bring theory into better agreement with experiment.[38] However, this can only ever be approximate and neglects the fact that the percentage deviation between theory and experiment is mode specific. In terms of absolute accuracy for unscaled harmonic frequencies, it has been found that B3LYP provides a more accurate description by 65% than MP2,[39] when the frequency calculations were run using both methods and a 6-311(d,p) basis set on the G2 test set of molecules.[40]

## 3.9    *Transition State Optimisation*

In cases where a number of isomers of a given system are under study, it is often useful to 'connect' the isomers by determination of a transition state structure. As well as providing geometric information about the transition state, the energies of the determined structures can give an indication of the barrier to isomerisation. As discussed in section 3.2, in attempting to minimise the energy of an isomer it is important to have a feeling for the nature of the chemical system so that the initial geometry is close to that of the true minimum in order to avoid locating saddle points. In most cases, searching for transition state structures is usually carried out after the minimum energy structures of the isomers has already been determined. Therefore, by using an educated guess for what the transition state geometry could be, it is relatively easy to locate them on a PES. The bottom line is that, in order to calculate transition states, the chemist must be able to provide a reasonable guess of the initial structure before optimisation. Once the structure of the transition state has been optimised it is important to carry out a harmonic frequency calculation in order to ensure the Hessian is giving a single negative value, thus ensuring the calculated structure is a real transition state on the PES.

## 3.10  *Computational Details*

### 3.10.1  Hardware and Software Configurations

As high-level calculations require large amounts of system memory and fast processors, PC-based *ab initio* packages are often too slow. Instead, three different

high-performance computer systems were utilised for the calculations reported in this thesis. All of these are based on multiprocessor systems and offer high speed hard disk drives and data transfer capabilities to facilitate efficient calculations. Each cluster ran under a GNU/Linux based operating system and had the following specifications:

Marvin:        6 AMD Opteron 244 64-bit processors in 3 nodes
               6 Gb of RAM per node
               140 Gb scratch disk per node


Newton:        160 AMD Opteron 848 64-bit processors in 40 nodes
               8 Gb of RAM per node
               72 Gb scratch disk per node


Magellan:      224 Silicon Graphics Altix 4700, 1.6 GHz Montecito Itanium 2 processors, 896 Gb of RAM and 15 Tb scratch disk space


Marvin is a custom-built system, solely for use by members of the Leicester Chemistry Department's laser group. The Newton cluster is part of the University of Leicester's Mathematical Modelling Centre, which was funded by the UK Strategic Research Infrastructure Fund. Magellan is funded by the Engineering and Physical Sciences Research Council and operated by the National Service for Computational Chemistry. All calculations were run using either Gaussian 03[41] (edited with GaussView 3.07[42]), Molpro[43] (edited with Molden[44]). All calculation input and output files can be found in the addendum accompanying this thesis.

## 3.11 REFERENCES FOR CHAPTER 3

(1)     Green, N. J. B. *Quantum Mechanics 1: Foundations*; Oxford University Press: Oxford, **1997**.

(2)     Arfken, G. B.; Weber, H.-J. *Mathematical methods for physicists*, 4th ed.; Academic Press: San Diego, **1995**.

(3)     Dirac, P. A. M. *Proc. R. Soc. London, Ser. A* **1926**, *110*, 561.

(4)     Atkins, P. W. *Molecular Quantum Mechanics*, 3 ed.; Oxford University Press, **1997**.

(5)     Jensen, F. *An introduction to computational chemistry*; Wiley: Chichester, UK. ; New York, **1998**.

(6)     Møller, C.; Plesset, M. S. *Phys. Rev.* **1934**, *46*, 618.

(7)     Halkier, A.; Helgaker, T.; Jorgensen, P.; Klopper, W.; Koch, H.; Olsen, J.; Wilson, A. K. *Chem. Phys. Lett.* **1998**, *286*, 243.

(8)     Cramer, C. J. *Essentials of computational chemistry : theories and models*, 2nd ed.; J. Wiley: Hoboken, N.J., **2004**.

(9)     Pople, J. A.; Head-Gordon, M.; Raghavachari, K. *J. Chem. Phys.* **1987**, *87*, 5968.

(10)   Cramer, C. J. *Essentials of computational chemistry : theories and models*; John Wiley: New York, **2002**.

(11)   Bohme, M.; Frenking, G. *Chem. Phys. Lett.* **1994**, *224*, 195.

(12)   Roos, B. O.; Taylor, P. R. *Chem. Phys.* **1980**, *48*, 157.

(13)   Nakatsuji, H. *Chem. Phys. Lett.* **1978**, *59*, 362.

(14)   Kohn, W.; Becke, A. D.; Parr, R. G. *J. Phys. Chem.* **1996**, *100*, 12974.

(15)   Hohenberg, P.; Kohn, W. *Phys. Rev.* **1964**, *136*, B864.

(16)   Kohn, W.; Sham, L. J. *AEC Access. Nos.* **1965**, 21.

(17)   Becke, A. D. *Phys. Rev. A* **1988**, *38*, 3098.

(18)   Lee, C. T.; Yang, W. T.; Parr, R. G. *Phys. Rev. B: Condens. Matter* **1988**, *37*, 785.

(19)   Burke, K.; Perdew, J. P.; Levy, M. *Phys. Rev. A* **1996**, *53*, R2915.

(20)   Curtiss, L. A.; Raghavachari, K.; Redfern, P. C.; Pople, J. A. *J. Chem. Phys.* **2000**, *112*, 7374.

(21)   Harriman, J. E. *J. Chem. Phys.* **1964**, *40*, 2827.

(22)   Amos, T.; Snyder, L. C. *J. Chem. Phys.* **1964**, *41*, 1773.

(23)   Schlegel, H. B. *J. Phys. Chem.* **1988**, *92*, 3075.

(24)   Rossky, P. J.; Karplus, M. *J. Chem. Phys.* **1980**, *72*, 6085.

(25)   Slater, J. C. *Phys. Rev.* **1930**, *36*, 57.

(26)   Boys, S. F. *Proc. R. Soc. London, Ser. A* **1950**, *200*, 542.

(27)   Hehre, W. J.; Stewart, R. F.; Pople, J. A. *Symp. Farad. Soc.* **1968**, *2*, 15.

(28)   Dunning, T. H. *J. Chem. Phys.* **1971**, *55*, 716.

(29)   Rauk, A.; Armstrong, D. A. *Int. J. Quantum Chem.* **2003**, *95*, 683.

(30)   Yu, H. T.; Goddard, J. D.; Clouthier, D. J. *Chem. Phys. Lett.* **1991**, *178*, 341.

(31)   Dunning, T. H. *J. Chem. Phys.* **1989**, *90*, 1007.

(32)   Curtiss, L. A.; Raghavachari, K. *Theor. Chem. Acc.* **2002**, *108*, 61.

(33)   Curtiss, L. A.; Raghavachari, K.; Trucks, G. W.; Pople, J. A. *J. Chem. Phys.* **1991**, *94*, 7221.

(34)   Curtiss, L. A.; Raghavachari, K.; Redfern, P. C.; Pople, J. A. *J. Chem. Phys.* **1997**, *106*, 1063.

(35)   Curtiss, L. A.; Redfern, P. C.; Raghavachari, K.; Rassolov, V.; Pople, J. A. *J. Chem. Phys.* **1999**, *110*, 4703.

(36)   Glendening;, E. D.; Reed;, A. E.; Carpenter;, J. E.; Weinhold, F. NBO; 3.0 ed.; Theoretical Chemistry Institute and Department of Chemistry, University

of Wisconsin, Madison, Wisconsin **1993**; pp Natural Bond Orbital / Natural Population Analysis / Natural Localized Molecular Orbital Programs.

(37)   Wilson, E. B.; Cross, P. C.; Decius, J. C. *Molecular vibrations ; the theory of infrared and Raman vibrational spectra*; McGraw-Hill: New York, **1955**.

(38)   Sinha, P.; Boesch, S. E.; Gu, C. M.; Wheeler, R. A.; Wilson, A. K. *J. Phys. Chem. A* **2004**, *108*, 9213.

(39)   Adamo, C.; Barone, V. *J. Chem. Phys.* **1998**, *108*, 664.

(40)   Johnson, B. G.; Gill, P. M. W.; Pople, J. A. *J. Chem. Phys.* **1993**, *98*, 5612.

(41)   Frisch, M. J.; Trucks, G. W.; Schlegel, H. B.; Scuseria, G. E.; Robb, M. A.; Cheeseman, J. R.; Montgomery, J., J. A.; Vreven, T.; Kudin, K. N.; Burant, J. C.; Millam, J. M.; Iyengar, S. S.; Tomasi, J.; Barone, V.; Mennucci, B.; Cossi, M.; Scalmani, G.; Rega, N.; Petersson, G. A.; Nakatsuji, H.; Hada, M.; Ehara, M.; Toyota, K.; Fukuda, R.; Hasegawa, J.; Ishida, M.; Nakajima, T.; Honda, Y.; Kitao, O.; Nakai, H.; Klene, M.; Li, X.; Knox, J. E.; Hratchian, H. P.; Cross, J. B.; Bakken, V.; Adamo, C.; Jaramillo, J.; Gomperts, R.; Stratmann, R. E.; Yazyev, O.; Austin, A. J.; Cammi, R.; Pomelli, C.; Ochterski, J. W.; Ayala, P. Y.; Morokuma, K.; Voth, G. A.; Salvador, P.; Dannenberg, J. J.; Zakrzewski, V. G.; Dapprich, S.; Daniels, A. D.; Strain, M. C.; Farkas, O.; Malick, D. K.; Rabuck, A. D.; Raghavachari, K.; Foresman, J. B.; Ortiz, J. V.; Cui, Q.; Baboul, A. G.; Clifford, S.; Cioslowski, J.; Stefanov, B. B.; Liu, G.; Liashenko, A.; Piskorz, P.; Komaromi, I.; Martin, R. L.; Fox, D. J.; Keith, T.; Al-Laham, M. A.; Peng, C. Y.; Nanayakkara, A.; Challacombe, M.; Gill, P. M. W.; Johnson, B.; Chen, W.; Wong, M. W.; Gonzalez, C.; Pople, J. A. Gaussian 03; Revision D.02 ed.; Gaussian Inc.: Wallington CT, **2004**.

(42)   R. Dennington II; T. Keith; J. Millam; K. Eppinnett; W. L. Hovell; Gilliland, R. GaussView, Version 3.07, **2003**.

(43)   Werner, H. J.; Knowles, P. J.; Lindh, R.; Manby, F. R.; Schütz, M.; Celani, P.; Korona, T.; Rauhut, G.; Amos, R. D.; Bernhardsson, A.; Berning, A.; Cooper, D. L.; Deegan, M. J. O.; Dobbyn, A. J.; Eckert, F.; Hampel, C.; Hetzer, G.; Lloyd, A. W.; McNicholas, S. J.; Meyer, W.; Mura, M. E.; Nicklaß, A.; Palmieri, P.; Pitzer, R.; Schumann, U.; Stoll, H.; Stone, A. J.; Tarroni, R.; Thorsteinsson, T. MOLPRO version (2002.1) Cardiff, UK, **2002**.

(44)   Schaftenaar, G.; Noordik, J. H. *J. Comput. Aid. Mol. Des.* **2000**, *14*, 123.

# Chapter Four

*Theoretical, Laser Induced Fluorescence (LIF) and Dispersed Fluorescence (DF) studies of HSiNC*

## 4.1  Introduction

The first electronic spectroscopic study of the halosilylenes was conducted many years ago. The spectra of HSiCl and HSiBr were first studied by flash photolysis of $SiH_3Cl$ and $SiH_3Br$ at room temperature.[1] In this important paper the authors were able to rotationally resolve fine structure, but were unable to assign asymmetry splittings at low $K'_a$ due to congestion in the spectra. The most interesting feature of the halosilylene spectra is the occurrence of 'forbidden' $\Delta K_a = 0$ and $\pm 2$ sub-bands. In the original work of Herzberg and Verma, the authors assessed these anomalies and suggested that they were caused by a triplet-singlet transition, although there were no apparent spin splittings (*i.e.*, the observed transitions were of the singlet-singlet type) detected in the spectra.

Another possible reasoning for these sub-bands, added as a note in the proof, was that the anomalies were a result of an axis-switching mechanism. This was assumed not to be the case, as the preliminary calculations carried out indicated that the appearance of these sub-bands would not be as intense as those observed in the spectrum. Subsequent work by Hougen and Watson[2] showed that axis-switching was a better explanation for these anomalous sub-bands. A more detailed account of axis-switching is given in section 4.5.5 below. In brief, axis-switching occurs when there is a change in orientation of the principle axes upon excitation, giving rise to anomalous branches in molecules of low symmetry due to the appearance of forbidden transitions corresponding to $\Delta K_a = 0$ and $\pm 2$.

Later, re-investigations of HSiCl and HSiBr were carried out by Clouthier *et al.* using high resolution LIF spectroscopy and supersonic jet techniques[3,4] allowing the authors to better resolve the spectra of both species. As a result, the authors were able to further confirm the identity of the spectral carriers, and conclusively identify the peaks attributed to axis-switching, as there was no evidence of spin splittings.

As the interest in silicon containing species has grown, to help in the search for new ones a number of groups have carried out theoretical and experimental studies in order to obtain spectroscopic parameters to aid in the detection of these species in the interstellar medium, in addition to helping in the search for previously unobserved species.[5-14] One of these investigations lead to two new species, HSiCN and HSiNC, being spectroscopically observed in the laboratory. Both of these species were

regarded as being very strong candidates for detection in the interstellar medium due to fact that similar species have already been observed in space (e.g., SiCN). In this work, Sanz *et al.* used a high voltage electric discharge source coupled to a molecular beam Fourier transform microwave spectrometer to study both HSiCN and HSiNC, and to obtain rotational constants for a number of different isotopomers of each species allowing the elucidation of their structures.[15] They found that both HSiCN and HSiNC are bent molecules with $C_s$ symmetry, with the H-Si-X (X=C or N) angle being ~95°. The spectra also indicated that there was very little observed difference in the intensity profiles of the spectra recorded for each species and there was no indication, other than citation of previous theoretical work,[16] as to which of the two species was more stable. The theoretical study referenced, indicated that the HSiCN isomer was more stable by 3.2 kcal/mol.

Of particular interest in terms of the experimental work detailed in this chapter are two other theoretical studies carried out on the [H, Si, C, N] isomers by Flores *et al.* and Wang *et al.*[8,13] In the first of these studies, Flores *et al.* carried out high level calculations on the six lowest lying singlet ground states as well as the corresponding triplet states at the B3LYP/6-311(d, p) level of theory. In all cases it was found that the triplet isomers were considerably higher in energy. The two lowest lying isomers were found to be HSiCN and HSiNC (lying 2.2 kcal/mol higher in energy), and in both cases the symmetry of the ground electronic state was determined to be $^1A'$ with an H-Si-X (X=C or N) determined to be ~95°. This agrees well with the previous experimental work.[15] Furthermore, Flores *et al.* carried out calculations on the vertical excitation energies for each isomer in the $^1A''$ state, providing vertical electronic spectra by means of multi-configuration self-consistent field (MCSCF) and multi-reference configuration interaction (MRCI) calculations. For the two isomers of interest here, HSiCN and HSiNC, the determined vertical excitation energies were 2.55 eV (20567 cm$^{-1}$) and 2.72 eV (21938 cm$^{-1}$), respectively. The importance of this information will become clear in the discussion of the results later in this chapter.

In the more recent theoretical study by Wang *et al.*[13] the potential energy surfaces (PESs) of the neutral, cationic and anionic isomers of the [H, Si, C, N] system were determined at the slightly lower B3LYP/6-311(d) level of theory. Compared with the Flores *et al.* study, there is little extra information of use, but the point to note from

this study is that the lowest two isomers were determined to be the HSiCN and HSiNC isomers. In this case the HSiCN isomer was predicted to be the most stable by 2.4 kcal/mol.

This chapter focuses on the first electronic spectroscopic study of the HSiNC species, using LIF. It will be broken into sections as follows: a brief overview of the experimental and theoretical techniques used, a review of the theoretical findings and vibrational and rotational analysis of the experimentally observed spectra together with comparisons of the previous work. Finally there is a discussion of why the previously determined lower energy species (HSiCN) has not been detected together with some concluding remarks.

## 4.2    Experiment

The precursor used to produce the radical species under investigation was trimethylsilylcyanide ($(CH_3)_3SiCN$, Acros Chemicals, 98%), and was used without further purification. The room temperature sample of trimethylsilylcyanide was placed in a glass bubbler and a stream of Ar passed through the sample at a pressure of 2 bar to allow the vapour to mix. This gas flow was then expanded through a pulsed valve (General Valve, Series 9) into a 3 mm flow channel drilled through a 26 mm long Delrin$^{TM}$ cylinder ($d$=50 mm) attached to the end of the pulsed valve. Inside the Delrin$^{TM}$ cylinder are housed two stainless steel ring electrodes separated by a 1 mm PTFE spacer positioned such that the discharge occurs along the flow channel. At the appropriate time delay after the pulsed valve has fired, a high voltage (2-6 kV) pulse of 4 μs duration was applied to one of the electrodes via a Tesla coil, while the other was grounded. By allowing the sample jet to pass through the discharge the reactive species was created with little disturbance to the flow of the supersonic jet.

The discharge efficiently dissociates the pseudohalosilane precursor into readily detectable amounts of HSiNC. The pulsed discharge apparatus was mounted near the centre of a vacuum chamber pumped by a large turbo molecular pump, backed by a roots blower and rotary pump. The base pressure of the system was typically around $5 \times 10^{-7}$ torr, rising to about $5 \times 10^{-4}$ torr when the pulsed valve was in operation.

Low (0.5 cm$^{-1}$) and medium (0.12 cm$^{-1}$) resolution laser induced fluorescence (LIF) spectra were recorded using a 355 nm pumped tuneable pulsed dye laser (Quanta-

Ray PDL-3). The laser beam crossed the supersonic expansion approximately 50 mm downstream of the end of the Delrin$^{TM}$ cylinder mounted on the pulsed valve. The resulting fluorescence was imaged through an appropriate cut-off filter, at right angles to the jet, onto the photocathode of a photomultiplier tube (Electron Tubes B2F/RFI). To gain maximum light collection, an aluminium coated concave spherical mirror (*D*=50 mm, *EFL*=50 mm) was mounted inside the vacuum chamber directly opposite the fluorescence collection optics.

All spectra were calibrated with lines from a neon-filled hollow cathode lamp and simultaneously recorded etalon fringes (FSR 1.0 cm$^{-1}$). The LIF spectra and calibration signals were digitized on an oscilloscope (LeCroy Waverunner LT342), and captured by a PC using software written in LabVIEW,[17] interfaced to the PC using a GPIB card.

Dispersed fluorescence (DF) spectra were obtained by fixing the wavelength of the dye laser to the $^PQ_1$ branch of a vibrational band in the LIF spectrum and imaging the resultant fluorescence onto the entrance slit of a 0.5 m scanning monochromator (Acton Research SpectraPro 2500i) fitted with a 1800 lines/mm grating blazed at 500 nm. The wavelength resolved fluorescence signals were detected with a Peltier cooled CCD camera (PI-MAX system), amplified with a gain of 255 and processed using the supplied software (WinSpec32). The monochromator scan was calibrated to an estimated accuracy of $\pm 2$ cm$^{-1}$ using known emission lines from a mercury lamp.

## 4.3 *Computational Methods*

As discussed above, there has been much theoretical work already carried out on the isomers of the [H, Si, C, N] system. To aid in the assignment of experimental data, additional calculations were performed on both the ground ($\tilde{X}^1A'$) and excited ($\tilde{A}^1A''$) electronic states of the HSiNC species using the GAUSSIAN 03 program package.[18] The geometries of the [H, Si, C, N] isomers were fully optimised at different levels of theory using the augmented triple zeta correlated consistent basis set (aug-cc-pVTZ) of Dunning *et al.*[19-21] The methods used include, the hybrid density functional method B3LYP,[22] the 2$^{nd}$ order Møller-Plesset (MP2) method using both the frozen core (MP2(FC)) and full (MP2(full)) (*i.e.*, the inclusion of core electrons) methods,[23-26] and the quadratic configuration interaction method including

singles and doubles, QCISD.[27] Further single-point calculations were carried out using QCISD(T), using the QCISD structure to obtain more accurate energies.[27] Finally, to obtain accurate energies for the transition energy the symmetry adapted cluster/configuration interaction (SAC-CI) method of Nakatsuji *et al.*[28] was implemented. Firstly "level-two" calculations were carried out to optimise the structure, followed by further single-point calculations at "level-three" to obtain the energies. All the resulting structures were checked by calculating the vibrational wavenumbers where possible, to ensure that true minima and not transition states were identified, and to obtain the zero point energy to correct the energy.

## *4.4   Computational Results*

### 4.4.1   Energy Calculations

In all cases the energies given have been zero-point corrected from values taken from the vibrational frequency calculations run in parallel to the optimisation procedures, with the exception of the SAC-CI calculations where this procedure was beyond the practical time constraints of running the calculations.

The results of the *ab initio* calculations at the MP2 level of theory using the aug-cc-pVTZ basis sets give a gross underestimation of the observed transition wavenumber value, $T_0$ for the $\tilde{A}^1A'' - \tilde{X}^1A'$ transition of HSiNC. The experimental value is ~19950 cm$^{-1}$, while the *ab initio* calculations predict it to be ~15940 cm$^{-1}$ giving a discrepancy of ~4000 cm$^{-1}$. To examine the validity of this result, a series of calculations were carried out on the halosilylene systems, HSiX, (where X= F, Cl, Br) for which there already exists accurate experimental data for comparison.[3,4,29] The results of these calculations are summarised in Table 4.1. The results in Table 4.1 indicate that in systems, such as this one, the underestimation of $T_0$ is present in all cases.

In contrast to the underestimation observed in the MP2(FC) calculations the vertical excitation energy determined by Flores *et al.* mentioned in section 4.1 above overestimates the observed $T_0$ value by ~2000 cm$^{-1}$. The value given by Flores is 21938 cm$^{-1}$.

Table 4.1: Experimental ($T_{0 \text{ Obs}}$), *ab initio* ($T_{0 \text{ Calc}}$) for the $\tilde{A}^1A'' - \tilde{X}^1A'$ transition of various species calculated at MP2/aug-cc-pVTZ, and the difference between

experiment and calculated values ($T_{0 \text{ Obs-Calc}}$) for the halosilylenes (HSiX; X=F, Cl, Br), HSiNC and HSiNCO. All values are given in cm$^{-1}$.

|  | $T_{0 \text{ (Obs)}}$ | $T_{0 \text{ (Calc)}}$ | $\Delta T_{0 \text{ (Obs-Calc)}}$ |
|---|---|---|---|
| HSiF | 23260.025[a] | 18385.8 | 4874.2 |
| HSiCl | 20717.769[b] | 16329.1 | 4388.7 |
| HSiBr | 19902.851[c] | 15689.0 | 4213.9 |
| HSiNC (This work) | 19950.569 | 15938.3 | 4012.3 |
| HSiNC (Flores et al.) | 19950.569 | 21938.0 | -1987.4 |
| HSiNCO (Chapter 6) | 20346.335 | 16386.6 | 3959.8 |

[a]Values taken from Ref [29]
[b]Values taken from Ref [4]
[c]Values taken from Ref [3]

Similarly large discrepancies between the calculated and experimentally observed transition energies were seen in the B3LYP calculations. To see if it was possible to obtain a more accurate value for the transition energy of the HSiNC radical more sophisticated calculations were undertaken using the symmetry adapted cluster-configuration interaction (SAC-CI) methods of Nakatsuji *et al.*[28] utilising the aug-cc-pVDZ basis set to optimise the geometries. Once this was complete, further single point calculations were run using the larger aug-cc-pVTZ (except in the HSiNCO case where no augmentation to the basis set was used) and the structures fixed to those obtained from the smaller basis set calculations. This was necessary as optimisation of the full structures using the larger basis set was deemed too computationally demanding, and would have taken far too long. The results of these calculations are shown in Table 4.2.

Table 4.2: Experimental ($T_{0 \text{ Obs}}$), *ab initio* ($T_{0 \text{ Calc}}$) for the $\tilde{A}^1 A'' - \tilde{X}^1 A'$ transition of various species calculated at SAC-CI/aug-cc-pVTZ (cc-pVTZ for HSiNCO), and the difference between experiment and calculated values ($T_{0 \text{ Obs-Calc}}$) for the halosilylenes (HSiX; X=F, Cl), HSiNC and HSiNCO. All values are given in cm$^{-1}$.

| Species | $T_{0 \text{ (Obs)}}$ | $T_{0 \text{ (Calc)}}$ | $\Delta T_{0 \text{ (Obs-Calc)}}$ |
|---|---|---|---|
| HSiF | 23260.025[a] | 23240.0 | 559.3 |
| HSiCl | 20717.769[b] | 21199.3 | 481.5 |
| HSiNC | 19950.569 | 21938.3[c] | 1987.7 |
| HSiNC (This work) | 19950.569 | 19820.1 | 130.5 |
| HSiNCO (Chapter 6) | 20346.335 | 20914.8 | 568.5 |

[a]Values taken from Ref [29]
[b]Values taken from Ref [4]
[c]Value taken from Ref [8]
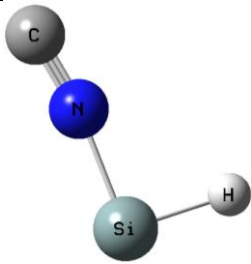
Although still not perfect, the results of the SAC-CI calculations show that the estimations of the transition energies are much closer to the observed values than for any other level of theory considered.

## 4.4.2   Determination of Molecular Geometry

The parameters for optimised geometries of the ground ($\tilde{X}^1 A'$) and excited ($\tilde{A}^1 A''$) electronic states for HSiNC are given in Tables 4.3 and 4.4, respectively. Included in each of the tables is an image of HSiNC produced using the geometric parameters given. In the ground ($\tilde{X}^1 A'$) state, there is very good agreement between the values calculated at the MP2 level of theory and those obtained from the microwave study.[15] As there has not been any previous experimental work carried out on the excited ($\tilde{A}^1 A''$) state, there is no experimental data for comparison. However, it can be assumed that the values obtained from these calculations will be valid given the good agreement found in the ground state data. As discussed earlier, the appearance of axis-switching peaks in the experimental spectrum suggests that there is a significant geometry change upon excitation from the $\tilde{X}^1 A'$ to $\tilde{A}^1 A''$ electronic state of HSiNC. The structural parameters given in Tables 4.3 and 4.4 show that on excitation the H-Si-N angle increases significantly, and this is due to electron density being transferred from the hybridised Si-H molecular orbital to an out of plane $p$ orbital also located on the silicon. This shift in the electron density explains the increase in the H-Si-N angle as it results in a change in electron density on the silicon from purely $p$ in character to sp$^2$ hybridised. This can be seen in Figure 4.1 which gives a

three dimensional representation of the HOMO orbital (using natural bond orbitals) in both the ground electronic state and the $\tilde{A}^1A''$ excited electronic state of HSiNC at the B3LYP level of theory. Therefore, it is predicted that the appearance of the axis-switching peaks may be attributed to the large change in the H-Si-N bond angle, which increases from ~93° to 116°.
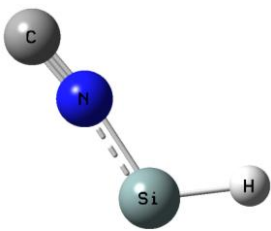
Table 4.3: Equilibrium geometric parameters for the ground ($\tilde{X}^1A'$) electronic state of HSiNC. All bond lengths are given in angstroms and all bond angles are given in degrees.

| Parameter | MP2 | B3LYP | SAC-CI | Experiment[a] |
|---|---|---|---|---|
| r(H-Si) | 1.512 | 1.524 | 1.521 | 1.5261(3) |
| r(Si-N) | 1.778 | 1.768 | 1.800 | 1.763(7) |
| r(N-C) | 1.190 | 1.178 | 1.186 | 1.170[b] |
| ∠(H-Si-N) | 93.2 | 93.7 | 93.6 | 92.90(2) |
| ∠(Si-N-C) | 170.9 | 169.9 | 170.1 | 169.31(5) |

[a] Values taken from Ref [15]
[b] Fixed to value obtained from Ref [30]

Table 4.4: Equilibrium geometric parameters for the excited ($\tilde{A}^1A''$) electronic state of HSiNC. All bond lengths are given in angstroms and all bond angles are given in degrees.

| Parameter | MP2 | B3LYP | SAC-CI |
|---|---|---|---|
| r(H-Si) | 1.479 | 1.497 | 1.497 |
| r(Si-N) | 1.735 | 1.719 | 1.731 |
| r(N-C) | 1.187 | 1.183 | 1.192 |
| ∠(H-Si-N) | 116.2 | 115.2 | 115.1 |
| ∠(Si-N-C) | 172.9 | 173.5 | 175.1 |

H
|
Si
|
N
|
C
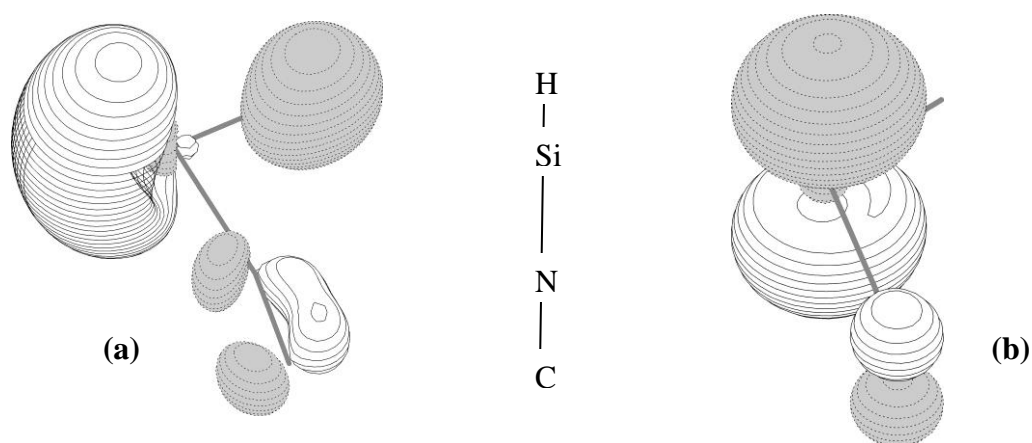
Figure 4.1: Three dimensional representations of the HOMO of HSiNC in the (a) ground electronic state ($^1A'$) and (b) the first $\widetilde{A}\,^1A''$ electronic state (contours are in 0.08 steps).

### 4.4.3 Vibrational Wavenumbers

As mentioned in the text previously, harmonic wavenumber calculations were also carried out so as to obtain zero-point energy corrections, and to make sure the determined structures were true minima and not transition states. These calculations also yielded estimations of the vibrational wavenumbers which were used to aid in the assignments of the observed vibrational bands in the LIF spectra and the assignments of the progressions observed in the DF spectra. The unscaled values obtained from these calculations are given in Tables 4.5 and 4.6 for the ground and excited states, respectively. To see how they compare, anharmonic wavenumber calculations were also run at the MP2/aug-cc-pVTZ level of theory to see if more accurate values could be obtained. However, it was found that the anharmonic wavenumber calculations did not provide significantly different values from the harmonic wavenumbers. These values are also given in Tables 4.5 and 46 for the ground and excited states, respectively.

Table 4.5: Vibrational assignments and wavenumber values for the ground ($\tilde{X}\,^1A'$) state vibrational modes of HSiNC calculated at different levels of theory. In all cases, the aug-cc-pVTZ basis set was used and all values are given in cm$^{-1}$.

| Vibrational mode (symmetry) | | Assignment | MP2(FC)[a] (harmonic) | MP2(FC)[a] (anharmonic) | B3LYP[a] | QCISD[a] |
|---|---|---|---|---|---|---|
| $\nu_1$ | ( a′) | Si-H stretch | 2125.9 | 2052.3 | 2029.3 | 2102.4 |
| $\nu_2$ | ( a′) | N-C stretch | 2037.2 | 2007.2 | 2096.6 | 2077.8 |
| $\nu_3$ | (a′) | Si-H wag | 882.9 | 867.2 | 868.1 | 879.8 |
| $\nu_4$ | (a′) | Si-N stretch | 624.4 | 620.8 | 626.4 | 635.6 |
| $\nu_5$ | (a′) | Si-N-C in-plane bend | 204.7 | 208.7 | 219.9 | 205.4 |
| $\nu_6$ | (a″) | Si-N-C out-of-plane bend | 159.2 | 164.6 | 167.0 | 155.0 |

[a] Unscaled wavenumbers

Table 4.6: Vibrational assignments and wavenumber values for the excited ($\tilde{A}\,^1A''$) state vibrational modes of HSiNC calculated at different levels of theory. In all cases, the aug-cc-pVTZ basis set was used and all values are given in cm$^{-1}$.

| Vibrational mode (symmetry) | | Assignment | MP2(FC)[a] (harmonic) | MP2(FC)[a] (anharmonic) | B3LYP[a] | QCISD[a] |
|---|---|---|---|---|---|---|
| $\nu_1$ | ( a′) | Si-H stretch | 2234.1 | 2135.7 | 2065.6 | 2138.7 |
| $\nu_2$ | ( a′) | N-C stretch | 2172.9 | 2216.3 | 2022.1 | 2003.3 |
| $\nu_3$ | (a′) | Si-H wag | 700.6 | 689.3 | 685.9 | 697.6 |
| $\nu_4$ | (a′) | Si-N stretch | 669.0 | 662.0 | 656.0 | 665.2 |
| $\nu_5$ | (a′) | Si-N-C in-plane bend | 234.3 | 211.8 | 268.6 | 254.1 |
| $\nu_6$ | (a″) | Si-N-C out-of-plane bend | 200.4 | 246.2 | 203.3 | 191.3 |

[a] Unscaled wavenumbers

## 4.5    *Experimental Results*

### 4.5.1   Laser Induced Fluorescence Spectra

Laser induced fluorescence (LIF) spectra of HSiNC were recorded across the wavelength region 520-420 nm using a variety of laser dyes. All spectra were calibrated by a combination of an optogalvanic cell and etalon details of which are given in section 2.6.2 in Chapter 2. The calibration process was carried out by means of the *DataProcessing_LIFv2.m* MATLAB®[31] program written by the author, a copy of which is given in the addendum.

### 4.5.2   Rotational Analysis

The $0_0^0$ band of HSiNC was studied in more detail by medium resolution LIF spectroscopy in order to obtain accurate rotational constants. In our spectra the *Q*-branches could not be rotationally resolved, so the analysis relies only on assignments of *P* and *R* branches. Figure 4.2 shows a portion of the medium resolution scan of the $0_0^0$ band, where the asymmetric splittings of the $^rR_1$ sub-band are partially resolved.

The HSiNC spectrum of the $0_0^0$ band was fitted using Colin Western's spectral fitting program PGOPHER.[32] In the HSiNC spectrum, transitions with $K_a'' = 0$, 1 and 2 and $K_a' = 0$-3 in the excited state were assigned with *J''* values up to 15 for the strongest branches. Once the assignments were complete, the rotational constants were determined using least-squares fitting of Watson's *A* reduction of the asymmetric top rotational Hamiltonian in PGOPHER.[33] The Hamiltonian takes the form given in Equations [2.1] and [2.3] in Chapter 2.

In this Hamiltonian the model parameters follow the conventional spectroscopic notation, showing the rotational constants (*A*, *B*, *C*), as well as the quartic centrifugal distortion constants ($\Delta_J$, $\Delta_{JK}$, $\Delta_K$, $\delta_J$, $\delta_K$) shown explicitly. The expression could also be extended to show sextic (and beyond) centrifugal distortion constants, but this is not necessary in this case as the inclusion of the quartic terms provides an adequate fit of the data. In fact, the inclusion of the $\delta_J$ and $\delta_K$ centrifugal distortion constants (corresponding to off-diagonal terms in the matrix) was not necessary to obtain a good fit.

It is crucial when fitting this sort of data that the correct representation of the Hamiltonian is used. In this case, the $I^r$ representation was used to fit the observed line wavenumber values. The reason the $I^r$ representation was used is that, as will be seen, the asymmetry parameter, $\kappa$, takes a value very near -1 corresponding to a near prolate symmetric rotor. Therefore, the $I^r$ representation is the most suitable to use (Table 7.3; page 236 of Ref [34]).

In cases where the asymmetry doubling was not sufficiently resolved to unambiguously assign the peaks, care was taken to appropriately weight these lines in the fit. In PGOPHER, the weight given to a line is the standard deviation of the measured peak position. If this is given a value of one it indicates that this line is good. For less certain measurements larger values are used. In this case, the limit for defining a 'good' line was if the error associated with it was <0.03 cm$^{-1}$. Where the error in the measurement was >0.03 cm$^{-1}$ a suitable weight was applied to the line in question.

In all cases the overall standard deviation of the fit was comparable to the estimated uncertainties in the measurements. The resulting constants for the ground state are given in Table 4.7 together with the constants obtained from *ab initio* calculations, the previous microwave study,[15] and the previous *ab initio* study.[8] Table 4.8 gives the excited state constants obtained from this work and the constants determined from the *ab initio* work carried out in this study. The correlation matrix for this fit may be found in Appendix A.

The rotational constants provided in Table 4.7 may be substituted into the following equation to obtain a value for Ray's asymmetry parameter ($\kappa$) of -0.99842. Therefore, the use of the $I^r$ representation is justified.
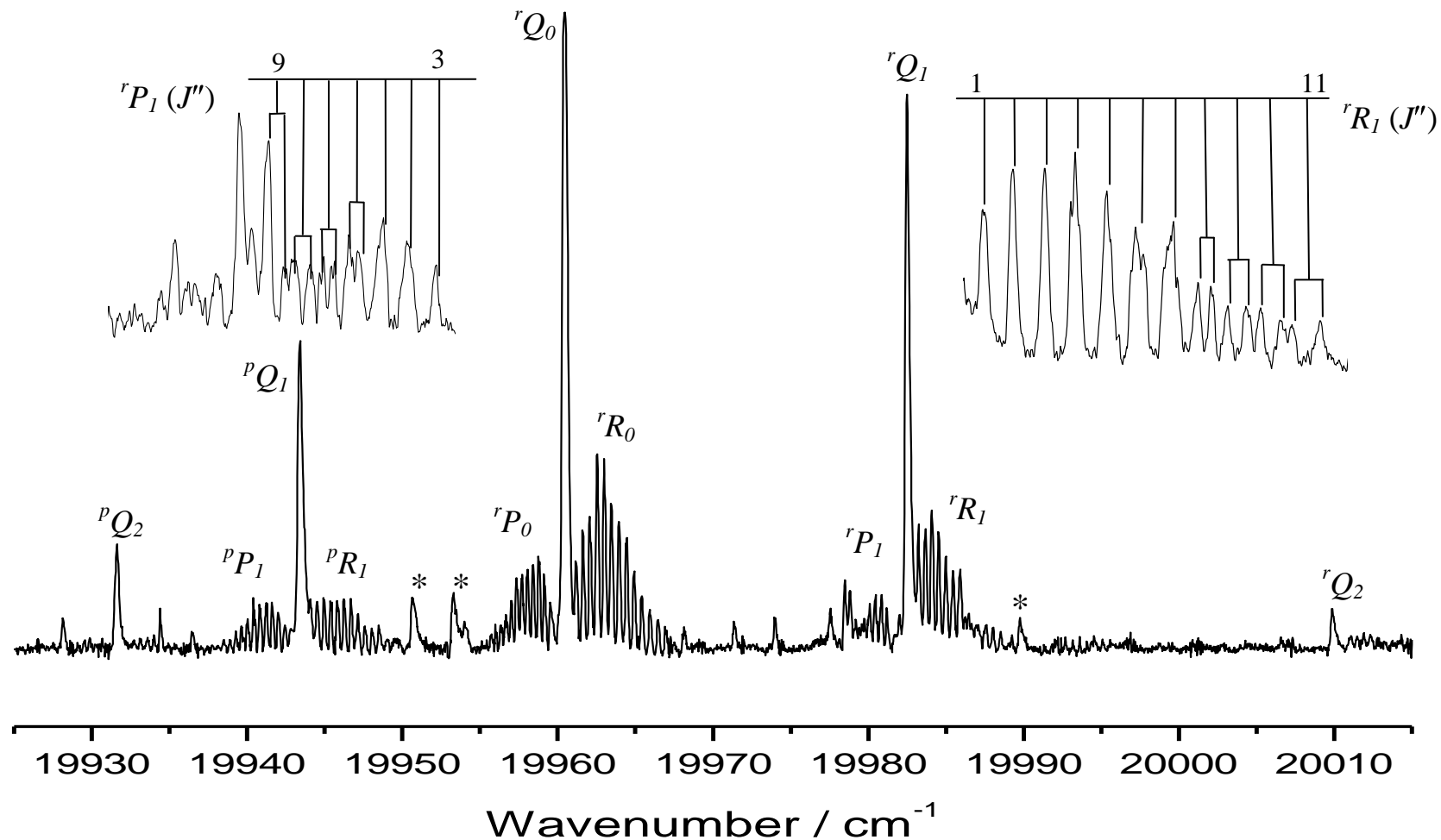
Figure 4.2: The medium resolution spectrum of the $0_0^0$ band of HSiNC showing some of the rotational branch assignments. The asterisks mark the axis-switching peaks. The inserts in the upper left and right corners shows the resolved asymmetry splittings in the $^rP_1$ and $^rR_1$ branches, respectively. The spectrum was recorded using an incremental laser step size of 0.0008 nm with 64 shot averaging at each step. The temperature of the spectrum is estimated to be 15 K.

Table 4.7: The ground state rotational constants (cm$^{-1}$) of HSiNC .

| Constant | $0_0^0$ (this work)[a] | Ab initio[d] | Microwave from Ref [15] | Ab initio from Ref [8] |
|---|---|---|---|---|
| $A$...............  | 7.5151(87) | 7.4353 | 7.5552(912) | 7.2928 |
| $B$............... | 0.2071391(15)[b] | 0.2023 | 0.2071391(15) | 0.2044 |
| $C$............... | 0.201351247(16)[b] | 0.1969 | 0.201351247(16) | 0.1988 |
| $\Delta_J \times 10^8$...... | 9.1[b] | - | 9.1(13) | - |
| $\Delta_{JK} \times 10^6$..... | 1.769[b] | - | 1.769(19) | - |
| $\Delta_K$............. | 0.0203(20) | - | - | - |
| Std. Dev.[c].... | 0.014 | - | - | - |
| No. of fitted transitions.... | 103 | - | 26 | - |

[a] Numbers in parentheses are 1$\sigma$ uncertainties in units of the last significant digit
[b] Fixed to the values obtained from Ref [15]
[c] Overall standard deviation of fit (in cm$^{-1}$)
[d] Caclulated at the MP2(FC) level of theory using the aug-cc-pVTZ basis set

Table 4.8: The excited state rotational constants (cm$^{-1}$) of the $0_0^0$ band of the $\tilde{A}\,^1A''-\tilde{X}\,^1A'$ transition of HSiNC.

| Constant | $0_0^0$ (this work) | Ab initio[b] |
|---|---|---|
| $A$........................... | 10.0438(28) | 10.2333 |
| $B$........................... | 0.20916(20) | 0.2047 |
| $C$........................... | 0.20601(21) | 0.2007 |
| $\Delta_J \times 10^8$................... | 8.35(77) | - |
| $\Delta_{JK} \times 10^6$................. | 47.95(35) | - |
| $\Delta_K$ ........................ | 0.00467(44) | - |
| $T_0$........................... | 19950.5623(77) | 15850 |
| Std. Dev[a]................. | 0.014 | - |
| No. of fitted transitions.. | 103 | - |

[a] Overall standard deviation of fit (in cm$^{-1}$)
[b] Caclulated at the MP2(FC) level of theory using the aug-cc-pVTZ basis set

It is important to note that there is a large difference between the $\Delta_{JK}$ and $\Delta_K$ values in the ground state and excited states. It is deemed necessary to include these terms in the fitting of the spectrum, as without them the RMS error in the fit becomes very large, and the constants do not fit the data for the two smallest sub-bands of the spectrum. This difference in the parameters in going from one state to another is not

observed in the triatomic HSiX (X= F, Cl, Br) species. This discrepancy between the halo- and pseudohalosilylene systems is accounted for by the lack of data obtained for the HSiNC system where the highest $K$ value obtained for lines in the ground state was only two and in the excited states only three. The observed lines with assignments are given in Table 4.9. In the halogen analogues the highest $K$ values went up to four and five for the ground and excited states, respectively.

Table 4.9: Observed transition frequencies (in cm$^{-1}$) for the $\tilde{A}^1A'' - \tilde{X}^1A'$ transition of the $0_0^0$ band of HSiNC used for fitting the rotational parameters.

| Transition ($J'_{K_aK_c} - J''_{K_aK_c}$) | Observed | Calculated | O-C | Weight |
|---|---|---|---|---|
| $5_{14} - 6_{24}$ | 19929.1190 | 19929.1466 | -0.0276 | 1 |
| $5_{15} - 6_{25}$ | 19929.1190 | 19929.0600 | 0.0590 | 4 |
| $4_{13} - 5_{23}$ | 19929.5450 | 19929.5088 | 0.0362 | 2 |
| $3_{12} - 4_{22}$ | 19929.8760 | 19929.8801 | -0.0041 | 1 |
| $3_{13} - 4_{23}$ | 19929.8760 | 19929.8454 | 0.0306 | 2 |
| $2_{11} - 3_{21}$ | 19930.2800 | 19930.2607 | 0.0193 | 1 |
| $2_{12} - 3_{22}$ | 19930.2800 | 19930.2433 | 0.0367 | 2 |
| $1_{10} - 2_{20}$ | 19930.6670 | 19930.6505 | 0.0165 | 1 |
| $1_{11} - 2_{21}$ | 19930.6670 | 19930.6447 | 0.0223 | 1 |
| $3_{12} - 2_{20}$ | 19932.7060 | 19932.7396 | -0.0336 | 2 |
| $3_{13} - 2_{21}$ | 19932.7060 | 19932.7048 | 0.0012 | 1 |
| $4_{13} - 3_{21}$ | 19933.1270 | 19933.1852 | -0.0582 | 4 |
| $4_{14} - 3_{22}$ | 19933.1270 | 19933.1274 | -0.0004 | 1 |
| $5_{14} - 4_{22}$ | 19933.5950 | 19933.6400 | -0.0450 | 3 |
| $5_{15} - 4_{23}$ | 19933.5950 | 19933.5532 | 0.0418 | 3 |
| $6_{16} - 5_{24}$ | 19934.0140 | 19933.9823 | 0.0317 | 2 |
| $10_{010} - 11_{110}$ | 19938.9346 | 19938.9503 | -0.0157 | 1 |
| $9_{09} - 10_{19}$ | 19939.3439 | 19939.3298 | 0.0141 | 1 |
| $8_{08} - 9_{18}$ | 19939.7011 | 19939.7118 | -0.0107 | 1 |
| $7_{07} - 8_{17}$ | 19940.0992 | 19940.0965 | 0.0027 | 1 |
| $6_{06} - 7_{16}$ | 19940.4687 | 19940.4842 | -0.0155 | 1 |
| $4_{04} - 5_{14}$ | 19941.2535 | 19941.2689 | -0.0154 | 1 |
| $3_{03} - 4_{13}$ | 19941.6554 | 19941.6662 | -0.0108 | 1 |
| $2_{02} - 3_{12}$ | 19942.0431 | 19942.0670 | -0.0239 | 1 |
| $1_{01} - 2_{11}$ | 19942.4453 | 19942.4713 | -0.0260 | 1 |
| $0_{00} - 1_{10}$ | 19942.8471 | 19942.8791 | -0.0320 | 2 |

Table 4.9 (cont.)

| | | | | |
|---|---|---|---|---|
| $3_{03} - 2_{11}$ | 19944.5225 | 19944.5459 | -0.0234 | 1 |
| $4_{04} - 3_{12}$ | 19944.9263 | 19944.9713 | -0.0450 | 3 |
| $5_{05} - 4_{13}$ | 19945.3744 | 19945.4000 | -0.0256 | 1 |
| $6_{06} - 5_{14}$ | 19945.7976 | 19945.8319 | -0.0343 | 2 |
| $7_{07} - 6_{15}$ | 19946.2145 | 19946.2669 | -0.0524 | 4 |
| $8_{08} - 7_{16}$ | 19946.6741 | 19946.7047 | -0.0306 | 2 |
| $10_{0\,10} - 9_{18}$ | 19947.5658 | 19947.5882 | -0.0224 | 1 |
| $14_{1\,13} - 15_{0\,15}$ | 19955.1659 | 19955.1596 | 0.0063 | 1 |
| $13_{1\,12} - 14_{0\,14}$ | 19955.4251 | 19955.4453 | -0.0202 | 1 |
| $12_{1\,11} - 13_{0\,13}$ | 19955.7394 | 19955.7388 | 0.0006 | 1 |
| $11_{1\,10} - 12_{0\,12}$ | 19956.0308 | 19956.0401 | -0.0093 | 1 |
| $10_{19} - 11_{0\,11}$ | 19956.3283 | 19956.3496 | -0.0213 | 1 |
| $9_{18} - 10_{0\,10}$ | 19956.6850 | 19956.6674 | 0.0176 | 1 |
| $8_{17} - 9_{09}$ | 19956.9911 | 19956.9938 | -0.0027 | 1 |
| $7_{16} - 8_{08}$ | 19957.3459 | 19957.3288 | 0.0171 | 1 |
| $6_{15} - 7_{07}$ | 19957.6756 | 19957.6728 | 0.0028 | 1 |
| $5_{14} - 6_{06}$ | 19958.0575 | 19958.0257 | 0.0318 | 2 |
| $4_{13} - 5_{05}$ | 19958.3990 | 19958.3877 | 0.0113 | 1 |
| $3_{12} - 4_{04}$ | 19958.8020 | 19958.7589 | 0.0431 | 3 |
| $2_{11} - 3_{03}$ | 19959.1606 | 19959.1393 | 0.0213 | 1 |
| $1_{10} - 2_{02}$ | 19959.5805 | 19959.5291 | 0.0514 | 4 |
| $2_{11} - 1_{01}$ | 19961.2403 | 19961.1817 | 0.0586 | 4 |
| $3_{12} - 2_{02}$ | 19961.6585 | 19961.6182 | 0.0403 | 3 |
| $4_{13} - 3_{03}$ | 19962.1064 | 19962.0639 | 0.0425 | 3 |
| $5_{14} - 4_{04}$ | 19962.5606 | 19962.5187 | 0.0419 | 3 |
| $6_{15} - 5_{05}$ | 19962.9981 | 19962.9826 | 0.0155 | 1 |
| $7_{16} - 6_{06}$ | 19963.4886 | 19963.4554 | 0.0332 | 2 |
| $8_{17} - 7_{07}$ | 19963.9488 | 19963.9370 | 0.0118 | 1 |
| $9_{18} - 8_{08}$ | 19964.4339 | 19964.4271 | 0.0068 | 1 |
| $10_{19} - 9_{09}$ | 19964.9437 | 19964.9257 | 0.0180 | 1 |
| $11_{1\,10} - 10_{0\,10}$ | 19965.4413 | 19965.4325 | 0.0088 | 1 |
| $12_{1\,11} - 11_{0\,11}$ | 19965.9453 | 19965.9474 | -0.0021 | 1 |
| $13_{1\,12} - 12_{0\,12}$ | 19966.4763 | 19966.4699 | 0.0064 | 1 |
| $14_{1\,13} - 13_{0\,13}$ | 19966.9638 | 19967.0000 | -0.0362 | 2 |
| $15_{1\,14} - 14_{0\,14}$ | 19967.5306 | 19967.5373 | -0.0067 | 1 |
| $9_{28} - 10_{1\,10}$ | 19978.9077 | 19978.9050 | 0.0027 | 1 |
| $8_{26} - 9_{18}$ | 19978.9077 | 19978.9690 | -0.0613 | 5 |
| $7_{26} - 8_{18}$ | 19979.5186 | 19979.5614 | -0.0428 | 3 |

Table 4.9 (cont.)

| | | | | |
|---|---|---|---|---|
| $6_{24} - 7_{16}$ | 19979.6889 | 19979.7407 | -0.0518 | 4 |
| $6_{25} - 7_{17}$ | 19979.8406 | 19979.9026 | -0.0620 | 5 |
| $5_{23} - 6_{15}$ | 19980.0759 | 19980.1313 | -0.0554 | 4 |
| $5_{24} - 6_{16}$ | 19980.1996 | 19980.2528 | -0.0532 | 4 |
| $4_{22} - 5_{14}$ | 19980.5382 | 19980.5252 | 0.0130 | 1 |
| $3_{21} - 4_{13}$ | 19980.9002 | 19980.9224 | -0.0222 | 1 |
| $2_{20} - 3_{12}$ | 19981.2987 | 19981.3232 | -0.0245 | 1 |
| $2_{21} - 3_{13}$ | 19981.2987 | 19981.3579 | -0.0592 | 4 |
| $2_{21} - 1_{11}$ | 19983.3738 | 19983.3859 | -0.0121 | 1 |
| $2_{20} - 1_{10}$ | 19983.3738 | 19983.3801 | -0.0063 | 1 |
| $3_{22} - 2_{12}$ | 19983.7873 | 19983.8194 | -0.0321 | 2 |
| $3_{21} - 2_{11}$ | 19983.7873 | 19983.8021 | -0.0148 | 1 |
| $4_{23} - 3_{13}$ | 19984.2468 | 19984.2622 | -0.0154 | 1 |
| $4_{22} - 3_{12}$ | 19984.2468 | 19984.2275 | 0.0193 | 1 |
| $5_{24} - 4_{14}$ | 19984.6758 | 19984.7141 | -0.0383 | 2 |
| $5_{23} - 4_{13}$ | 19984.6758 | 19984.6564 | 0.0194 | 1 |
| $6_{25} - 5_{15}$ | 19985.1363 | 19985.1751 | -0.0388 | 2 |
| $6_{24} - 5_{14}$ | 19985.1363 | 19985.0884 | 0.0479 | 3 |
| $9_{27} - 8_{17}$ | 19986.4259 | 19986.4030 | 0.0229 | 1 |
| $9_{28} - 8_{18}$ | 19986.6328 | 19986.6105 | 0.0223 | 1 |
| $10_{28} - 9_{18}$ | 19986.8524 | 19986.8467 | 0.0057 | 1 |
| $10_{29} - 9_{19}$ | 19987.1331 | 19987.1059 | 0.0272 | 1 |
| $11_{29} - 10_{19}$ | 19987.3289 | 19987.2929 | 0.0360 | 2 |
| $11_{2\,10} - 10_{1\,10}$ | 19987.6269 | 19987.6094 | 0.0175 | 1 |
| $12_{2\,10} - 11_{1\,10}$ | 19987.7765 | 19987.7414 | 0.0351 | 2 |
| $12_{2\,11} - 11_{1\,11}$ | 19988.1765 | 19988.1208 | 0.0557 | 4 |
| $13_{2\,11} - 12_{1\,11}$ | 19988.1765 | 19988.1919 | -0.0154 | 1 |
| $3_{31} - 2_{21}$ | 20011.0650 | 20011.0338 | 0.0312 | 2 |
| $3_{30} - 2_{20}$ | 20011.0650 | 20011.0338 | 0.0312 | 2 |
| $4_{32} - 3_{22}$ | 20011.4870 | 20011.4679 | 0.0191 | 2 |
| $4_{31} - 3_{21}$ | 20011.4870 | 20011.4679 | 0.0191 | 2 |
| $5_{33} - 4_{23}$ | 20011.9060 | 20011.9083 | -0.0023 | 2 |
| $5_{32} - 4_{22}$ | 20011.9060 | 20011.9082 | -0.0022 | 2 |
| $6_{34} - 5_{24}$ | 20012.3390 | 20012.3547 | -0.0157 | 2 |
| $6_{33} - 5_{23}$ | 20012.3390 | 20012.3546 | -0.0156 | 2 |

### 4.5.3 Axis-Switching

As mentioned in the introduction of this chapter, one of the most interesting features of this spectrum is the occurrence of axis-switching peaks. Originally this phenomenon was discussed by Hougen and Watson.[2] When there is a geometry change on electronic excitation, the inertial axes of the ground and excited states do not coincide. This is due to the molecule fixed axis system for each state as defined by the Eckart conditions. These conditions allow, to a large extent, separation of the rotational motion from the internal vibrational motions. Although the coupling between these motions cannot be completely separated, the Eckart conditions minimise the energy between them. When a molecule undergoes an optical transition to a different electronic state, the definition of the body fixed axis system switches abruptly, hence the term *axis-switching*. The calculation of axis-switching parameters requires a common frame for both states, and this is achieved by application of a rotation transformation matrix. This transformation has the effect of mixing the rotational wavefunctions with $K'$ differing by one unit, and causes the observation of 'forbidden' sub-bands, as well as a decrease in the intensity of lines in the main (*i.e.*, perpendicular) sub-bands.

There are two categories of molecular transitions which may occur to result in axis-switching. These are non-linear to non-linear transitions and linear to non-linear transitions. Further to this, these transitions may be further divided into two sub-categories with the molecular system adopting a planar or non-planar geometry in either of the states under consideration. For linear to non-linear transitions the planar-to-planar geometry is always observed, while for linear to non-linear transitions either planar-to-planar or planar-to-non-planar geometries may occur.

Previous examples of molecular species exhibiting axis-switching of the linear to non-linear type are HCO, HCN, HND and acetylene ($C_2H_2$).[35-37] Previous examples of species exhibiting, the most common, non-linear to non-linear (planar-to-planar) type axis-switching are HNF, HSiF, HSiCl, HSiBr, HSiI, HCF, HCCl, HCBr and HNO.[3,4,29,35,36,38-40] Finally, there is one example of the far less common case of non-linear to non-linear (planar-to-non-planar) type axis-switching which is thiosphosgene ($Cl_2CS$).[2,37,41]

To our knowledge, this is the first occurrence of non-linear to non-linear (planar to planar) axis-switching observed in a system more complex than a triatomic, other

than in thiosphosgene ($Cl_2CS$) which is a very different system as it involves a planar to non-planar axis-switching mechanism. Although slightly different, acetylene provides the only example of a similar species and therefore is useful to consider in the determination of the axis-switching seen in HSiNC.

The assignment of the axis-switching peaks was very difficult in the spectrum of the $0_0^0$ band of HSiNC, as the intensity of the axis-switching peaks is comparable to those of the various contamination peaks observed in the spectrum. There is not enough data for accurate determination of the equilibrium geometries for the two electronic states. Therefore, to obtain an estimate for the axis-switching angle a trial and error approach was undertaken. Firstly, to unambiguously assign these peaks, it was necessary to simulate the spectrum with the inclusion of the axis-switching peaks and compare this simulation to the experimentally observed spectrum. This was done using the Jet Beam 95 (JB95) spectral fitting program,[42] and the resulting simulation together with the experimental spectrum may be found in Figure 4.3. The simulation was produced by using the rotational constants obtained from the fit of the medium resolution spectrum of the $0_0^0$ band and adjusting the axis-switching angle until there was good agreement between the experiment and simulation. Unfortunately one of the contaminants occurs in exactly the same region as the $^qQ_0$ and $^qQ_1$ axis-switching peaks, therefore the trial and error approach may only be applied to the $^sQ_0$ axis-switching peak. This trial and error approach gave the best estimate for the axis-switching angle ($\theta_T$) to be 1.0° ±0.2°.

There is a clear discrepancy between the simulation and experimentally observed spectra in terms of the relative intensity of the peaks. This can be attributed to the fact that the $^rQ_0$ branch is saturated in the experimental spectrum, giving the other $Q$-branches their relatively stronger appearance. Figures 4.4 and 4.5 show expanded views of the axis-switching regions, without showing the saturated $Q$-branch, thus eliminating the saturation issue. There is very good agreement, in terms of both intensity and position of the axis-switching peaks, between the simulated and experimental spectra. Also included in these figures are the $Q$-branch assignments for each of the peaks indicating the forbidden transitions corresponding to $\Delta K_a = 0$ ($^qQ_n$ $n=0,1$) and $\pm 2$ ($^sQ_0$).

Figure 4.4 shows quite clearly the problem with overlap between the assigned axis-switching peak at ~ 19953.2 cm$^{-1}$ and some unknown contaminant (marked with an asterisk) in the experimental spectrum. However, the simulation seems to match very accurately with what has been observed in terms of both intensity and position.

**(a) Simulated Spectrum**

**(b) Experimental Spectrum**

Unknown
contaminant

Unknown
contaminant

Unknown
contaminant

Wavenumber/cm-1
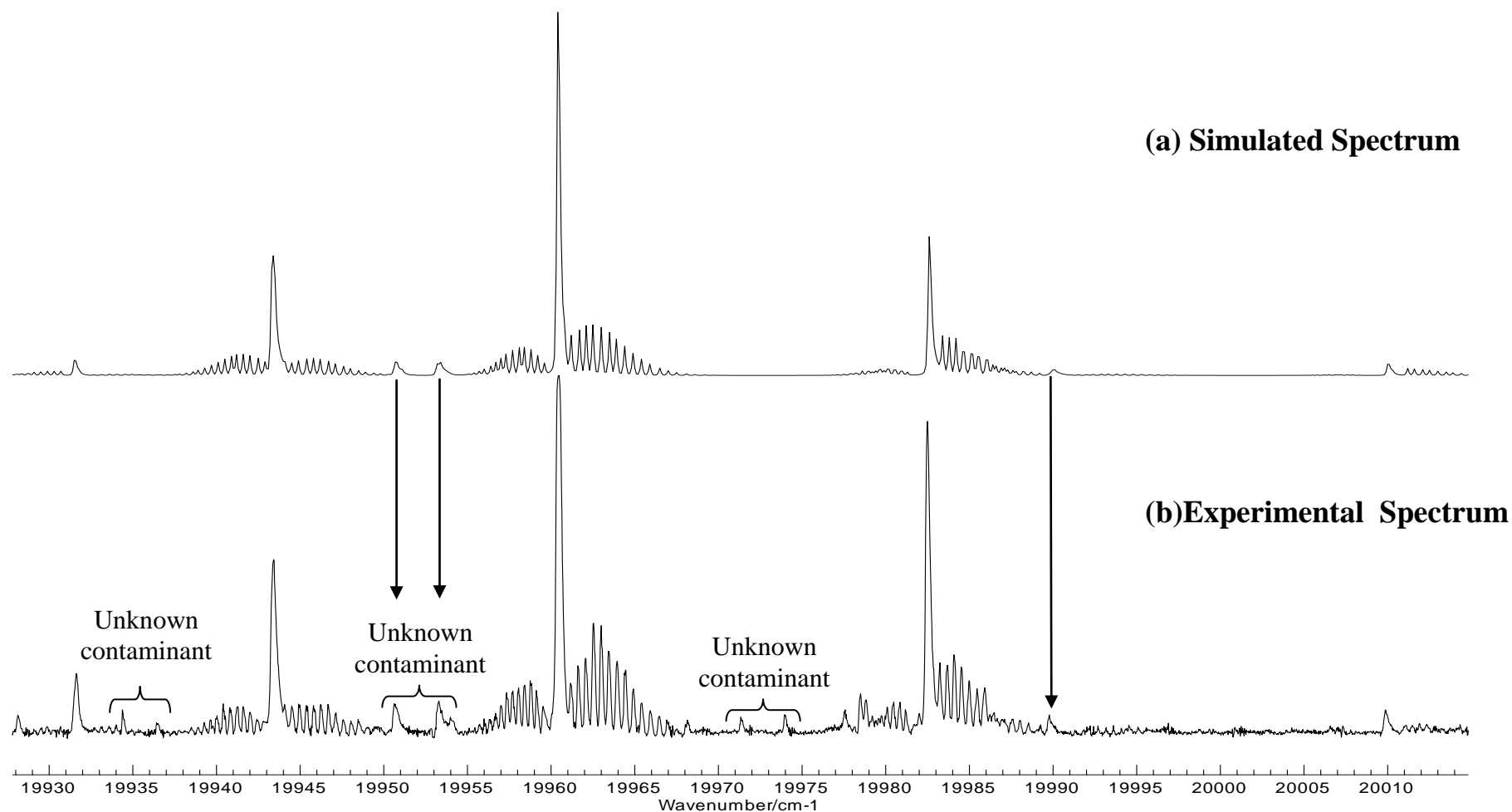
Figure 4.3: A comparison of the simulated (a) and experimental (b) spectra of the $0_0^0$ band of HSiNC. The arrows are clearly showing that the peaks attributed to axis-switching in the experimental spectrum may be simulated with good accuracy. Unfortunately, peaks attributed to an unknown contaminant lie in the same region as two of the axis-switching peaks. The temperature is estimated to be 12 K. The Gaussian linewidth is 0.15 cm$^{-1}$ and the Lorentzian linewidth is 0.05 cm$^{-1}$.
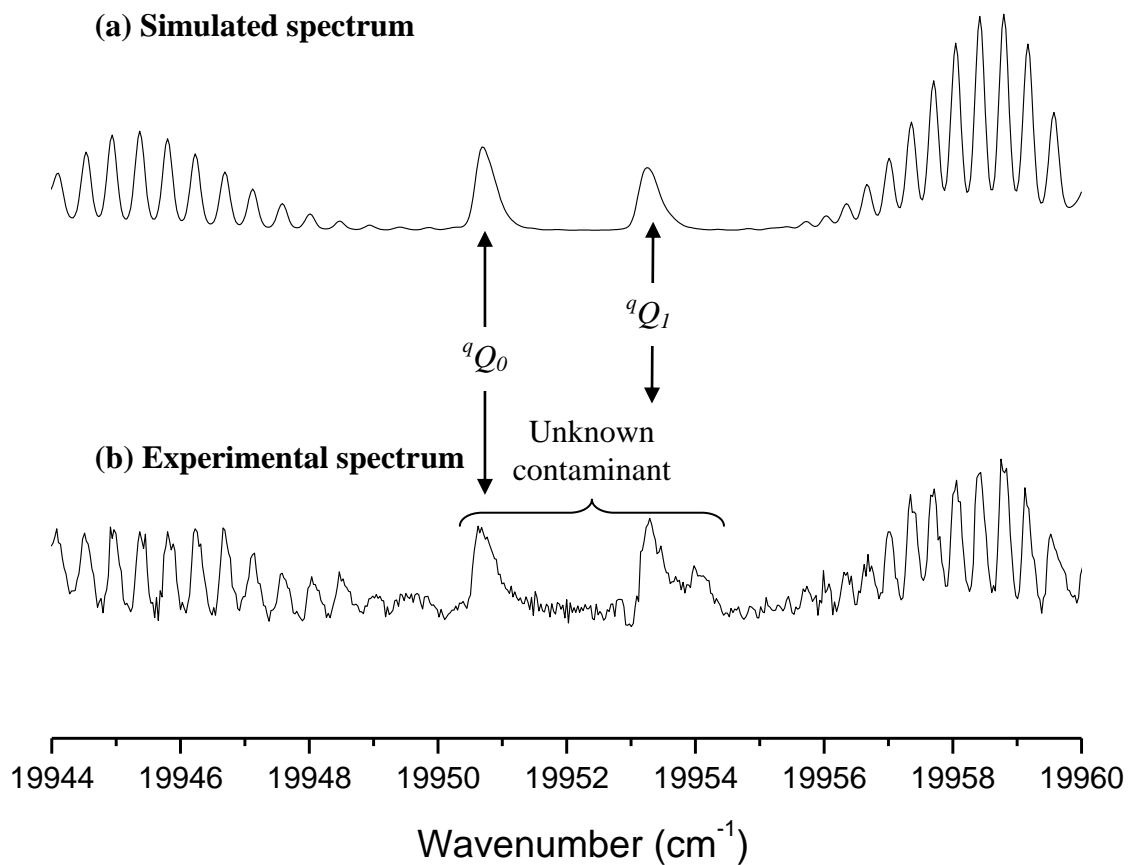
Figure 4.4: An expanded view of the axis-switching region between 19950 and 19955 cm$^{-1}$. (a) shows the simulated spectrum and (b) shows the experimental spectrum. The peaks shown unfortunately overlap with an unknown contaminant (as shown) making the exact determination of the axis-switching angle from these peaks very difficult.

**(a) Simulated spectrum**

**(b) Experimental spectrum**

$^{s}Q_0$

Wavenumber (cm$^{-1}$)
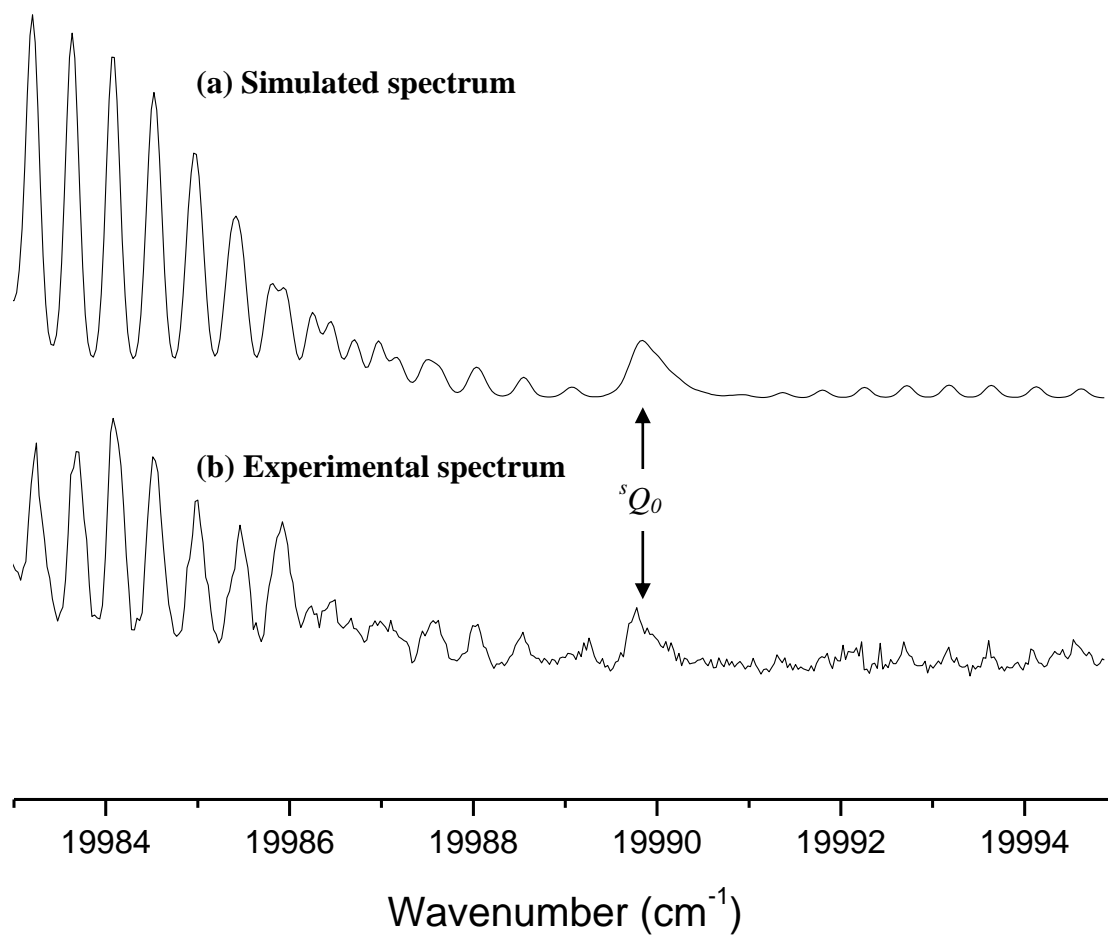
Figure 4.5: An expanded view of the axis-switching region between 19988 and 19992 cm$^{-1}$. (a) shows the simulated spectrum and (b) shows the experimental spectrum. This peak was used to determine the estimate for the axis-switching angle ($\theta_T$) of 1.0° ±0.2°.

To get another estimate of the axis-switching angle, a combination of the *ab initio* data together with the structural data from the microwave study was used. The *ab initio* data suggests that on electronic excitation from the ground ($\tilde{X}^1A'$) to first excited ($\tilde{A}^1A''$) state there is a significant change in the H-Si-N angle from approximately 93° to 116°. There is good agreement between the geometry determined by *ab initio* methods and that observed in the microwave study for the ground state. It is thought that this change in the H-Si-N angle is responsible for the appearance of the axis-switching peaks. Following the procedure described in the paper by Hougen and Watson,[2] it is possible to determine the axis-switching angle from the equilibrium geometries of the two electronic states calculated and compare the result against the value of 1.0° ±0.2° determined experimentally.

To determine the axis-switching angle from the equilibrium geometries, a coordinate axis system must be defined such that the centre of mass of the nuclei is at the origin and so that the moment of inertia tensor matrix contains no off-diagonal terms for the two states *A* and *B* (where *A* is the ground state and *B* is the excited state under consideration). Once this is done a rotation transformation matrix for the *A* to *B* transition must be defined, according to the Eulerian angles as given by Wilson, Decuis and Cross,[43] which has the form $c\chi = \cos\chi$, $s\chi = \sin\chi$, etc.

$$S = \begin{bmatrix} c\chi\ c\theta\ c\phi - s\chi\ s\phi & c\chi\ c\theta\ s\phi + s\chi\ c\phi & -c\chi\ s\theta \\ -s\chi\ c\theta\ c\phi - c\chi\ s\phi & -s\chi\ c\theta\ s\phi + c\chi\ c\phi & s\chi\ s\phi \\ s\theta\ c\phi & s\theta\ s\phi & c\theta \end{bmatrix} \qquad [4.1]$$

As the molecule in question is planar in its nature, the Eulerian angle $\theta$ is the only one which takes a value, while $\chi$ and $\phi$ are equal to zero so the rotation transformation matrix collapses down and takes the following form

$$S = \begin{bmatrix} \cos\theta & 0 & -\sin\theta \\ 0 & 1 & 0 \\ \sin\theta & 0 & \cos\theta \end{bmatrix} \qquad [4.2]$$

In this case the *y*-axis is in the plane of the molecule so does not need to be considered. This transformation matrix may now be applied to the *x* and *z*

coordinates for the equilibrium positions of the nuclei in the excited state of the molecule (*i.e.*, $x_B$ and $z_B$) as shown below:

$$\begin{bmatrix} cos\,\theta & 0 & -sin\,\theta \\ 0 & 1 & 0 \\ sin\,\theta & 0 & cos\,\theta \end{bmatrix} \begin{bmatrix} x_B \\ 0 \\ z_B \end{bmatrix} = \begin{bmatrix} x_B\,cos\,\theta - z_B\,sin\,\theta \\ 0 \\ x_B\,sin\,\theta + z_B\,cos\,\theta \end{bmatrix} \qquad [4.3]$$

*N.B.*, It is possible to consider the transition taking place in the other direction (*i.e.*, *B* to *A*). If this is required, then the inverse of the rotation transformation matrix ($S^{-1}$) must be used and applied to the *x* and *z* coordinates for the equilibrium positions of the nuclei in the ground state of the molecule.

The angle ($\theta$) in the resulting matrix given in Equation [4.3] corresponds to the axis-switching angle in going from state *A* to state *B*. This matrix must now be applied to the mass weighted *x* and *z* (*y* is in the plane and may therefore be neglected) coordinates of the ground state parameters for each atom in the system as follows:

$$0 = \sum_i \begin{bmatrix} m_i x_A & 0 & m_i z_A \end{bmatrix} \otimes \begin{bmatrix} x_B\,cos\,\theta - z_B\,sin\,\theta \\ 0 \\ x_B\,sin\,\theta + z_B\,cos\,\theta \end{bmatrix} \qquad [4.4]$$

Where $m_i$ is the mass of the $i^{th}$ nucleus in the molecule and $x_A$ and $z_A$ are the equilibrium positions of the nuclei in the ground state of the molecule. From this expression the axis-switching angle may be evaluated as follows:

$$cos\,\theta \left[ \sum_i m_i (z_A x_B - x_A z_B) \right] = sin\,\theta \left[ \sum_i m_i (x_A x_B + z_A z_B) \right]$$

$$[4.5]$$

$$tan\,\theta_T = \frac{sin\,\theta}{cos\,\theta} = \frac{\displaystyle\sum_i (m_i z_A x_B - m_i x_A z_B)}{\displaystyle\sum_i (m_i x_A x_B + m_i z_A z_B)}$$

where $\theta$ is the Eulerian angle about which the defined axis-system must be rotated for the switching mechanism to occur. This is represented schematically in Figure 4.6.
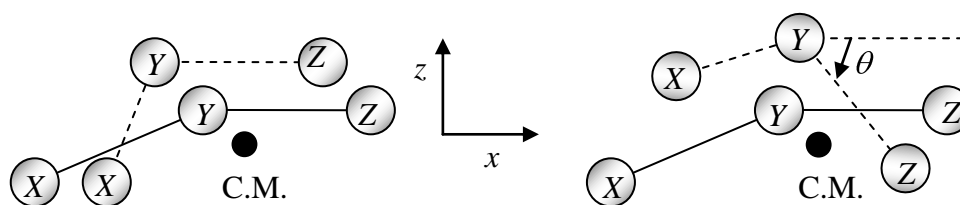
Figure 4.6: Schematic diagram showing the axis-switching angle $\theta$ for a triatomic molecule *XYZ*. Solid and dashed lines refer to the molecule in states *A* and *B*, respectively. (a) shows initial relative orientations and (b) shows relative orientations when the molecule has been rotated about the common frame such that the Eckart conditions are met. This rotation occurs about the centre of mass (C.M.), and is described by the rotation transformation matrix taking the general form of Equation [4.1].

As stated previously, this is the first time the phenomenon of planar-to-planar axis-switching has been observed in a more complex system than a triatomic. By applying the Hougen and Watson (H&W) method directly to the four atom HSiNC system the axis-switching angle is predicted to be 0.81°, which is in reasonable agreement with 1.0° ±0.2° determined by experiment (see above). This procedure was carried out using the *Axis_Switching_MFv2.m* program, written in MATLAB®[31] by the author, a copy of which may be found in the addendum.

To ensure that the procedure was working accurately other examples of axis-switching systems were examined from previous studies where the angle had been determined from the structural parameters determined within each reference unless otherwise stated.[2,29,36,37] It was found that when the procedure described above was applied to these systems good agreement with the previous experimentally determined values was achieved, so we may be confident in the application of the procedure on the HSiNC system. Details of these data may be found in Table 4.10.

Table 4.10: Table giving the axis-switching angle (in degrees) for various molecular species based on the most accurate available structural parameters

| Molecular species | Axis-switching angle determined by H&W method | Axis-switching angle determined from experimental data |
| --- | --- | --- |
| HNO | 0.73 | 0.72[a] |
| HCF | 2.91 | 2.90[a] |
| HSiF | 2.32 | 2.30[b] |
| HSiCl | 0.70 | 0.70[d] |
| $C_2H_2$ | 2.53 | 2.55[e] |
| HSiCN | 1.05 | -[f] |
| HSiNC | 0.81 | 1.0 ±0.2 (this work) |

[a] Value taken from Ref [36]
[b] Value taken from Ref [29]
[c] Structural data taken from Ref [4]
[d] Value taken from Ref [2]
[e] Vaule taken from Ref [37]
[f] Prediction based on *ab initio* results (SAC-CI/ aug-cc-pVTZ)

### 4.5.4 Vibrational Analysis

The 520-420 nm band system is assigned to the $\tilde{A}^1A''-\tilde{X}^1A'$ electronic transition of HSiNC, with the transition moment oriented perpendicular to the molecular plane, giving rise to *C*-type bands. This transition corresponds to the promotion of an electron from an H-Si molecular orbital to an unoccupied out-of-plane *p* orbital located on the silicon atom.

The spectrum of HSiNC was recorded in the 25000-19900 cm$^{-1}$ region and the low energy portions of this spectrum are shown in Figure 4.7. The HSiNC LIF spectrum shown in Figure 4.7 consists of an intense origin band at ~19950 cm$^{-1}$, with a number of additional vibrational bands at ~20570, 20645, 20717, 21183, 21260, 21333, 22331, 22357, 22385 and 22872 cm$^{-1}$. The spectrum is quite complicated as there are many contaminants also detected. Most of these may be attributed to LIF signals from the SiC$_2$ band system[44] which starts at ~20075 cm$^{-1}$ and bands from the Swann band system of C$_2$.[45] In some cases these signals overlap with those of the HSiNC signals making assignments tricky. Also, apart from the $0_0^0$ band, the intensities of the observed vibrational bands are very weak relative to the signals of the various contaminants.

In total, eleven vibrational bands of the HSiNC species have been located. Each of the vibrational bands was fitted using the spectral fitting program PGOPHER.[32] For each band, a rough fit was first obtained by fitting the $Q$-branches, and floating the origin wavenumber value only. Once the rough fit was complete, a more accurate fit was obtained by adding in any rotational lines which were sufficiently resolved from the low resolution fits, and the excited state rotational constants $A$ and $\overline{B}$ were floated together with the origin transition frequency. In all cases the ground state parameters were fixed to those obtained from the medium resolution fit of the $0_0^0$ band (see section 4.5.4 above).
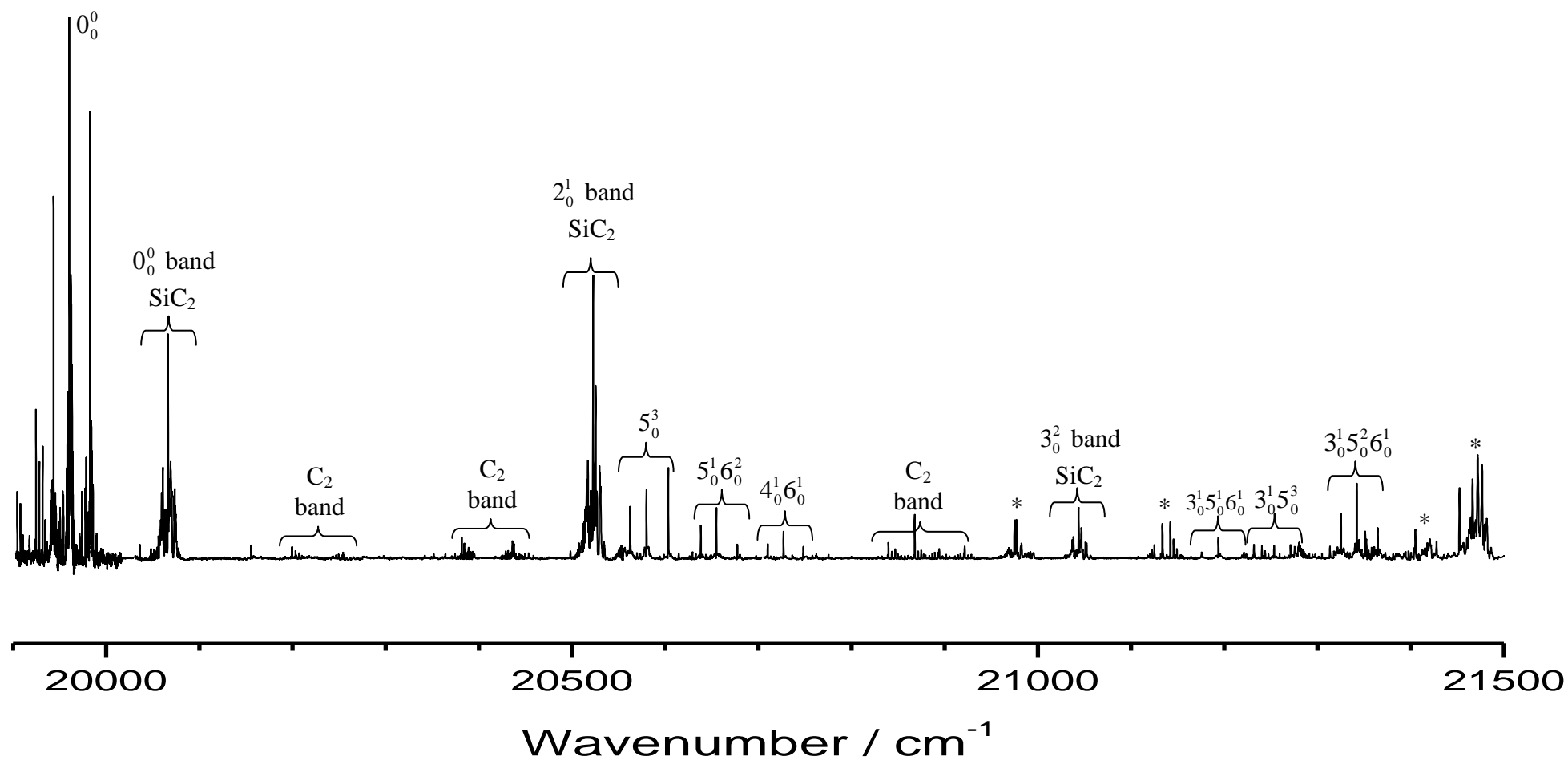
Figure 4.7: A portion of the low resolution spectrum of HSiNC showing the vibrational assignments. Peaks from $SiC_2$ and $C_2$ are also indicated. The peaks marked with asterisks are due to unknown contaminants.

The assignments, band origins, offset from the $0_0^0$ band, *ab initio* predictions (based on the MP2(FC) anharmonic calculation of the excited state), approximate values of $(A - \bar{B})'$ and the overall error in the fit for each band are given in Table 4.11. In all cases the overall standard deviation of the fit was comparable to the estimated uncertainties in the measurements.

HSiNC is a bent molecule of $C_s$ symmetry with five $a'$ vibrational modes labelled $\nu_1$ (Si-H stretch), $\nu_2$ (N-C stretch), $\nu_3$ (Si-H wag), $\nu_4$ (Si-N stretch) and $\nu_5$ (Si-N-C in-plane bend), as well as one $a''$ vibrational mode labelled $\nu_6$ (Si-N-C out-of-plane bend).

Assignment of the observed vibrational bands is difficult as all of the bands observed are all either overtones or combination bands. The $(A - \bar{B})'$ values are useful to consider in giving assignments as values which are significantly greater than that for the $0_0^0$ band indicate that at least one quanta of a bending / wagging mode is present. All of the assignments given in Table 4.11 should therefore, be considered tentative.

Table 4.11: Possible assignments, band origins, offset from the $0_0^0$ band, approximate excited state $(A - \bar{B})$ values and the overall error in the fit for each of the observed vibrational bands in the LIF spectrum of HSiNC in the $\tilde{A}^1 A''$ state (in cm$^{-1}$)

| Assignment[a] (symmetry) | Band origin[b] | Offset from $0_0^0$ band | Ab initio prediction[c] | $(A - \bar{B})'$ | RMS error in fit |
|---|---|---|---|---|---|
| $0_0^0$ (a′) | 19950.5623(77) | 0.00 | - | 9.8087 | 0.017 |
| $5_0^3$ (a′) | 20569.721(16) | 619.16 | 635.4 | 10.28(1) | 0.028 |
| $5_0^1 6_0^2$ (a′) | 20645.224(19) | 694.65 | 704.2 | 9.82(2) | 0.044 |
| $6_0^2$ (a′) | 20717.17(11) | 766.70 | 738.6 | 9.60(21) | 0.13 |
| $3_0^1 6_0^2$ (a′) | 21183.055(27) | 1232.49 | 1181.7 | 10.84(2) | 0.061 |
| $3_0^1 5_0^3$ (a′) | 21260.9236(86) | 1310.35 | 1324.7 | 10.29(1) | 0.027 |
| $3_0^1 5_0^1 6_0^2$ (a′) | 21332.697(16) | 1382.13 | 1393.5 | 9.87(2) | 0.043 |
| $1_0^1 6_0^1$ (a″) | 22331.367(18) | 2380.77 | 2381.9 | 10.30(2) | 0.039 |
| $1_0^1 6_0^1$ (a′) | 22357.184(16) | 2406.58 | 2381.9 | 10.40(2) | 0.039 |
| $2_0^1 5_0^1$ (a′) | 22384.619(18) | 2434.00 | 2428.1 | 10.31(2) | 0.045 |
| $2_0^1 3_0^1$ (a′) | 22871.616(43) | 2920.99 | 2905.6 | 10.53(20) | 0.11 |

[a] All of these assignments are based on the *ab initio* results and as such must be considered tentative
[b] Numbers in parentheses are 1σ uncertainties in units of the last significant digit
[c] Values taken from the anharmonic MP2(FC) calculation

### 4.5.5 Dispersed Fluorescence Spectra

In the previous work carried out on the halosilylene species it has been repeatedly noted that strong emission has meant that valuable information may be obtained about the ground state vibrational manifold. It therefore seemed prudent to attempt to carry out emission experiments on the HSiNC radical to see if similar information about the energies may be gained.

Figure 4.8 show the dispersed fluorescence (DF) spectrum obtained by pumping the strong $^r Q_0$ branch of the $0_0^0$ band of HSiNC. Initially, this was deemed the most suitable branch to pump as it is the strongest observed in the LIF spectrum. However, as can be seen in Figure 4.8, the observed DF peaks are split. The magnitude of the splitting is approximately 28 cm$^{-1}$, indicating that it is most likely due to emission

back down to different rotational energy levels in the $^PQ_2$ sub-band. Another feature to note in the spectrum is the appearance of a peak which does not fit with the others observed at 2962.615 cm$^{-1}$. This peak could signal the start of another very weak progression, but there is nothing which can be matched to this either from the experimental LIF data or the theoretical results. It is, therefore, thought that this peak is most likely just an artefact of the stitching process used to obtain the full spectrum. Table 4.12 gives the data obtained from the DF spectrum shown in Figure 4.8.
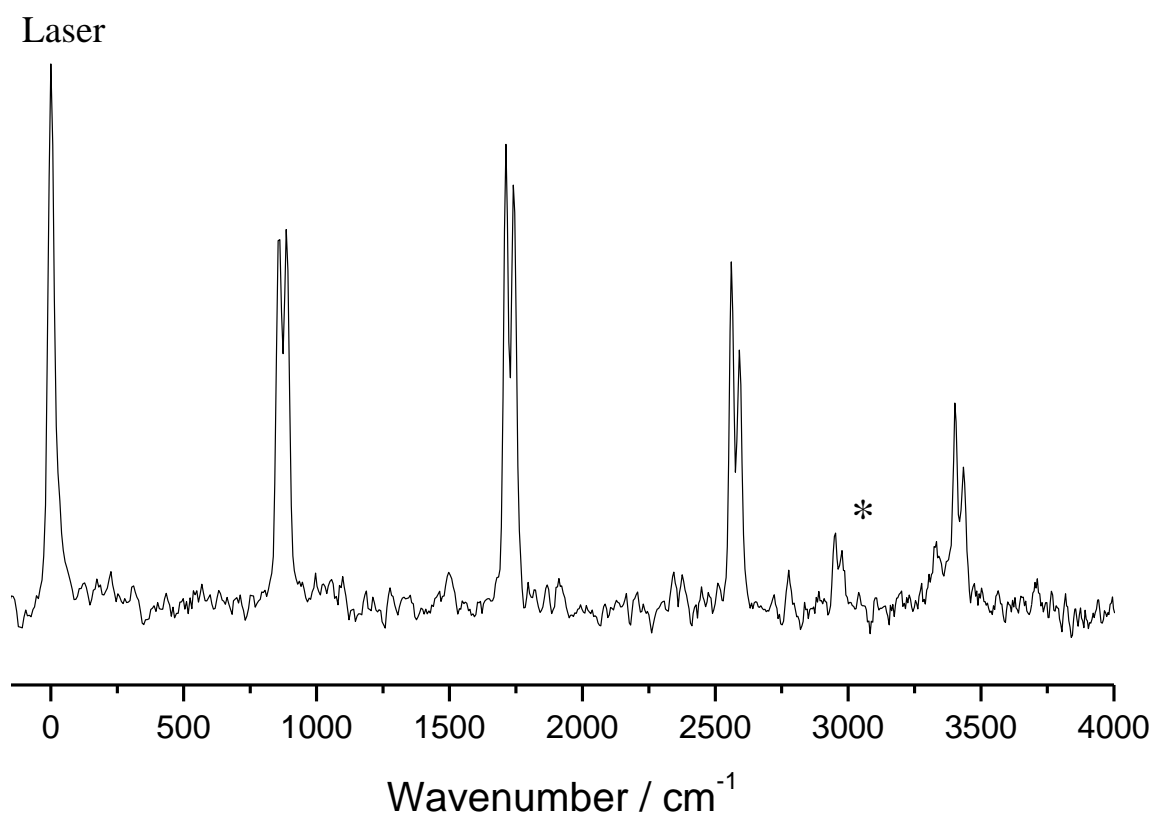


Figure 4.8: Dispersed fluorescence spectrum obtained by pumping the $^rQ_0$ branch of the $0^0_0$ band of HSiNC. The peak marked with the asterisk indicates the start of another possible progression. The spectrum was recorded by averaging 5000 laser shots using a slit width of 100 μm over the range 16300-20100 cm$^{-1}$.

Table 4.12: Assignment for each peak, wavenumber of the peaks relative to the laser (in cm$^{-1}$) and wavenumber relative to the previous peak in the progression (in cm$^{-1}$) for the dispersed fluorescence spectrum obtained by pumping the $^rQ_0$ branch of the $0_0^0$ band of HSiNC in the $\tilde{X}\,^1A'$ state.

| Assignment | Peak position relative to laser | Peak position relative to previous peak in progression |
|---|---|---|
| $3_0^1$ | 873.793 | 873.793 |
| $3_0^2$ | 1726.293 | 852.4995 |
| $3_0^3$ | 2575.881 | 849.5885 |
| Unknown | 2962.615 | - |
| $3_0^4$ | 3419.713 | 843.832 |

As a result of this splitting of the peaks in the DF spectrum, it was decided that a different $Q$-branch should be pumped. Figure 4.9 shows the DF spectum obtained by pumping the strong $^pQ_1$ branch of the $0_0^0$ band of HSiNC. As mentioned above, HSiNC is a bent molecule of $C_s$ symmetry with six vibrational modes. The electronic transition is accompanied by a change in the H-Si-N bond angle of ~25°, so the emission spectra are dominated by a progression of the $\nu_3$ (Si-H wag) mode, and nothing else. As can be seen by the data collected, the observed progression is very short (~3500 cm$^{-1}$) and no further signals were detected when the scanning range of the monochromator was extended over 10000 cm$^{-1}$. This corresponds to what is seen in the LIF spectra, where the entire LIF spectrum is covered in the range of 19915-23000 cm$^{-1}$. Beyond this there are no other band systems which may be attributed to HSiNC.
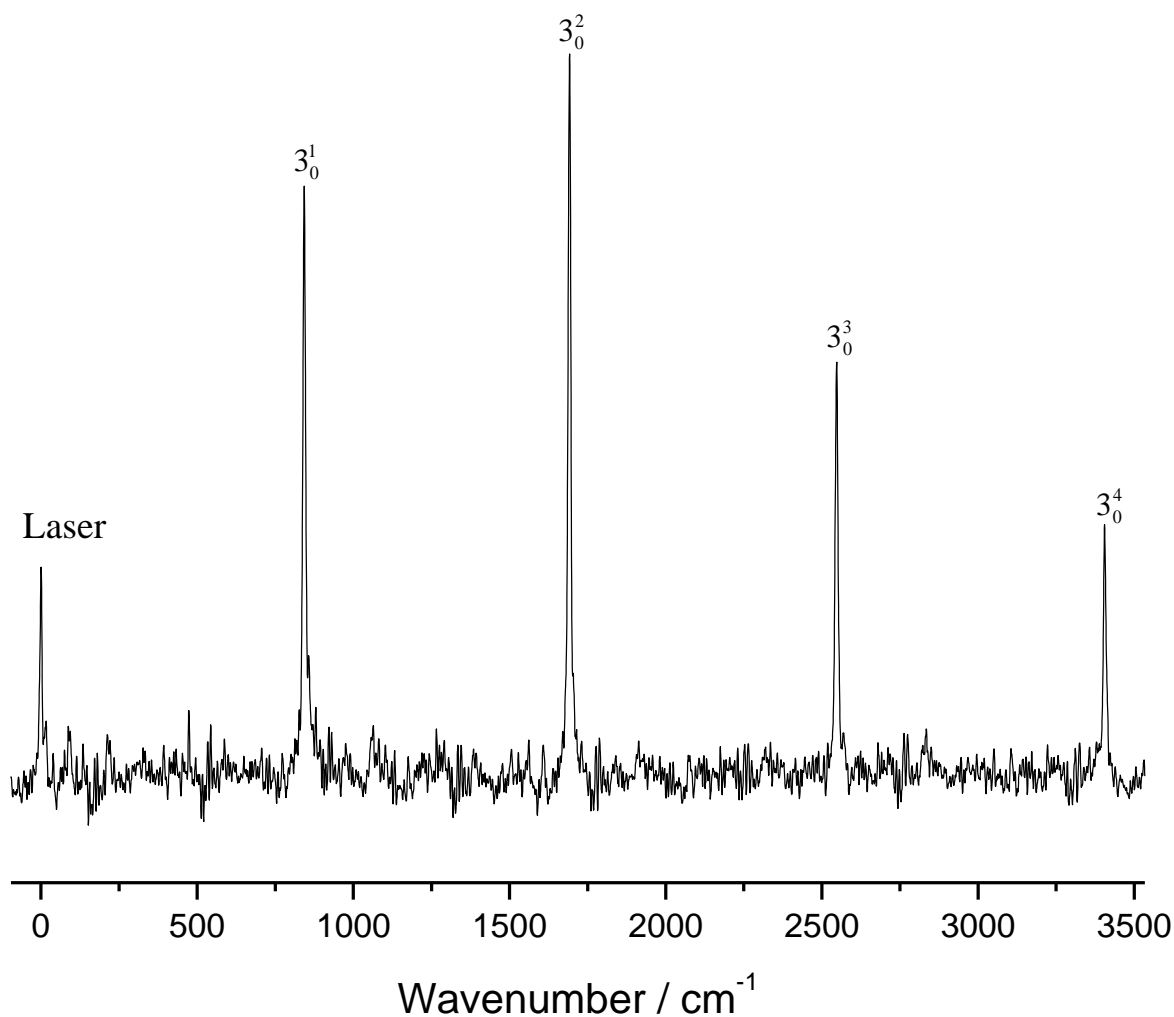
Figure 4.9: Dispersed fluorescence spectrum obtained by pumping the $^PQ_1$ branch of the $0^0_0$ band of HSiNC. The spectrum was recorded by averaging 2000 laser shots using a slit width of 175 μm over the range 16300-20100 cm$^{-1}$.

As can be seen in Figure 4.9, the anomalous peak observed at ~2960 cm$^{-1}$ detected in the DF spectrum from the pumping of the $^rQ_0$ branch is absent in the $^PQ_1$ branch pumped spectrum. This adds further credence to the idea that the peak is an artefact of the scan. The slit width of the monochromator had to be increased to obtain a good spectrum, because the intensity of the fluorescence achieved by pumping this slightly weaker Q-branch was diminished. This results in a decrease in the resolution achieved, but still provides good information.

As before, the first peak observed in the spectrum is from the laser. Table 4.13 gives the data obtained from the DF spectrum shown in Figure 4.9.

Table 4.13: Assignment for each peak, wavenumber of the peaks relative to the laser (in cm$^{-1}$) and wavenumber relative to the previous peak in the progression (in cm$^{-1}$) for the dispersed fluorescence spectrum obtained by pumping the $^PQ_1$ branch of the $0_0^0$ band of HSiNC in the $\tilde{X}\,^1A'$ state.

| Assignment | Peak position relative to laser | Peak position relative to previous peak in progression |
|---|---|---|
| $3_0^1$ | 857.067 | 857.067 |
| $3_0^2$ | 1710.010 | 852.943 |
| $3_0^3$ | 2558.793 | 848.783 |
| $3_0^4$ | 3403.226 | 844.433 |

As can be seen from these results there is relatively good agreement between the observed frequencies of the $\nu_3$ vibrational transitions and those calculated by the *ab initio* methods described in section 4.4.3, above. The theoretical values are in the range of ~855-880 cm$^{-1}$ depending on the level of theory used.

### 4.5.6 Anharmonic analysis

Unfortunately, there is not enough data from the LIF spectra to calculate any meaningful anharmonic terms for HSiNC, as not enough vibrational bands have been observed. Therefore, the following anharmonic analysis relies solely on the DF spectra discussed above. Using the DF data given in Table 4.13 above it is only possible to carry out an anharmonic analysis on the $\nu_3$ vibrational mode of HSiNC. To do this the standard power series expression shown in Equation [4.6] was used.

$$G_{v_1 v_2 v_3 \ldots} = \omega_1 v_1 + \omega_2 v_2 + \omega_3 v_3 + \ldots + x_{11}\left(v_1 + \frac{1}{2}\right)^2 + x_{22}\left(v_2 + \frac{1}{2}\right)^2 + x_{33}\left(v_3 + \frac{1}{2}\right)^2 +$$
$$x_{12}\left(v_1 + \frac{1}{2}\right)\left(v_2 + \frac{1}{2}\right) + x_{13}\left(v_1 + \frac{1}{2}\right)\left(v_3 + \frac{1}{2}\right) + x_{23}\left(v_2 + \frac{1}{2}\right)\left(v_3 + \frac{1}{2}\right) + \ldots$$

[4.6]

As the only observed progression in the DF spectra was for the $\nu_3$ vibrational mode the analysis is very simple, and Equation [4.6] collapses down to the form given in Equation [4.7].

$$G_{\nu_3} = \omega_3 \nu_3 + x_{33}\left(\nu_3 + \frac{1}{2}\right)^2 \qquad\qquad [4.7]$$

This little amount of information still gives an indication of the accuracy of the theoretically determined values for this particular mode with regards to the anharmonic frequency calculation carried out at the MP2(FC)/aug-cc-pVTZ level of theory. The DF data given in Table 4.13 has been fitted to Equation [4.7], and the results of the fit are given in Table 4.14 together with a comparison of the values obtained by *ab initio* methods. This procedure was carried out using *Anharmonic_v1.0.m* program written in MATLAB®[31] by the author, a copy of which is given in the addendum. As can be seen by the data there is very good agreement between the experimentally determined values and those determined by the anharmonic *ab initio* calculation.

Table 4.14: A comparison between the experimentally and theoretically determined values for the anharmonic terms in the $\nu_3$ vibrational mode. All values are given in cm$^{-1}$.

| Vibrational constant | Energy from DF spectrum[a] | Energy from anharmonic calculation[b] |
|:---:|:---:|:---:|
| $\omega_3$ | 861.67 (45) | 867.19 |
| $x_{33}$ | -2.17 (7) | -2.53 |

[a] Numbers in parentheses are $1\sigma$ uncertainties in units of the last significant digit
[b] Calculated at the MP2(FC)/aug-cc-pVTZ level of theory

This anharmonic analysis is clearly very limited in the information it provides, but the parameters obtained from fitting the progression observed in the DF spectrum do seem to agree very favourably with those obtained from the anharmonic calculation. Therefore, we may tentatively assume that the other anharmonic terms obtained from this calculation may be accurate too.

## 4.6    $^{15}$N Isotopic Enrichment

To aid in the determination of the spectral carrier in these experiments attempts were made to produce spectra of isotopically enriched HSi$^{15}$NC. The reason $^{15}$N enrichment was chosen instead of $^{13}$C or D enrichment was based purely on the cost of the starting materials for the synthesis. Unfortunately the attempts made were unsuccessful. This section details the synthesis and spectroscopy of this species.

### 4.6.1 Synthesis

Unfortunately it is not possible to purchase $^{15}N$ enriched trimethylsilylcyanide to use as the precursor to producing $HSi^{15}NC$. Therefore, it was necessary to synthesise the precursor. The synthetic approach of Reetz and Chatziiosifidis was followed.[46]

Trimethylsilylcyanide (**2**) was prepared in ~80 % yield by the reaction of equimolar amounts of chlorotrimethylsilane (**1**) $((CH_3)_3SiCl$, Sigma-Aldrich, ≥99%) and $^{15}N$ enriched potassium cyanide ($KC^{15}N$, Sigma-Aldrich, 98 atom % $^{15}N$) in the presence of 10 mol % potassium iodide (KI, Sigma-Aldrich, ≥99%) and 20 mol % of *N*-methylpyrrolidinone ($C_5H_9NO$, Sigma-Aldrich, 99.5%) at room temperature for 72 hours. Under these conditions, the reaction continued to completion and the pure product was distilled directly from the reaction flask. The scale of the synthesis was determined by the cost of the $^{15}N$ enriched potassium cyanide, of which there was 2 g available. The reaction is represented by Scheme 4.1. Without further characterisation of the compound (**2**), the spectroscopic study discussed below was carried out.

Scheme 4.1:

                    (**1**)                                                (**2**)

### 4.6.2 Spectroscopic Observation

Once the $^{15}N$ enriched precursor had been synthesised, attempts were made to spectroscopically observe the $HSi^{15}NC$ species. Figure 4.10 shows the low-resolution scan over the $0_0^0$ band origin for the $\tilde{A}^1A'' - \tilde{X}^1A'$ transition of $HSi^{15}NC$ with *Q*-branch assignments. As can be seen the $0_0^0$ band of $HSi^{15}NC$ overlaps with the $0_0^0$ band of HSiNC making assignment of rotational structure very difficult.
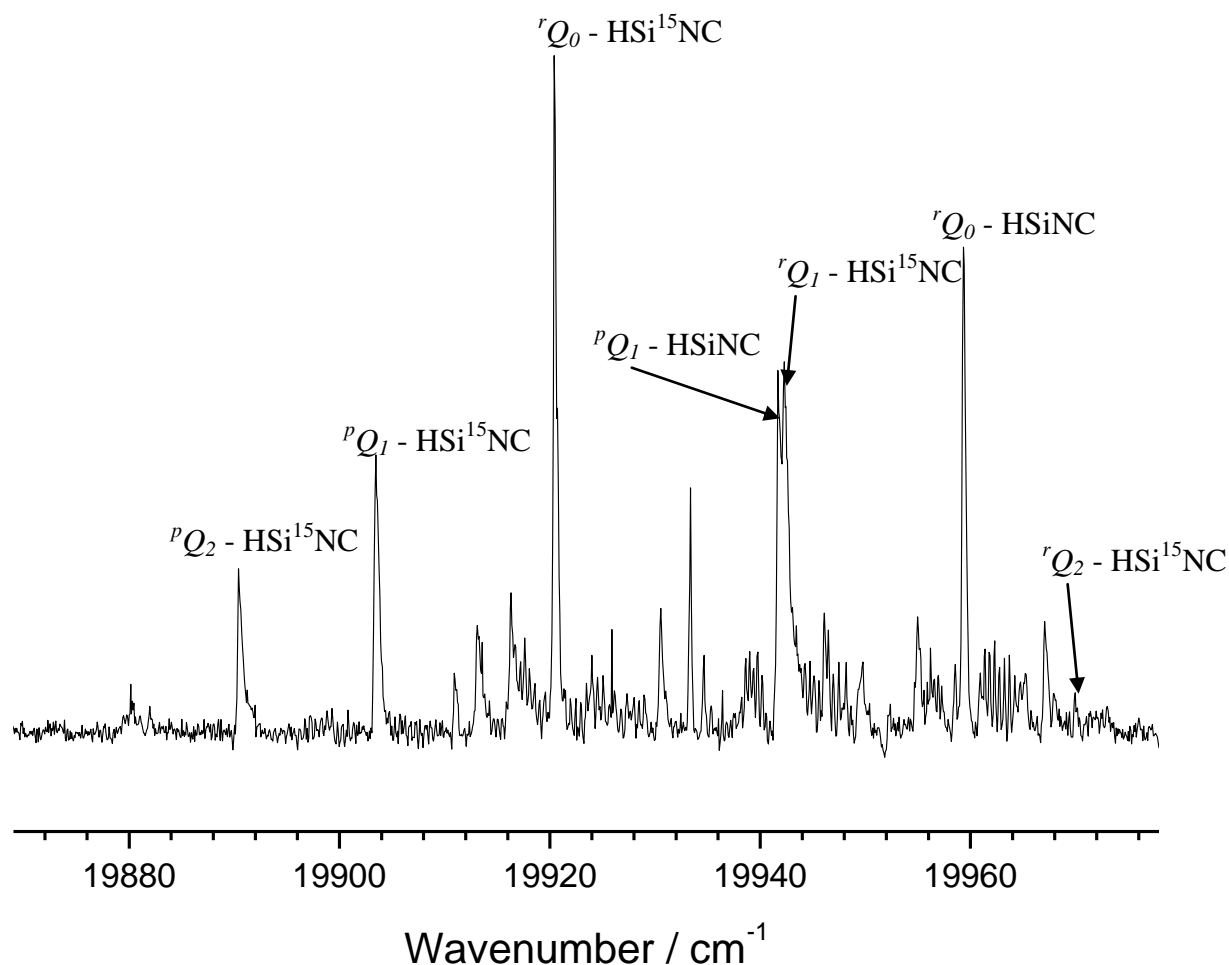
Figure 4.10: A low resolution spectrum of the $0_0^0$ band for the $\tilde{A}\,^1A'' - \tilde{X}\,^1A'$ transition of $HSi^{15}NC$ with $Q$-branch assignments.

The next step in the process would have been to optimise the signal from $HSi^{15}NC$, while trying to minimise the signal from HSiNC. Unfortunately, over a short time period, the signal for the $HSi^{15}NC$ species diminished to almost nothing, while the signal for HSiNC increased, meaning that there was not time to optimise the spectrum and deduce any useful information. The only feasible reason for this is that during distillation of the product (**2**), the *N*-methylpyrrolidinone solvent used must have also been carried over, contaminating the product with a source of [14]N. When the contaminated precursor was pulsed through the discharge, the presence of the ^{14}N in the sample may account for the diminishing signal from the ^{15}N enriched species. Also present was a large signal at ~20717 cm^{-1} (482.5 nm), which may be attributed to the HSiCl species, indicating the presence of unreacted chlorotrimethylsilane (**1**).

The spectrum shown in Figure 4.10 is the best available, and allows only a very rough estimate of the HSi$^{15}$NC $0_0^0$ band origin for the $\tilde{A}^1A'' - \tilde{X}^1A'$ transition of ~19910.22 cm$^{-1}$, corresponding to an isotope shift of ~40 cm$^{-1}$ to the red. This direction of this shift is predicted by *ab initio* calculations at the MP2(FC)/aug-cc-pVTZ level, but the relative magnitude of the shift is predicted to be only ~20 cm$^{-1}$.

## 4.7    HSiCN

As mentioned in the introduction of this chapter, previous experimental and theoretical work has indicated that the most stable [H, Si, C, N] isomer is that of the cyanide analogue of the species discussed here, HSiCN. The obvious question at this point is why has this lower energy species not been spectroscopically observed in this study? The answer to this question is quite simple, assuming that the accuracy of the SAC-CI calculation seen in the HSiNC case is as good for predicting the transition energy for the HSiCN. The wavelength region at which it is predicted the $0_0^0$ band HSiCN spectrum would appear from the SAC-CI calculation was unfortunately not accessible with the equipment used in this study. The predicted transition energy is 17152 cm$^{-1}$ (corresponding to a wavelength of 583 nm), which is too far to the red end of the visible region for the PMT used to detect. Therefore, it is predicted that the electronic spectrum of HSiCN may be observable, but has not been carried out for the purposes of this thesis, due to the inadequate spectral range of the equipment used. On the other hand, if the spectrum of HSiCN is similar to that seen for HSiNC which would seem likely, it is feasible that during the course of searching for HSiNC, some vibrational bands of HSiCN would have been encountered, and this was not the case. Therefore the question of whether or not the electronic spectrum of HSiCN remains unanswered, and open to further study.

## 4.8    Concluding Remarks

In this chapter we have seen the first electronic spectroscopic study of the $\tilde{A}^1A'' - \tilde{X}^1A'$ transition of the HSiNC species. Previous microwave and *ab initio* studies together with some further theoretical work have provided a strong basis for us to be confident in the assignment of the observed spectra. A number of vibrational bands have been tentatively assigned based on the *ab initio* predictions of vibrational frequencies together with dispersed fluorescence study of the $\nu_3$ (Si-H wag) vibrational mode. Detailed rotational analysis has been carried out resulting in the

assessment of rotational and quartic centrifugal distortion constants, with improvements made in the accuracy of some of these constants compared to the previous microwave study. The ground state constants obtained appear to be in good agreement with those determined by the microwave study, and the previously undetermined excited state constants agree reasonably well with those obtained by the *ab initio* work.

The most interesting aspect of the spectrum is the appearance of the 'forbidden' transitions corresponding to $\Delta K_a = 0$ and $\pm 2$. These peaks, known as 'axis-switching' peaks and the details of why they arise have been covered in depth together with determination of the axis-switching angle. The determination of this angle has been carried out in two ways; a trial and error approach based on simulation versus experimental data, and accurate determination following the approach proposed by Hougen and Watson[2] based on a combination of the structural data provided by the microwave study for the ground state and the high-level theoretical (SAC-CI) data for the excited state. Both methods provided an axis-switching angle of ~1.0° with an estimated uncertainty of ±0.2° indicating that the *ab inito* data has accurately described the geometry of the excited state, assuming the ground state data from the microwave study[15,30] is also accurate.

Also given are the details of the attempt to synthesise ^{15}N enriched trimethylsilylcyanide to act as the precursor to production of ^{15}N enriched HSiNC. The sythesis was conducted, but the resulting spectroscopy was unfortunately not successful in yielding any useful rotational constants for reasons discussed. The rough fit which was achieved simply gave a very rough estimate of the HSi[15]NC $0^0_0$ band origin for the $\tilde{A}^1A'' - \tilde{X}^1A'$ transition of ~19912 cm$^{-1}$. Finally, there is a brief discussion of why the isomeric HSiCN species, deemed to be approximately 2.2 kcal/mol lower in energy when compared to HSiNC, has not been spectroscopically observed.

Overall, there is still scope for further work on HSiNC. It would be useful to conduct high resolution LIF spectroscopy to obtain better separation of the asymmetry splittings and the $Q$-branches, and to obtain spectroscopic constants and geometric information for both the ground ($\tilde{X}^1A'$) and excited ($\tilde{A}^1A''$) states. Also, it would be

instructive to carry out isotopic enrichment of the precursor ($^{15}$N, $^{13}$C and D) to help further confirm the identity of the spectral carrier.

It would be interesting to see if the HSiCN radical is observable via LIF spectroscopy based on the *ab initio* predictions discussed, and this would lead to information on the previously unobserved excited state. Finally, there are the other potential isomers which remain purely theoretical at this point. Although these isomers are higher in energy than HSiCN and HSiNC, it is still feasible that they may exist and be open to future spectroscopic investigations.

## 4.9     REFERENCES FOR CHAPTER 4

(1)     Herzberg, G.; Verma, R. D. *Can. J. Phys.* **1964**, *42*, 395.
(2)     Hougen, J. T.; Watson, J. K. G. *Can. J. Phys.* **1965**, *43*, 298.
(3)     Harjanto, H.; Harper, W. W.; Clouthier, D. J. *J. Chem. Phys.* **1996**, *105*, 10189.
(4)     Harper, W. W.; Clouthier, D. J. *J. Chem. Phys.* **1997**, *106*, 9461.
(5)     Apponi, A. J.; McCarthy, M. C.; Gottlieb, C. A.; Thaddeus, P. *Astrophys. J.* **2000**, *536*, L55.
(6)     Bailleux, S.; Bogey, M.; Breidung, J.; Burger, H.; Fajgar, R.; Liu, Y. Y.; Pola, J.; Senzlober, M.; Thiel, W. *Angew. Chem. Int. Ed.* **1996**, *35*, 2513.
(7)     Chen, G. H.; Ding, Y. H.; Huang, X. R.; Zhang, H. X.; Li, Z. S.; Sun, C. C. *J. Phys. Chem. A* **2002**, *106*, 10408.
(8)     Flores, J. R.; Perez-Juste, I.; Carballeira, L. *Chem. Phys.* **2005**, *313*, 1.
(9)     Liu, H. L.; Huang, X. R.; Chen, G. H.; Ding, Y. H.; Sun, C. C. *J. Phys. Chem. A* **2004**, *108*, 6919.
(10)    McCarthy, M. C.; Thaddeus, P. *J. Mol. Spectrosc.* **2002**, *211*, 228.
(11)    Srinivas, R.; Vivekananda, S.; Schroder, D.; Schwarz, H. *Chem. Phys. Lett.* **2000**, *316*, 243.
(12)    Stanton, J. F.; Dudek, J.; Theule, P.; Gupta, H.; McCarthy, M. C.; Thaddeus, P. *J. Chem. Phys.* **2005**, *122*,124314.
(13)    Wang, Q.; Ding, Y. H.; Sun, C. C. *Chem. Phys.* **2006**, *323*, 413.
(14)    Yu, H. T.; Fu, H. G.; Chi, Y. J.; Huang, X. R.; Li, Z. S.; Sun, C. C. *Chem. Phys. Lett.* **2002**, *359*, 373.
(15)    Sanz, M. E.; McCarthy, M. C.; Thaddeus, P. *Astrophys. J.* **2002**, *577*, L71.
(16)    Maier, G.; Reisenauer, H. P.; Egenolf, H.; Glatthaar, J. *Eur. J. Org. Chem.* **1998**, 1307.
(17)    LabVIEW; 7.0 ed.; National Instruments, **2003**.
(18)    Frisch, M. J.; Trucks, G. W.; Schlegel, H. B.; Scuseria, G. E.; Robb, M. A.; Cheeseman, J. R.; Montgomery, J., J. A.; Vreven, T.; Kudin, K. N.; Burant, J. C.; Millam, J. M.; Iyengar, S. S.; Tomasi, J.; Barone, V.; Mennucci, B.; Cossi, M.; Scalmani, G.; Rega, N.; Petersson, G. A.; Nakatsuji, H.; Hada, M.; Ehara, M.; Toyota, K.; Fukuda, R.; Hasegawa, J.; Ishida, M.; Nakajima, T.; Honda, Y.; Kitao, O.; Nakai, H.; Klene, M.; Li, X.; Knox, J. E.; Hratchian, H. P.; Cross, J. B.; Bakken, V.; Adamo, C.; Jaramillo, J.; Gomperts, R.; Stratmann, R. E.; Yazyev, O.; Austin, A. J.; Cammi, R.; Pomelli, C.; Ochterski, J. W.; Ayala, P. Y.; Morokuma, K.; Voth, G. A.; Salvador, P.; Dannenberg, J. J.; Zakrzewski, V. G.; Dapprich, S.; Daniels, A. D.; Strain, M. C.; Farkas, O.; Malick, D. K.; Rabuck, A. D.; Raghavachari, K.; Foresman, J. B.; Ortiz, J. V.; Cui, Q.; Baboul, A. G.; Clifford, S.; Cioslowski, J.; Stefanov, B. B.; Liu, G.; Liashenko, A.; Piskorz, P.; Komaromi, I.; Martin, R. L.; Fox, D. J.; Keith, T.; Al-Laham, M. A.; Peng, C. Y.; Nanayakkara, A.; Challacombe, M.; Gill, P. M. W.; Johnson, B.; Chen, W.; Wong, M. W.; Gonzalez, C.; Pople, J. A. Gaussian 03; Revision D.02 ed.; Gaussian Inc.: Wallington CT, **2004**.
(19)    Dunning, T. H. *J. Chem. Phys.* **1989**, *90*, 1007.
(20)    Kendall, R. A.; Dunning, T. H.; Harrison, R. J. *J. Chem. Phys.* **1992**, *96*, 6796.
(21)    Woon, D. E.; Dunning, T. H. *J. Chem. Phys.* **1993**, *98*, 1358.
(22)    Becke, A. D. *J. Chem. Phys.* **1993**, *98*, 5648.
(23)    Frisch, M. J.; Head-Gordon, M.; Pople, J. A. *Chem. Phys. Lett.* **1990**, *166*, 275.

(24) Frisch, M. J.; Head-Gordon, M.; Pople, J. A. *Chem. Phys. Lett.* **1990**, *166*, 281.

(25) Head-Gordon, M.; Pople, J. A.; Frisch, M. J. *Chem. Phys. Lett.* **1988**, *153*, 503.

(26) Møller, C.; Plesset, M. S. *Phys. Rev.* **1934**, *46*, 618.

(27) Pople, J. A.; Head-Gordon, M.; Raghavachari, K. *J. Chem. Phys.* **1987**, *87*, 5968.

(28) Nakatsuji, H. *Chem. Phys. Lett.* **1978**, *59*, 362.

(29) Dixon, R. N.; Wright, N. G. *Chem. Phys. Lett.* **1985**, *117*, 280.

(30) Sanz, M. E. *Private communication* **2006**.

(31) MATLAB; 7.4.0.287 (R2007a) ed.; The MathWorks, Inc., **2007**.

(32) Western, C. PGOPHER; 5.2.343 ed.; Bristol laser group: Bristol, **2005**; A program for simulating rotational structure; http://pgopher.chm.bris.ac.uk.

(33) Watson, J. K. G. *J. Chem. Phys.* **1967**, *46*, 1935.

(34) Gordy, W.; Cook, R. L. *Microwave Molecular Spectra*; Wiley: New York, **1984**.

(35) Brown, J. M.; Ramsay, D. A. *Can. J. Phys.* **1975**, *53*, 2232.

(36) Ozkan, I. *J. Mol. Spectrosc.* **1990**, *139*, 147.

(37) Huet, T. R.; Godefroid, M.; Herman, M. *J. Mol. Spectrosc.* **1990**, *144*, 32.

(38) Billingsley, J. *Can. J. Phys.* **1972**, *50*, 531.

(39) Lin, A.; Kobayashi, K.; Yu, H. G.; Hall, G. E.; Muckerman, J. T.; Sears, T. J.; Merer, A. J. *J. Mol. Spectrosc.* **2002**, *214*, 216.

(40) Woodman, C. M. *J. Mol. Spectrosc.* **1970**, *33*, 311.

(41) Fujiwara, T.; Lim, E. C.; Kodet, J.; Judge, R. H.; Moule, D. C. *J. Mol. Spectrosc.* **2005**, *232*, 331.

(42) Plusquellic, D. F. Jb95 Spectral Fitting Program, (verison 2.05.1); http://physics.nist.gov/jb95 **2002**.

(43) Wilson, E. B.; Cross, P. C.; Decius, J. C. *Molecular vibrations ; the theory of infrared and Raman vibrational spectra;* McGraw-Hill: New York, **1955**.

(44) Butenhoff, T. J.; Rohlfing, E. A. *J. Chem. Phys.* **1991**, *95*, 1.

(45) Kini, K. S.; Savadatti, M. I. *J. Phys. B - At. Mol. Opt.* **1969**, *2*, 307.

(46) Reetz, M. T.; Chatziiosifidis, I. *Synthesis-Stuttgart* **1982**, 330.

# Chapter Five

*Theoretical Study of the*

*[H, Si, N, C, O] isomers*

## 5.1  Introduction

There has been considerable interest in the chemistry of organosilicon compounds over the last thirty years. This interest stems from that fact that organosilicon radicals play an important role in a number of chemical deposition methods used by the semi-conductor industry, in addition to the fact that a number of silicon containing species have been detected in the interstellar medium. The cosmic abundance of silicon is thought to be only slightly lower than those of carbon, nitrogen and oxygen.[1] Unfortunately, due to the limitation of accurate spectroscopic data, the number of detected silicon containing molecules is far fewer than those containing carbon, nitrogen and oxygen. Up to now, only about ten silicon containing species have been detected in space including, SiO, SiC, $SiC_2$, cyclic-$SiC_3$ and just recently SiCN and SiNC.[3-6] To help in the search for new silicon containing species a number of groups have carried out theoretical and experimental studies in order to obtain spectroscopic parameters to aid in the detection of these species in the interstellar medium.[7-18] One of these investigations lead to two new species, HSiCN and HSiNC, being spectroscopically observed in the laboratory. Both of these species were regarded as being very strong candidates for detection in the interstellar medium due to fact that similar species have already been observed in space (e.g., SiCN). In this work, Sanz *et al*. used a high voltage electric discharge source coupled to a molecular beam Fourier transform microwave spectrometer to study both isomers (HSiCN and HSiNC) and to obtain rotational constants for a number of different isotopomers of each species allowing the elucidation of their structures.[19]

Chapter 4 details the first experimental study of the $\tilde{A}^1 A'' - X^1 A'$ electronic state of HSiNC using laser induced fluorescence spectroscopy and found that upon excitation the H-Si-N angle increases by ~20° giving rise to the observation of forbidden transitions as a result of axis-switching. This work also examined a number of vibrational bands in both the excited and ground electronic states. Further work was pursued on an analogous system resulting in the observation of the $\tilde{A}^1 A'' - X^1 A'$ electronic state of HSiNCO, details of which are in Chapter 6. HSiNCO has the same potential of being found in the interstellar medium as HSiCN and HSiNC as the cosmic abundance of oxygen is only slightly less than carbon and nitrogen.[1] To date, there have been no previous studies on HSiNCO or on any of its isomers. This chapter aims to look at possible isomers of [H, Si, N, C, O] using *ab initio* methods

and to investigate their stability and spectroscopic constants to aid in the detection of these species in both the laboratory and in space.

## 5.2    Theoretical Methods

For the most part calculations were carried out using the Gaussian 03 (G03) suite of programs.[20] The geometries of the different species and their isomers were fully optimized at different levels of theory using the augmented triple zeta correlated consistent basis set (aug-cc-pVTZ) of Dunning *et al.*[21-23] The methods used include, the hybrid density functional method B3LYP,[24] the 2nd order Moller-Plesset method (MP2)[25-28] and the Quadratic configuration interaction method including singles and doubles, QCISD.[29] Further single-point calculations were carried out using QCISD(T), with the structure fixed to the QCISD structure.[29] For accurate relative energies and evaluation of thermodynamic properties, the G3B3 and G3MP2 methods, as implemented in G03, were used.[30,31] Vibrational wavenumbers were calculated at the MP2 and B3LYP levels of theory to check if the optimised structures were true minima. The MP2 calculations were carried out using both full electron correlation (*i.e.*, including the core electrons) [MP2(Full)] and the standard frozen core method [MP2(FC)]. As the difference in the zero point energies (ZPEs) between MP2(FC) and MP2(Full) was negligible the MP2 energies were corrected using the MP2(FC) ZPE. For the QCISD calculations the vibrational wavenumbers were calculated using the aug-cc-pVDZ basis set.[21-23] Like the MP2 calculations QCISD/QCISD(T) calculations were carried using both the frozen core and full electron correlation methods. Multiconfiguration SCF (MC-SCF) calculations were carried out as implemented in the MOLPRO suite of programs using the aug-cc-pVTZ basis set with (11,6) closed and (9,3) active orbitals.[32] Single excitation configuration interaction (CIS) and symmetry-adapted cluster configuration interaction (SAC-CI) calculations were carried out as implemented in the G03 suite of programs. Natural bond analysis (NBO 5.0) was carried out at the B3LYP/aug-cc-pVTZ level of theory using the NBO 3.0 as implemented in Gaussian 03. Calculations were run on several computer clusters including the system managed by EPSRC National Service for Computational Chemistry Software[33] in addition to the University of Leicester Mathematical Modelling Centre's supercomputer which was purchased through the HEFCE Science Research Investment Fund. Plots of molecular orbitals were generated using MOLDEN.[34]

## 5.3 Results and Discussion

A series of calculations were carried out on a number of different isomeric forms of the [H, Si, N, C, O] system. The optimised geometries and vibrational wavenumbers of approximately 20 different isomers were calculated at the MP2(FC) level of theory. A full list of these isomers may be found in Appendix B. Figure 5.1 shows the 10 lowest [H, Si, N, C, O] isomers in their $\widetilde{X}\,^1A'$ electronic state using the MP2(FC) level theory. In all cases, the electronic configuration of the singlet species is $15\,a'^2\;3\,a''^2$. As can be seen from Figure 5.1 the five lowest isomers (S1-S5) are all within approximately 6 kcal/mol of each other. At the MP2(FC) level of theory the lowest isomer (S1) was found to be *cis*-HOSiCN, while the *trans* form of this isomer (S2) lies 1.02 kcal/mol higher in energy. Isomers S3 and S4 are the isocyanide analogues to species S1 and S2. The next two isomers, S5 and S6, are HSi(O)CN and HSi(O)NC, which are the silicon analogues to formyl cyanide and formyl isocyanide and are 6.10 and 11.1 kcal/mol higher in energy, respectively than isomer S1.[35-37] Isomer S7 is the isocyanate analogue to HSiNC and is 14.7 kcal/mol higher in energy than the S1 isomer. It was found that the corresponding cyanate species (HSiCNO) is significantly higher in energy (~88 kcal/mol) than the HSiNCO isomer which is similar to that seen for HNCO/ HCNO[38,39] (0.0/70.1 kcal/mol) and $CH_3NCO/CH_3CNO$[40] (0.0/54.9 kcal/mol). The S8 isomer is a cyclic system with the oxygen double bonded to the carbon and the hydrogen bonded to the nitrogen and is 35.5 kcal/mol higher in energy than the S1 isomer. Lastly, the S9 and S10 isomers, which are cyanatosilylene and isocyanatosilylene, are found to be 36.7 and 36.8 kcal/mol, respectively higher in energy than the S1 isomer. All of these isomers gave non-imaginary vibrational wavenumbers indicating that their optimised structures are true minima.

In order to check if the MP2(FC) calculations were giving the correct ordering of the seven lowest isomers, further calculations were carried out using different levels of theory. To look at the influence core electrons have on the relative energies of the proposed isomers the MP2 calculations were re-run with inclusion of the core electrons. Higher-level calculations were carried out at the QCISD(T) levels of theory as implemented in the G03 package, while to test the reliability of the DFT methods the B3LYP hybrid functional was employed. For each calculation the geometries were re-optimized and where possible the vibrational wavenumbers calculated. In the case of the QCISD(T) calculations, the geometry was re-optimised

at the QCISD level of theory and a single-point calculation at this geometry was carried out. Similar to the MP2 calculations, QCISD/QCISD(T) calculations were carried out with the inclusion of core electrons. Table 5.1 shows the relative energy differences between the lowest seven isomers found at each level of theory. The results in Table 5.1 show there is some confusion with regards to the ordering of the lowest lying isomers. Both the B3LYP and QCISD(T) results show that the S3 isomer is the lowest in energy with the S4 isomer, the *trans* form of S3, being the second lowest in energy. The relative difference between the S1-S2 and the S3-S4 isomers is consistent from of one level of theory to the next. The other main difference can be seen in the energy of the S5 isomer which is predicted to change significantly with the inclusion of triple excitations (QCISD(T)), while for the analogous isocyanide isomer the predicted relative energy is fairly consistent from one level of theory to the next. The B3LYP calculations predict the separation between isomers S6 and S7 is only 0.1 kcal/mol, while the other methods predict a much larger separation.

The inclusion of the core electrons is important, especially for the lowest four isomers. The MP2(Full) calculations agree with the MP2(FC) calculations with isomer S1 being the lowest in energy, however, the second lowest isomer was determined to be the *cis*-HOSiNC isomer (S3) which is predicted to be only 0.15 kcal/mol higher in energy than isomer S1. The MP2(Full) calculation also predict the $3^{rd}$ and $4^{th}$ lowest isomers to be isomers S2 and S4, respectively with a separation of only 0.3 kcal/mol. For the other isomers the MP2(Full) calculations give smaller relative energies than the MP2(FC) calculations, but predict the same order. Similar calculations have also been carried out using QCISD/QCISD(T). As can be seen in Table 5.1 the inclusion of core electrons does affect the relative energies of the isomers considerably. For isomers S1 to S4 the separation is similar that found using B3LYP and G3MP2. However, for isomers S5 and S6 the predicted energy difference is only 0.1 kcal/mol and is very similar to that predicted using G3MP2. The inclusion of the core electrons has resulted in isomer S6 being slightly more energetically stable than isomer S5. Lastly, the inclusion of core electrons has resulted in the relative energy of isomer S7 to drop from 13.8 to 11.2 kcal/mol, which is similar to that seen with the MP2 calculations.

The G3MP2 and G3B3 composite methods were carried out on the lowest seven isomers (in the $\tilde{X}\,^1A'$ electronic state) in order to determine more accurate relative energies.[30,31,41] As can be seen from Table 5.1 the G3B3 and G3MP2 results agree fairly well with the QCISD(T) results and both methods show that isomer S3 is the lowest lying isomer and not isomer S1 as found at the MP2 level of theory.

There has been a lot of work on comparing the bonding and differences in reactivities of carbon and silicon containing compounds. Looking at the most stable [H, $C_2$, N, O] isomers it is found that HC(O)CN (0.0 kcal/mol) is the most stable isomer followed by HC(O)NC (12.0 kcal/mol), HNCCO (31.2 kcal/mol), HOCCN (45.0 kcal/mol) and HCCNO (81.0 kcal/mol) using B3LYP with a 6-311++G(d, p) basis set.[42] The ordering of the carbon based isomers is in complete contrast to the silicon containing species. It is interesting that the isocyanate analogue, HCNCO, has not been investigate as a potential [H, $C_2$, N, O] isomer.

Table 5.1: The energies of the lowest seven [H, Si, N, C, O] isomers (in kcal/mol). All energies are relative to isomer S1 (as in Figure 5.1). All Energies have been ZPE corrected.

| Isomer | B3LYP | MP2[a] | QCISD(T)[b] | G3MP2 | G3B3 |
|---|---|---|---|---|---|
| S1 | 0.0 | 0.0(0.0) | 0.0 (0.0) | 0.0 | 0.0 |
| S2 | 1.1 | 1.0(1.1) | 1.1 (1.2) | 1.2 | 1.1 |
| S3 | -2.5 | 1.3(0.15) | -1.6 (-2.8) | -1.6 | -2.4 |
| S4 | -1.2 | 2.5(1.4) | -0.4 (-1.5) | -0.2 | -1.2 |
| S5 | 6.9 | 6.1(5.9) | 10.0 (9.6) | 7.6 | 7.7 |
| S6 | 10.6 | 11.1(9.8) | 11.0 (9.5) | 8.6 | 7.7 |
| S7 | 10.7 | 14.7(12.2) | 13.8 (11.2) | 12.4 | 12.5 |

[a]Number in parentheses are the MP2 values with inclusion of the core electrons [MP2(Full)]
[b] Zero-point energy calculated at QCISD level of theory with an aug-cc-pVDZ basis set. Number in parentheses are the QCISD(T) values with inclusion of the core electrons.
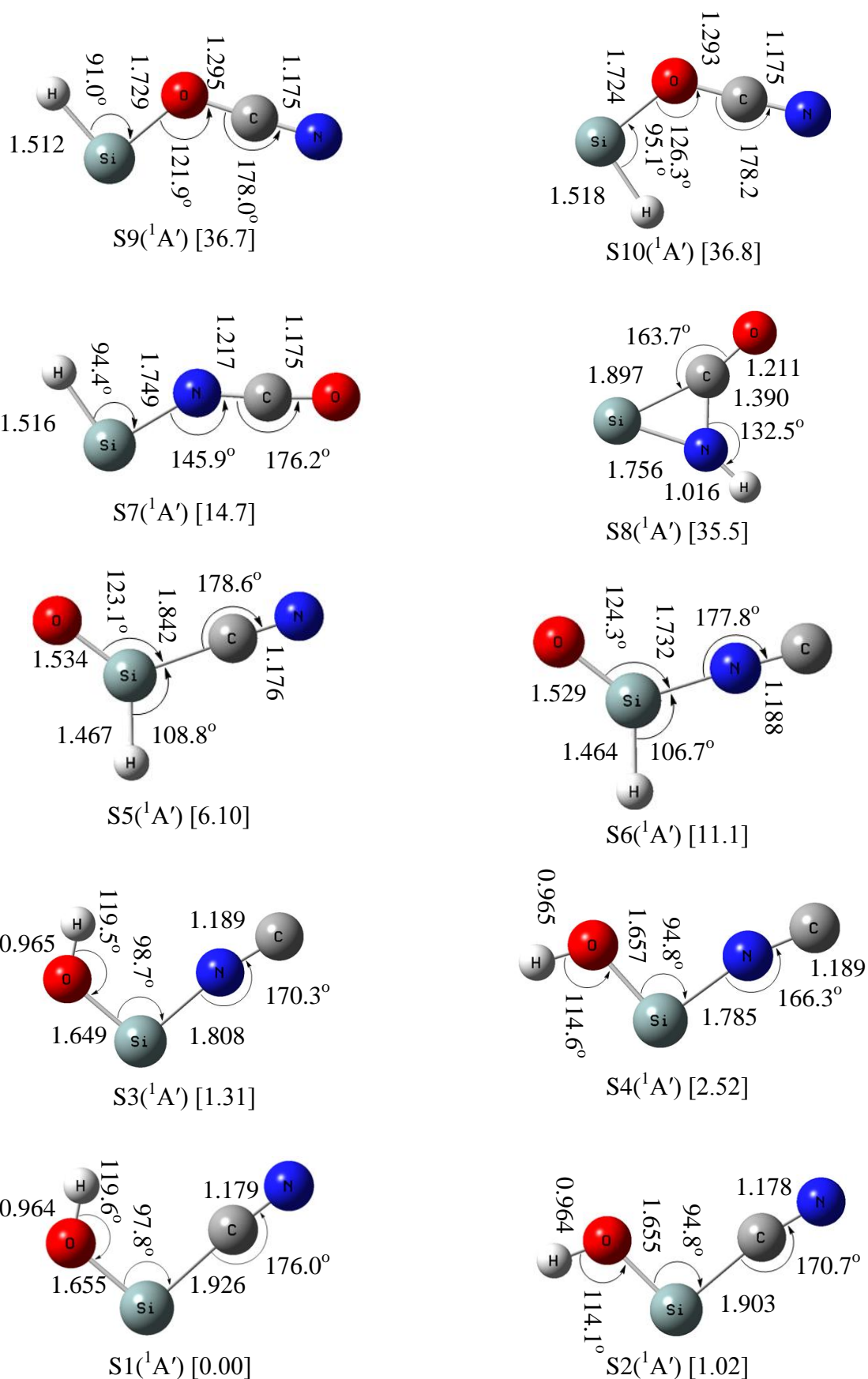
Figure 5.1: Optimized geometries (in Å and degrees) of the ten lowest singlet state isomers of [H, Si, C, N,O] computed at the MP2(FC)/aug-cc-pVTZ level of theory. Relative energies [in kcal/mol] to the lowest energy isomer (S1).

### 5.3.1 HO-SiCN/HO-SiNC

As can be seen from Figure 5.1 the geometry of these silanols shows a short O-H bond length, which is analogous to that observed for light alcohols and is similar to that predicted for alkylsilanols.[43] The average Si-O bond length is 1.654 Å, which is much shorter than the covalent radii sum (1.87 Å) and is similar to that seen in other silanols. The C-N/N-C bond lengths are similar to that observed in SiCN/NC and HSiCN/NC and are longer than the average CN/NC bond.[7,9,19] The two most interesting aspect with these species are the O-Si-C/N and Si-O-H angles. The O-Si-C/N angle is small, ~90° and is similar to the H-Si-X angle found in HSiNC/CN (~95°)[7,9,19], while the Si-O-H angle is in line with that observed for the alkylsilanols (~120°) and is 10° larger than the alcohol analogues.[44] A close look at the structures reveals more differences. Going from the *cis* to the *trans* forms results in a shortening of the Si-X (X=C, N) bond length by ~0.02 Å, while the Si-C-N/Si-N-C angle decreases by up to 6°.

*5.3.1.1 Natural Bond Analysis: (cis/trans)HO-SiCN*

Natural bond analysis (NBA) on HO-SiCN indicates that C-N bond is triple in nature with the Si-O bond being a double bond, while the bonding between Si-C and O-H is single in nature. The bonding of Si-O is counter-acted slightly by population of anti-bonding MOs and results in the Si-O bond length being 0.1 Å longer than the diatomic SiO, which is regarded to be double bonded.[45] The NBA also indicates the presence of three lone-pairs situated on the Si, O and N. The Si lone pair has *s* character (*cis*: $sp^{0.24}$ (19.2% *p* character), *trans*: $sp^{0.24}$(19.4% *p* character)). For O and N the lone-pairs are, to a fair extent, hybridised; for O ($p_z$) *cis*: $sp^{1.83}$ (64.4% *p* character) and *trans*: $sp^{1.53}$(60.2% *p* character), while for N *cis*: $sp^{0.92}$ (47.8% *p* character) and *trans*: $sp^{0.91}$ (47.5% *p* character). The bonding between Si-O is almost pure *p* in character on the silicon atom (*cis*: 86.8% *p* character, *trans*: 87.6% *p* character), while the bonding between Si-C is again almost pure *p* in character on the silicon atom (*cis*: 89.7% *p* character, *trans*: 88.6% *p* character). The almost pure *p* character of these MOs explains the relative small O-Si-C angle seen in both isomers. No additional resonance structures are thought to contribute to the structural characteristics of these isomers.

*5.3.1.2 Natural Bond Analysis: (cis/trans)HO-SiNC*

The NBA on HO-SiNC indicates that N-C bond is triple in nature, the bonding between Si-N and O-H bonds are single in nature, while like HO-SiCN the Si-O bond is considered a double bond. The NBA indicates the presence of three lone-pairs situated on the Si, O and C. The Si lone pair is mainly *s* in character (*cis*: $sp^{0.23}$ (18.8% *p* character), *trans*: $sp^{0.23}$(18.9% *p* character)), while for O and C the lone-pair are hybridised to a fair extent; for O *cis*: $sp^{1.84}$ (64.6% *p* character) and *trans*: $sp^{1.51}$ (60.0% *p* character), while for C *cis*: $sp^{0.45}$ (31.1% *p* character) and *trans*: $sp^{0.45}$ (31.2% *p* character). The bonding between Si-O is almost pure *p* in character on silicon atom (*cis*: 86.9% *p* character, *trans*: 87.7% *p* character), while the bonding between Si-N again is almost pure *p* in character on the silicon atom (*cis*: 89.8% *p* character, *trans*: 88.6% *p* character). As seen for HO-SiCN, the almost pure *p* character of these MOs explains the relatively small O-Si-N angle as seen in both isomers. Again, there is thought to be no additional resonance structures that will contribute to the structural characteristics for these isomers.

*5.3.1.3 Isomerisation*

For the *cis* and *trans* forms of HO-SiCN and HO-SiNC, calculations were performed on both species in order to determine the potential of rotation of the hydrogen about the oxygen atom. Figure 5.2 shows the potential for both HO-SiCN and HO-SiNC. The potentials were generated by changing the HOSiC/HOSiN dihedral angle, while relaxing the rest of the structure at the MP2(Full) level of theory using the aug-cc-pVTZ basis set. A total of 20 points were calculated for each species. From Figure 5.2 it can be seen that the potential has a double minimum at 0 and 180° corresponding to the *cis* and *trans* forms, respectively. Where $\theta$ is the dihedral angle between H-O-Si-C/N. In both cases the *trans* form is higher in energy by ~0.3 kcal mol$^{-1}$, which opposes the trends found for formic, thiolformic, thionformic and dithioformic acids.[46] The potentials have been fitted using the function of Torro-Labbe *et al.*:[46,47]

$$V(\theta) = \frac{1}{2}\Delta V^{\circ}\left(1-\cos\theta\right) + \frac{1}{4}\left(k_t + k_c\right)\left(1-\cos^2\theta\right)$$
$$+ \frac{1}{4}\left(k_t - k_c - \Delta V^{\circ}\right)\left(1-\cos^2\theta\right)\cos\theta$$

[5.1]

The results from the fits are shown in Table 5.2 and are compared against the results found for formic, thiolformic, thionformic and dithioformic acids using the same method.[46] It can be seen that HO-SiCN and HO-SiNC have similar, although lower barrier heights than thiolformic and dithioformic acids. The values of $k_c$ and $k_t$ are slightly different from those of thiolformic and dithioformic acids with the $k_c$ force constant larger than $k_t$. These force constants indicate that for the *trans* form there is a repulsive interaction between the hydrogen and the silicon and oxygen atoms. The parameters $\alpha_0$ and $\Delta V^{\ddagger}$ are the angle at which the potential is at a maximum and the barrier height, respectively. For HO-SiCN $\alpha$=95.4° and $\Delta V^{\ddagger}$=3169 cm$^{-1}$, while for HO-SiNC $\alpha_0$=95.3 and $\Delta V^{\ddagger}$=2841.3 cm$^{-1}$.

Table 5.2: Isomerisation parameters for HOSiCN and HOSiNC

| Parameters[a] | HOSiCN | HOSiNC | HOOCH[b] | HSOCH[b] | HOSCH[b] | HSSCH[b] |
|---|---|---|---|---|---|---|
| $k_c$ | 18.63 | 15.93 | 15.08 | 15.41 | 16.63 | 17.17 |
| $k_t$ | 15.23 | 13.92 | 27.24 | 20.4 | 30.79 | 25.45 |
| $V_1$ | -278.17 | -278.59 | - | - | - | - |
| $V_2$ | -1480.45 | -1304.99 | - | - | - | - |
| $V_3$ | 97.08 | 69.91 | - | - | - | - |
| $\Delta V_0$ | 362.2 | 417.4 | 2098.6 | 495.6 | 2236.7 | 611 |
| $\alpha_0$ | 95.42 | 95.29 | 98.2 | 92.0 | 93.0 | 92 |
| $\Delta V^{\ddagger}$ | 3169.04 | 2841.28 | 4768.5 | 3379.7 | 5162.9 | 4037 |

[a] $k_c$ and $k_t$ (force constants) in kcal mol$^{-1}$ rad$^{-2}$, $V_1$, $V_2$, $V_3$, $\Delta V_0$ and $\Delta V^{\ddagger}$ in cm$^{-1}$ and $\alpha_0$ in degrees.
[b] Values taken from Ref [46]

*5.3.1.4 Vibrational Wavenumbers*

Vibrational wavenumbers have been calculated for all the species at the B3LYP and MP2(FC) levels of theory. Table 5.3 shows the ground electronic state unscaled vibrational wavenumbers for *cis/trans* HO-SiCN and *cis/trans* HO-SiNC. There is good agreement between the B3LYP and MP2(FC) results except for the C-N stretching mode where there is a 200 cm$^{-1}$ difference. The rotational constants at the equilibrium geometry are also given for each species in Table 5.3. At the MP2(Full) level of theory the dipole moments ($\mu_x/\mu_y$) of *cis* and *trans* HO-SiCN are 1.66/1.36, and 2.71/4.82 Debye, respectively, while for *cis/trans* HO-SiNC they are, 1.70/1.21 and 2.57/3.51 Debye, respectively. The dipole moments for all these species are

sufficiently high enough that detection using microwave spectroscopy should be possible.
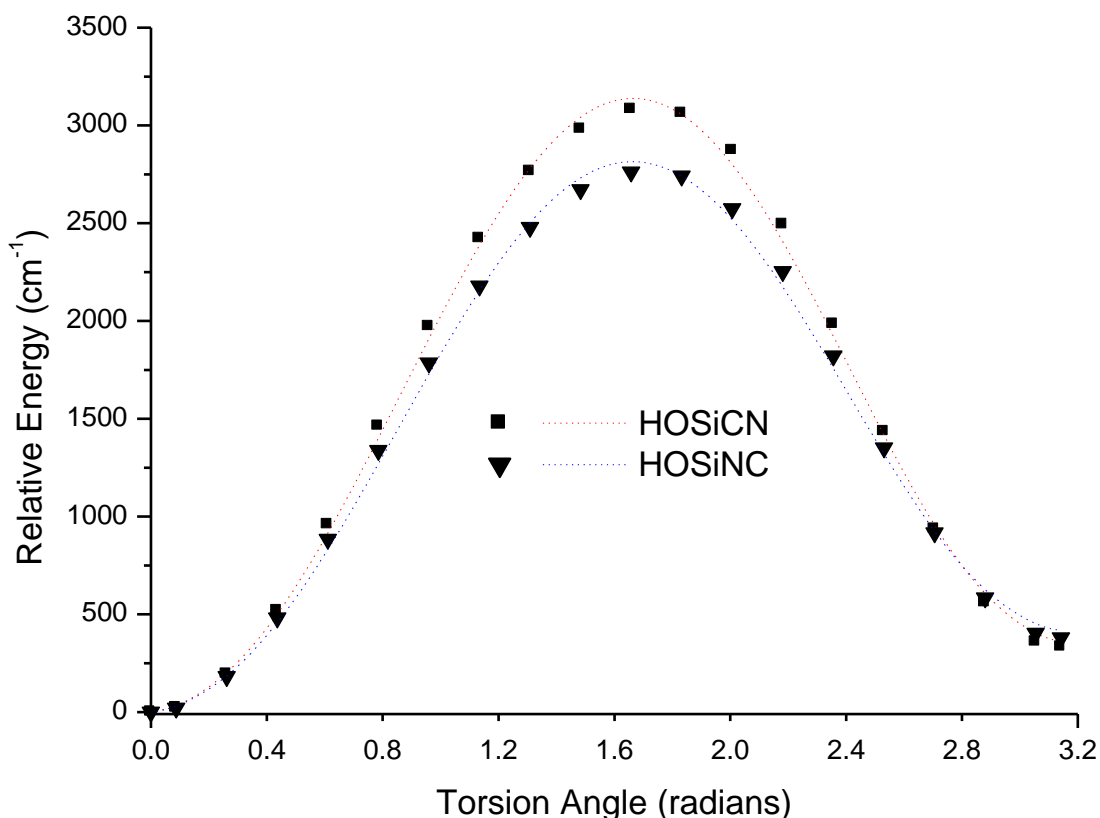


Figure 5.2: *cis* to *trans* isomerisation of HOSiCN and HOSiNC

### 5.3.1.5 Excited States

Calculations were carried out on the $\tilde{A}^1A''$ excited state for both species at the MP2 and B3LYP levels of theory. For each species an optimized structure was determined, which showed that the H-O-Si angle opens up to ~115° as expected with electron density being transferred to a *p* orbital on the silicon. At both the MP2(FC) and B3LYP levels theory, vibrational wavenumber calculations gave one imaginary value for the H-O-Si out-of-plane bending mode for both isomers, which probably indicates the optimised structure is a 1st order transition point. The structures for these excited state isomers are shown in Figure 5.3.

### 5.3.1.6 Out-of-Plane Excited States

As the planar structures for the excited state isomers gave an imaginary wavenumber value corresponding to the Si-H out-of-plane wagging mode, further investigation was necessary. It was found that by allowing the hydrogen atom to bend out of the plane with respect to the rest of the molecule, lower energy isomers were found

giving no imaginary values indicating that the true minima had been located. The resulting isomer (labelled E1/E2 in Figure 5.4) has $^1A$ symmetry and is lower in energy than the planar $^1A''$ isomers. This breaking of the symmetry in going from the ground state ($\tilde{X}^1A'$) to the newly located excited state ($^1A$) provides a new problem in determination of the transition energy ($T_0$). It is not possible to carry out MP2 or B3LYP calculations on the out-of-plane structures, and it is not possible to carry out the CIS calculations on the ground state. Therefore to obtain accurate energies of the two states a different approach is required. It was found that carrying out the SAC-CI calculations allowed calculation of both states with the required consistency from one state to the other. The resulting structures and energies are given in Figure 5.4.

## 5.3.2 HSiNCO

The ground electronic state structure of HSiNCO is analogous to HSiCN and HSiNC with the H-Si-X angle being around 95°. The small H-Si-X angle is also seen for the analogous halogen species HSiX (X= F, Cl, Br, I) with the H-Si-X angle being 97.6°, 102.8°, 102.9°, and 102.7°, respectively.[48-50] The Si-H bond length of 1.516 Å is similar to that observed for HSiNC (1.526 Å), however, it is ~0.03 Å longer than the Si-H bond in $H_3SiNCO$.[19,51] Table 5.4 compares the N-C and C-O bond distances against other molecules containing an isocyanate group. From Table 5.4 it can seen that in all cases the N=C bond is longer than the C=O bond. The question of linearity or non-linearity of the N=C=O bond has been of much interest for several decades. The NBA proposes three resonance structures with the N=C=O being the most probable, while $^+N\equiv C\text{-}O^-$ and $^-N\text{-}C\equiv O^+$ being the other minor forms. It is therefore possible that the N=C=O group is in fact non-linear based on the proposed resonance structures. However, in most of the early microwave spectroscopy and electron diffraction studies the N=C=O group was assumed to be linear. Only in a few cases has the N=C=O angle actually been determined. For the microwave spectroscopy studies it has been found that fixing the NCO group to being linear typically gives a poor fit to the observed frequencies. However, fits have been improved by using increasingly complex Hamiltonians, incorporating bending and rotational terms.

Table 5.3: Harmonic vibrational wavenumbers[a] [intensities (in km/mole)] and rotational constants (in GHz) of the five lowest [H,Si,N,C,O] isomers in the $\widetilde{X}\,^1A'$ state at the B3LYP and MP2(FC) levels of theory

| Species | Wavenumbers (infared intensities) | Rotational constants (A, B, C) |
|---|---|---|
| cis-HOSiCN | 135.9(14), 183.9(19), 384.8(10), 518.3(118), 551.2(138), 803.9(235), 895.5(42), 2259(48), 3816.4(81) | 194.293, 3.738, 3.135 |
| cis-HOSiCN[b] | 131.2(14), 189.4(19), 387.5(10), 527.5(123), 563.8(138), 816.6(232), 906.8(41), 2073.5(87), 3828.5(101) | 190.331, 3.756, 3.137 |
| trans-HOSiCN | 154.3(2), 194.9(0.4), 385.2(0.5), 551.3(140), 559.6(81), 851.3(233), 878.6(52), 2266.3(51), 3833.8(140) | 206.697, 3.718, 3.151 |
| trans-HOSiCN[b] | 149.1(2), 199.5(0.5), 382.7(0.1), 562.5(141), 578.1(76), 863.5(235), 890.4(47), 2085.4(91), 3834.3(157) | 202.381, 3.731, 3.150 |
| cis-HOSiNC | 136.9(8), 139.5(8), 351.5(22), 530.0(139), 576.0(143), 793.3(254), 894.1(59), 2110.6(386), 3807.5(69) | 210.356, 4169, 3.479 |
| cis-HOSiNC[b] | 126.2(10), 134.8(10), 353.4(23), 539.1(139), 574.1(159), 803.9(248), 910.0(63), 2042.5(293), 3821.0(92) | 203.705, 4.192, 3.477 |
| trans-HOSiNC | 146.6(1), 150.0(0), 363.1(2), 524.1(80), 613.6(183), 844.8(272), 860.3(31), 2117.4(413), 3839.1(130) | 221.349, 4.167, 3.507 |
| trans-HOSiNC[b] | 138.6(1), 143.7(0.1), 361.0(2), 541.6(79), 615.5(199), 854.4(244), 877.0(56), 2050.5(310), 3839.5(153) | 215.215, 4.187, 3.505 |
| HSi(O)CN | 167.5(28), 228.1(6), 387.6(13), 556.3(37), 604.0(97), 847.9(65), 1237.4(89), 2293.3(39), 2300.6(58) | 32.245, 3.387, 3.065 |
| HSi(O)CN[b] | 159.3(25), 223.9(6), 372.7(14), 565.0(36), 610.1(94), 859.1(73), 1201.0(58), 2107.6(84), 2347.3(44) | 31.881, 3.338, 3.022 |
| HSi(O)NC | 140.4(13), 162.4(1), 357.7(38), 556.1(43), 682.0(125), 854.4(65), 1250.4(118), 2133.9(455), 2312.7(34) | 33.975, 3.784, 3.405 |
| HSi(O)NC[b] | 134.2(14), 151.1(1), 347.8(33), 567.0(42), 675.1(141), 863.1(72), 1223.4(92), 2080.3(361), 2367.6(34) | 33.973, 3.726, 3.357 |
| HSiNCO | 103.9(1), 147.0(0.1), 569.0(73), 625.2(52), 652.9(24), 869.7(84), 1452.7(31), 2002.3(368), 2330.8(1619) | 134.174, 2.687, 2.635 |
| HSiNCO[b] | 103.5(2), 159.2(0.5), 569.1(63), 638.4(17), 643.9(72), 885.5(88), 1412.7(62), 2097.1(370), 2323.3(1528) | 101.827, 2.736, 2.665 |

[a] Unscaled wavenumbers [b] MP2(FC) calculations

E7 $\tilde{A}^1A''$ [46.81]
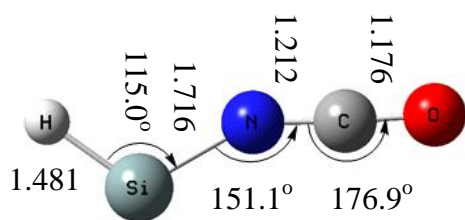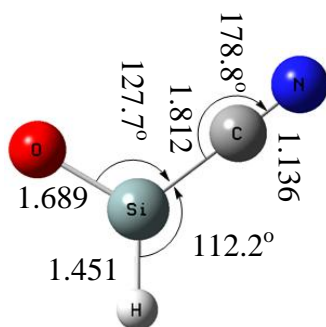
E5 $\tilde{A}^1A''$ [97.11]
Gives a single imaginary vibration
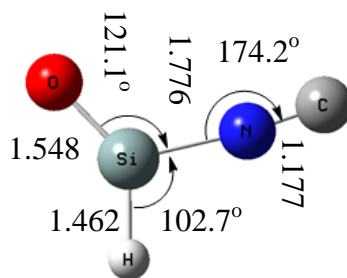
E6 $\tilde{A}^1A''$ [131.45]
Gives a single imaginary vibration
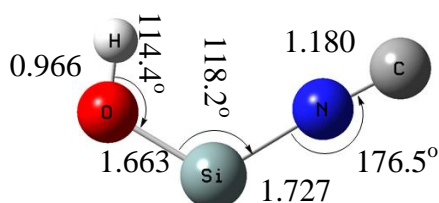
E3 $\tilde{A}^1A''$ [83.25]
Gives a single imaginary vibration
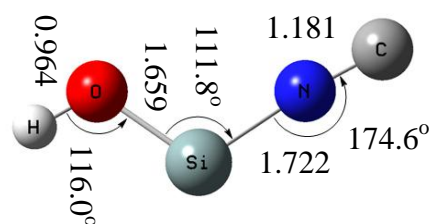
E4 $\tilde{A}^1A''$ [78.87]
Gives a single imaginary vibration
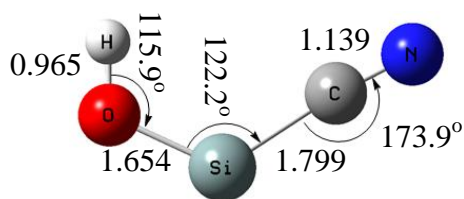
E1 $\tilde{A}^1A''$ [74.95]
Gives a single imaginary vibration
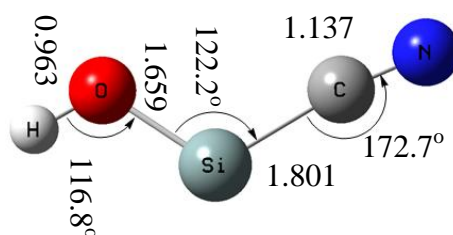
E2 $\tilde{A}^1A''$ [72.64]
Gives a single imaginary vibration

Figure 5.3: Optimized geometries of the excited states $\tilde{A}^1A''$ of the seven lowest energy isomers given in Figure 5.1 (bond lengths in Å; bond angles in degrees) computed at the MP2(FC)/aug-cc-pVTZ level of theory. All energies [in kcal/mol] are relative to their corresponding $^1A'$ isomers as in Figure 5.1.

Figure 5.4: Optimized geometries of the excited states (S1-S6: $\tilde{a}^1A$ and S7: $\tilde{A}^1A''$) of the seven lowest energy isomers given in Figure 5.1 (bond lengths in Å; bond angles in degrees) computed at the CIS/aug-cc-pVTZ level of theory. Numbers in parentheses correspond to the SAC-CI values. All excitation energies [in kcal/mol] are computed from the SAC-CI calculations.
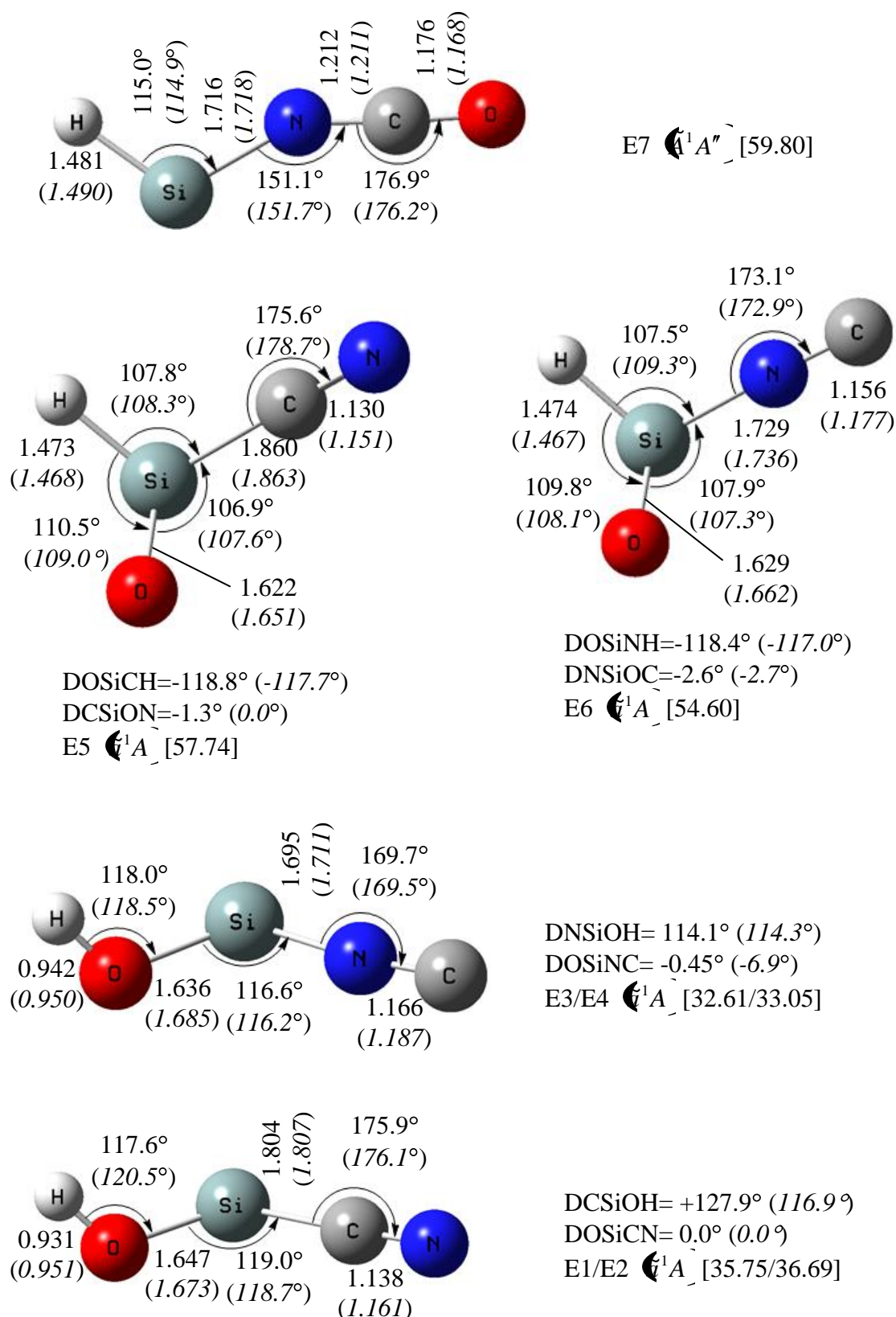
The results from the electron diffraction and microwave work are heavily dependent on the model used to fit the experimental data and are therefore open to much debate. In comparison, *ab initio* studies on species containing the NCO group have typically found the N-C-O angle to be less than 180°, with the average angle being between 172° and 178°.[51-54]

The variation in the bond angle of the atom adjacent to the isocyanate group has also been of much interest. It can be seen from Table 5.4 the X-N-C angles can range from being linear to 120°. It has been put forward that this is a result of the $p_\pi$-$d_\pi$ character of the bonding involving the available 3$d$ orbitals of silicon.[55] It has also been suggested that there is a good correlation between the variation of the X-N-C angle and the $r$(X-N) bond length. It is found that as the X-N-C angle decreases, the double bond character of the X-N bonds also seems to decrease.[55] By this argument, the Si-N bond in HSiNCO would be more likely a single bond which is in agreement with that found by the NBA (see below). On average, the X-N-C angle when X-Si seems to be larger than for those when X-C. Furthermore, the Si-N-C angle for HSiNC is 169.3°, which is substantially higher than HSiNCO (145.9°) and would indicate the Si-N bond is more a double bond in character.[19]

Vibrational wavenumbers and rotational constants for HSiNCO in its ground electronic state where also calculated and are given in Table 5.3. The dipole moments ($\mu_x$/$\mu_y$) at the MP2(Full) level of theory were calculated to be -1.49/0.20 Debye, respectively. Again, the dipole moments are sufficiently high enough that the rotational spectrum of HSiNCO should be observable using standard microwave spectroscopy techniques.

*5.3.2.1 Natural Bond Analysis*

The NBA shows the Si-H and Si-N bonds are single in nature. On the oxygen the LP is mainly *s* in character with $sp^{0.63}$ (38.5% *p* character), which is different from that seen in the HO-SiCN/NC isomers where the oxygen LP was situated out-of-plane and was mainly *p* in character. The bonding between Si-H and Si-N is mainly *p* in character with 88.4% and 86.9% *p* character which, as seen in the HO-SiCN/NC isomers, explains the small H-Si-N bond angle of 95°.

Table 5.4: The distances (in Å) and angles (in degrees) for molecules containing the isocyanate group

| Compound | $r$(N=C) | $r$(C=O) | $\angle$(N=C=O) | $\angle$(X-N-C) | $r$(X-N) | Reference |
|---|---|---|---|---|---|---|
| HSiNCO | 1.217 | 1.175 | 176.2 | 145.9 | 1.749 | This Work (MP2(FC)) |
| HSiNCO | 1.203 | 1.168 | 177.5 | 154.1 | 1.742 | This Work (B3LYP) |
| HSiNCO | 1.198 | 1.15 | 174.7 | 144.1 | 1.748 | This Work (MC-SCF) |
| HNCO | 1.214 | 1.166 | 172.6 | 123.9 | 0.995 | Reference[58] |
| CH$_3$NCO | 1.214 | 1.166 | 172.6 | 140.3 | 1.45 | Reference [59] |
| CH$_3$CH$_2$NCO | 1.217 | 1.173 | 174.1 | 138.8 | 1.439 | Reference[60] |
| H$_3$SiNCO | 1.197 | 1.174 | (180)[a,b] | 163.8 | 1.704 | Reference[61] |
| (CH$_3$)$_3$SiNCO | 1.202 | 1.176 | 165.8 | 156.9 | 1.74 | Reference[62] |
| F$_3$SiNCO | 1.19 | 1.168 | (180)[b] | 160.7 | 1.648 | Reference[63] |
| Cl$_3$SiNCO | 1.219 | 1.139 | (180)[b] | 138 | 1.646 | Reference[64] |
| ClNCO | 1.226 | 1.162 | 170.9 | 118.8 | 1.705 | Reference[65] |

[a] Electron diffraction data put this angle at 173.3° [56]
[b] Angle is assumed to 180°

*5.3.2.2 Excited State*

Chapter 6 details the experimental laser-induced fluorescence and dispersed fluorescence experiments on HSiNCO in the $\tilde{A}^1A''$ electronic state. Table 5.5 shows calculations carried out on the $\tilde{A}^1A''$ state of HSiNCO. It shows that on excitation the H-Si-N angle increases significantly, and this is due to electron density being transferred from the hybridised Si-H molecular orbital to an out-of-plane *p* orbital on the silicon. This can be seen in Figure 5.5 which gives a three dimensional representation of the HOMO orbital (using natural bond orbitals) in both the ground electronic state and the $\tilde{A}^1A''$ excited electronic state of HSiNCO at the B3LYP level of theory. On excitation all levels of theory predict the H-Si-N angle increases from ~94° to ~115°. Similar increases are seen for the analogous halogen species HSiX (X= F, Cl, Br, I) where on excitation the H-Si-X angles opens up to 115.3°, 116.1°, 116.6°, and 116.2°, respectively.[48-50] For all but the MC-SCF calculations the Si-H bond contracts by ~0.03 Å on excitation, while the Si-N bond length decreases by ~0.04 Å and the Si-N-C angle increases from ~146° to ~151°.

The excitation transition frequencies calculated using B3LYP, MP2(FC), MP2(Full) and QCISD(T) levels of theory are significant lower than the observed value of ~20000 cm$^{-1}$ (see Chapter 4; section 4.4.1). On the other hand the MC-SCF transition frequency is in reasonably good agreement with the observed value, although slightly higher. Obviously, this particular excitation involves more than one configuration, which standard methods such as MP2 and B3LYP are not able to describe correctly. Similar discrepancies in excitation energy has been found for the halogen species (HSiX; X=F, Cl, Br), where similar B3LYP and MP2 calculations underestimated the transition energy by ~4000 cm$^{-1}$. The CIS and SAC-CI calculations on HSiNCO show the lowest lying $^1A''$ state is located around ~20000 cm$^{-1}$, which is in good agreement with the experimental results. This state is predicted to have an oscillator strength of *f*=0.04, and results from $15\,a' \rightarrow 4\,a''$ and $15\,a' \rightarrow 5\,a''$ excitations.

Table 5.5: Bond distances (Å), Bond angles (degrees), Dipole Moments ($D$) and Transition Energy (cm$^{-1}$) for the $\tilde{A}^1A''$ state of HSiNCO calculated at various levels of theory.

| Parameter | B3LYP | MP2(FC) | MP2(Full) | QCISD[a] | MC-SCF | SAC-CI |
|---|---|---|---|---|---|---|
| $r$(H-Si) | 1.499 | 1.481 | 1.478 | 1.482 | 1.534 | 1.490 |
| $r$(Si-N) | 1.710 | 1.716 | 1.696 | 1.697 | 1.717 | 1.718 |
| $r$(N-C) | 1.202 | 1.212 | 1.203 | 1.194 | 1.195 | 1.211 |
| $r$(C-O) | 1.169 | 1.176 | 1.173 | 1.165 | 1.153 | 1.168 |
| $\angle$(H-Si-N) | 113.1 | 115.0 | 115.5 | 115.1 | 114.1 | 114.9 |
| $\angle$(Si-N-C) | 156.9 | 151.1 | 163.0 | 165.6 | 150.8 | 151.7 |
| $\angle$(N-C-O) | 177.8 | 176.9 | 178.0 | 178.5 | 177.3 | 176.2 |
| $\mu_x$ | -1.70 | -1.65 | -1.70 | -1.83 | -2.03 | -1.32 |
| $\mu_y$ | -0.05 | -0.14 | -0.04 | -0.10 | 0.08 | 0.88 |
| $T_0$ | 14485 | 16342 | 16355 | 15313 14659[b] | 21700 | 20914[c] |

[a] ZPE correction taken from a QCISD/aug-cc-pVDZ calculation.
[b] QCISD(T) value.
[c] Not zero point energy corrected
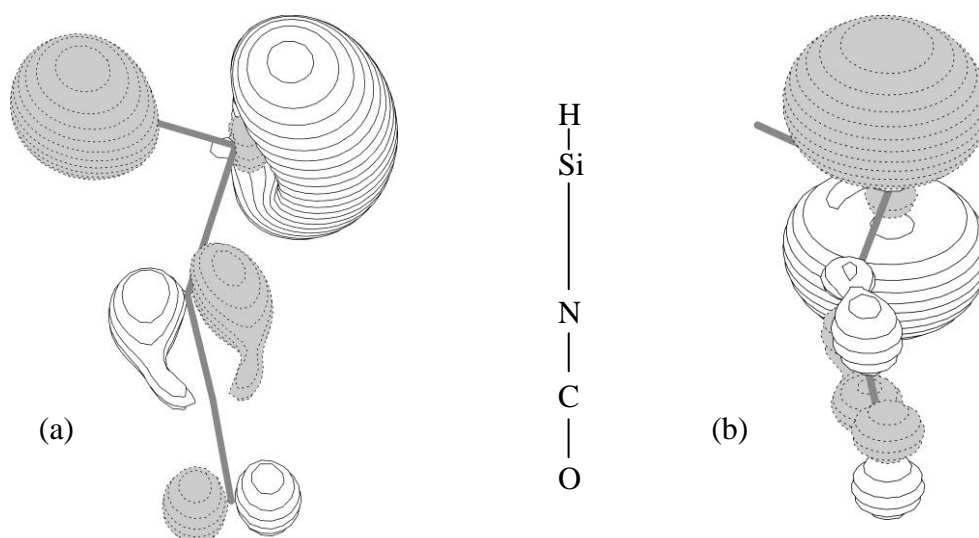


Figure 5.5: Three dimensional representations of the HOMO of HSiNCO in the (a) ground electronic state ($^1A'$) and (b) the first $\tilde{A}^1A''$ electronic state (contours are in 0.08 steps).

### 5.3.3 HSi(O)CN and HSi(O)NC

The fifth and sixth lowest isomers are the HSi(O)CN and HSi(O)NC species which are analogous to the formyl cyanide and isocyanide species.[14] For both isomers the Si-H bond length is ~1.47 Å, which is smaller to that found in HSiNCO and is similar to that observed for $H_3SiNCO$. The Si-X (X=C and N) bond length decreases by 0.1 Å going from C to N, which is seen in the other isomers. The Si-O bond length is ~1.52 Å which is much shorter than the ~1.65 Å observed in HO-SiCN/NC and is similar to the 1.51 Å bond length observed for the diatomic SiO which indicates that this a double bond.[45] In going from CN to NC the C-N bond length increase by 0.02 Å, again this is similar to the trend seen in HO-SiCN/NC. The H-Si-C angle of 109.1° with the O-Si-C angle of 122.8° indicates that some $sp^2$ hybridisation is occurring on Si resulting in the ~120° angles. The dipole moments ($\mu_x/\mu_y$) in the ground state for HSi(O)CN and HSi(O)NC are -2.55/1.78 and -2.61/1.62 respectively, and are sufficiently high that these species should be easily observed using standard microwave techniques. Table 5.3 shows the vibrational wavenumbers and rotational constants for these species. Excited state calculations on these species at the MP2(FC) level of theory show that the first $^1A''$ state of HSi(O)CN is located around ~25000 cm$^{-1}$, while for HSi(O)NC the transition energy is predicted to be shifted to the blue and is ~28000 cm$^{-1}$. On excitation, there is a significant change in the geometry with the Si-O bond increasing by more 0.1 Å and the C-N bond decreasing by 0.04 Å. However, the biggest change is in the C-Si-O angle which decreases by ~15°, while the C-Si-H angle increases by ~20°. This is a result of electron density being shifted into a *p* orbital on the silicon. Upon excitation both isomers gave an imaginary wavenumber value for the out-of-plane Si-H wag, in the planar form.

*5.3.3.1 Natural Bond Analysis (NBA)*

For HSi(O)CN the NBA assigns the C-N bond as a triple bond and the Si-O bond as a double bond. It gives three lone-pairs, one on the nitrogen and two on the oxygen. The LP on nitrogen is substantially hybridised with $sp^{0.88}$ (46.8% *p* character). On the oxygen the first LP is mainly *s* in character ($sp^{0.57}$ (36.2% *p* character)), while the other lone-pair is mainly *p* in character and is similar to the out-of-plane LP seen for HO-SiCN/NC. The bonding contributions from the Si for Si-H, Si-C and Si-O shows a fair amount of hybridisation 65.5%, 70.7% and 61% *p* character, respectively which would explain the slightly larger H-Si-C and O-Si-C angles seen than in the

other isomers. For HSi(O)NC the bonding is very similar to that seen for HSi(O)CN except there is now a lone-pair on the carbon which, like the lone-pair on the nitrogen in HSi(O)CN, is substantially hybridised, $sp^{0.43}$ (30.2% $p$ character).

### 5.3.3.2 Excited States

As stated above, the planar structures of $\tilde{A}^1A''$ symmetry give one imaginary wavenumber value corresponding to the Si-H out-of plane wagging mode at all levels of theory. This is indicative of a saddle point on the potential and not a true minimum. Therefore, as with the HOSiCN/NC isomers discussed above, further calculations were undertaken with deviations from a planar geometry (thus breaking the symmetry) to see if the true minima could be found for the HSi(O)CN/NC isomers. To obtain consistency in the energy calculations, the SAC-CI method was again used in determination of both the ground and excited states. The resulting structures and energies are given in Figure 5.4.

As these isomers are similar in structure to formaldehyde it is likely that they will exhibit similar properties. In most cases, a stable non-degenerate electronic state has a potential function with a single minimum. However, the potential functions for a few electronic states have been found to have two equivalent minima at $Q = \pm Q_m$ where $Q$ is a mass weighted out-of-plane bending coordinate describing an antisymmetric displacement and $Q_m$ is the magnitude of $Q$ at the potential minima. The origin of $Q$ is defined such that at $Q = 0$ the most symmetrical configuration of the nuclei is used. Therefore, it is thought that like formaldehyde, the HSi(O)CN/NC isomers will give double minima potentials with some out-of-plane geometries giving the minima ($Q = \pm Q_m$) and the planar structures being the saddle points between them ($Q = 0$).

The molecular system of interest is shown in Figure 5.6 where planar $C_s$ symmetry is assumed. The rigid bender model allows displacement of only the nucleus labelled 1 in Figure 5.6 (corresponding in this case to the hydrogen) with respect to the plane formed by nuclei 2, 3 and 4 which correspond to the CN/NC unit, the oxygen and the silicon, respectively. The displacement of the hydrogen nucleus out of this plane gives the out-of-plane angle $\theta$. The bond lengths $r_{41}$, $r_{42}$ and $r_{43}$ are fixed to their equilibrium geometry values from the SAC-CI calculation as is the bond angle $\phi_1$,

while the bond angles $\phi_2$ and $\phi_3$ vary with the out-of-plane angle $\theta$. Therefore, this model represents motion along the pure out-of-plane bending normal coordinate.
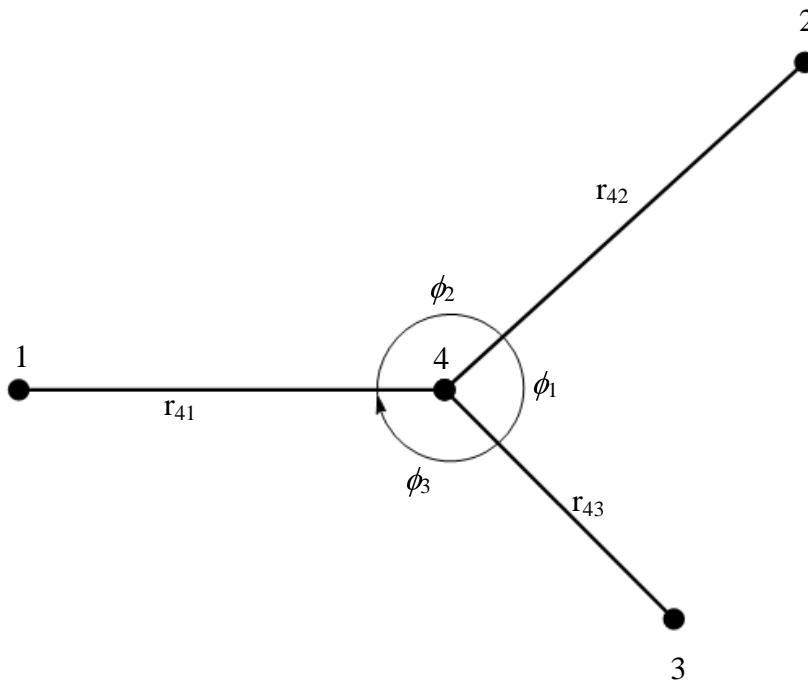


Figure 5.6: Molecular geometry and labelling assumed in the rigid bender model (figure modified from Ref [2])

Following the methodology developed by Coon *et al.*[57,58] the function to fit the double minimum potentials in molecules takes the following form

$$V(Q) = \tfrac{1}{2}\lambda Q^2 + \delta e^{\rho} \exp(-\lambda Q^2/2\delta) - \delta(\rho+1) \qquad [5.2]$$

where $\delta = \dfrac{Bhcv_0}{e^{\rho} - \rho - 1}$, and $\lambda = (2\pi c v_0)^2$. The parameter $v_0$ is the frequency of the parabolic part of the potential, $Bv_0$ is the barrier height in cm$^{-1}$, and $\rho$ is a parameter which governs the shape of the potential. For small values of $\rho$ the outer walls of the potential are steeper than the barrier walls, while for larger values the converse is true.

Energies for the rigid bender potentials were calculated by first calculating the geometries of the two molecules at the CIS/aug-cc-pVTZ level of theory. This was followed by further CIS/aug-cc-pVDZ calculations where the bond lengths and angles were fixed to the planar values and the hydrogen nuclei allowed to move out-

of-plane with respect to the rest of the molecules with a step size of 5°. This procedure was carried out on both isomers over a range of $\theta = 0\text{-}110°$ (where $\theta = 0°$ corresponds to the planar conformation). Corresponding $Q$ values were determined using the methodology of Clouthier et al.[2] by numerical integration of the following equation

$$Q(\theta') = \int_0^{\theta'} \frac{1}{\sqrt{C + D\cos\theta}}\, d\theta \qquad [5.3]$$

with

$$C = \frac{A^2}{M_2} + \frac{B^2}{M_3} + \frac{(A+B)^2}{M_4} \qquad [5.4]$$

and

$$D = \frac{M_1 + M_4}{r_{41}^2 M_1 M_4} + \frac{2(A+B)}{M_4 r_{41}} \qquad [5.5]$$

where $A = \dfrac{\cos\phi_1 \cos\phi_2^0 - \cos\phi_3^0}{\sin^2\phi_1 r_{42}}$ and $B = \dfrac{\cos\phi_1 \cos\phi_3^0 - \cos\phi_2^0}{\sin^2\phi_1 r_{43}}$. The values of $Q_m$ were determined according to the following equation

$$Q_m^2 = \frac{h}{4\pi^2 c} \frac{2\rho}{e^\rho - \rho - 1} \frac{B}{v_0} \qquad [5.6]$$

from which the related value of $\theta_m$ is readily tractable.

Once the $Q$ values were determined the potential functions were fitted according to Equation [5.2], and the resulting plots are shown in Figure 5.7. The parameters derived from these fits are given in Table 5.6. $Q$ values were determined by means of the *ReducedQProg.m* written in MATLAB®[59] by the author, a copy of which is given in the addendum. As can be seen from the Figure 5.7 and Table 5.6, the two potentials are very similar as one would expect, with such similar isomers. The only real difference appears in the barrier height ($B v_0$) with the HSi(O)NC isomer having a value of 4861.1 cm$^{-1}$ compared to the HSi(O)CN isomer which has a barrier height of 2788.4 cm$^{-1}$. This, in turn, has an effect on the shape factor ($\rho$) which as predicted is higher for HSi(O)NC as the barrier height approaches the height of the walls of the potential.
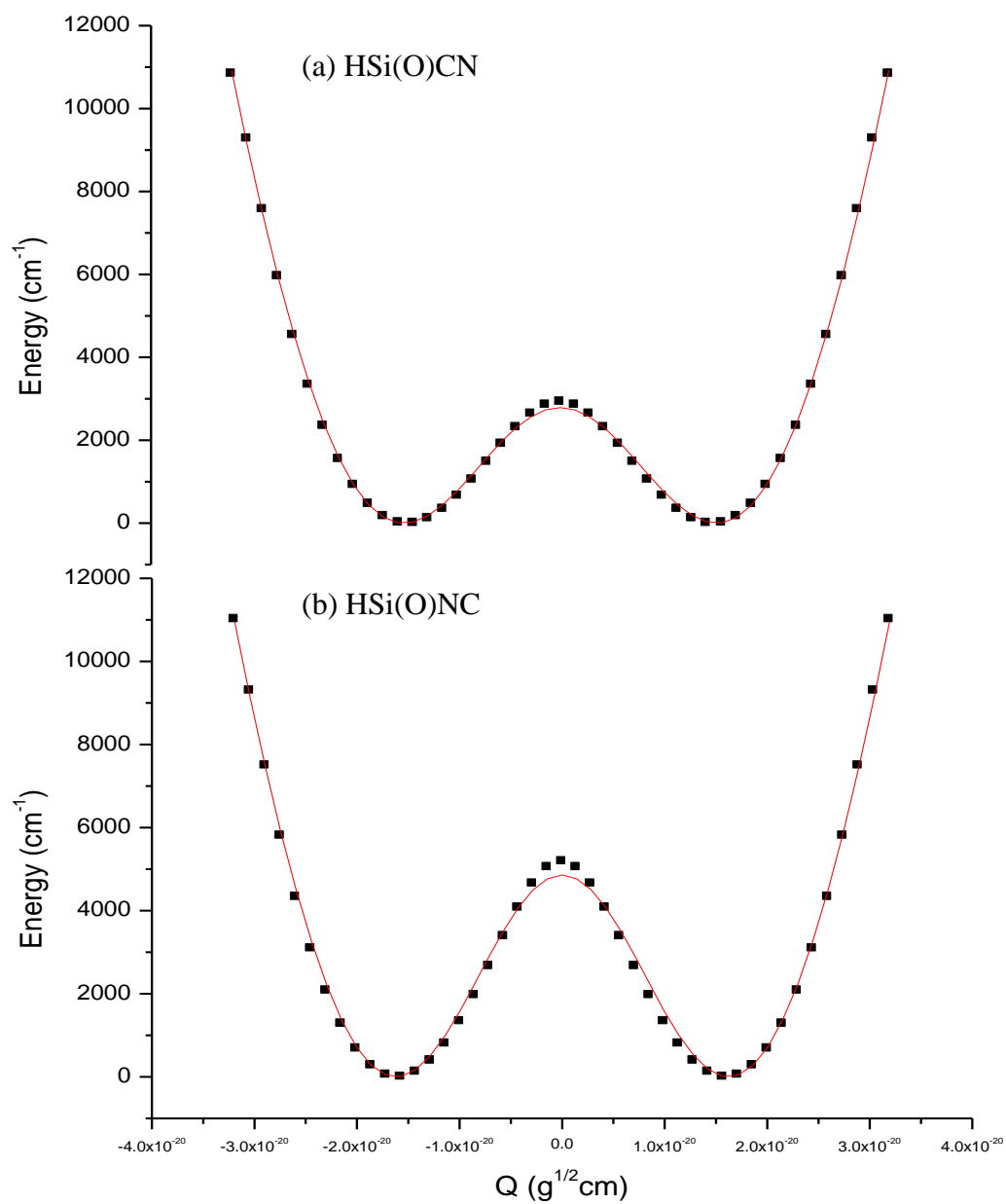
Figure 5.7: The double minimum potentials fitted according to Equation [5.2] for (a) the HSi(O)CN isomer and (b) the HSi(O)NC isomer in their excited states.

Table 5.6: Parameters from the fit of the double minima potentials for the HSi(O)CN/NC isomers in their excited ($^1A$) states

| Parameter | HSi(O)CN | HSi(O)NC |
|---|---|---|
| $\nu_0$ | 474.75 | 476.42 |
| $B$ | 5.87 | 10.20 |
| $\rho$ | 0.868 | 1.180 |
| $B\nu_0$ (cm$^{-1}$) | 2788.4 | 4861.1 |
| $Q_m$ (g$^{1/2}$ cm $\times$ 10$^{-20}$) | $\pm$1.528 | $\pm$1.622 |
| $\theta_m$ ($^\circ$) | $\pm$53.2 | $\pm$56.8 |

### 5.3.4  Enthalpies of Formation

In order to get some understanding of how the chemical structure of the isomers relate to their reactivity the enthalpies of formation for some isomers where calculated.  Table 5.7 shows the enthalpy of formation at 0 and 298 K of the seven lowest isomers using the G3MP2 and G3B3 multilevel methods. The enthalpies were calculated using the method of Curtiss *et al.* where the theoretical enthalpies were calculated by subtracting the calculated atomization energies from the known enthalpies of formation of the isolated atoms.[41] To calculate the enthalpy of formation at 0 K Equation [5.7] was employed:

$$\Delta H^{\circ}_{f,0}(M) = E(M) + ZPE(M) - \sum_{z}^{atoms} E(X_z) + \sum_{z}^{atoms} \Delta H^{\circ}_{f,0}(X_z) \qquad [5.7]$$

while for the enthalpy of formation at 298 K Equation [5.8] was used:

$$\Delta H^{\circ}_{f,298}(M) = E(M) + ZPE(M) + \left[ H_{298}(M) - H_0(M) \right]$$
$$- \sum_{z}^{atoms} \left\{ E(X_z) + \left[ H_{298}(X_z) - H_0(X_z) \right] \right\} \sum_{z}^{atoms} \Delta H^{\circ}_{f,298}(X_z) \qquad [5.8]$$

In Equation [5.8], $H_{298}(M)$ and $H_0(M)$ are taken from the theoretical calculations, while the values of $H_{298}$-$H_0$ for the atoms where taken from the JANAF tables, as were the values for $\Delta H^{\circ}_{f,0}$ and $\Delta H^{\circ}_{f,298}$ for the atoms.[60]

It is very difficult to compare these results with previous data as there is no thermodynamic data on any species containing all five atoms [H, Si, C, N, O]. The

enthalpies of formation of the isomers lies in the same range as those for silane (8.2 kcal/mol, 298K) and disilane (19.1 kcal/mol, 298K).[61] If we compare the enthalpies of formations against those from other transient species then we see that the generation and detection of the [H, Si, N, C, O] isomers is, from a thermodynamic standpoint, highly possible. For instance, the enthalpy of formation of HNCO (298 K) has been estimated to be -27 kcal/mol, with HOCN -3.1 kcal/mol, HCNO 40.9 kcal/mol and HONC 56.4 kcal/mol.[62] Furthermore, work on NCO has estimated that its enthalpy of formation to be around +30.3 kcal/mol.[63] If we compare the results against some important silicon containing transient species we see that SiCH ($\Delta_f H^\circ(298\,K)$ =123.1 kcal/mol), H$_2$Si=CH$_2$ ($\Delta_f H^\circ(298\,K)$ = 43.0 kcal/mol) SiC ($\Delta_f H^\circ(298\,K)$ =178.6 kcal/mol) SiC$_2$ ($\Delta_f H^\circ(298\,K)$ =149.1 kcal/mol), and SiCH$_2$ ($\Delta_f H^\circ(298\,K)$ =74.6 kcal/mol).[64] Further work by Flores has estimate the $\Delta_f H^\circ(298\,K)$ of SiCN, SiNC, HSiCN and HSiNC to be 103.6, 106.3, 85.1 and 87.4 kcal/mol, respectively.[9,65] Of these species SiC$_2$, SiC, SiCN and SiNC have already been observed in the interstellar medium. Overall, if the correct generation technique is employed (*i.e.*, photolysis, pyrolysis, laser ablation or electric discharge) in conjunction with the right pre-cursor then the spectroscopic detection of the proposed isomers is highly feasible with the best chance of detection being with microwave spectroscopy.

Table 5.7: Enthalpy of formation at 0 and 298 K of the seven lowest [H, Si, N, C, O] isomers.

| Isomer | $\Delta_f H^\circ$ [G3MP2] | | $\Delta_f H^\circ$ [G3B3] | |
| --- | --- | --- | --- | --- |
| | 0 K | 298 K | 0 K | 298 K |
| *cis*- HOSiCN | 7.84 | 6.42 | 6.93 | 5.71 |
| *trans*- HOSiCN | 8.92 | 13.47 | 8.14 | 12.67 |
| *cis*- HOSiNC | 5.4 | 8.8 | 5.35 | 8.7 |
| *trans*- HOSiNC | 6.64 | 10.97 | 6.72 | 11.03 |
| HSi(O)CN | 15.55 | 18.03 | 14.53 | 16.95 |
| HSi(O)NC | 15.55 | 10.51 | 15.55 | 10.56 |
| HSiNCO | 20.36 | 14.01 | 19.28 | 12.98 |

### 5.3.5 Transition States

Figure 5.8 shows the structures of various transition states and Figure 5.9 shows the corresponding isomerisation processes of the [H, Si, N, C, O] isomers with their relative energies. In all cases, the calculations have been carried out at the B3LYP level of theory using the aug-cc-pVTZ basis set, and the symmetry of all the calculated transition states is $^1A$. The given nomenclature of these transition states is ts X/Y (where X and Y refer to the isomers SX and SY from Figure 5.1). The barrier heights given refer to the relative difference between the energy of the first isomer (*i.e.*, X in the ts X/Y nomenclature described above) and the energy of the transition state.

The two lowest energy transition states calculated are for isomers S1 and S3, ts 1/2 and ts 3/4. These transition states represent the barrier to isomerisation between the *cis-* to *trans*-HOSiCN and *cis-* to *trans*-HOSiNC, respectively, which have already been discussed in section 5.3.1.3 above. The barrier heights of these two processes are 6.80 and 6.20 kcal/mol. The barriers to reverse these processes are slightly lower with values of 5.66 and 4.89 kcal/mol, respectively, but given the very small difference in energy it is likely that these isomerisation processes could occur in either direction. Isomers S1 and S3 also have two higher energy transition states, ts 1/3 and ts 2/4, which correspond to the CN $\leftrightarrow$ NC interconversion process for the *cis-* and *trans*-HOSiCN isomers via an Si-C-N ring closure. The barriers to these isomerisation processes are 15.87 and 17.41 kcal/mol, respectively. The heights of these barriers are higher than for the *cis-* to *trans-* processes due to the ring closing mechanism. The barriers to the reverse of these processes are slightly higher in energy being 18.39 and 19.76 kcal/mol, respectively, but again the relative difference between the isomers suggests that it is likely that the isomerisation processes may occur in either direction.

Isomers S2 and S4 have two high energy transitions states, ts 2/5 and ts 4/6, which correspond to the *trans*-HOSiCN $\leftrightarrow$ HSi(O)CN and *trans*-HOSiNC $\leftrightarrow$ HSi(O)NC interconversions. The energies for these processes are 62.69 and 62.71 kcal/mol, respectively. In this case the barriers to the reverse of these processes are significantly lower being 53.20 and 50.83 kcal/mol, respectively. Therefore, it seems likely that, if formed, the S5 and S6 isomers would undergo these isomerisation processes if enough energy was available to them.

Transition state, ts 5/6 links the HSi(O)CN and HSi(O)NC isomers, again by a Si-C-N ring closure. The calculated energy difference between these two isomers is only 0.05 kcal/mol, but the barrier height which governs the ease of this interconversion is 19.12 kcal/mol. The barrier to the reverse isomerisation process is 19.08 kcal/mol, but given the almost isoenergetic nature of these two isomers it would seem unlikely that this process would occur.

Isomer S6 shows the highest energy transition state, ts 6/7, which corresponds to the HSi(O)NC to HSiNCO interconversion. The barrier to this isomerisation process is calculated to be 59.43 kcal/mol. The barrier to the reverse isomerisation process is 63.24 kcal/mol, but again it would seem unlikely that such a process would occur given the height of the barrier compared to the small relative energy difference between the two isomers.

Finally, the transition state corresponding to the interconversion of isomer HSiNCO (S7) to HSiONC (S10), ts 7/10, has been calculated. The barrier to this isomerisation process is calculated to be 38.64 kcal/mol. The barrier to the reverse isomerisation process is 13.09 kcal/mol, and therefore, in this case, it would seem highly feasible for the relatively high energy HSiONC species to isomerise to the more stable HSiNCO species if it were formed.

DNSiOH=99.1°;
DOSiNC=-179.7°
ts 3/4 ($^1A$) [6.20]

∠SiNC=72.0°;
DHOSiN=162.4°; DHOSiC=-165.6°
ts 2/4 ($^1A$) [21.07]

∠CSiH=157.6°; ∠OSiH=59.8°;
DCSiOH=154.0°; DOSiCN=173.2°
ts 2/5 ($^1A$) [66.35]

DCSiOH=99.6°; DOSiCN=-174.6°
ts 1/2 ($^1A$) [9.32]

∠SiNC=72.7°;
DHOSiN=-14.8°; DHOSiC=16.4°
ts 1/3 ($^1A$) [18.39]
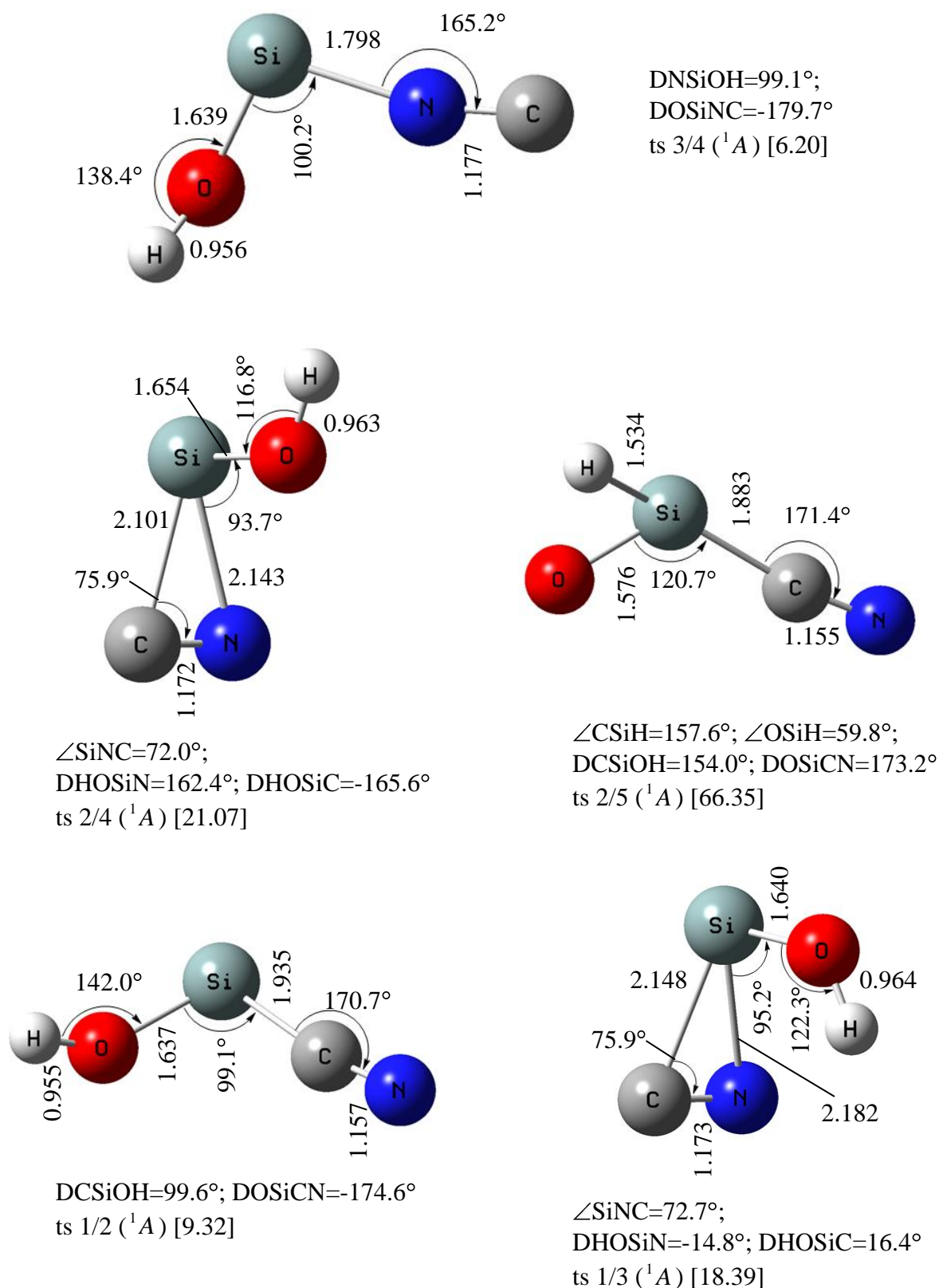
Figure 5.8: Optimized geometries of some of the transition state structures connecting the ten lowest energy isomers given in Figure 5.1 (bond lengths in Å; bond angles in degrees) computed at the B3LYP/aug-cc-pVTZ level of theory. All energies [in kcal/mol] are relative to the corresponding lowest energy $^1A'$ isomers also claculated at the B3LYP/aug-cc-pVTZ level of theory.
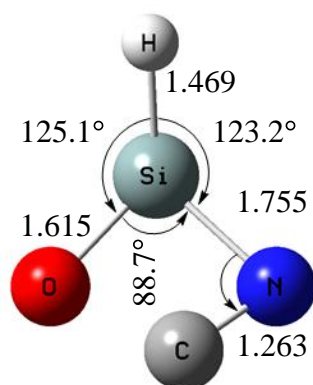
∠SiNC=83.9°;
DNSiOH=130.8°;
DOSiNC=-15.7°
ts 6/7 ($^{1}A$) [72.62]
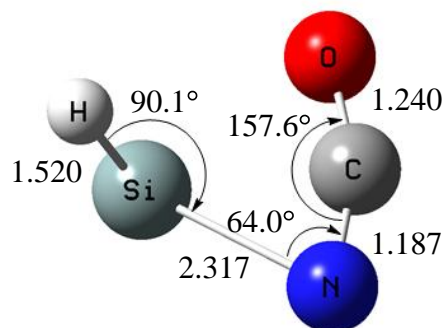
DSiNCO=-1.7°;
DCNSiH=-89.1°
ts 7/10 ($^{1}A$) [48.02]
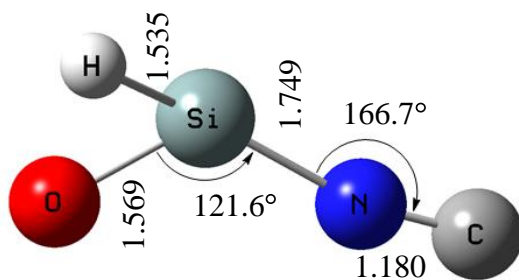
∠NSiH=159.8°; ∠OSiH=60.5°;
DNSiOH=156.6°; DOSiNC=171.1°
ts 4/6 ($^{1}A$) [64.02]
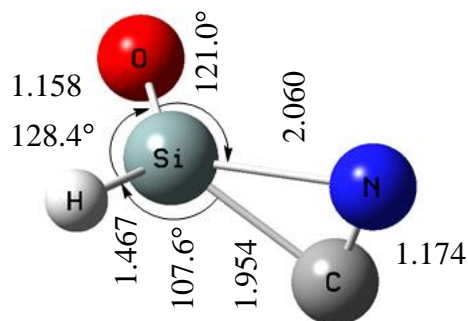
∠SiNC=68.1°; ∠NCSi=78.0°; ∠CSiN=33.9°;
DNCSiH=-92.9°; DNCSiO=97.7°
ts 5/6 ($^{1}A$) [32.27]

Figure 5.8 (cont.): Optimized geometries of some of the transition state structures connecting the ten lowest energy isomers given in Figure 5.1 (bond lengths in Å; bond angles in degrees) computed at the B3LYP/aug-cc-pVTZ level of theory. All energies [in kcal/mol] are relative to the corresponding lowest energy $^{1}A'$ isomers also claculated at the B3LYP/aug-cc-pVTZ level of theory.
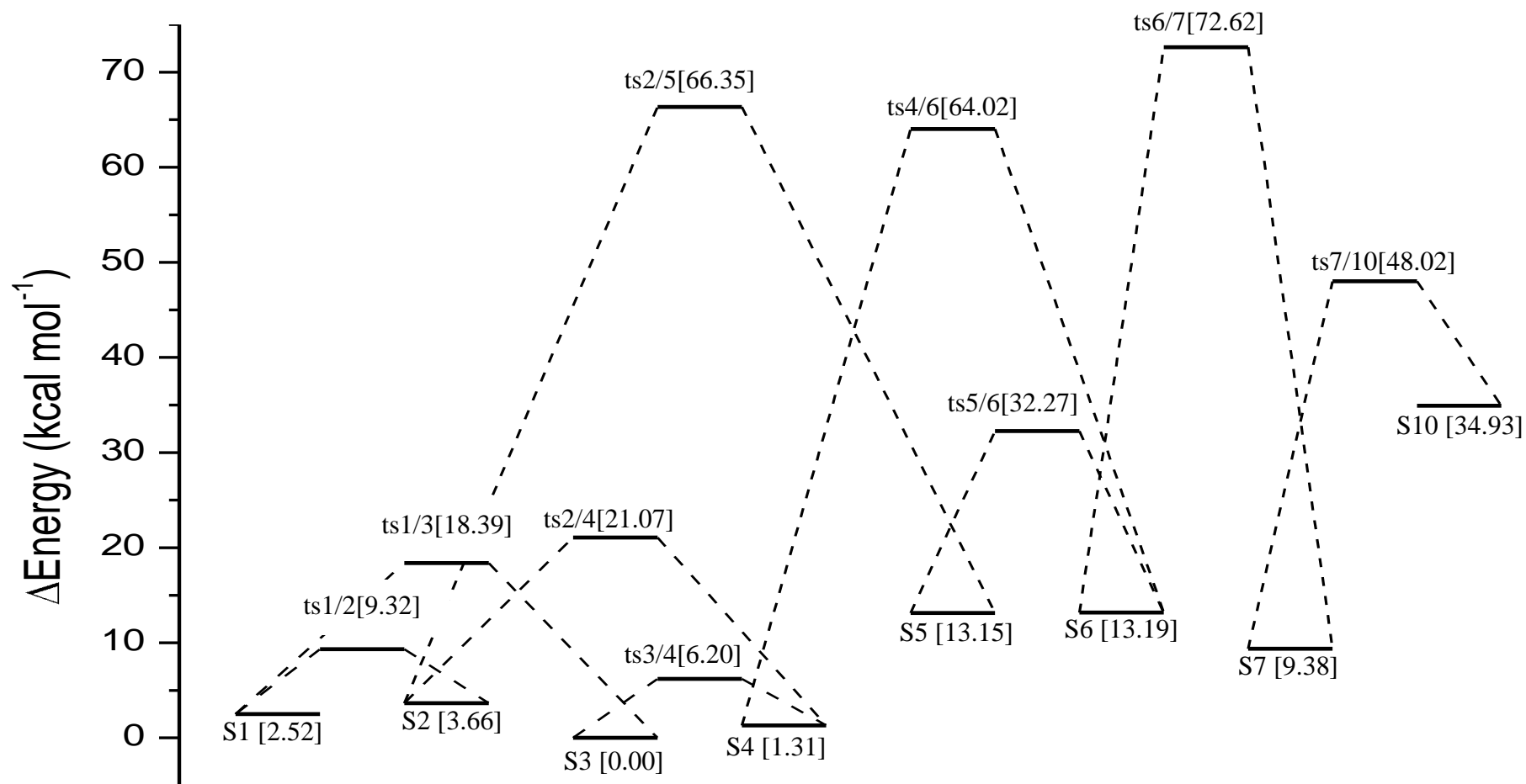
Figure 5.9: Schematic potential energy surface showing relative energies for some of the transition states of [H, Si, N, C, O] calculated at the B3LYP/aug-cc-pVTZ level of theory.

### 5.3.6 Triplet States

As with the excited states, it was found that the lowest lying triplet states deviated from planarity. At first calculations were carried out on the $^3A''$ triplet state of the seven lowest [H, Si, C, N, O] isomers at the MP2 and B3LYP levels of theory. The $^3A''$ triplet state was found to be the lowest lying triplet state for each species with the $^3A'$ state being substantially higher in energy. The results from these calculations gave very similar structures and relative energies. At the MP2(FC) level of theory the isomers T1-T5 had one imaginary vibration (the out-of-plane Si-H wag), which is indicative of a saddle point or transition state. At the MP2(FC) level of theory isomers T6 and T7 did not give an imaginary vibration. However, at the B3LYP level of theory isomer T6 had one imaginary vibration (the out-of-plane Si-H wag). As the isomers T1-T6 gave imaginary vibrations, calculations were then carried out to search for non-planar structures.

Calculations were carried out on the $\tilde{a}^3A$ state of the four lowest isomers, and the $^3A''$ state for the fifth lowest isomer (corresponding to the seven lowest ground state isomers in Figure 5.1). Figure 5.10 shows the structures of the $\tilde{a}^3A/^3A''$ triplet state of each isomer and their energies relative to their $^1A'$ isomer as given in Figure 5.1 at the B3LYP level of theory. For the first four isomers (T1-T6 in Figure 5.10) the electronic configuration of the triplet species is $19\alpha17\beta$, while for isomer T7 in Figure 5.10 the electronic configuration for the triplet state is $14a'^2 15a'^1 3a''^2 4a''^1$.

It has been found that the lowest energy electronic excited state of simple polyatomic inorganic anions is a triplet state.[66,67] For inorganic species, the cyanate ion (CNO⁻) exhibits distinct phosphorescence at ~415 nm. The vibrational structure observed with this phosphorescence indicates that it originates with the NCO⁻ ion. Work by Rabalais *et al.* showed that the organic isocyanates $CH_3NCO$, $C_6H_5NCO$ and $CH_3CH_2NCO$ also exhibit phosphorescence spectra.[66,67] For these species the phosphorescence spectra resulted from a $^3A'-^1A'$ transition. It would be of interest to see whether the HSiNCO species follows the same trend to that of the alkyl isocyanates and phosphoresces. For HSiNCO the frequency for the $^3A''-^1A'$ transition at the MP2(FC) level of theory is ~11000 cm⁻¹, while the frequency for $^3A'-^1A'$ transitions is ~40000 cm⁻¹. For the $^3A'$ state, vibrational analysis shows the out-of-plane Si-H wag gives an imaginary vibration, and therefore is non-planar.
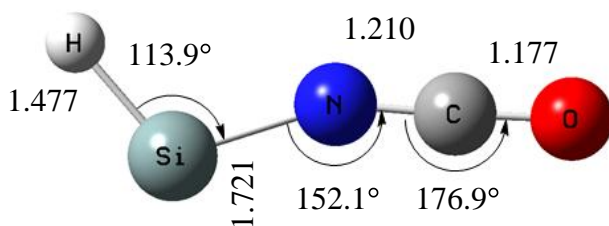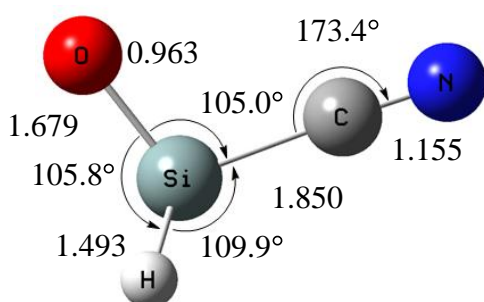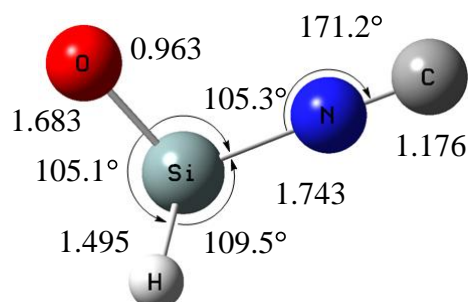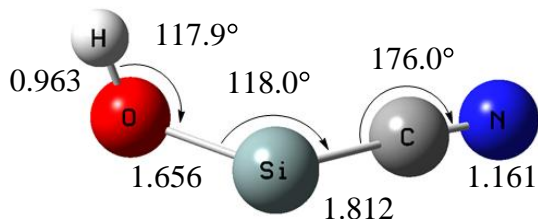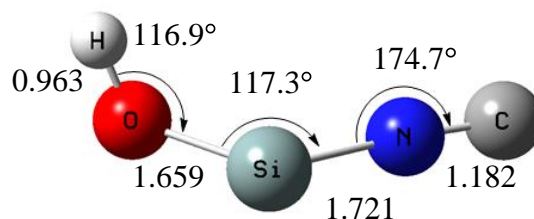
Figure 5.10: Optimized geometries of seven triplet states of the [H, Si, C, N,O] system (in Å and degrees) computed at the B3LYP/aug-cc-pVTZ level of theory. All energies [kcal/mol] are relative to their corresponding $^1A'$ isomers also calculated at the B3LYP/aug-cc-pVTZ level of theory.

## 5.4    Concluding Remarks

In this chapter we have looked in detail at the seven lowest energy [H, Si, N, C, O] isomers. This is the first ever study on these species. It has been shown that the identity of the lowest energy isomer is dependent on the level of theory applied to the isomers. The B3LYP and QCISD(T) methods give the *cis*-HOSiNC isomer as being the lowest isomer, while the MP2(FC) and MP2(Full) methods give the *cis*-HOSiCN isomer as being the lowest. The corresponding *trans* isomers are situated ~1.0 kcal/mol above their *cis* analogues. Overall, the lowest four isomers are situated within approximately 2.5 kcal/mol of one another. The other isomers were predicted to be between 6.0 and 14.0 kcal/mol above the lowest energy isomer. It has been shown that the inclusion of core electrons does have a significant impact on the structure and relative energies of the isomers.

The motive for this study was to collect data to aid in the detection and assignment of these species spectroscopically. This has been done by calculating vibrational wavenumbers and rotational constants for each isomer in their ground electronic state.

For each of the lowest seven isomers the structure and transition energy of the first $^1A$ / $^1A''$ electronic state has also been determined. The lowest six isomers show deviations from the planarity observed in their ground states necessitating that the transition energies for these excited states were carried out using the SAC-CI method. The seventh lowest isomer did not exhibit this deviation from planarity, but for the sake of consistency, the transition energy of this isomer was also calculated using the SAC-CI method. For the most part, each isomer also shows a significant change in its geometry on excitation resulting mainly from electron density being shifted to an out-of-plane orbital resulting in the X-Si-C/N angle increasing by ~20°.

We have also determined the enthalpy of formation for each of the isomers using the G3B3 and G3MP2 methods and have found that, for the most part, the species are relatively thermodynamically stable and are comparable to that of silane and disilane. We have also looked at the electronic structure of each isomer using natural bond analysis in its ground electronic state, giving a detailed description of the hybridisation and, therefore, the likely bonding occurring and location of any lone pairs present.

Lastly, we have looked at the lowest lying triplet state ($^3A''$) for each of the seven lowest isomers and have shown that on excitation there is a substantial change in geometry for the lowest five isomers where, as with their respective excited states, there is deviation from the planar geometry observed in the ground state isomers together with a significant change in the X-Si-C/N angle.

Overall it is thought the species investigated in this work should be easily observable using spectroscopic techniques, in particular, microwave spectroscopy. Given that these species are fairly thermodynamically stable it is reasonable to assume that they may also be present in the interstellar medium, and thus may be remotely detected. In Chapter 6 there are details of the experimental laser induced fluorescence (LIF) study of the HSiNCO isomer (isomer S7 in Figures 5.1, 5.3 and 5.4), where the calculations carried out in this chapter will provide useful comparison data.

## 5.5 REFERENCES FOR CHAPTER 5

(1)     Duley, W. W.; Williams, D. A. *Interstellar Chemistry*; Academic Press: London, **1984**.

(2)     Clouthier, D. J.; Goddard, J. D. *J. Chem. Phys.* **1982**, *76*, 5034.

(3)     Cernicharo, J.; Gottlieb, C. A.; Guelin, M.; Thaddeus, P.; Vrtilek, J. M. *Astrophys. J.* **1989**, *341*, L25.

(4)     Guelin, M.; Muller, S.; Cernicharo, J.; Apponi, A. J.; McCarthy, M. C.; Gottlieb, C. A.; Thaddeus, P. *Astron. Astrophys.* **2000**, *363*, L9.

(5)     Guelin, M.; Muller, S.; Cernicharo, J.; McCarthy, M. C.; Thaddeus, P. *Astron. Astrophys.* **2004**, *426*, L49.

(6)     Apponi, A. J.; McCarthy, M. C.; Gottlieb, C. A.; Thaddeus, P. *Astrophys. J.* **1999**, *516*, L103.

(7)     Wang, Q.; Ding, Y. H.; Sun, C. C. *Chem. Phys.* **2006**, *323*, 413.

(8)     Stanton, J. F.; Dudek, J.; Theule, P.; Gupta, H.; McCarthy, M. C.; Thaddeus, P. *J. Chem. Phys.* **2005**, *122*.

(9)     Flores, J. R.; Perez-Juste, I.; Carballeira, L. *Chem. Phys.* **2005**, *313*, 1.

(10)    Liu, H. L.; Huang, X. R.; Chen, G. H.; Ding, Y. H.; Sun, C. C. *J. Phys. Chem. A* **2004**, *108*, 6919.

(11)    McCarthy, M. C.; Gottlieb, C. A.; Thaddeus, P. *Mol. Phys.* **2003**, *101*, 697.

(12)    Yu, H. T.; Fu, H. G.; Chi, Y. J.; Huang, X. R.; Li, Z. S.; Sun, C. C. *Chem. Phys. Lett.* **2002**, *359*, 373.

(13)    McCarthy, M. C.; Thaddeus, P. *J. Mol. Spectrosc.* **2002**, *211*, 228.

(14)    Yu, H. T.; Ding, Y. H.; Huang, X. R.; Li, Z. S.; Fu, H. G.; Sun, C. C. *J. Mol. Struc.-Theochem.* **2001**, *574*, 47.

(15)    Chen, G. H.; Ding, Y. H.; Huang, X. R.; Zhang, H. X.; Li, Z. S.; Sun, C. C. *J. Phys. Chem. A* **2002**, *106*, 10408.

(16)    Srinivas, R.; Vivekananda, S.; Schroder, D.; Schwarz, H. *Chem. Phys. Lett.* **2000**, *316*, 243.

(17)    Apponi, A. J.; McCarthy, M. C.; Gottlieb, C. A.; Thaddeus, P. *Astrophys. J.* **2000**, *536*, L55.

(18)    Bailleux, S.; Bogey, M.; Breidung, J.; Burger, H.; Fajgar, R.; Liu, Y. Y.; Pola, J.; Senzlober, M.; Thiel, W. *Angew. Chem. Int. Ed.* **1996**, *35*, 2513.

(19)    Sanz, M. E.; McCarthy, M. C.; Thaddeus, P. *Astrophys. J.* **2002**, *577*, L71.

(20)    Frisch, M. J.; Trucks, G. W.; Schlegel, H. B.; Scuseria, G. E.; Robb, M. A.; Cheeseman, J. R.; Montgomery, J., J. A.; Vreven, T.; Kudin, K. N.; Burant, J. C.; Millam, J. M.; Iyengar, S. S.; Tomasi, J.; Barone, V.; Mennucci, B.; Cossi, M.; Scalmani, G.; Rega, N.; Petersson, G. A.; Nakatsuji, H.; Hada, M.; Ehara, M.; Toyota, K.; Fukuda, R.; Hasegawa, J.; Ishida, M.; Nakajima, T.; Honda, Y.; Kitao, O.; Nakai, H.; Klene, M.; Li, X.; Knox, J. E.; Hratchian, H. P.; Cross, J. B.; Bakken, V.; Adamo, C.; Jaramillo, J.; Gomperts, R.; Stratmann, R. E.; Yazyev, O.; Austin, A. J.; Cammi, R.; Pomelli, C.; Ochterski, J. W.; Ayala, P. Y.; Morokuma, K.; Voth, G. A.; Salvador, P.; Dannenberg, J. J.; Zakrzewski, V. G.; Dapprich, S.; Daniels, A. D.; Strain, M. C.; Farkas, O.; Malick, D. K.; Rabuck, A. D.; Raghavachari, K.; Foresman, J. B.; Ortiz, J. V.; Cui, Q.; Baboul, A. G.; Clifford, S.; Cioslowski, J.; Stefanov, B. B.; Liu, G.; Liashenko, A.; Piskorz, P.; Komaromi, I.; Martin, R. L.; Fox, D. J.; Keith, T.; Al-Laham, M. A.; Peng, C. Y.; Nanayakkara, A.; Challacombe, M.; Gill, P. M. W.; Johnson, B.; Chen, W.; Wong, M. W.; Gonzalez, C.; Pople, J. A. Gaussian 03; Revision D.02 ed.; Gaussian Inc.: Wallington CT, **2004**.

(21)    Dunning, T. H. *J. Chem. Phys.* **1989**, *90*, 1007.

(22)  Kendall, R. A.; Dunning, T. H.; Harrison, R. J. *J. Chem. Phys.* **1992**, *96*, 6796.

(23)  Woon, D. E.; Dunning, T. H. *J. Chem. Phys.* **1993**, *98*, 1358.

(24)  Becke, A. D. *J. Chem. Phys.* **1993**, *98*, 5648.

(25)  Frisch, M. J.; Head-Gordon, M.; Pople, J. A. *Chem. Phys. Lett.* **1990**, *166*, 275.

(26)  Frisch, M. J.; Head-Gordon, M.; Pople, J. A. *Chem. Phys. Lett.* **1990**, *166*, 281.

(27)  Head-Gordon, M.; Pople, J. A.; Frisch, M. J. *Chem. Phys. Lett.* **1988**, *153*, 503.

(28)  Møller, C.; Plesset, M. S. *Phys. Rev.* **1934**, *46*, 618.

(29)  Pople, J. A.; Head-Gordon, M.; Raghavachari, K. *J. Chem. Phys.* **1987**, *87*, 5968.

(30)  Baboul, A. G.; Curtiss, L. A.; Redfern, P. C.; Raghavachari, K. *J. Chem. Phys.* **1999**, *110*, 7650.

(31)  Curtiss, L. A.; Redfern, P. C.; Raghavachari, K.; Rassolov, V.; Pople, J. A. *J. Chem. Phys.* **1999**, *110*, 4703.

(32)  Werner, H. J.; Knowles, P. J.; Lindh, R.; Manby, F. R.; Schütz, M.; Celani, P.; Korona, T.; Rauhut, G.; Amos, R. D.; Bernhardsson, A.; Berning, A.; Cooper, D. L.; Deegan, M. J. O.; Dobbyn, A. J.; Eckert, F.; Hampel, C.; Hetzer, G.; Lloyd, A. W.; McNicholas, S. J.; Meyer, W.; Mura, M. E.; Nicklaß, A.; Palmieri, P.; Pitzer, R.; Schumann, U.; Stoll, H.; Stone, A. J.; Tarroni, R.; Thorsteinsson, T. MOLPRO version (2002.1) Cardiff, UK, **2002**.

(33)  *EPSRC National Service for Computational Chemistry Software (http://www.nsccs.ac.uk)*.

(34)  Schaftenaar, G.; Noordik, J. H. *J. Comput. Aid. Mol. Des.* **2000**, *14*, 123.

(35)  Chang, N. Y.; Yu, C. H. *Chem. Phys. Lett.* **1995**, *242*, 232.

(36)  Clouthier, D. J.; Karolczak, J.; Rae, J.; Chan, W. T.; Goddard, J. D.; Judge, R. H. *J. Chem. Phys.* **1992**, *97*, 1638.

(37)  Judge, R. H.; Moule, D. C.; Biernacki, A.; Benkel, M.; Ross, J. M.; Rustenburg, J. *J. Mol. Spectrosc.* **1986**, *116*, 364.

(38)  Shapley, W. A.; Bacskay, G. B. *J. Phys. Chem. A* **1999**, *103*, 6624.

(39)  East, A. L. L.; Johnson, C. S.; Allen, W. D. *J. Chem. Phys.* **1993**, *98*, 1299.

(40)  Pasinszki, T.; Westwood, N. P. C. *J. Phys. Chem. A* **2001**, *105*, 1244.

(41)  Curtiss, L. A.; Raghavachari, K.; Redfern, P. C.; Pople, J. A. *J. Chem. Phys.* **1997**, *106*, 1063.

(42)  Sengupta, D.; Peeters, J.; Nguyen, M. T. *Chem. Phys. Lett.* **1998**, *283*, 91.

(43)  Carteret, C. *Spectrochim. Acta A* **2006**, *64*, 670.

(44)  Koput, J. *J. Phys. Chem. A* **2000**, *104*, 10017.

(45)  Manson, E. L.; Clark, W. W.; Delucia, F. C.; Gordy, W. *Phys. Rev. A* **1977**, *15*, 223.

(46)  Smeyers, Y. G.; Villa, M.; Cardenas-Jiron, G. I.; Toro-Labbe, A. *THEOCHEM-J. Mol. Struc.* **1998**, *426*, 155.

(47)  Toro-Labbe, A. *THEOCHEM-J. Mol. Struc.* **1988**, *49*, 209.

(48)  Billingsley.J. *Can. J. Phys.* **1972**, *50*, 531.

(49)  Dixon, R. N.; Wright, N. G. *Chem. Phys. Lett.* **1985**, *117*, 280.

(50)  Herzberg, G.; Verma, R. D. *Can. J. Phys.* **1964**, *42*, 395.

(51)  Palmer, M. H.; Nelson, A. D. *J. Mol. Struct.* **2004**, *689*, 161.

(52)  Palmer, M. H.; Guest, M. F. *Chem. Phys. Lett.* **1992**, *196*, 183.

(53)  Koput, J. *Chem. Phys. Lett.* **1996**, *259*, 661.

(54)  Zanchini, C.; Crispini, A. *THEOCHEM-J. Mol. Struc.* **2004**, *682*, 17.

(55)   Hargittai, I.; Paul, I. C. Structural Chemistry of the Cyanates and their Thio Derivatives. In *The Chemistry of Cyanates and their Thio Derivatives*; Patai, S., Ed.; John Wiley & Sons: Chichester, **1977**; Vol. 1; pp 69.

(56)   Glidewel.C; M., S. G.; Robiette, A. G. *Chem. Phys. Lett.* **1972**, *16*, 526.

(57)   Coon, J. B.; Naugle, N. W.; McKenzie, R. D. *J. Mol. Spectrosc.* **1966**, *20*, 107.

(58)   Jones, V. T.; Coon, J. B. *J. Mol. Spectrosc.* **1969**, *31*, 137.

(59)   MATLAB; 7.4.0.287 (R2007a) ed.; The MathWorks, Inc., **2007**.

(60)   Chase, M. W., Jr. *J. Phys. Chem. Ref. Data (Monograph 9)* **1998**.

(61)   Walsh, R. In *The Chemistry of Organic Silicon Compounds*; Patai, S., Rappoport, Z., Eds.; Wiley: Chichester, **1989**.

(62)   Schuurman, M. S.; Muir, S. R.; Allen, W. D.; Schaefer, H. F. *J. Chem. Phys.* **2004**, *120*, 11586.

(63)   Zyrianov, M.; Droz-Georget, T.; Sanov, A.; Reisler, H. *J. Chem. Phys.* **1996**, *105*, 8111.

(64)   Ketvirtis, A. E.; Bohme, D. K.; Hopkinson, A. C. *J. Phys. Chem.* **1995**, *99*, 16121.

(65)   Flores, J. R. *Chem. Phys.* **2005**, *310*, 303.

(66)   Rabalais, J. W.; McDonald, J. R.; McGlynn, S. P. *J. Chem. Phys.* **1969**, *51*, 5095.

(67)   Rabalais, J. W.; McDonald, J. R.; McGlynn, S. P. *J. Chem. Phys.* **1969**, *51*, 5103.

# Chapter Six

*Laser Induced Fluorescence (LIF) and Dispersed Fluorescence (DF) Study of HSiNCO*

## 6.1 Introduction

In Chapter 4, we saw a detailed analysis of the electronic spectrum of HSiNC. This chapter details the first investigation of the $\tilde{A}\,^1A'' - \tilde{X}\,^1A'$ electronic transition of the analogous species, isocyanatosilylene (HSiNCO) using LIF spectroscopy. It is expected that similar properties will be exhibited by this species. In this chapter HSiNCO is examined in detail, looking at the $0_0^0$ band using high resolution LIF spectroscopy to gain accurate spectroscopic constants as well as examining a number of vibrational bands in both the ground and excited electronic states, together with comparison with the *ab initio* results detailed in Chapter 5. HSiNCO has the same potential of being found in the interstellar medium as HSiCN and HSiNC as the cosmic abundance of oxygen is only slightly less than carbon and nitrogen.[1] As discussed in the Chapter 4, it was found that upon excitation from the ground ($\tilde{X}\,^1A'$) to the excited ($\tilde{A}\,^1A''$) state of HSiNC that the H-Si-N angle increases by ~20° giving rise to the observation of forbidden transitions as a result of axis-switching.[1]

In the previous chapter a detailed investigation of the possible isomers of [H, Si, N, C, O] using *ab initio* methods has been carried out to investigate their stability and spectroscopic constants. This work is mentioned later on in this chapter and parts of the data are used for comparison with the experimental results discussed in this chapter.

## 6.2 Experiment

The room temperature vapour of trimethylsilylisocyanate (($CH_3$)$_3$SiNCO, >95%, Fluorochem) was placed in a glass bubbler and a stream of Ar passed through the sample at a pressure of 2 bar. This gas flow was then expanded through a pulsed valve (General Valve, Series 9) into a 3 mm flow channel drilled through a 26 mm long Delrin$^{TM}$ cylinder attached to the end of the pulsed valve. Inside the Delrin$^{TM}$ cylinder are housed two stainless steel ring electrodes separated by a 1 mm spacer positioned such that the discharge occurs along the flow channel. At the appropriate time delay after the pulsed valve has fired, a 4 μs high voltage (2-6 kV) pulse is applied to one of the electrodes, while the other is grounded. By allowing the sample to pass through the discharge the reactive species is created with little disturbance to the flow of the supersonic jet.

The discharge efficiently dissociates the pseudohalosilane precursor into readily detectable amounts of HSiNCO. The pulsed discharge apparatus is mounted near the centre of a vacuum chamber pumped by a large turbo molecular pump. The base pressure of the system is typically around $5 \times 10^{-7}$ torr, rising to about $5 \times 10^{-4}$ torr when the pulsed valve is in operation.

Low ($0.5$ cm$^{-1}$) and medium ($0.12$ cm$^{-1}$) resolution laser induced fluorescence (LIF) spectra were recorded using a 355 nm pumped tuneable pulsed dye laser (Quanta-Ray PDL-3). The laser beam crossed the supersonic expansion approximately 50 mm downstream of the end of the Delrin cylinder mounted on the pulsed valve. The resulting fluorescence was imaged through an appropriate cut-off filter at right angles onto the photocathode of a photomultiplier tube (Electron Tubes B2F/RFI). To maximise light collection, an aluminium coated concave spherical mirror ($D$=50 mm, $EFL$=50 mm) was mounted inside the vacuum chamber directly opposite the fluorescence collection optics.

All spectra were calibrated with lines from a neon-filled hollow cathode lamp and simultaneously recorded etalon fringes (FSR 1.0 cm$^{-1}$). The LIF spectra and calibration signals were digitized on an oscilloscope (LeCroy Waverunner LT342), and captured by a PC using software written in LabVIEW.[2]

High resolution spectra were recorded using a pulsed optical parametric oscillator laser system in the laboratory of Dr C. M. Western at the University of Bristol. The system is briefly described here, but a more detailed description may be found in section 2.4.3 of Chapter 2 and in Ref. [3,4]. The overall linewidth achieved for the OPO was ~0.015 cm$^{-1}$ FWHM. Fluorescence from the intersection of the laser and molecular beams was imaged onto an adjustable slit placed in front of a photomultiplier tube (PMT). The slit was set so that only light from the central core of the jet was collected, to minimize Doppler broadening of the spectra, and a suitable coloured glass filter was put in place to reduce scattered light reaching the detector. The signal from the PMT was recorded via a digital oscilloscope onto a computer. To calibrate the spectra, a portion of the signal wave was directed to a wavemeter (Cluster LM-007 Lambdameter), which measured the absolute signal wavelength; this was recorded simultaneously with the spectrum on the computer.

Single vibronic level (SVL) emission spectra were obtained by fixing the wavelength of the dye laser to the $^PQ_1$ branch of a vibrational band in the LIF spectrum and imaging the resultant fluorescence onto the entrance slit of a 0.5 m scanning monochromator (Acton Research SpectraPro 2500i) fitted with a 1800 lines/mm grating blazed at 500 nm. The wavelength resolved fluorescence signals were detected with an air cooled CCD camera (PI-MAX system), amplified with a gain of 255 and processed using the supplied software (WinSpec32). The monochromator scan was calibrated to an estimated accuracy of $\pm 10$ cm$^{-1}$ using known emission lines from a mercury lamp. This large error is due to the significant drift of the spectrometer over very short time periods. If possible it would be useful to be able to calibrate the spectrometer in tandom with running the experiments, but this was not possible in this study.

## 6.3    *Computational Methods*

As mentioned above, the data contained in Chapter 5 covers a full and detailed theoretical analysis of the isomers of the [H, Si, N, C, O] system. Therefore, the details of the computational results discussed in this chapter have already been covered, but it is important to consider the results of these calculations in this chapter as there is no other comparison data available for the experimental findings discussed here. Briefly, all the calculations were carried out using the Gaussian 03 program package.[5] The geometries of the [H, Si, N, C, O] isomers were fully optimized at different levels of theory using the augmented triple zeta correlated consistent basis set (aug-cc-pVTZ) of Dunning *et al*.[6-8] The methods used include, the hybrid density functional method B3LYP,[9] the 2$^{nd}$ order Møller-Plesset method (MP2)[10-13] and the Quadratic configuration interaction method including singles and doubles, QCISD.[14] Further single-point calculations were carried out using QCISD(T), using the QCISD structure to obtain more accurate energies.[14] Finally the symmetry adapted cluster/configuration interaction (SAC-CI)[15] method was used for determination of accurate structures and transition energies in both the ground and excited states.

## *6.4* *Results and Discussion*

### 6.4.1 Introduction

As discussed in Chapter 5, the [H, Si, N, C, O] system has a variety of isomers which according to the calculations may exist. Since the work contained in this thesis constitutes the first study (experimental or theoretical) of these isomeric species, the first thing that must be considered is how the identity of the spectral carrier of the observed LIF signals may be identified from the variety of possibilities. Therefore, to start with, a comparison between the simulations of the most probable species using the spectral constants obtained from the *ab initio* calculations and the experimentally observed spectrum will be conducted.

Once the identity of the spectral carrier has been established the rest of the chapter will follow a very similar structure to that of Chapter 4, with detailed rotational and vibrational analyses, together with comparison with the high-level *ab initio* data.

### 6.4.2 Identity of the Observed Species

Figure 6.1 shows a low resolution spectrum of what is attributed to be the $0_0^0$ band of the $\tilde{A}'A''$ electronic state of HSiNCO. As can be seen, it bears a strong resemblance to the spectra of the halosilylene species which have been studied previously,[16-18] and to the spectrum of HSiNC discussed in Chapter 4. This resemblance is a good start in identifying the spectral carrier as that of another pseudohalosilylene, in this case HSiNCO; however, much more must be done to satisfy us that this is indeed the species responsible for the observed spectrum. To that end, Figure 6.2 shows simulations of four of the most likely candidates to be formed from the breakdown of the precursor. The rotational constants used to produce these simulations come directly from the *ab initio* calculations given in Chapter 5.
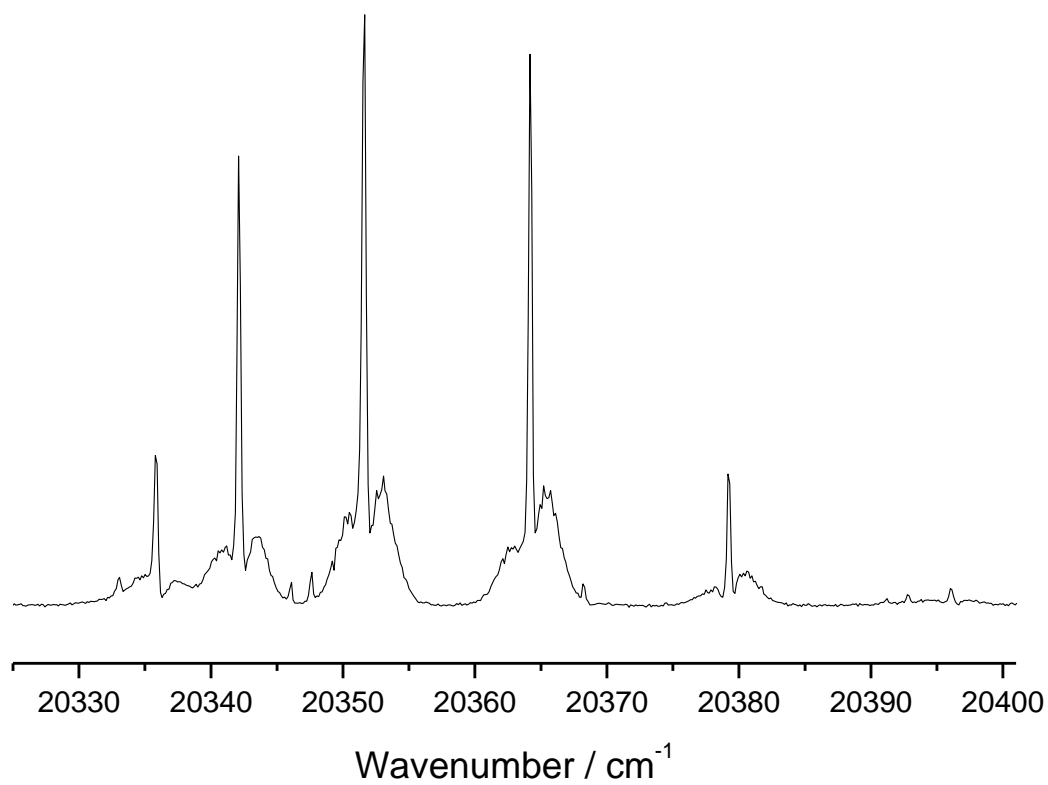
Figure 6.1: A low resolution spectrum of what is attributed to be the $0_0^0$ band of the experimentally observed spectrum
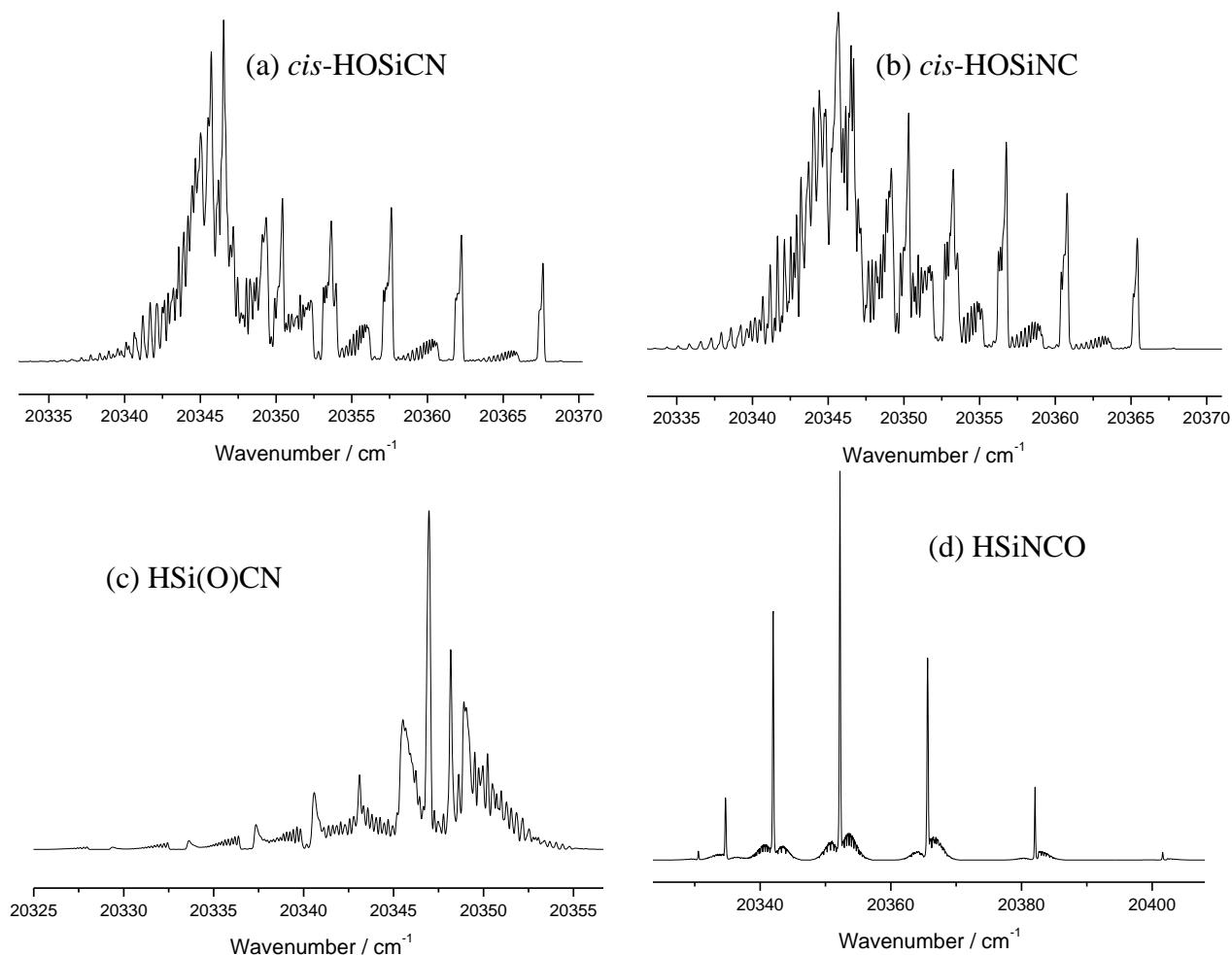
Figure 6.2: Simulations of four of the likely candidates for the spectral carrier of the LIF signal of the experimentally observed spectrum. All simulations are at a temperature of 12 K with a Gaussian linewidth of 0.15 cm$^{-1}$ and a Lorentzian linewidth of 0.05 cm$^{-1}$.

In Figure 6.2: (a) shows the simulation obtained when the rotational constants for the lowest lying calculated isomer are used (S1); (b) shows the simulation for the third lowest lying isomer (S3); (c) shows the simulation for the fifth lowest lying isomer (S5); and (d) shows the simulation for the seventh lowest lying isomer (S7). The nomenclature follows that detailed in Chapter 5. S7 corresponds to the pseudohalosilylene HSiNCO, and as can be seen is the simulation which agrees most favourably with that of the observed spectrum shown in Figure 6.1. It is worth noting that the simulations (a) to (c) are produced using the rotational constants obtained from the planar ($\tilde{X}^1A'$) ground state and the planar ($\tilde{A}^1A''$) excited state, where these excited states gave imaginary vibrations. However, given the obvious differences between the simulations and the experimentally observed spectrum these isomers may be safely disregarded.

Similar simulations of the other singlet and triplet isomers have been carried out, but none of these appear to correspond to the experimentally observed spectrum as closely as that of the S7 isomer.

### 6.4.3 Rotational Analysis

All low and medium resolution spectra were calibrated by a combination of an optogalvanic cell and fringes from an etalon. Details of this are given in section 2.6.2 in Chapter 2, and the calibration was carried out by means of the *DataProcessing_LIFv2.m* MATLAB®[19] program written by the author, a copy of which is given in the addendum. High resolution spectra were calibrated as described in section 6.2, above. The $0_0^0$ band of HSiNCO was studied in more detail by medium and high resolution LIF spectroscopy in order to obtain accurate rotational constants. The medium resolution spectra were recorded using the pulsed dye laser system as detailed in section 2.4 of Chapter 2, and the high resolution spectra were recorded using the optical parametric oscillator (OPO) system described in section 2.4.3 of Chapter 2. Figure 6.3 shows the medium resolution spectrum of the $0_0^0$ band of HSiNCO, with *Q*-branch assignments. The temperature of the spectrum shown is approximately ~12 K. Since the HSiNCO radical species is heavier than the HSiNC radical species covered in the Chapter 4, the degree of rotational structure resolved is significantly less. However, from this spectrum it is clear that, as with HSiNC, anomalous peaks are again present, which may be attributed to axis-switching. The assignment of these peaks is much clearer than before, as the level of contamination in the spectra recorded for HSiNCO is significantly less than that observed for HSiNC. The peaks attributed to axis-switching are marked with asterisks in Figure 6.3, and a discussion of these peaks is given in section 6.4.4. The level of resolution achieved in this case is not suitable and therefore, this species has been investigated further at high resolution using the OPO system in the laboratory of Colin Western at the University of Bristol.
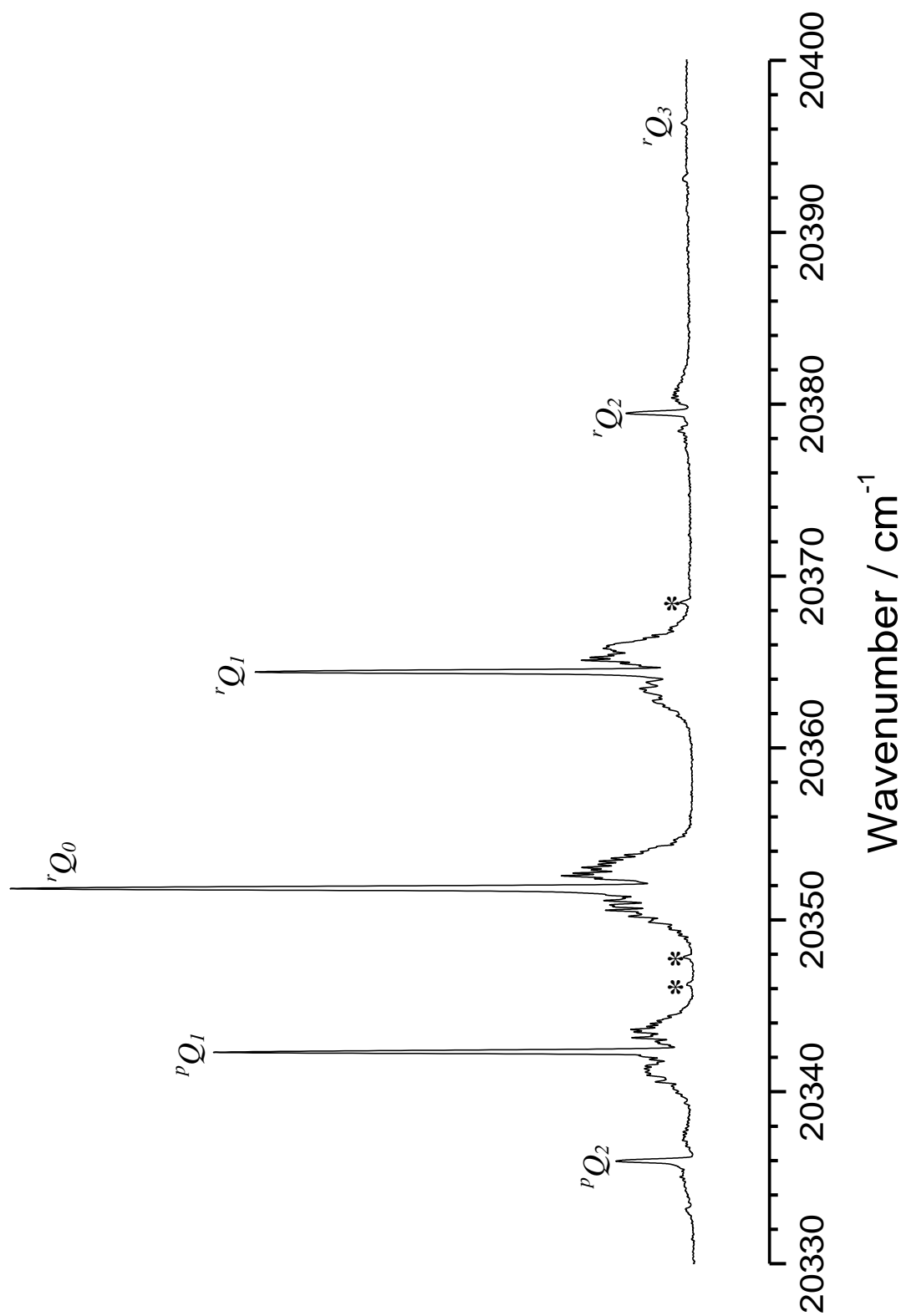
Figure 6.3: The medium resolution spectrum of the $0_0^0$ band of HSiNCO showing $Q$- branch assignments. The peaks marked with asterisks denote axis-switching peaks. The degree of rotational resolution here is not sufficient for accurate determination of rotational constants. The temperature of the spectrum is approximately 12 K.

The use of a high resolution system to study this species brings with it a new set of problems. Chiefly, the intensity of the transitions using the high resolution system is significantly lower. Therefore, the LIF signal is more difficult to monitor for the weaker sub-bands of the $0_0^0$ band. This also means that detection of the axis-switching peaks is not possible. Only the $0_0^0$ band has been investigated at high resolution, and this is purely due to the time constraints of the project carried out in Bristol.

The linewidth of the high resolution system (~0.015 cm$^{-1}$) is an order of magnitude better than the medium resolution system affording almost full rotational resolution of the $Q$-branches for the strongest sub-bands. The high resolution spectra also reveal asymmetric splittings which were not apparent in the medium resolution spectra. These appear in the $P$ and $R$-branch structure of the sub-bands centred around the $^PQ_2$ and $^rQ_1$ branches as shown in Figures 6.4 and 6.5, respectively. Figure 6.6 shows the resolved $^rQ_0$-branch to give an indication of the high resolution achieved.

As with HSiNC in Chapter 4, the $0_0^0$ band of the HSiNCO spectrum was fitted using Colin Western's spectral fitting program PGOPHER.[20] In the HSiNCO spectrum, transitions with $K_a$= 0, 1 and 2 in the ground state and $K_a$= 0-3 in the excited state were assigned with $J''$ values up to 23 for the strongest branches. Where the intensity of the LIF signal was strong enough to achieve good rotational resolution of the $Q$-branches, these lines were included in the fit. In cases where there was a degree of uncertainty in the assignments (due to lines being overlapped or not fully resolved), care was taken to weight them suitably. In PGOPHER, the weight given to a line is the standard deviation of the measured peak position. If the weight is given a value of one it indicates that this line is good. For less certain measurements larger values are used. In SPFIT the error limit is set to a suitable value and the program automatically weights lines appropriately. In this case the limit of a 'good' line was if the error associated with it was <0.003 cm$^{-1}$.

As in Chapter 4, once the assignments were complete, the rotational constants were determined using least-squares fitting of Watson's $A$ reduction of the asymmetric top rotational Hamiltonian.[21] The Hamiltonian takes form given in Equations [2.1 and 2.3] in Chapter 2. In this Hamiltonian the model parameters follow the conventional

spectroscopic notation, showing the rotational constants ($A$, $B$, $C$), as well as the quartic centrifugal distortion constants ($\Delta_J$, $\Delta_{JK}$, $\Delta_K$, $\delta_J$, $\delta_K$) shown explicitly. In this case the inclusion of the quartic terms provides an adequate fit of the data.

As discussed previously, the choice of the representation for fitting the rotational constants is crucial in order to obtain a good fit. The rotational constants determined by *ab initio* calculation may be substituted into Equation [2.1] in section 2.7.2 of Chapter 2 to obtain a value for Ray's asymmetry parameter, $\kappa$, of -0.99894. As with HSiNC in Chapter 4, the $I^r$ representation should therefore be used as Ray's asymmetry parameter, $\kappa$, takes a value very near -1 corresponding to the near prolate limit of an asymmetric top. In all cases, the overall standard deviation of the fit was comparable to the estimated uncertainties in the measurements. The resulting constants for the ground state are given in Table 6.1, and Table 6.2 gives the excited state constants obtained from this work. In both cases the constants obtained from the *ab initio* work carried out in Chapter 5 are given for comparison. The correlation matrix for this fit may be found in Appendix C.

To assess the validity of this fit, further work was carried out to obtain accurate rotational constants, by carrying out both ground and excited state combination differences. This allows the fitting of the constants without the dependence on the excited state for ground state combination differences (GSCDs), and *vice versa* for the excited state combination differences (ESCDs). This should allow us to examine the accuracy of the constants determined in the global fit. In total 167 lines were used in the GSCD fit and 199 lines were used in the ESCD fit using the same weighting criteria as used in the global fit. The fitting of these lines was carried out using Herb Pickett's spectral fitting program SPFIT.[22] The resulting parameters may be found together with the parameters determined by the global fit in Tables 6.3 and 6.4, respectively. Table 6.5 lists the lines used to produce these fits.
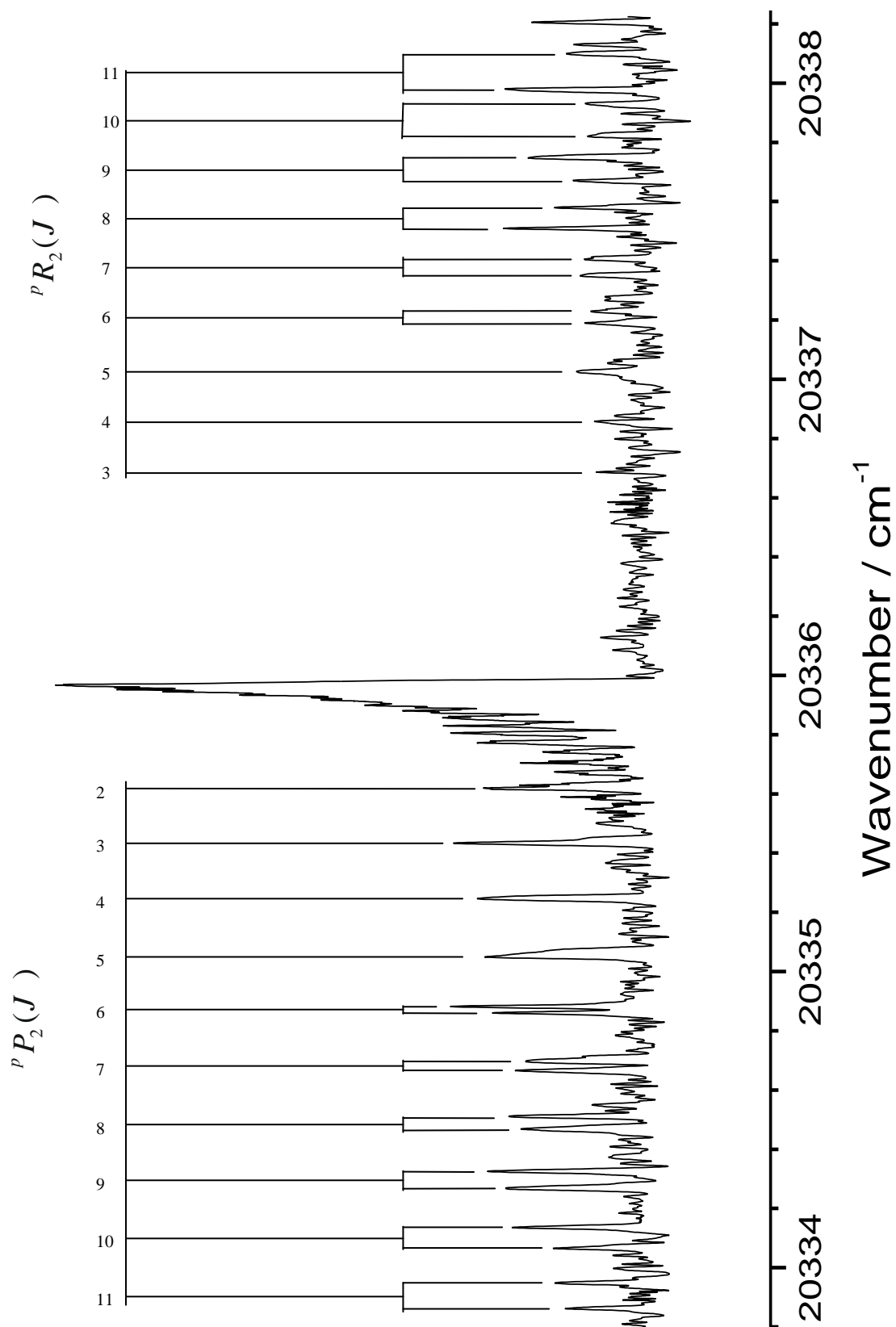
Figure 6.4: A portion of the high resolution spectrum of the LIF spectrum of the $0_0^0$ band of HSiNCO. Shown here is the sub-band centred around the $^PQ_2$ branch, showing asymmetric splittings and partial resolution of the $Q$-branch.
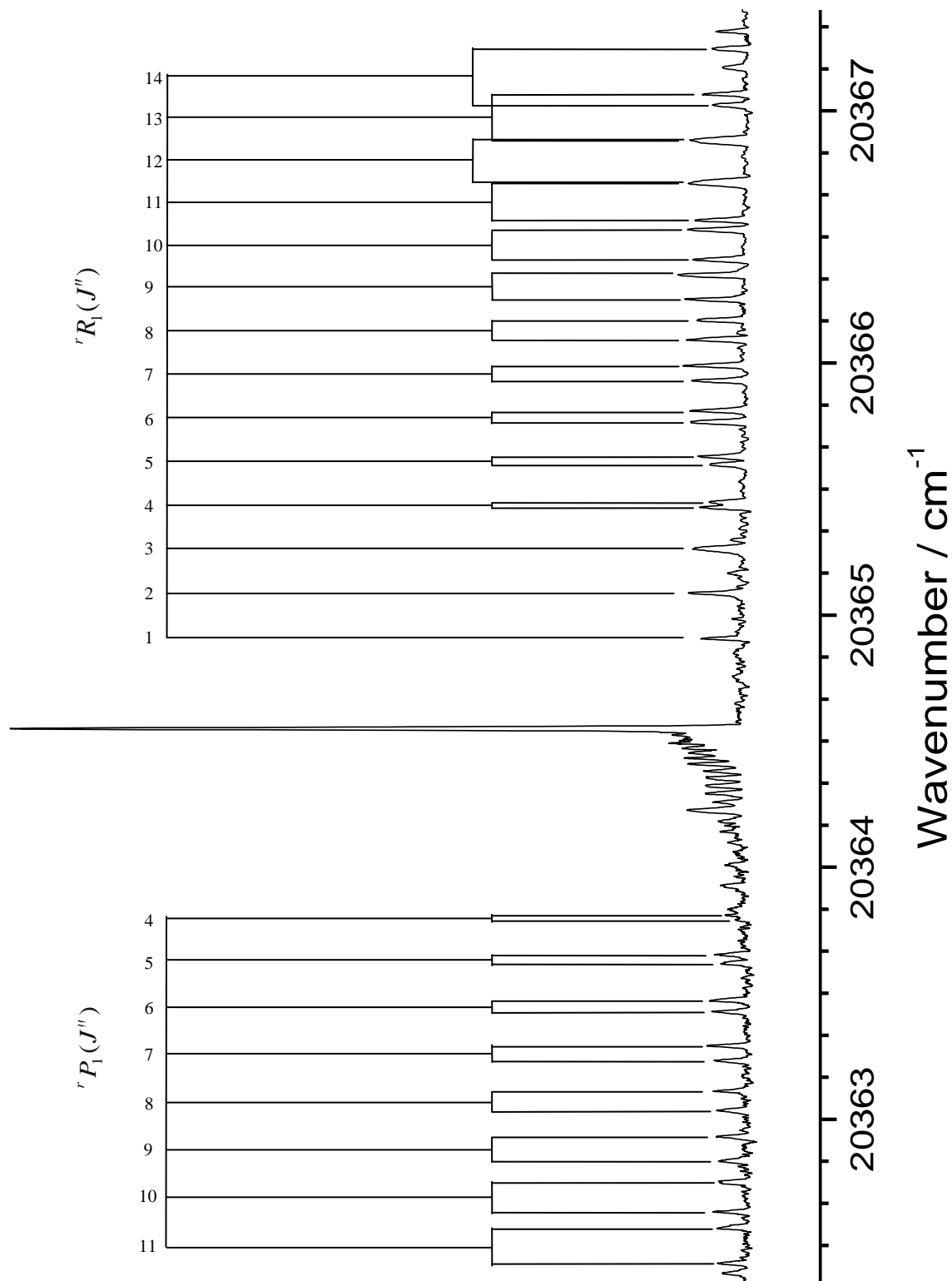
Figure 6.5: A portion of the high resolution spectrum of the LIF spectrum of the $0_0^0$ band of HSiNCO. Shown here is the sub-band centred around the $^rQ_1$ branch, showing asymmetric splittings and partial resolution of the $Q$-branch.
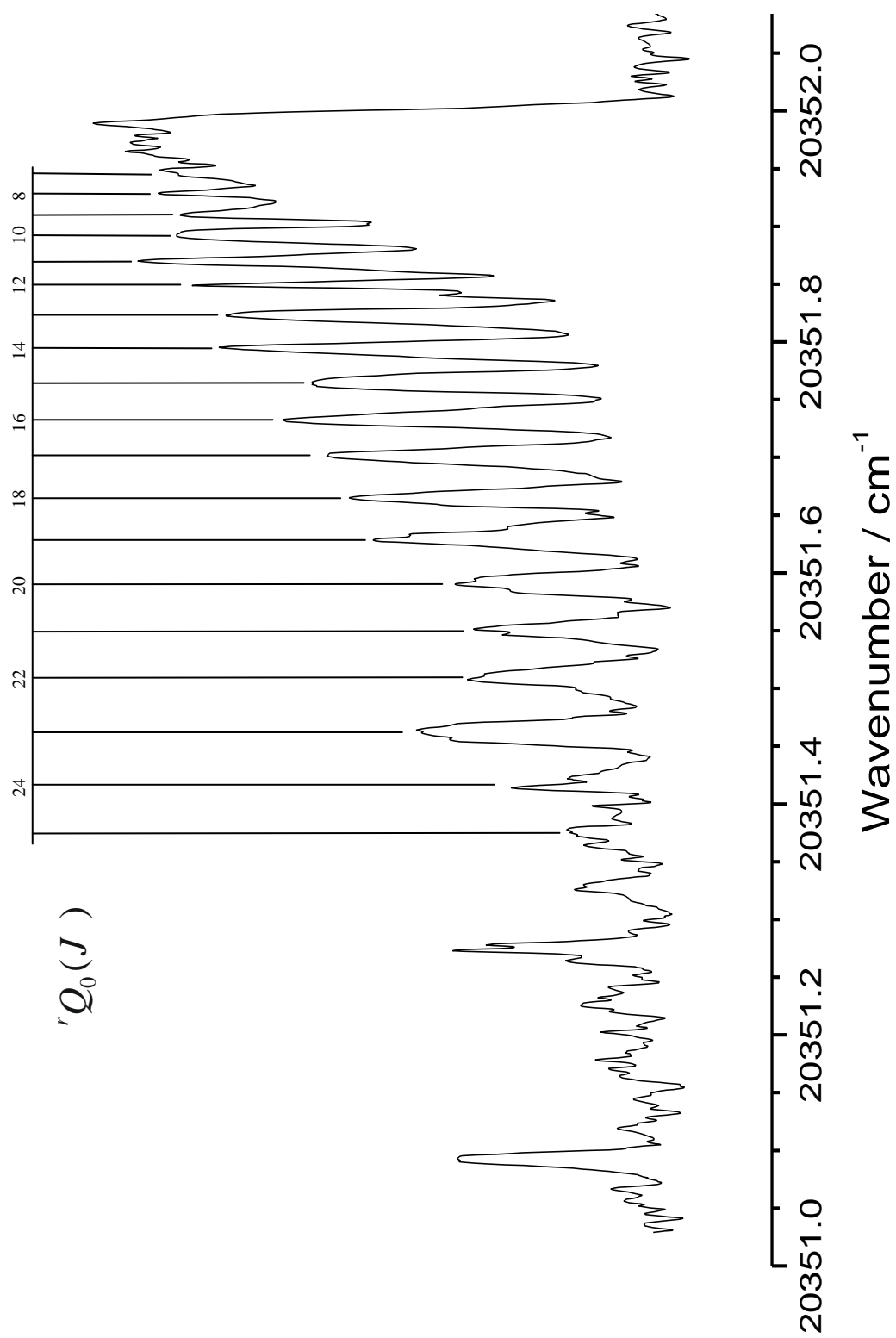
Figure 6.6: A portion of the high resolution spectrum of the LIF spectrum of the $0_0^0$ band of HSiNCO. Shown here is the sub-band centred around the $^rQ_0$ branch.

Table 6.1: The ground state rotational constants (cm$^{-1}$) for the $0_0^0$ band of the $\tilde{A}^1 A'' - \tilde{X}^1 A'$ transition of HSiNCO obtained from the global fit.

| Constant | $0_0^0$ (this work)[a] | Ab initio (this work)[c] |
|---|---|---|
| $A$………………………. | 4.13160(41) | 4.4756 |
| $B$………………………. | 0.0915068(23) | 0.0896 |
| $C$………………………. | 0.0893388(22) | 0.0879 |
| $\Delta_J \times 10^8$………………….. | -1.81(56) | - |
| $\Delta_{JK} \times 10^5$………………….. | -3.18(15) | - |
| $\Delta_K$…………………….. | 0.011667(43) | - |
| $\delta_K \times 10^8$………………….. | -1.3(11) | - |
| Std. Dev.[b]……………….... | 0.0014 | - |
| No. of fitted transitions….. | 228 | - |

[a] Numbers in parentheses are 1 $\sigma$ uncertainties in units of the last significant digit
[b] Overall standard deviation of fit (in cm$^{-1}$)
[c] Calculated at the MP2(FC) level of theory using the aug-cc-pVTZ basis set

Table 6.2: The excited state rotational constants (cm$^{-1}$) for the $0_0^0$ band of the $\tilde{A}^1 A'' - \tilde{X}^1 A'$ transition of HSiNCO obtained from the global fit.

| Constant | $0_0^0$ (this work)[a] | Ab initio (this work)[c] |
|---|---|---|
| $A$…………………………. | 5.72390(27) | 6.0116 |
| $B$…………………………. | 0.0905619(21) | 0.0894 |
| $C$…………………………. | 0.0890147(22) | 0.0880 |
| $\Delta_J \times 10^8$………………….. | -4.22(54) | - |
| $\Delta_{JK} \times 10^5$………………….. | -2.88(13) | - |
| $\Delta_K$…………………….. | 0.018353(30) | - |
| $\delta_K \times 10^9$………………….. | -9.4(48) | - |
| $T_0$…………………………. | 20346.33915(67) | 16386.57 |
| Std. Dev.[b]……………….... | 0.0014 | - |
| No. of fitted transitions….. | 228 | - |

[a] Numbers in parentheses are 1 $\sigma$ uncertainties in units of the last significant digit
[b] Overall standard deviation of fit (in cm$^{-1}$)
[c] Calculated at the MP2(FC) level of theory using the aug-cc-pVTZ basis set

Table 6.3: Comparison of ground state rotational constants (cm$^{-1}$) for the $0_0^0$ band of the $\tilde{A}^1A''-\tilde{X}^1A'$ transition of HSiNCO obtained from the global fit and a fit of ground state combination differences.

| Constant | $0_0^0$ (global fit)[a] | $0_0^0$ (GSCD fit)[a] |
|---|---|---|
| $A$…………………….. | 4.13160(41) | 4.12680(21) |
| $B$…………………….. | 0.0915068(23) | 0.0914125(73) |
| $C$…………………….. | 0.0893388(22) | 0.0893389(74) |
| $\Delta_J \times 10^8$………………….. | -1.81(56) | -1.81[c] |
| $\Delta_{JK} \times 10^5$………….……… | -3.18(15) | -3.09(88) |
| $\Delta_K$…………………….... | 0.011667(43) | 0.01175(18) |
| $\delta_K \times 10^9$………………….. | -1.3(11) | -1.3[c] |
| Std. Dev.[b]………………... | 0.0014 | 0.0023 |
| No. of fitted transitions….. | 228 | 167 |

[a] Numbers in parentheses are 1 σ uncertainties in units of the last significant digit
[b] Overall standard deviation of fit (in cm$^{-1}$)
[c] Fixed to values obtained from the global fit

Table 6.4: Comparison of the excited state rotational constants (cm$^{-1}$) for the $0_0^0$ band of the $\tilde{A}^1A''-\tilde{X}^1A'$ transition of HSiNCO obtained from the global fit and a fit of excited state combination differences.

| Constant | $0_0^0$ (global fit)[a] | $0_0^0$ (ESCD fit)[a] |
|---|---|---|
| $A$………………….............. | 5.72390(27) | 5.7164(12) |
| $B$…………………............. | 0.0905619(21) | 0.090432(95) |
| $C$…………………............... | 0.0890147(22) | 0.088882(95) |
| $\Delta_J \times 10^8$………………….. | -4.22(54) | -8.66(24) |
| $\Delta_{JK} \times 10^5$………………… | -2.88(13) | -2.821(55) |
| $\Delta_K$…………………….. | 0.018353(30) | 0.01856(12) |
| $\delta_K \times 10^9$………………….. | -9.4(48) | -9.4[c] |
| $T_0$………………………... | 20346.33915(67) | - |
| Std. Dev.[b]………………... | 0.0014 | 0.0019 |
| No. of fitted transitions…. | 228 | 199 |

[a] Numbers in parentheses are 1 σ uncertainties in units of the last significant digit
[b] Overall standard deviation of fit (in cm$^{-1}$)
[c] Fixed to the value obtained from the global fit

Table 6.5: Observed transition frequencies (in cm$^{-1}$) for the $\tilde{A}^1A'' - \tilde{X}^1A'$ transition of the $0_0^0$ band HSiNCO used for the global fit of the rotational parameters.

| Transition ($J'_{K_aK_c} - J''_{K_aK_c}$) | Observed | Calculated | $O-C$ | Weight |
|---|---|---|---|---|
| $9_{28} - 10_{38}$ | 20331.2646 | 20331.2697 | -0.0051 | 4 |
| $9_{27} - 10_{37}$ | 20331.2646 | 20331.2699 | -0.0053 | 4 |
| $8_{26} - 9_{36}$ | 20331.4643 | 20331.4657 | -0.0014 | 2 |
| $8_{27} - 9_{37}$ | 20331.4643 | 20331.4656 | -0.0013 | 2 |
| $7_{25} - 8_{35}$ | 20331.6576 | 20331.6600 | -0.0024 | 2 |
| $7_{26} - 8_{36}$ | 20331.6576 | 20331.6599 | -0.0023 | 2 |
| $6_{24} - 7_{34}$ | 20331.8507 | 20331.8526 | -0.0019 | 2 |
| $6_{25} - 7_{35}$ | 20331.8507 | 20331.8526 | -0.0019 | 2 |
| $19_{1\,19} - 20_{2\,19}$ | 20331.9309 | 20331.9306 | 0.0003 | 2 |
| $5_{23} - 6_{33}$ | 20332.0425 | 20332.0437 | -0.0012 | 2 |
| $5_{24} - 6_{34}$ | 20332.0425 | 20332.0437 | -0.0012 | 2 |
| $18_{1\,18} - 19_{2\,18}$ | 20332.1551 | 20332.1539 | 0.0012 | 1 |
| $4_{22} - 5_{32}$ | 20332.2295 | 20332.2332 | -0.0037 | 1 |
| $4_{23} - 5_{33}$ | 20332.2295 | 20332.2331 | -0.0036 | 2 |
| $17_{1\,17} - 18_{2\,17}$ | 20332.3740 | 20332.3751 | -0.0011 | 1 |
| $3_{21} - 4_{31}$ | 20332.4202 | 20332.4210 | -0.0008 | 2 |
| $3_{22} - 4_{32}$ | 20332.4202 | 20332.4210 | -0.0008 | 2 |
| $2_{20} - 3_{30}$ | 20332.6059 | 20332.6073 | -0.0014 | 2 |
| $2_{21} - 3_{31}$ | 20332.6059 | 20332.6073 | -0.0014 | 2 |
| $2_{20} - 3_{30}$ | 20332.6070 | 20332.6073 | -0.0003 | 2 |
| $2_{21} - 3_{31}$ | 20332.6070 | 20332.6073 | -0.0003 | 2 |
| $16_{1\,15} - 17_{2\,15}$ | 20332.8039 | 20332.8036 | 0.0003 | 1 |
| $15_{1\,15} - 16_{2\,15}$ | 20332.8078 | 20332.8109 | -0.0031 | 2 |
| $16_{1\,15} - 17_{2\,15}$ | 20332.8078 | 20332.8036 | 0.0042 | 3 |
| $7_{25} - 7_{35}$ | 20333.1126 | 20333.1114 | 0.0012 | 2 |
| $7_{26} - 7_{34}$ | 20333.1126 | 20333.1113 | 0.0013 | 2 |
| $6_{24} - 6_{34}$ | 20333.1126 | 20333.1226 | -0.0100 | 5 |
| $6_{25} - 6_{33}$ | 20333.1126 | 20333.1225 | -0.0099 | 5 |
| $14_{1\,13} - 15_{2\,13}$ | 20333.1880 | 20333.1874 | 0.0006 | 1 |
| $13_{1\,13} - 14_{2\,13}$ | 20333.2396 | 20333.2378 | 0.0018 | 1 |
| $13_{1\,12} - 14_{2\,12}$ | 20333.3784 | 20333.3782 | 0.0002 | 1 |
| $12_{1\,12} - 13_{2\,12}$ | 20333.4474 | 20333.4480 | -0.0006 | 1 |
| $12_{1\,11} - 13_{2\,11}$ | 20333.5703 | 20333.5683 | 0.0020 | 1 |
| $11_{1\,11} - 12_{2\,11}$ | 20333.6578 | 20333.6559 | 0.0019 | 1 |
| $11_{1\,10} - 12_{2\,10}$ | 20333.7589 | 20333.7578 | 0.0011 | 1 |
| $10_{1\,10} - 11_{2\,10}$ | 20333.8635 | 20333.8616 | 0.0019 | 1 |
| $10_{1\,9} - 11_{2\,9}$ | 20333.9490 | 20333.9465 | 0.0025 | 1 |
| $9_{1\,9} - 10_{2\,9}$ | 20334.0643 | 20334.0651 | -0.0008 | 1 |
| $9_{1\,8} - 10_{2\,8}$ | 20334.1361 | 20334.1346 | 0.0015 | 1 |
| $8_{1\,8} - 9_{2\,8}$ | 20334.2683 | 20334.2663 | 0.0020 | 1 |

Table 6.5 (cont.)

| | | | | |
|---|---|---|---|---|
| $8_{1\,7}-9_{2\,7}$ | 20334.3255 | 20334.3220 | 0.0035 | 2 |
| $7_{1\,7}-8_{2\,7}$ | 20334.4652 | 20334.4653 | -0.0001 | 1 |
| $7_{1\,6}-8_{2\,6}$ | 20334.5118 | 20334.5086 | 0.0032 | 2 |
| $6_{1\,6}-7_{2\,6}$ | 20334.6656 | 20334.6621 | 0.0035 | 2 |
| $6_{1\,5}-7_{2\,5}$ | 20334.6986 | 20334.6946 | 0.0040 | 3 |
| $5_{1\,5}-6_{2\,5}$ | 20334.8602 | 20334.8567 | 0.0035 | 2 |
| $5_{1\,4}-6_{2\,4}$ | 20334.8821 | 20334.8798 | 0.0023 | 1 |
| $3_{1\,2}-4_{2\,2}$ | 20335.2468 | 20335.2483 | -0.0015 | 1 |
| $3_{1\,3}-4_{2\,3}$ | 20335.2468 | 20335.2390 | 0.0078 | 5 |
| $2_{1\,1}-3_{2\,1}$ | 20335.4339 | 20335.4315 | 0.0024 | 1 |
| $2_{1\,2}-3_{2\,2}$ | 20335.4339 | 20335.4268 | 0.0071 | 5 |
| $11_{1\,10}-10_{2\,8}$ | 20337.9282 | 20337.9235 | 0.0047 | 3 |
| $12_{1\,12}-11_{2\,10}$ | 20337.9780 | 20337.9759 | 0.0021 | 1 |
| $20_{0\,20}-21_{1\,20}$ | 20337.9780 | 20337.9834 | -0.0054 | 4 |
| $18_{0\,18}-19_{1\,18}$ | 20338.4345 | 20338.4406 | -0.0061 | 5 |
| $15_{1\,15}-14_{2\,13}$ | 20338.4345 | 20338.4258 | 0.0087 | 5 |
| $17_{0\,17}-18_{1\,17}$ | 20338.6611 | 20338.6657 | -0.0046 | 3 |
| $15_{0\,15}-16_{1\,15}$ | 20339.1023 | 20339.1087 | -0.0064 | 5 |
| $12_{0\,12}-13_{1\,12}$ | 20339.7502 | 20339.7556 | -0.0054 | 4 |
| $7_{0\,7}-8_{1\,7}$ | 20340.7811 | 20340.7861 | -0.0050 | 4 |
| $6_{0\,6}-7_{1\,6}$ | 20340.9804 | 20340.9850 | -0.0046 | 3 |
| $5_{0\,5}-6_{1\,5}$ | 20341.1791 | 20341.1814 | -0.0023 | 1 |
| $4_{0\,4}-5_{1\,4}$ | 20341.3702 | 20341.3755 | -0.0053 | 4 |
| $3_{0\,3}-4_{1\,3}$ | 20341.5629 | 20341.5672 | -0.0043 | 3 |
| $2_{0\,2}-3_{1\,2}$ | 20341.7527 | 20341.7564 | -0.0037 | 2 |
| $1_{0\,1}-2_{1\,1}$ | 20341.9393 | 20341.9432 | -0.0039 | 2 |
| $2_{0\,2}-1_{1\,0}$ | 20342.6641 | 20342.6664 | -0.0023 | 1 |
| $3_{0\,3}-2_{1\,1}$ | 20342.8371 | 20342.8411 | -0.0040 | 3 |
| $4_{0\,4}-3_{1\,2}$ | 20343.0085 | 20343.0135 | -0.0050 | 4 |
| $5_{0\,5}-4_{1\,3}$ | 20343.1818 | 20343.1834 | -0.0016 | 1 |
| $7_{0\,7}-6_{1\,5}$ | 20343.5138 | 20343.5160 | -0.0022 | 1 |
| $8_{0\,8}-7_{1\,6}$ | 20343.6743 | 20343.6787 | -0.0044 | 3 |
| $9_{0\,9}-8_{1\,7}$ | 20343.8345 | 20343.8390 | -0.0045 | 3 |
| $10_{0\,10}-9_{1\,8}$ | 20343.9915 | 20343.9969 | -0.0054 | 4 |
| $11_{0\,11}-10_{1\,9}$ | 20344.1483 | 20344.1525 | -0.0042 | 3 |
| $12_{0\,12}-11_{1\,10}$ | 20344.3047 | 20344.3056 | -0.0009 | 1 |
| $13_{0\,13}-12_{1\,11}$ | 20344.4522 | 20344.4564 | -0.0042 | 3 |
| $14_{0\,14}-13_{1\,12}$ | 20344.6042 | 20344.6048 | -0.0006 | 1 |
| $15_{0\,15}-14_{1\,13}$ | 20344.7455 | 20344.7508 | -0.0053 | 4 |
| $19_{1\,18}-20_{0\,20}$ | 20348.2634 | 20348.2637 | -0.0003 | 1 |
| $18_{1\,17}-19_{0\,19}$ | 20348.4518 | 20348.4512 | 0.0006 | 1 |
| $17_{1\,16}-18_{0\,18}$ | 20348.6385 | 20348.6385 | 0.0000 | 1 |
| $15_{1\,14}-16_{0\,16}$ | 20349.0130 | 20349.0124 | 0.0006 | 1 |
| $14_{1\,13}-15_{0\,15}$ | 20349.1991 | 20349.1990 | 0.0001 | 1 |
| $13_{1\,12}-14_{0\,14}$ | 20349.3871 | 20349.3853 | 0.0018 | 1 |

Table 6.5 (cont.)

| | | | | |
|---|---|---|---|---|
| $12_{1\,11} - 13_{0\,13}$ | 20349.5735 | 20349.5713 | 0.0022 | 1 |
| $11_{1\,10} - 12_{0\,12}$ | 20349.7584 | 20349.7570 | 0.0014 | 1 |
| $10_{1\,9} - 11_{0\,11}$ | 20349.9434 | 20349.9423 | 0.0011 | 1 |
| $9_{1\,8} - 10_{0\,10}$ | 20350.1302 | 20350.1273 | 0.0029 | 1 |
| $8_{1\,7} - 9_{0\,9}$ | 20350.3142 | 20350.3119 | 0.0023 | 1 |
| $7_{1\,6} - 8_{0\,8}$ | 20350.4989 | 20350.4961 | 0.0028 | 1 |
| $6_{1\,5} - 7_{0\,7}$ | 20350.6825 | 20350.6799 | 0.0026 | 1 |
| $5_{1\,4} - 6_{0\,6}$ | 20350.8653 | 20350.8633 | 0.0020 | 1 |
| $4_{1\,3} - 5_{0\,5}$ | 20351.0504 | 20351.0463 | 0.0041 | 3 |
| $3_{1\,2} - 4_{0\,4}$ | 20351.2316 | 20351.2289 | 0.0027 | 1 |
| $22_{1\,22} - 22_{0\,22}$ | 20351.4668 | 20351.4674 | -0.0006 | 1 |
| $21_{1\,21} - 21_{0\,21}$ | 20351.5083 | 20351.5086 | -0.0003 | 1 |
| $20_{1\,20} - 20_{0\,20}$ | 20351.5492 | 20351.5482 | 0.0010 | 1 |
| $19_{1\,19} - 19_{0\,19}$ | 20351.5876 | 20351.5860 | 0.0016 | 1 |
| $18_{1\,18} - 18_{0\,18}$ | 20351.6227 | 20351.6222 | 0.0005 | 1 |
| $17_{1\,17} - 17_{0\,17}$ | 20351.6590 | 20351.6566 | 0.0024 | 1 |
| $16_{1\,16} - 16_{0\,16}$ | 20351.6899 | 20351.6892 | 0.0007 | 1 |
| $15_{1\,15} - 15_{0\,15}$ | 20351.7223 | 20351.7200 | 0.0023 | 1 |
| $14_{1\,14} - 14_{0\,14}$ | 20351.7524 | 20351.7490 | 0.0034 | 2 |
| $13_{1\,13} - 13_{0\,13}$ | 20351.7809 | 20351.7762 | 0.0047 | 3 |
| $11_{1\,11} - 11_{0\,11}$ | 20351.8276 | 20351.8249 | 0.0027 | 1 |
| $10_{1\,10} - 10_{0\,10}$ | 20351.8508 | 20351.8464 | 0.0044 | 3 |
| $9_{1\,9} - 9_{0\,9}$ | 20351.8689 | 20351.8660 | 0.0029 | 1 |
| $8_{1\,8} - 8_{0\,8}$ | 20351.8860 | 20351.8837 | 0.0023 | 1 |
| $2_{1\,1} - 1_{0\,1}$ | 20352.3181 | 20352.3153 | 0.0028 | 1 |
| $3_{1\,2} - 2_{0\,2}$ | 20352.4990 | 20352.4948 | 0.0042 | 3 |
| $4_{1\,3} - 3_{0\,3}$ | 20352.6761 | 20352.6739 | 0.0022 | 1 |
| $5_{1\,4} - 4_{0\,4}$ | 20352.8577 | 20352.8526 | 0.0051 | 4 |
| $6_{1\,5} - 5_{0\,5}$ | 20353.0360 | 20353.0309 | 0.0051 | 4 |
| $7_{1\,6} - 6_{0\,6}$ | 20353.2129 | 20353.2087 | 0.0042 | 3 |
| $8_{1\,7} - 7_{0\,7}$ | 20353.3899 | 20353.3862 | 0.0037 | 2 |
| $9_{1\,8} - 8_{0\,8}$ | 20353.5657 | 20353.5632 | 0.0025 | 1 |
| $10_{1\,9} - 9_{0\,9}$ | 20353.7428 | 20353.7399 | 0.0029 | 1 |
| $12_{1\,11} - 11_{0\,11}$ | 20354.0961 | 20354.0922 | 0.0039 | 3 |
| $13_{2\,11} - 14_{1\,13}$ | 20361.8049 | 20361.8073 | -0.0024 | 1 |
| $14_{2\,13} - 15_{1\,15}$ | 20361.8509 | 20361.8540 | -0.0031 | 2 |
| $13_{2\,12} - 14_{1\,14}$ | 20362.0253 | 20362.0339 | -0.0086 | 5 |
| $11_{2\,10} - 12_{1\,12}$ | 20362.3892 | 20362.3937 | -0.0045 | 3 |
| $10_{2\,8} - 11_{1\,10}$ | 20362.4297 | 20362.4309 | -0.0012 | 1 |
| $10_{2\,9} - 11_{1\,11}$ | 20362.5702 | 20362.5736 | -0.0034 | 2 |
| $9_{2\,7} - 10_{1\,9}$ | 20362.6327 | 20362.6345 | -0.0018 | 1 |
| $9_{2\,8} - 10_{1\,10}$ | 20362.7500 | 20362.7535 | -0.0035 | 2 |
| $8_{2\,6} - 9_{1\,8}$ | 20362.8355 | 20362.8360 | -0.0005 | 1 |
| $8_{2\,7} - 9_{1\,9}$ | 20362.9322 | 20362.9334 | -0.0012 | 1 |
| $7_{2\,5} - 8_{1\,7}$ | 20363.0359 | 20363.0354 | 0.0005 | 1 |

Table 6.5 (cont.)

| | | | | |
|---|---|---|---|---|
| $7_{2\,6} - 8_{1\,8}$ | 20363.1121 | 20363.1134 | -0.0013 | 1 |
| $6_{2\,4} - 7_{1\,6}$ | 20363.2318 | 20363.2326 | -0.0008 | 1 |
| $6_{2\,5} - 7_{1\,7}$ | 20363.2914 | 20363.2933 | -0.0019 | 1 |
| $5_{2\,3} - 6_{1\,5}$ | 20363.4270 | 20363.4277 | -0.0007 | 1 |
| $5_{2\,4} - 6_{1\,6}$ | 20363.4719 | 20363.4732 | -0.0013 | 1 |
| $4_{2\,2} - 5_{1\,4}$ | 20363.6186 | 20363.6206 | -0.0020 | 1 |
| $4_{2\,3} - 5_{1\,5}$ | 20363.6541 | 20363.6531 | 0.0010 | 1 |
| $3_{2\,1} - 4_{1\,3}$ | 20363.8081 | 20363.8113 | -0.0032 | 2 |
| $3_{2\,2} - 4_{1\,4}$ | 20363.8335 | 20363.8330 | 0.0005 | 1 |
| $2_{2\,1} - 3_{1\,3}$ | 20364.0088 | 20364.0129 | -0.0041 | 3 |
| $22_{2\,21} - 22_{1\,21}$ | 20364.0088 | 20364.0049 | 0.0039 | 2 |
| $21_{2\,20} - 21_{1\,20}$ | 20364.0540 | 20364.0521 | 0.0019 | 1 |
| $20_{2\,19} - 20_{1\,19}$ | 20364.0993 | 20364.0972 | 0.0021 | 1 |
| $19_{2\,18} - 19_{1\,18}$ | 20364.1409 | 20364.1402 | 0.0007 | 1 |
| $18_{2\,17} - 18_{1\,17}$ | 20364.1839 | 20364.1811 | 0.0028 | 1 |
| $16_{2\,15} - 16_{1\,15}$ | 20364.2578 | 20364.2567 | 0.0011 | 1 |
| $15_{2\,14} - 15_{1\,14}$ | 20364.2934 | 20364.2914 | 0.0020 | 1 |
| $14_{2\,13} - 14_{1\,13}$ | 20364.3244 | 20364.3239 | 0.0005 | 1 |
| $13_{2\,12} - 13_{1\,12}$ | 20364.3562 | 20364.3542 | 0.0020 | 1 |
| $12_{2\,11} - 12_{1\,11}$ | 20364.3822 | 20364.3824 | -0.0002 | 1 |
| $11_{2\,10} - 11_{1\,10}$ | 20364.4091 | 20364.4085 | 0.0006 | 1 |
| $10_{2\,9} - 10_{1\,9}$ | 20364.4329 | 20364.4325 | 0.0004 | 1 |
| $9_{2\,8} - 9_{1\,8}$ | 20364.4545 | 20364.4542 | 0.0003 | 1 |
| $2_{2\,0} - 1_{1\,0}$ | 20364.9074 | 20364.9099 | -0.0025 | 1 |
| $2_{2\,1} - 1_{1\,1}$ | 20364.9074 | 20364.9120 | -0.0046 | 3 |
| $3_{2\,1} - 2_{1\,1}$ | 20365.0869 | 20365.0853 | 0.0016 | 1 |
| $3_{2\,2} - 2_{1\,2}$ | 20365.0869 | 20365.0918 | -0.0049 | 3 |
| $4_{2\,2} - 3_{1\,2}$ | 20365.2632 | 20365.2586 | 0.0046 | 3 |
| $5_{2\,3} - 4_{1\,3}$ | 20365.4276 | 20365.4297 | -0.0021 | 1 |
| $5_{2\,4} - 4_{1\,4}$ | 20365.4481 | 20365.4513 | -0.0032 | 2 |
| $6_{2\,4} - 5_{1\,4}$ | 20365.5971 | 20365.5986 | -0.0015 | 1 |
| $6_{2\,5} - 5_{1\,5}$ | 20365.6287 | 20365.6310 | -0.0023 | 1 |
| $7_{2\,5} - 6_{1\,5}$ | 20365.7661 | 20365.7654 | 0.0007 | 1 |
| $7_{2\,6} - 6_{1\,6}$ | 20365.8105 | 20365.8108 | -0.0003 | 1 |
| $8_{2\,6} - 7_{1\,6}$ | 20365.9295 | 20365.9300 | -0.0005 | 1 |
| $8_{2\,7} - 7_{1\,7}$ | 20365.9894 | 20365.9905 | -0.0011 | 1 |
| $9_{2\,7} - 8_{1\,7}$ | 20366.0926 | 20366.0925 | 0.0001 | 1 |
| $9_{2\,8} - 8_{1\,8}$ | 20366.1698 | 20366.1702 | -0.0004 | 1 |
| $10_{2\,8} - 9_{1\,8}$ | 20366.2529 | 20366.2528 | 0.0001 | 1 |
| $10_{2\,9} - 9_{1\,9}$ | 20366.3484 | 20366.3500 | -0.0016 | 1 |
| $11_{2\,9} - 10_{1\,9}$ | 20366.4099 | 20366.4111 | -0.0012 | 1 |
| $11_{2\,10} - 10_{1\,10}$ | 20366.5295 | 20366.5297 | -0.0002 | 1 |
| $12_{2\,10} - 11_{1\,10}$ | 20366.5654 | 20366.5672 | -0.0018 | 1 |
| $12_{2\,11} - 11_{1\,11}$ | 20366.7134 | 20366.7095 | 0.0039 | 2 |
| $15_{2\,13} - 14_{1\,13}$ | 20367.0233 | 20367.0232 | 0.0001 | 1 |

Table 6.5 (cont.)

| | | | | |
|---|---|---|---|---|
| $14_{2\,13} - 13_{1\,13}$ | 20367.0662 | 20367.0691 | -0.0029 | 1 |
| $16_{2\,14} - 15_{1\,14}$ | 20367.1714 | 20367.1711 | 0.0003 | 1 |
| $15_{2\,14} - 14_{1\,14}$ | 20367.2454 | 20367.2490 | -0.0036 | 2 |
| $17_{2\,15} - 16_{1\,15}$ | 20367.3156 | 20367.3171 | -0.0015 | 1 |
| $16_{2\,15} - 15_{1\,15}$ | 20367.4268 | 20367.4289 | -0.0021 | 1 |
| $17_{2\,16} - 16_{1\,16}$ | 20367.6074 | 20367.6089 | -0.0015 | 1 |
| $19_{2\,17} - 18_{1\,17}$ | 20367.6074 | 20367.6030 | 0.0044 | 3 |
| $19_{2\,18} - 18_{1\,18}$ | 20367.9671 | 20367.9691 | -0.0020 | 1 |
| $22_{2\,20} - 21_{1\,20}$ | 20368.0187 | 20368.0174 | 0.0013 | 1 |
| $20_{2\,19} - 19_{1\,19}$ | 20368.1465 | 20368.1493 | -0.0028 | 1 |
| $24_{2\,22} - 23_{1\,22}$ | 20368.2835 | 20368.2843 | -0.0008 | 1 |
| $12_{3\,10} - 13_{2\,12}$ | 20377.1459 | 20377.1491 | -0.0032 | 2 |
| $12_{3\,9} - 13_{2\,11}$ | 20377.1459 | 20377.1487 | -0.0028 | 1 |
| $11_{3\,9} - 12_{2\,11}$ | 20377.3388 | 20377.3421 | -0.0033 | 2 |
| $11_{3\,8} - 12_{2\,10}$ | 20377.3388 | 20377.3419 | -0.0031 | 2 |
| $10_{3\,8} - 11_{2\,10}$ | 20377.5316 | 20377.5342 | -0.0026 | 1 |
| $10_{3\,7} - 11_{2\,9}$ | 20377.5316 | 20377.5341 | -0.0025 | 1 |
| $9_{3\,7} - 10_{2\,9}$ | 20377.7274 | 20377.7253 | 0.0021 | 1 |
| $9_{3\,6} - 10_{2\,8}$ | 20377.7274 | 20377.7252 | 0.0022 | 1 |
| $6_{3\,4} - 7_{2\,6}$ | 20378.2970 | 20378.2927 | 0.0043 | 3 |
| $6_{3\,3} - 7_{2\,5}$ | 20378.2970 | 20378.2927 | 0.0043 | 3 |
| $3_{3\,1} - 2_{2\,1}$ | 20380.1194 | 20380.1188 | 0.0006 | 1 |
| $3_{3\,0} - 2_{2\,0}$ | 20380.1194 | 20380.1188 | 0.0006 | 1 |
| $4_{3\,2} - 3_{2\,2}$ | 20380.3003 | 20380.2959 | 0.0044 | 1 |
| $4_{3\,1} - 3_{2\,1}$ | 20380.3003 | 20380.2959 | 0.0044 | 1 |
| $5_{3\,3} - 4_{2\,3}$ | 20380.4729 | 20380.4719 | 0.0010 | 1 |
| $5_{3\,2} - 4_{2\,2}$ | 20380.4729 | 20380.4719 | 0.0010 | 1 |
| $6_{3\,4} - 5_{2\,4}$ | 20380.6517 | 20380.6470 | 0.0047 | 1 |
| $6_{3\,3} - 5_{2\,3}$ | 20380.6517 | 20380.6470 | 0.0047 | 1 |
| $7_{3\,5} - 6_{2\,5}$ | 20380.8234 | 20380.8212 | 0.0022 | 2 |
| $7_{3\,4} - 6_{2\,4}$ | 20380.8234 | 20380.8211 | 0.0023 | 2 |
| $8_{3\,6} - 7_{2\,6}$ | 20380.9957 | 20380.9943 | 0.0014 | 2 |
| $8_{3\,5} - 7_{2\,5}$ | 20380.9957 | 20380.9942 | 0.0015 | 2 |
| $9_{3\,7} - 8_{2\,7}$ | 20381.1693 | 20381.1664 | 0.0029 | 1 |
| $9_{3\,6} - 8_{2\,6}$ | 20381.1693 | 20381.1664 | 0.0029 | 1 |
| $10_{3\,8} - 9_{2\,8}$ | 20381.3381 | 20381.3376 | 0.0005 | 2 |
| $10_{3\,7} - 9_{2\,7}$ | 20381.3381 | 20381.3375 | 0.0006 | 2 |
| $11_{3\,9} - 10_{2\,9}$ | 20381.5088 | 20381.5077 | 0.0011 | 2 |
| $11_{3\,8} - 10_{2\,8}$ | 20381.5088 | 20381.5076 | 0.0012 | 2 |
| $12_{3\,10} - 11_{2\,10}$ | 20381.6781 | 20381.6770 | 0.0011 | 2 |
| $12_{3\,9} - 11_{2\,9}$ | 20381.6781 | 20381.6768 | 0.0013 | 2 |
| $13_{3\,11} - 12_{2\,11}$ | 20381.8468 | 20381.8452 | 0.0016 | 2 |
| $13_{3\,10} - 12_{2\,10}$ | 20381.8468 | 20381.8450 | 0.0018 | 2 |
| $14_{3\,12} - 13_{2\,12}$ | 20382.0115 | 20382.0125 | -0.0010 | 2 |
| $14_{3\,11} - 13_{2\,11}$ | 20382.0115 | 20382.0122 | -0.0007 | 2 |

Table 6.5 (cont.)

| | | | | |
|---|---|---|---|---|
| $15_{3\,13} - 14_{2\,13}$ | 20382.1780 | 20382.1789 | -0.0009 | 2 |
| $15_{3\,12} - 14_{2\,12}$ | 20382.1780 | 20382.1784 | -0.0004 | 2 |
| $16_{3\,14} - 15_{2\,14}$ | 20382.3444 | 20382.3443 | 0.0001 | 2 |
| $16_{3\,13} - 15_{2\,13}$ | 20382.3444 | 20382.3437 | 0.0007 | 2 |

### 6.4.4  Axis-Switching

As in Chapter 4, there is not enough data for accurate determination of the equilibrium geometries for the two electronic states. Therefore, to prove that the peaks assigned as axis-switching peaks are real, the spectrum has been simulated using the Jet Beam 95 program.[23] The simulation is shown in the upper half of Figure 6.7, while the lower half shows the experimentally observed spectrum. For clarity the axis-switching peaks are marked with arrows, and there is good agreement between the simulation and experiment. Figures 6.8 and 6.9 show expanded views of the regions where the axis-switching peaks occur, and demonstrate that there is good agreement between the simulated spectrum and the experimentally observed spectrum. As before, a trial and error approach was taken to obtain a reasonable estimate of the axis-switching angle, and the estimated angle is ~0.6° ±0.2°.

As in Chapter 4, the high-level *ab initio* (SAC-CI) structural data was put through the fitting procedure originally described by Hougen and Watson to see if it agrees with the experimentally observed axis-switching angle. In this case, unlike for HSiNC, it was found that there is poor agreement with the experimental value, giving the axis-switching angle as 0.3°. As before, there is no other similar system available for comparison so it is very difficult to assess the validity of this result. However there is enough of a difference for careful consideration of what may be causing it.

There are two possible explanations for this difference: either the experimental data is poor resulting in an increased axis-switching angle prediction, or the more likely case, the *ab initio* data is incorrectly describing either or both of the geometries for each state. Given what was seen in Chapter 4, where the axis-switching angle was predicted to be within ~0.2° of the experimentally determined value, it is unlikely that the experimental data in this case would provide such a large discrepancy when compared to the predicted value.

As stated above, with no other species of this kind to compare against other than triatomics, there is every possibility that the axis-switching mechanism may be very sensitive to either the Si-N-C angle or the N-C-O angle. As discussed in Chapter 5 there is a great deal of debate over the linearity or non-linearity of the N-C-O group. The calculations in this case are predicting minor deviations for a linear geometry, but by varying this angle in all possible ways does not seem to provide any significant changes to the predicted axis-switching angle, unless the oxygen of the N-C-O group is placed directly on top of the nitrogen, which is of course very unrealistic. Therefore, the dependency of the axis-switching angle to the N-C-O angle may be ruled out, as it would seem unlikely that the *ab initio* data would be so wrong in the prediction of this angle in either state.

We may now turn our attention to the variation of the Si-N-C angle to see what effect this has on the axis-switching angle. It is easy to imagine that this angle will have an effect, as variation of it will cause significant shifts in the centre of mass of the system and therefore the axis-switching angle. In this case, the *ab initio* data suggests that there is an approximate $+5°$ change in the Si-N-C angle in going from the ground state to the excited state. If this relative difference is increased, then we observe a decrease in the axis-switching angle. If this relative difference in decreased then the converse is true. By variation of the Si-N-C angle in the opposite direction to that predicted by the *ab initio* data, the axis-switching angle predicted by experiment can be easily reached. If the change in Si-N-C angle in going from the ground to excited state lies in the range of $-1.5°$ to $-13°$ (a difference from the original *ab initio* data of only $6.5°$ to $18°$) then there is good agreement between the experimental and predicted axis-switching angle. Table 6.6 summarises how the axis-switching angle ($\theta_T$) varies with the Si-N-C angle. This data assumes that all geometric parameters are fixed to those obtained from the *ab initio* data (see Figure 6.10, below) with the exception of the Si-N-C angle which is varied in the excited ($\tilde{A}^1A''$) state.

It is very feasible that the *ab initio* data may miscalculate the geometry of the Si-N-C angle by this margin ($6-20°$), and it is therefore essential that further work is carried out in order to accurately determine the geometry of this species in both electronic states. Microwave spectroscopy would be ideal for the purposes of assessing the

geometry in the ground state, while further high resolution LIF data could provide useful information on the excited state geometry.

Table 6.6: Table showing how the axis-switching angle ($\theta_T$) varies with the Si-N-C angle. In this, case all geometric parameters were fixed to those obtained from the SAC/SAC-CI (for the $\tilde{X}^1A'/\tilde{A}^1A''$ states) calculations with the exception of the Si-N-C angle, which was varied in the excited ($\tilde{A}^1A''$) state. Also given is the relative change in the Si-N-C angle between the two electronic states. All values are in degrees.

| Si-N-C angle in the excited ($\tilde{A}^1A''$) state | Relative change in Si-N-C angle[a] | Predicted axis-switching angle ($\theta_T$) |
|---|---|---|
| 132.0 | -13.58 | 0.60 |
| 134.0 | -11.58 | 0.56 |
| 136.0 | -9.58 | 0.52 |
| 138.0 | -7.58 | 0.49 |
| 140.0 | -5.58 | 0.46 |
| 142.0 | -3.58 | 0.43 |
| 144.0 | -1.58 | 0.40 |
| 146.0 | +0.42 | 0.37 |
| 148.0 | +2.42 | 0.35 |
| 150.0 | +4.42 | 0.32 |
| 151.65[b] | +6.07 | 0.30 |

[a] In going from the ground ($\tilde{X}^1A'$) to excited ($\tilde{A}^1A''$) state
[b] Angle predicted by SAC-CI calculation
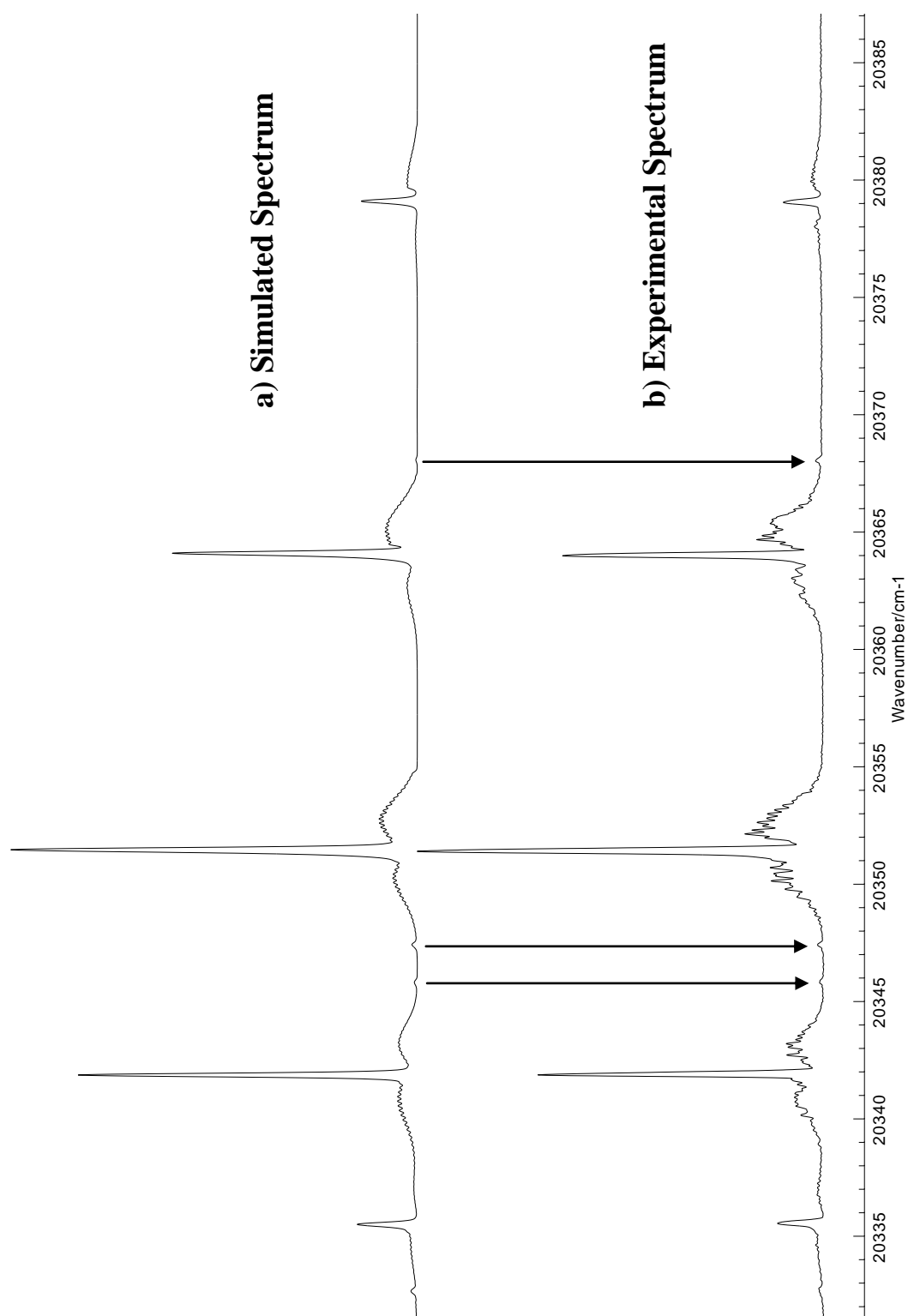
Figure 6.7: A comparison between the simulated (a) and experimental (b) spectra of the $0_0^0$ band of HSiNCO. The arrows are clearly showing that the peaks attributed to axis- switching in the experimental spectrum can be simulated with good accuracy. The temperature is estimated to be 12 K. The Gaussian linewidth is 0.15 cm$^{-1}$ and the Lorentzian linewidth is 0.05 cm$^{-1}$.

**(a) Simulated spectrum**

**(b) Experimental spectrum**

$^qQ_0$

$^qQ_1$

Wavenumber / cm$^{-1}$
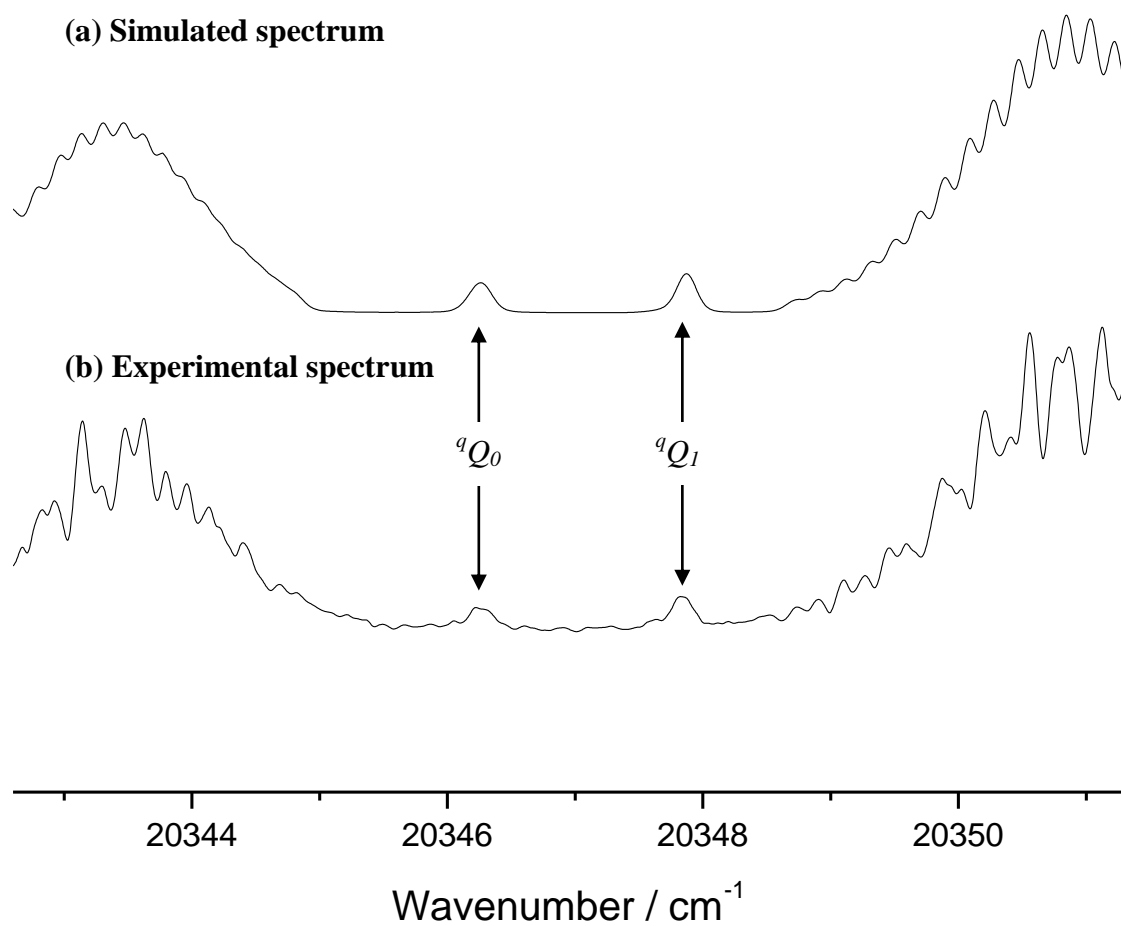
Figure 6.8: An expanded view of the axis-switching region between 20342 and 20352 cm$^{-1}$. (a) shows the simulated spectrum and (b) shows the experimental spectrum. The temperature of the spectra is ~8 K and from this $\theta_T$ is predicted to be ~0.6° ±0.2°.

**(a) Simulated spectrum**

**(b) Experimental spectrum**

$^sQ_0$

20366          20368          20370

Wavenumber / cm$^{-1}$
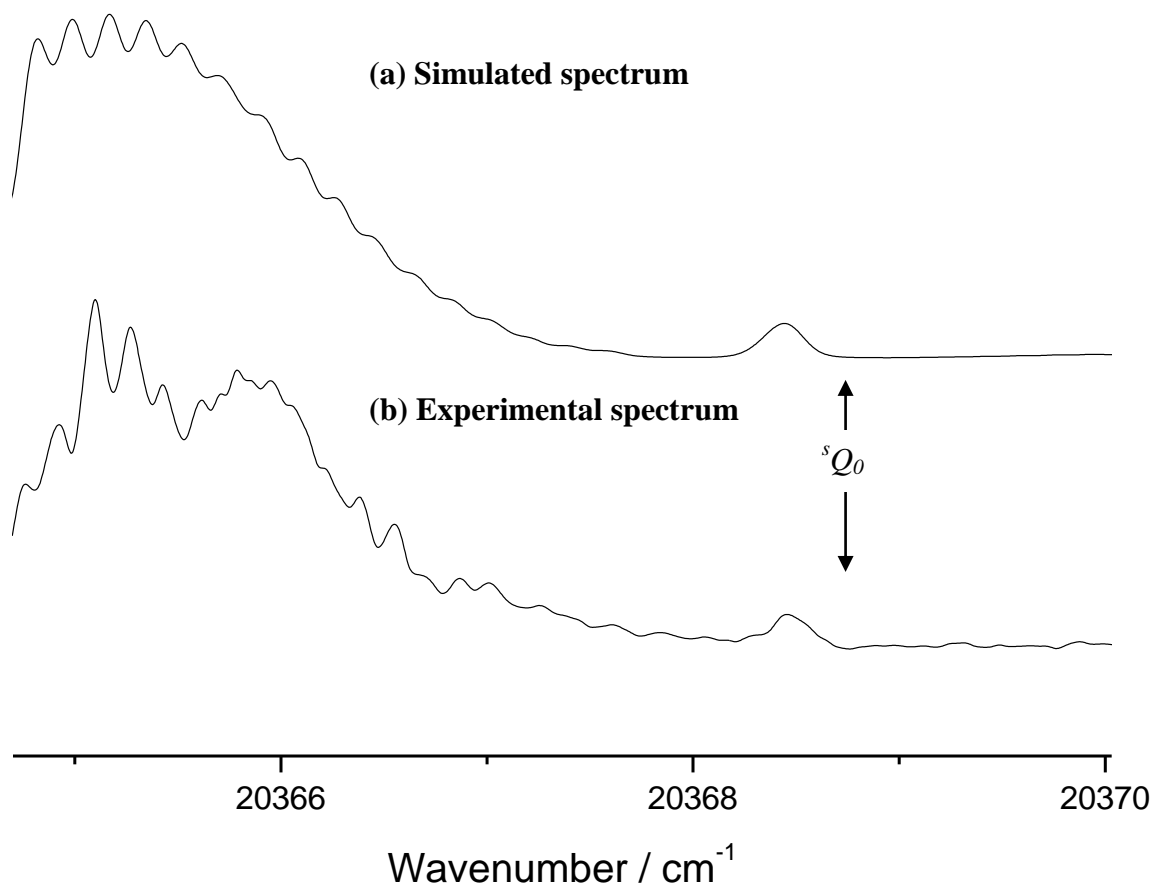
Figure 6.9: An expanded view of the axis-switching region between 20364 and 20370 cm$^{-1}$. (a) shows the simulated spectrum and (b) shows the experimental spectrum. The temperature of the spectra is ~8 K and from this $\theta_T$ is predicted to be ~0.6° ±0.2°.

### 6.4.5 Comparison with *Ab Initio* Results

As mentioned above, a detailed *ab initio* study has been conducted on the possible isomers of the [H, Si, N, C, O] system. Details of these calculations are given in Chapter 5. This section takes pieces of these data specifically related to the HSiNCO isomer, to use in comparison with the results detailed in this chapter.

### 6.4.6 Energy Calculations

Unless otherwise stated, the energies given have been corrected for zero-point energy from values taken from the vibrational wavenumber calculations run in parallel to the optimisation procedures.

The results of the *ab initio* calculations at the MP2 level of theory using the aug-cc-pVTZ basis sets give an underestimation of the observed transition frequency of approximately 4000 cm$^{-1}$ (see Table 4.1 in Chapter 4). This seems to follow the observed trend in energy calculations of this type for the halo- and pseudohalosilylene species discussed in Chapter 4. Again, the implementation of the SAC-CI calculations provides a far better estimate of the transition energy for this species giving a value of 20914.8 cm$^{-1}$, which is much more in line with what has been observed experimentally. *N.B.*, the SAC-CI were not subjected to any zero-point corrections as the running of frequency calculations goes beyond practical time constraints and computational cost.

### 6.4.7 Determination of Molecular Geometry

The parameters for optimised geometries of the ground ($\tilde{X}^1A'$) and excited ($\tilde{A}^1A''$) electronic states for HSiNCO are given in Figure 6.10. As there has not been any previous experimental work carried out on either the ground ($\tilde{X}^1A'$) or the excited ($\tilde{A}^1A''$) state, there is no experimental data for comparison. However, it can be assumed that the values obtained from these calculations will be valid given the good agreement found in the HSiNC work carried out in the Chapter 4.

As discussed earlier, the appearance of axis-switching peaks in the experimental spectrum suggests that there is a significant geometry change upon excitation from the ground to excited electronic state of HSiNCO. Looking at the parameters given in Figure 6.10 it is clear that the appearance of the axis-switching peaks can be attributed to the large change in the H-Si-N bond angle, which increases from ~94.5°

to 115°, as there is no other significant change in the other structural parameters. It is worth noting that this change is less than that observed for HSiNC in the previous chapter by ~5°. Using this calculated change in angle it has been possible to determine what the axis-switching angle should be, and compare it to the experimentally determined value. The results of this procedure indicates that the experimental data suggests the relative difference in the H-Si-N angle is smaller than predicted by the *ab initio* data, predicting the change to be in the region of ~10°
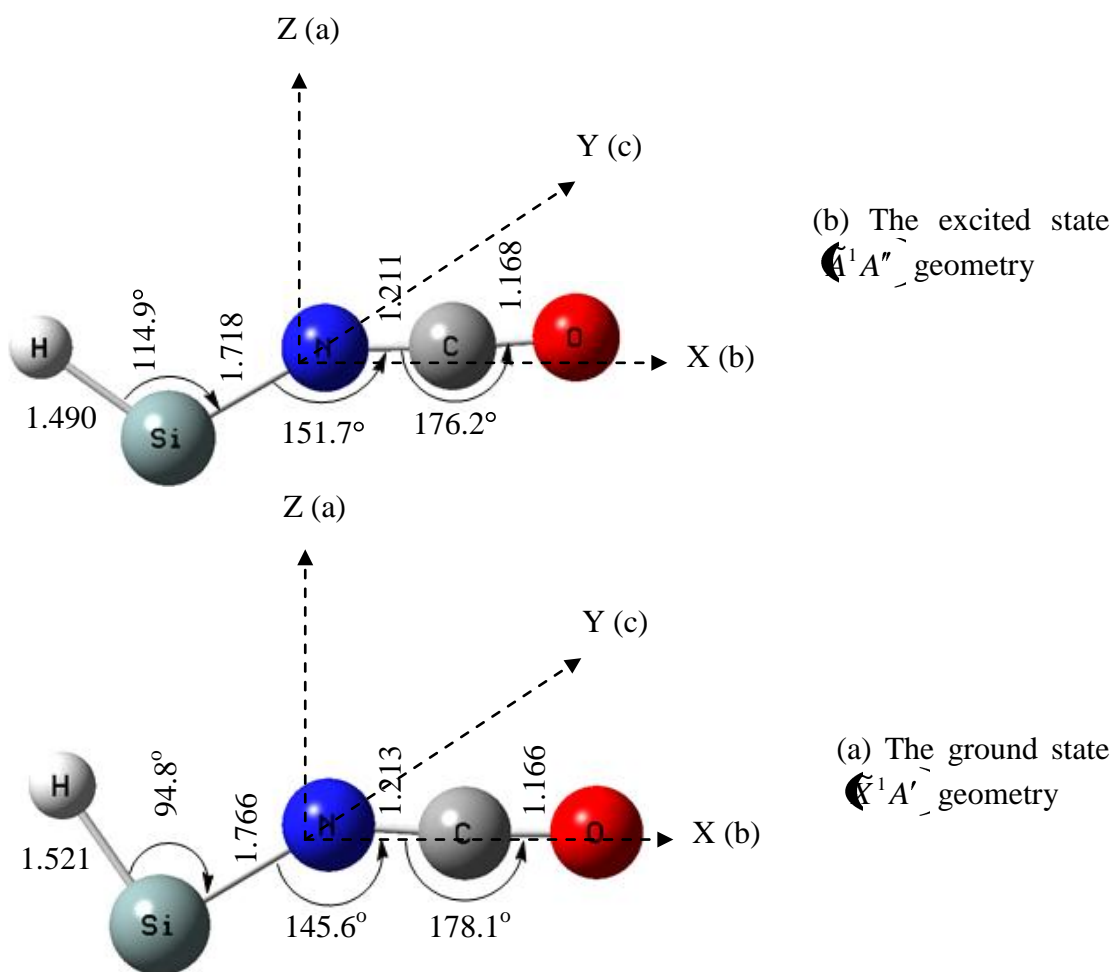


Figure 6.10: Figure showing the geometries of HSiNCO in (a) the ground $\tilde{X}\,^1A'$ state and (b) the excited $\tilde{A}\,^1A''$ state. Bond lengths are given in angstroms and bond angles in degrees.

## 6.4.8  Vibrational Analysis

The 490-450 nm band system is assigned to the $\tilde{A}^1A''-\tilde{X}^1A'$ electronic transition of HSiNCO, with the transition moment oriented perpendicular to the molecular plane, giving rise to $C$-type bands. This transition corresponds to the promotion of an electron from a non-bonding $s$ orbital on the silicon atom to an unoccupied out-of-plane $3p$ orbital also located on the silicon.

In total eleven vibrational bands of the HSiNCO species have been located. At low resolution these bands consist of seven partially resolved sub-bands with prominent $Q$-branches ($\Delta K$=0). The low resolution spectrum attributed to HSiNCO is given in Figure 6.11

Each of the vibrational bands was fitted using the spectral fitting program PGOPHER.[16] For each band, a rough fit was first obtained by fitting the $Q$-branches, and floating the origin frequency only. Once the rough fit was complete, a more accurate fit was obtained by adding in any rotational lines which were sufficiently resolved in the low resolution spectra, and the excited state rotational constants $A$ and $\bar{B}$ were floated together with the origin frequency. This process was not very accurate as the number of rotationally resolved lines in the low resolution spectra was very few. However, in most cases the rough fitting of the $Q$-branches gave a reasonable fit as can be seen from the RMS errors. In all cases the ground state parameters were fixed to those obtained from the medium resolution fit of the $0_0^0$ band (see below). The assignments, band origins, offset from the $0_0^0$ band, *ab initio* prediction, approximate values of $(A-\bar{B})'$ and the root mean square (RMS) error in the fit for each band are given in Table 6.8. The vibrational wavenumbers from the *ab initio* calculations used for these predictions are given in Table 6.7.

Table 6.7: Vibrational assignments and wavenumber values for the excited ($\widetilde{A}^1A''$) state vibrational modes of HSiNCO calculated at the MP2(FC)/aug-cc-pVTZ level. All values are given in cm$^{-1}$.

| Vibrational mode (symmetry) | Assignment | MP2(FC)[a] (harmonic) | MP2(FC)[a] (anharmonic) |
|---|---|---|---|
| $\nu_1$ (a′) | N-C-O antisymmetric stretch | 2347.78 | 2308.81 |
| $\nu_2$ (a′) | Si-H stretch | 2218.82 | 2115.83 |
| $\nu_3$ (a′) | N-C-O symmetric stretch | 1433.86 | 1429.53 |
| $\nu_4$ (a′) | Si-H in-plane wag | 690.90 | 675.71 |
| $\nu_5$ (a′) | Si-N stretch | 643.76 | 634.64 |
| $\nu_6$ (a′) | N-C-O in-plane bend | 597.52 | 595.54 |
| $\nu_7$ (a′) | Si-N-C bend | 107.64 | 107.38 |
| $\nu_8$ (a″) | N-C-O out-of-plane bend | 571.42 | 575.87 |
| $\nu_9$ (a″) | Si-N-C out-of-plane bend | 132.76 | 135.11 |

[a] Unscaled wavenumbers

HSiNCO is a bent molecule of $C_s$ symmetry with seven $a'$ vibrational modes labelled $\nu_1$ (N-C-O antisymmetric stretch), $\nu_2$ (Si-H stretch), $\nu_3$ (N-C-O symmetric stretch), $\nu_4$ (Si-H in-plane wag), $\nu_5$ (Si-N stretch), $\nu_6$ (N-C-O in-plane bend) and $\nu_7$ (Si-N-C bend), as well as two $a''$ vibrational modes labelled $\nu_8$ (N-C-O out-of-plane bend) and $\nu_9$ (Si-N-C out-of-plane bend).

Table 6.8: Assignments, band origins, offset from the $0_0^0$ band, approximate excited state $(A - \bar{B})$ values and the root mean square (RMS) error in the fit for each of the observed vibrational bands in the LIF spectrum of HSiNCO (in cm$^{-1}$) in the $\tilde{A}\,^1A''$ state.

| Assignment[a] (symmetry) | Band origin | Offset from $0_0^0$ band | *Ab initio* prediction[b] | $(A-\bar{B})'$ | RMS error in fit |
|---|---|---|---|---|---|
| $0_0^0$ $(a')$ | 20346.33(00) | 0.00 | 0.00 | 5.63 | 0.0014 |
| $7_0^1$ $(a')$ | 20455.968(40) | 99.63 | 107.38 | 4.13 | 0.094 |
| $9_0^1$ $(a'')$ | 20509.06(13) | 152.73 | 135.11 | 6.90 | 0.074 |
| $7_0^1 9_0^1$ $(a'')$ | 20580.270(43) | 223.94 | 242.49 | 4.32 | 0.098 |
| $9_0^2$ $(a')$ | 20640.51(24) | 284.18 | 270.23 | 6.06 | 0.097 |
| $6_0^1$ $(a')$ | 20934.276(17) | 577.94 | 595.54 | 5.94 | 0.045 |
| $5_0^1$ $(a')$ | 20991.09(22) | 634.76 | 634.64 | 6.67 | 0.057 |
| $6_0^1 8_0^1$ $(a'')$ | 21514.637(8) | 1158.46 | 1171.41 | 6.42 | 0.021 |
| $5_0^1 6_0^1$ $(a')$ | 21576.340(29) | 1220.01 | 1230.17 | 7.77 | 0.067 |
| $5_0^2$ $(a')$ | 21623.266(40) | 1266.93 | 1269.28 | 5.71 | 0.090 |
| $3_0^1 7_0^2 9_0^1$ $(a'')$ | 22139.680(17) | 1783.35 | 1779.40 | 5.67 | 0.044 |

[a] All of these assignments are tentative

b Unscaled frequencies based on anharmonic calculation at the MP2(FC) level of theory using the aug-cc-pVTZ basis set

As was the case in Chapter 4, the $(A-\bar{B})'$ values are useful to consider in making assignments, as values which are greater than that for the $0_0^0$ band indicate that at least one quanta of a bending / wagging mode is present. All of the assignments given in Table 6.8 should be considered tentative.
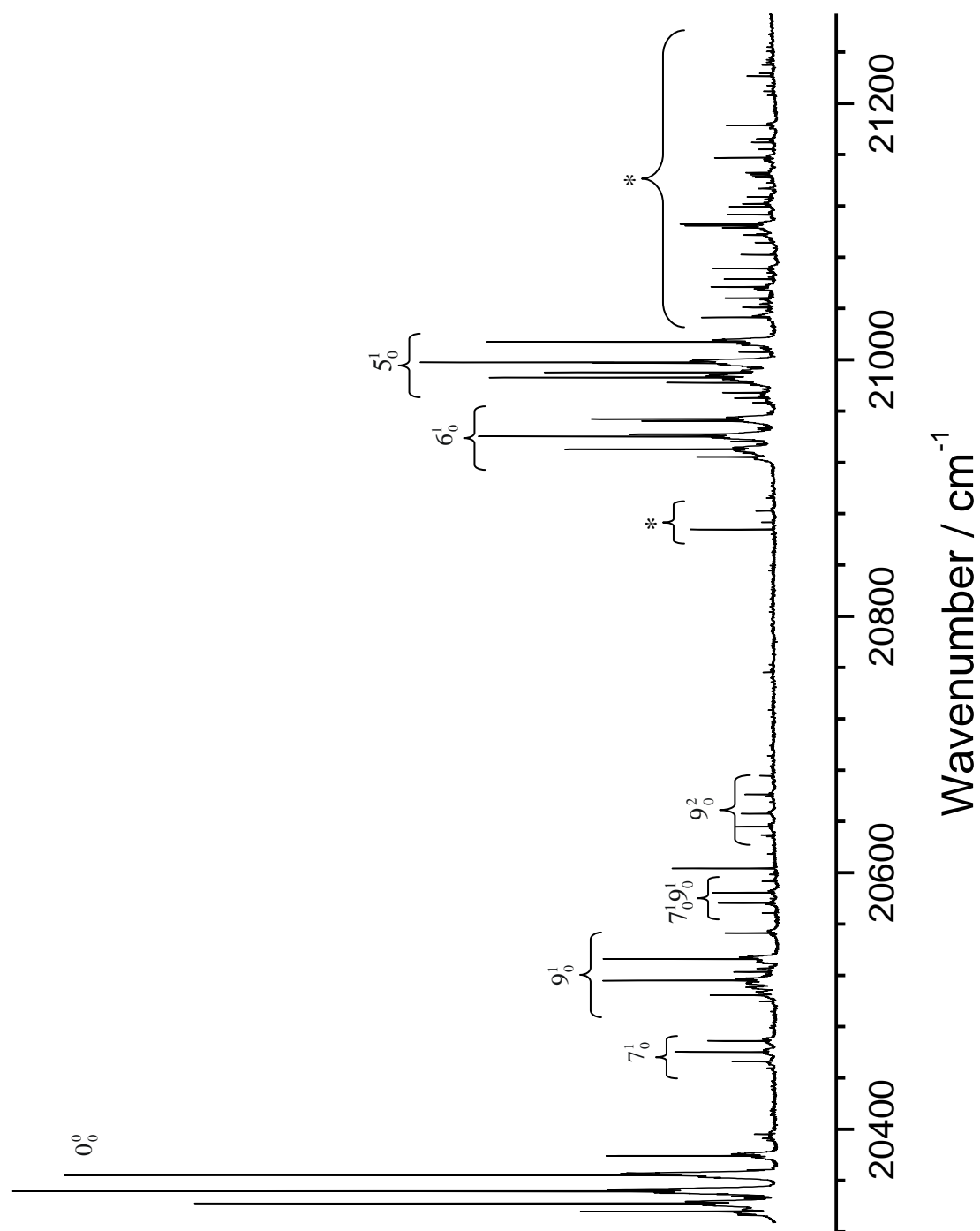
Figure 6.11: A portion of the low resolution spectrum of HSiNCO, showing the vibrational assignments. Peaks marked with asterisks indicate the carrier is unknown.
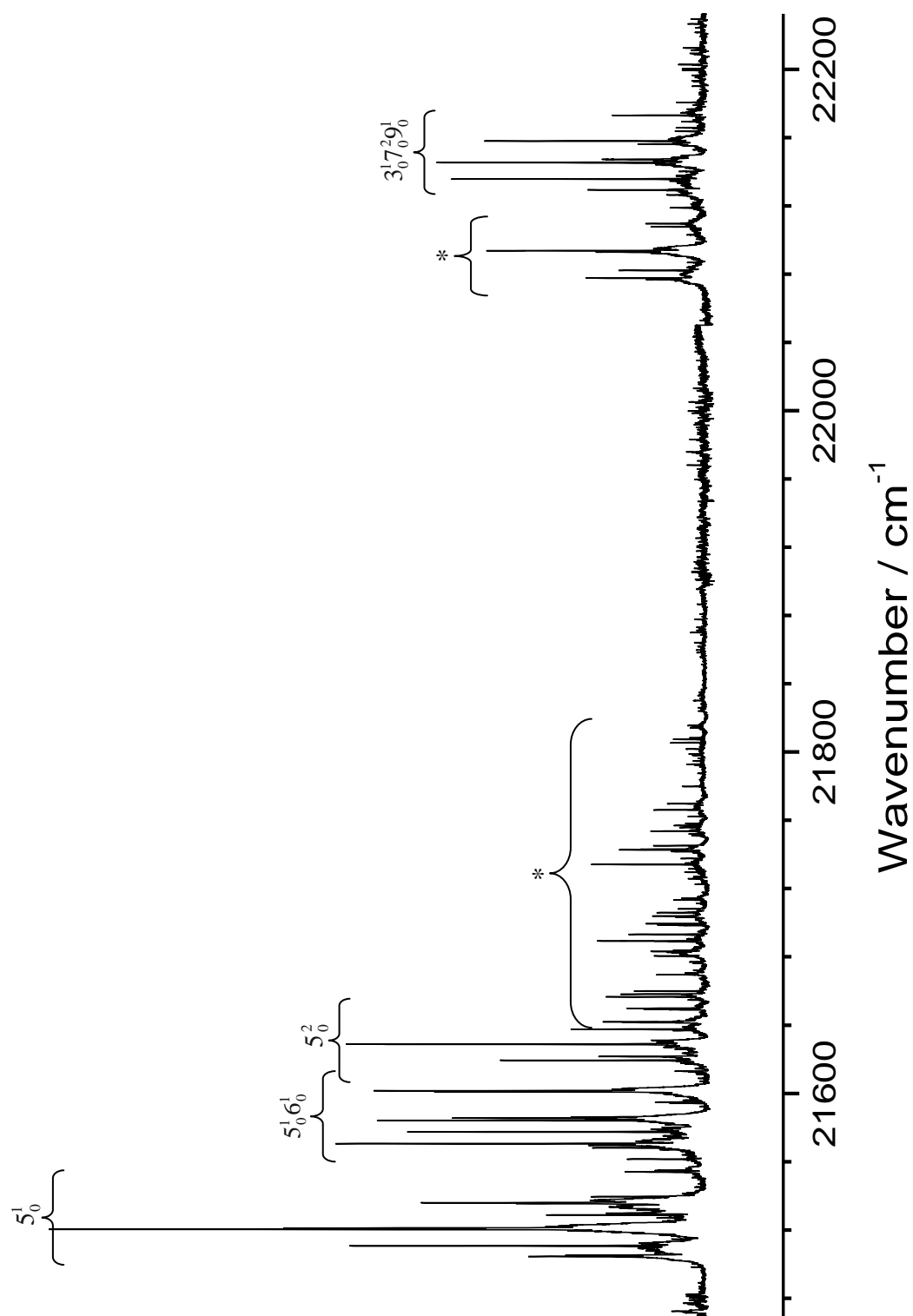
Figure 6.11 (cont.): A portion of the low resolution spectrum of HSiNCO, showing the vibrational assignments. Peaks marked with asterisks indicate the carrier is unknown.

### 6.4.9 Dispersed Fluorescence Spectra

As in the previous chapter, dispersed fluorescence (DF) spectra have been taken by pumping the strongest $Q$-branch ($^rQ_0$) of the $0_0^0$ band of HSiNCO, and as before it was found that pumping this branch led to splitting of the DF peaks, as shown in Figure 6.12. The magnitude of the observed splitting was approximately 34 cm$^{-1}$ indicating that the splitting is caused by emission back down to different rotational energy levels in the $^rQ_2$ sub-band.



Figure 6.12: Dispersed fluorescence spectrum obtained by pumping the $^rQ_0$ branch of the $0_0^0$ band of HSiNCO. The spectrum was recorded by averaging 1500 laser shots using a slit-width of 100 μm over the range 16800-20600 cm$^{-1}$.

The first peak observed in the spectrum is the result of the laser, and is therefore not split. Table 6.9 gives the assignment for each peak, position of the peaks relative to the laser (in cm$^{-1}$) and peak position relative to the previous peak in the progression (in cm$^{-1}$).

Table 6.9: Assignment for each peak, position of the peaks relative to the laser (in cm$^{-1}$) and peak position relative to the previous peak in the progression (in cm$^{-1}$) for the dispersed fluorescence spectrum obtained by pumping the $^rQ_0$ branch of the $0_0^0$ band of HSiNCO in the $\tilde{X}\,{}^1\!A'$ electronic state.

| Assignment | Peak position relative to laser | Peak position relative to previous peak in progression |
|---|---|---|
| $4_0^1$ | 878.00 | 878.00 |
| $4_0^2$ | 1737.77 | 859.77 |
| $4_0^3$ | 2587.41 | 849.64 |
| $4_0^4$ | 3431.55 | 844.14 |

Due to the observed splitting, another $Q$-branch was pumped. Figure 6.13 shows the DF spectrum obtained by pumping the $^PQ_1$ branch of the $0_0^0$ band of HSiNCO. As mentioned above, HSiNCO is a bent molecule of $C_s$ symmetry with nine vibrational modes. The electronic transition is accompanied by a change in the H-Si-N bond angle of ~25°, so the emission spectra are dominated by a progression of the $\nu_4$ (Si-H in-plane wag) mode. This progression is very short which corresponds to what is seen in the LIF spectra.

As seen in HSiNC in Chapter 4, pumping this weaker $Q$-branch has eliminated the observed splitting seen in Figure 6.12. The DF spectra obtained for HSiNCO mirror exactly the spectra observed for HSiNC, adding further to the argument, discussed in section 6.4.2 above, that the identity of the spectral carrier for the signals seen is indeed HSiNCO. As before, the first peak observed in the spectrum is the result of the laser. Table 6.10 gives the assignments and details of the progression.
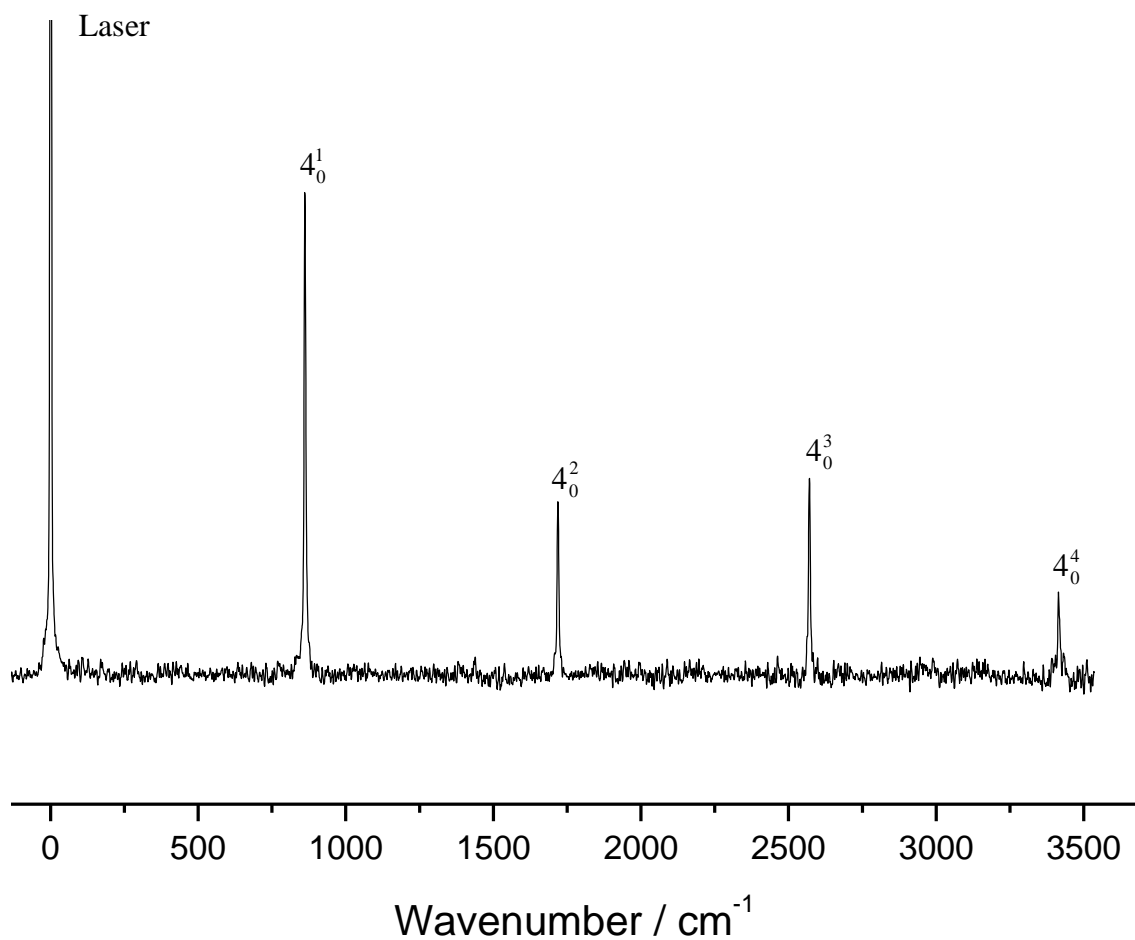
Figure 6.13: The dispersed fluorescence spectrum of the strong $^{P}Q_1$ branch of the $0_0^0$ band of HSiNCO. The spectrum was recorded by averaging 1500 laser shots using a slit-width of 100 μm over the range 16800-20600 cm$^{-1}$.

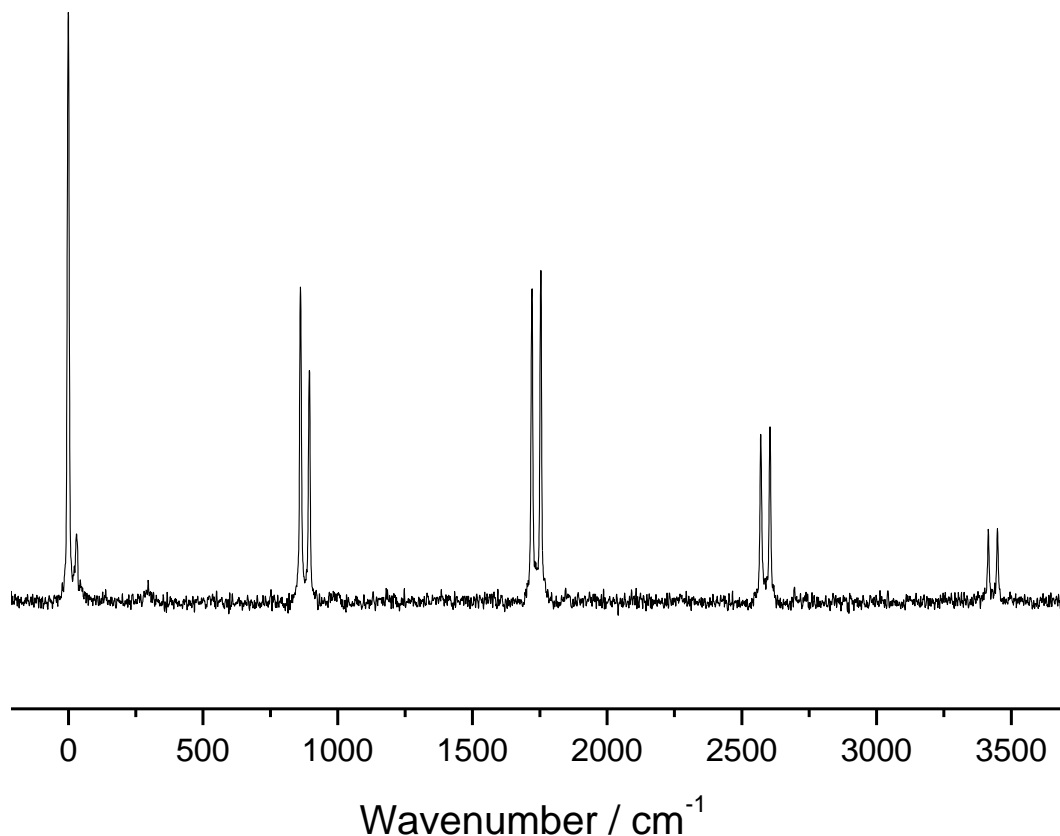Table 6.10: Assignment for each peak, position of the peaks relative to the laser (in cm$^{-1}$) and peak position relative to the previous peak in the progression (in cm$^{-1}$) for the dispersed fluorescence spectrum obtained by pumping the $^{P}Q_1$ branch of the $0_0^0$ band of HSiNCO in the $\tilde{X}\,^1A'$ electronic state.

| Assignment | Peak position relative to laser | Peak position relative to previous peak in progression |
| --- | --- | --- |
| $4_0^1$ | 861.87 | 861.87 |
| $4_0^2$ | 1717.71 | 855.84 |
| $4_0^3$ | 2566.88 | 849.17 |
| $4_0^4$ | 3409.95 | 843.07 |

As mentioned above the DF spectra observed bear a strong resemblance to those observed for HSiNC seen in Chapter 4. For HSiNC the strength of the fluorescence signal was not very strong so attempts made to see any further DF spectra by pumping $Q$-branches in other vibrational bands resulted in failure.

The fluorescence signal is an order of magnitude stronger in the case of HSiNCO so more DF spectra are accessible from other prominent bands of the LIF spectrum. DF spectra have been recorded for the $6_0^1$ and $8_0^1$ vibrational bands, and in both cases the same splitting of the peaks was observed if the strongest ($^{r}Q_0$) $Q$-branch was pumped. Therefore, as in the case of the $0_0^0$ band, the less prominent $^{P}Q_1$ branch was pumped to obtain the spectra.

Figure 6.14 show the DF spectrum produced by pumping the $^{P}Q_1$ branch of the $6_0^1$ vibrational band. The spectrum is more complicated than that of the $0_0^0$ band as there are two separate progressions present. As in the $0_0^0$ band spectrum, there is a progression of the $\nu_4$ (Si-H in-plane wag) mode which is the dominant feature of the spectrum. Along with this there is a second smaller progression which can be attributed to a combination of one quanta of the $\nu_8$ (N-C-O out-of-plane bend) mode – the peak observed at ~632 cm$^{-1}$. This is then followed by two further peaks where additional quanta of the $\nu_4$ (Si-H wag) mode have combined to give the observed progression. As can be seen there is a significant decrease in the expected intensity of

the observed peaks for the $4_0^2$ and $4_0^3$ bands in the first progression. As before, Table 6.11 gives the assignments and details of the progression.



Figure 6.14: The dispersed fluorescence spectrum of the strong $^PQ_1$ branch of the $6_0^1$ vibrational band of HSiNCO showing peak assignments. The spectrum was recorded by averaging 5000 laser shots using a slit-width of 170 μm over the range 17000-21200 cm$^{-1}$.

Table 6.11: Assignment for each peak, position of the peaks relative to the laser (in cm$^{-1}$) and peak position relative to the previous peak in the progression (in cm$^{-1}$) for the dispersed fluorescence spectrum obtained by pumping the $^PQ_1$ branch of the $6_0^1$ band of HSiNCO in the $\tilde{X}\,^1A'$ electronic state.

| Assignment | Peak position relative to laser | Peak position relative to previous peak in progression |
|---|---|---|
| $8_0^1$ | 631.97 | 631.97 |
| $4_0^1$ | 861.86 | 861.86 |
| $4_0^1 8_0^1$ | 1489.52 | 857.55 |
| $4_0^2$ | 1717.69 | 855.83 |
| $4_0^2 8_0^1$ | 2340.92 | 851.40 |
| $4_0^3$ | 2567.92 | 850.23 |
| $4_0^4$ | 3412.14 | 844.22 |
| $4_0^5$ | 4250.32 | 838.18 |
| $4_0^6$ | 5082.04 | 831.72 |
| $4_0^7$ | 5907.88 | 825.84 |

As mentioned above, the DF spectrum has also been recorded for the $8_0^1$ vibrational band. Figure 6.15 shows the DF spectrum obtained by pumping the strong $^PQ_1$ branch of the $6_0^1$ vibrational band of HSiNCO. The spectrum is quite simple and consists of a single progression which can be attributed to a combination band similar to that seen in the spectrum for the DF spectrum produced by pumping the $^PQ_1$ branch of the $6_0^1$ vibrational band. The first DF peak is located at ~633 cm$^{-1}$ which can be attributed to one quantum of the $\nu_8$ (N-C-O out-of-plane bend) mode. Following on from this there are four further peaks where quanta of the $\nu_4$ (Si-H wag) mode have combined to give the observed progression. As before, Table 6.12 gives the assignments and details of the progression.
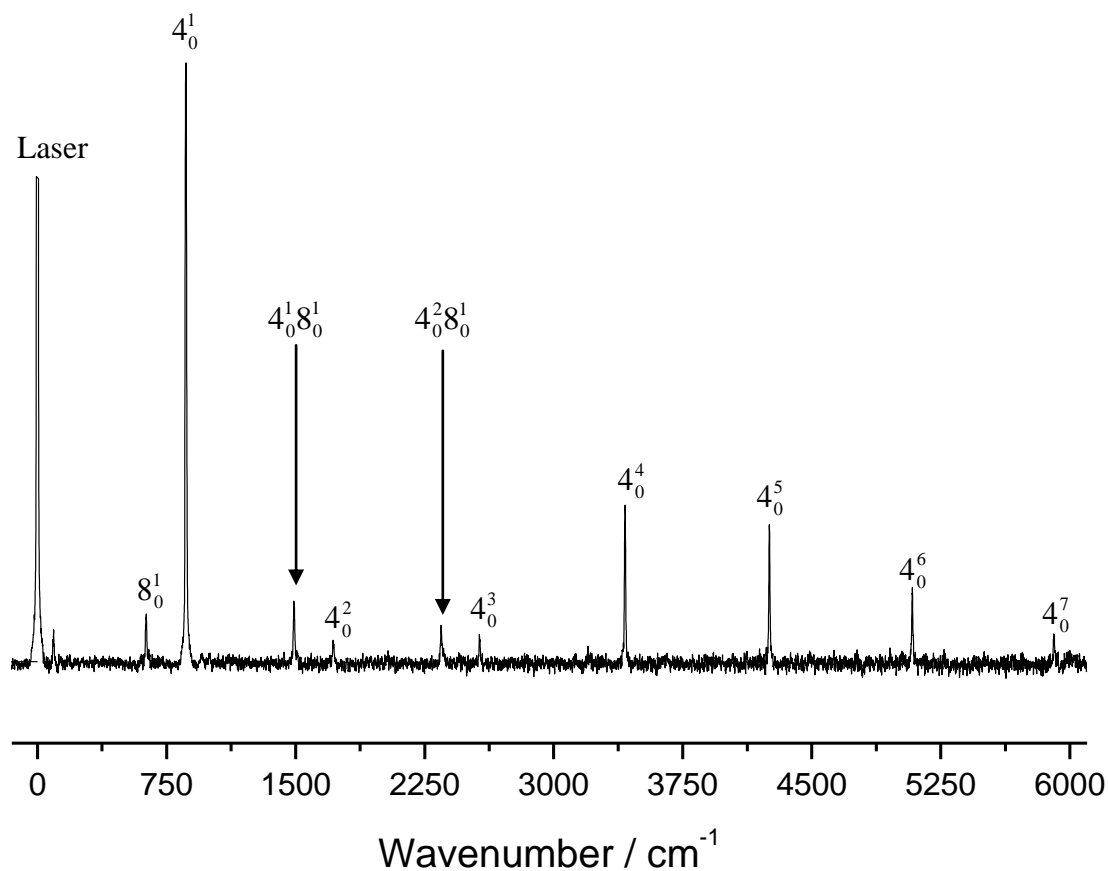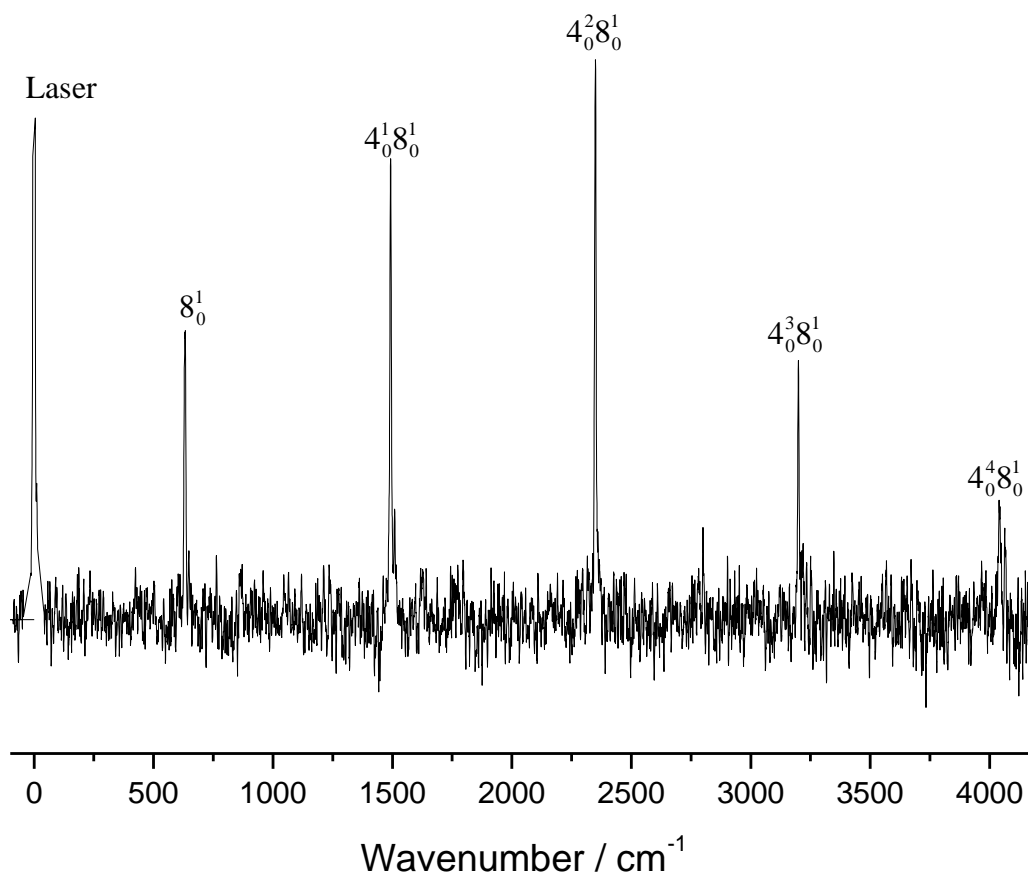
Figure 6.15: The dispersed fluorescence of the strong $^P Q_1$ branch of the $8^1_0$ vibrational band of HSiNCO showing peak assignments. The spectrum was recorded by averaging 2000 laser shots using a slit-width of 250 μm over the range 15600-21200 cm$^{-1}$.

Table 6.12: Assignment for each peak, position of the peaks relative to the laser (in cm$^{-1}$) and peak position relative to the previous peak in the progression (in cm$^{-1}$) for the dispersed fluorescence spectrum obtained by pumping the $^PQ_1$ branch of the $6_0^1$ band of HSiNCO in the $\tilde{X}\,^1A'$ electronic state.

| Assignment | Peak position relative to laser | Peak position relative to previous peak in progression |
|---|---|---|
| $8_0^1$ | 633.21 | 633.21 |
| $4_0^1 8_0^1$ | 1492.05 | 858.84 |
| $4_0^2 8_0^1$ | 2344.68 | 852.63 |
| $4_0^3 8_0^1$ | 3190.42 | 845.74 |
| $4_0^4 8_0^1$ | 4029.85 | 839.43 |

For comparison, the *ab initio* values determined for the ground state vibrational modes are given in Table 6.13.

Table 6.13: Vibrational assignments and wavenumber values for the ground ($\tilde{X}\,^1A'$) state vibrational modes of HSiNCO calculated at the MP2(FC)/aug-cc-pVTZ level. All values are given in cm$^{-1}$.

| Vibrational mode (symmetry) | Assignment | MP2(FC)[a] (harmonic) | MP2(FC)[a] (anharmonic) |
|---|---|---|---|
| $\nu_1$ (a′) | N-C-O antisymmetric stretch | 2309.613 | 2274.066 |
| $\nu_2$ (a′) | Si-H stretch | 2093.387 | 2016.993 |
| $\nu_3$ (a′) | N-C-O symmetric stretch | 1408.247 | 1406.928 |
| $\nu_4$ (a′) | Si-H in-plane wag | 885.895 | 869.795 |
| $\nu_5$ (a′) | Si-N stretch | 641.211 | 625.685 |
| $\nu_6$ (a′) | N-C-O in-plane bend | 568.226 | 563.672 |
| $\nu_7$ (a′) | Si-N-C bend | 101.063 | 94.097 |
| $\nu_8$ (a″) | N-C-O out-of-plane bend | 637.918 | 634.159 |
| $\nu_9$ (a″) | Si-N-C out-of-plane bend | 157.560 | 145.219 |

[a] Unscaled wavenumbers

### 6.4.10 Anharmonic Analysis

As was the case with HSiNC in Chapter 4, there is not enough data from the LIF spectra to calculate any meaningful anharmonic terms for HSiNCO, as not enough vibrational bands have been observed. Therefore, the following anharmonic analysis relies solely on the DF spectra discussed above. Using the DF data given in Tables 6.10, 6.11 and 6.12 above it is only possible to carry out an anharmonic analysis on the $\nu_4$ vibrational mode of HSiNCO. To do this the standard power series expression shown in Equation [6.1] was used. In this case, unlike in HSiNC, the $\nu_4$ progression has been observed in more than one vibrational band so it is possible to compare the result between these bands as well as with the anharmonic calculation.

$$
\begin{aligned}
G_{\nu_1\nu_2\nu_3\ldots} = {} & \omega_1\nu_1 + \omega_2\nu_2 + \omega_3\nu_3 + \ldots + x_{11}\left(\nu_1 + \frac{1}{2}\right)^2 + x_{22}\left(\nu_2 + \frac{1}{2}\right)^2 + x_{33}\left(\nu_3 + \frac{1}{2}\right)^2 + \\
& x_{12}\left(\nu_1 + \frac{1}{2}\right)\left(\nu_2 + \frac{1}{2}\right) + x_{13}\left(\nu_1 + \frac{1}{2}\right)\left(\nu_3 + \frac{1}{2}\right) + x_{23}\left(\nu_2 + \frac{1}{2}\right)\left(\nu_3 + \frac{1}{2}\right) + \ldots
\end{aligned}
\tag{6.1}
$$

As the only observed progression in the DF spectra was for the $\nu_4$ vibrational mode the analysis is very simple, and Equation [6.1] collapses down to the form given in Equation [6.2].

$$
G_{\nu_4} = \omega_4\nu_4 + x_{44}\left(\nu_4 + \frac{1}{2}\right)^2
\tag{6.2}
$$

This little amount of information still gives an indication of the accuracy of the theoretically determined values for this particular mode with regards to the anharmonic frequency calculation carried out at the MP2(FC)/aug-cc-pVTZ level of theory. The DF data given in Tables 6.9, 6.10 and 6.11 have been fitted to Equation [6.2], and the results of the fit are given in Table 6.14 together with a comparison of the values obtained by *ab initio* methods. As in Chapter 4 this procedure was carried out using the *Anharmonic_v1.0.m* program written in MATLAB®[19] by the author, a copy of which is given in the addendum. As can be seen by the data there is good agreement between the experimentally determined values and those determined by the anharmonic *ab initio* calculation.

Table 6.14: Table showing a comparison between the experimentally and theoretically determined values for the anharmonic terms in the $\nu_3$ vibrational mode. All values are given in cm$^{-1}$.

| Vibrational constant | Energy from $0_0^0$ band DF spectrum | Energy from $6_0^1$ band DF spectrum | Energy from $8_0^1$ band DF spectrum | Energy from anharmonic calculation[b] |
|---|---|---|---|---|
| $\omega_4$ | 869.12 (79) | 868.44 (18) | 866.33 (79) | 869.80 |
| $x_{44}$ | -3.29 (18) | -3.04 (3) | -3.40 (17) | -2.77 |

[a] Numbers in parentheses are $1\sigma$ uncertainties in units of the last significant digit
[b] Calculated at the MP2(FC)/aug-cc-pVTZ level of theory

## 6.5    Concluding Remarks

In this chapter we have seen the first electronic spectroscopic study of the $\tilde{A}\,^1A'' - \tilde{X}\,^1A'$ transition of the HSiNCO species. This is the first spectroscopic study ever conducted on this particular species. In Chapter 5, a detailed theoretical study of the [H, Si, N, C, O] isomers was carried out, and the data calculated for the HSiNCO isomer there has been used to support the assignment of the observed spectra in this chapter.

Detailed rotational analysis has been carried out on the $0_0^0$ band, where high-resolution LIF spectra have been taken in collaboration with Dr C. M. Western at the University of Bristol. The resulting analysis has provided assessment of rotational and quartic centrifugal distortion constants to high accuracy, in both the ground ($\tilde{X}\,^1A'$) and excited ($\tilde{A}\,^1A''$) states. Both the ground and excited state constants appear to be in good agreement with those determined by the theoretical work discussed in Chapter 5.

A number of the ground state vibrational bands have been tentatively assigned based on the *ab initio* predictions of anharmonic vibrational frequencies together with dispersed fluorescence study of the $\nu_4$ (Si-H wag) vibrational mode. This data has provided the assessment of the $\omega_4$ and $x_{44}$ anharmonic terms for the $\nu_4$ vibrational mode. The assessment of these terms shows very good agreement with those predicted by anharmonic MP2(FC) *ab initio* calculation.

As was seen in the LIF study of HSiNC in Chapter 4, the apparent appearance of 'forbidden' transitions corresponding to $\Delta K_a = 0$ and $\pm 2$ are present. These peaks,

known as 'axis-switching' peaks, have been analysed from both an experimental and theoretical point of view to determine the axis-switching angle. The determination of this angle has been carried out in two ways; a trial and error approach based on simulation versus experimental data, and accurate determination following the approach proposed by Hougen and Watson[1] based on the high level theoretical (SAC/SAC-CI) data to obtain geometries for the ground ($\tilde{X}^1A'$) and excited ($\tilde{A}^1A''$) states. In this case there is some discrepancy between these methods with the experimental data providing and axis-switching angle of ~0.6° ±2°, while the theoretical data provides a prediction of only 0.3° ±2°. This difference is tentatively attributed to poor geometric prediction from the *ab initio* calculations, and is most likely to arise as a result of poor prediction of the Si-N-C angle for which the axis-switching angle appears particularly sensitive.

There is clearly scope for further spectroscopic work on the HSiNCO species to provide firmer structural data and indeed improve on the fundamental constants obtained here. As this is the first spectroscopic observation of this species there is a lack of data to compare against, and particularly useful would be a microwave study on the ground state of HSiNCO to provide accurate structural data. On top of this are the other isomeric species discussed in Chapter 5 all of which could potentially be observed using standard microwave techniques.

From a vibronic perspective, it would be interesting to investigate some of the other vibrational bands at higher resolution, to investigate any possible perturbations which may exist between those bands which are especially close in vibrational wavenumbers, as well as to hopefully obtain further anharmonic terms to add to the very limited amount determined here.

## 6.6   REFERENCES FOR CHAPTER 6

(1)     Hougen, J. T.; Watson, J. K. G. *Can. J. Phys.* **1965**, *43*, 298.
(2)     LabVIEW; 7.0 ed.; National Instruments, 2003.
(3)     Ashworth, S. H.; Elks, J. M. F.; Western, C. M. *Chem. Phys. Lett.* **2000**, *328*, 197.
(4)     Chekhlov, O. V.; Fitzpatrick, J. A. J.; Rosser, K. N.; Western, C. M.; Ashworth, S. H. *J. Mod. Opt.* **2002**, *49*, 865.
(5)     Frisch, M. J.; Trucks, G. W.; Schlegel, H. B.; Scuseria, G. E.; Robb, M. A.; Cheeseman, J. R.; Montgomery, J., J. A.; Vreven, T.; Kudin, K. N.; Burant, J. C.; Millam, J. M.; Iyengar, S. S.; Tomasi, J.; Barone, V.; Mennucci, B.; Cossi, M.; Scalmani, G.; Rega, N.; Petersson, G. A.; Nakatsuji, H.; Hada, M.; Ehara, M.; Toyota, K.; Fukuda, R.; Hasegawa, J.; Ishida, M.; Nakajima, T.; Honda, Y.; Kitao, O.; Nakai, H.; Klene, M.; Li, X.; Knox, J. E.; Hratchian, H. P.; Cross, J. B.; Bakken, V.; Adamo, C.; Jaramillo, J.; Gomperts, R.; Stratmann, R. E.; Yazyev, O.; Austin, A. J.; Cammi, R.; Pomelli, C.; Ochterski, J. W.; Ayala, P. Y.; Morokuma, K.; Voth, G. A.; Salvador, P.; Dannenberg, J. J.; Zakrzewski, V. G.; Dapprich, S.; Daniels, A. D.; Strain, M. C.; Farkas, O.; Malick, D. K.; Rabuck, A. D.; Raghavachari, K.; Foresman, J. B.; Ortiz, J. V.; Cui, Q.; Baboul, A. G.; Clifford, S.; Cioslowski, J.; Stefanov, B. B.; Liu, G.; Liashenko, A.; Piskorz, P.; Komaromi, I.; Martin, R. L.; Fox, D. J.; Keith, T.; Al-Laham, M. A.; Peng, C. Y.; Nanayakkara, A.; Challacombe, M.; Gill, P. M. W.; Johnson, B.; Chen, W.; Wong, M. W.; Gonzalez, C.; Pople, J. A. Gaussian 03; Revision D.02 ed.; Gaussian Inc.: Wallington CT, **2004**.
(6)     Dunning, T. H. *J. Chem. Phys.* **1989**, *90*, 1007.
(7)     Kendall, R. A.; Dunning, T. H.; Harrison, R. J. *J. Chem. Phys.* **1992**, *96*, 6796.
(8)     Woon, D. E.; Dunning, T. H. *J. Chem. Phys.* **1993**, *98*, 1358.
(9)     Becke, A. D. *J. Chem. Phys.* **1993**, *98*, 5648.
(10)    Frisch, M. J.; Head-Gordon, M.; Pople, J. A. *Chem. Phys. Lett.* **1990**, *166*, 275.
(11)    Frisch, M. J.; Head-Gordon, M.; Pople, J. A. *Chem. Phys. Lett.* **1990**, *166*, 281.
(12)    Head-Gordon, M.; Pople, J. A.; Frisch, M. J. *Chem. Phys. Lett.* **1988**, *153*, 503.
(13)    Møller, C.; Plesset, M. S. *Phys. Rev.* **1934**, *46*, 618.
(14)    Pople, J. A.; Head-Gordon, M.; Raghavachari, K. *J. Chem. Phys.* **1987**, *87*, 5968.
(15)    Nakatsuji, H. *Chem. Phys. Lett.* **1978**, *59*, 362.
(16)    Dixon, R. N.; Wright, N. G. *Chem. Phys. Lett.* **1985**, *117*, 280.
(17)    Harjanto, H.; Harper, W. W.; Clouthier, D. J. *J. Chem. Phys.* **1996**, *105*, 10189.
(18)    Harper, W. W.; Clouthier, D. J. *J. Chem. Phys.* **1997**, *106*, 9461.
(19)    MATLAB; 7.4.0.287 (R2007a) ed.; The MathWorks, Inc., **2007**.
(20)    Western, C. PGOPHER; 5.2.343 ed.; Bristol laser group: Bristol, **2005**; A program for simulating rotational structure; http://pgopher.chm.bris.ac.uk.
(21)    Durig, J. R. *Vibrational spectra and structure : a series of advances. Vol.6*; Elsevier: Amsterdam ; Oxford, **1977**.
(22)    Pickett, H. M. SPFIT; a linear least squares fitting program, **1990**.
(23)    Plusquellic, D. F. Jb95 Spectral Fitting Program, (verison 2.05.1); http://physics.nist.gov/jb95 **2002**.

# Chapter Seven

*Theoretical Study of the*

*[H, Ge, N, C, O] isomers*

## 7.1    *Introduction*

As with the organosilicon species discussed in previous chapters, germanium containing species have attracted a lot of renewed attention in recent years from various fields. The main reasons for this interest stems from the fact that transient molecules containing silicon and germanium are important intermediates in the production of semiconductors using chemical vapour deposition (CVD) methods. For example, the laser-initiated photochemical decomposition of gaseous $SiH_4$ or $GeH_4$, by a KrF filled excimer laser (248 nm), results in the formation of semiconductor layers through CVD. Experimental studies have shown that the hydrides XH, $XH_2$ and $XH_3$ (X=Si, Ge) are important intermediate radicals in governing the reaction from the $XH_4$ precursor to the final $X_n$-film product.[1] Therefore, it is essential to obtain knowledge of properties such as dissociation energies, heats of formation, and possibility of vibrational frequencies and/or electronic transition energies (for optical identification of intermediates) to further our understanding of the deposition mechanism.

Until very recently, there has been little interest in the potential of germanium species in the interstellar medium. In 2002, an atomic transition of Ge III (1088.46 nm) was detected and measured for the first time in the planetary nebulae (PNe) SwSt 1, BD + 30°3639, NGC 3132 and IC 4593.[2] As with the silicon containing species it is expected that as more and better laboratory data is collected for germanium containing species, such as GeO, GeC, $GeC_2$, GeCN and GeNC, it is just a matter of time before germanium containing species are found in the interstellar medium. However, up to now, no such gas-phase species have been found in space. As mentioned above, as well the astronomical interest, many recently investigated germanium compounds are thought to be important intermediates in a variety of semiconductor growth processes in the production of germanium films. Therefore, the development of spectroscopic methods for the detection, quantification and characterization of these intermediates is of practical as well as fundamental interest.

In view of the recent astronomical discoveries and the general importance of germanium species in the semiconductor industry, there has been a recent growth in the area of experimental and theoretical studies on germanium containing species. The first experimental study of GeH was investigated in 1966, and interestingly has not been revisited since.[3] More recently, $GeH_2$, GeCH, $GeX_2$ and HGeX (X=Cl, Br,

I) have all been studied using LIF spectroscopy.[4-11] All of these species are potentially important intermediates in CVD processes in the manufacturing of semiconductor films and all are potentially observable in the interstellar medium.

The recent renewed interest in germanium containing species has also led to a dearth of systematic theoretical studies on a number of species, both in support of the aforementioned experimental studies and with a view to opening new avenues of experimental work.[12-16] Of particular interest here are those studies carried out by Wang *et al.*[15,16] which detail theoretical studies on the germanium cyanide radical (GeCN) and the various [H, Ge, C, N] isomers as these are analogous with species of interest in this thesis. As with the [H, Si, C, N] isomers mentioned in Chapter 4, it is found that the most stable isomer is HGeCN followed by HGeNC, and it would be interesting to see if either of these species could be spectroscopically observed.

The work in this chapter continues the systematic study of Wang *et al.* adding to their work on GeCN and the [H, Ge, C, N] isomers. The work here focuses on the [H, Ge, N, C, O] species. In view of the abundance of H, N, C and O in space, the combination of these elements with Ge are promising candidates for future astronomical detection. Added to this is the work detailed in the preceding chapters of this thesis detailing both the experimental and theoretical findings for the [H, Si, N, C, O] species. To date, there have been no previous studies on the [H, Ge, N, C, O] isomers. This chapter aims to look at possible isomers of [H, Ge, N, C, O] using theoretical methods and to investigate their stability and spectroscopic constants to aid in the detection of these species in both the laboratory and potentially in space.

## 7.2    *Computational Methods*

For the most part calculations were carried out using the Gaussian 03 suite of programs.[17] The geometries of the different species and their isomers were fully optimized at different levels of theory using the augmented triple zeta correlated consistent basis set (aug-cc-pVTZ) of Dunning *et al.*[18-20]. The methods used include, the hybrid density functional method B3LYP[21], the 2nd order Møller-Plesset method (MP2)[22-25] and the Quadratic configuration interaction method including singles and doubles, QCISD[26]. Further single-point calculations were carried out using QCISD(T), with the structure fixed to the QCISD structure[26]. For accurate relative energies and evaluation of thermodynamic properties, the G3B3 and G3MP2

methods, as implemented in Gaussian03, were used.[27,28] Vibrational wavenumbers were calculated at the MP2 and B3LYP levels of theory to check if the optimised structures were true minima. The MP2 calculations were carried out using both full electron correlation (*i.e.*, including the core electrons) [MP2(Full)] and the standard frozen core method [MP2(FC)]. As the difference in the ZPE between MP2(FC) and MP2(Full) was negligible the MP2 energies were corrected using the MP2(FC) ZPE. For the QCISD calculations the vibrational frequencies were calculated using the aug-cc-pVDZ basis set[18-20]. Finally the five lowest isomers were optimised using the SAC-CI / cc-pVDZ level of theory to obtain more accurate energies and geometries for both the ground and excited states.

## 7.3    Results and Discussion

A series of calculations were carried out on a number of different isomeric forms of [H, Ge, N, C, O]. The optimised geometries and vibrational frequencies of approximately 17 different isomers were calculated at the B3LYP level of theory. A full list of these isomers may be found in Appendix D. Figure 7.1 shows the 10 lowest [H, Ge, N, C, O] isomers in the $\widetilde{X}\,^1A'$ electronic state using the MP2(FC) level theory. In all cases, the electronic configuration of the singlet species is $21\,a'^2\;6\,a''^2$. As can be seen from Figure 7.1 the five lowest isomers (S1-S5) all lie within approximately 9 kcal/mol of each other.

At the MP2(FC) level of theory the lowest isomer (S1) was found to be *cis*-HOGeCN, while the *trans* form of this isomer (S2) lies 1.13 kcal/mol higher in energy. Isomers S3 and S4 are the isocyanide analogues to species S1 and S2, and are 3.68 and 5.29 kcal/mol higher in energy, respectively than isomer S1. This mirrors what was seen in the isomers of [H, Si, N, C, O] in Chapter 5. Isomer S5 is the germanium analogue to the HSiNCO species discussed previously and is 9.16 kcal/mol higher in energy than the S1 isomer. As before, it was found that the corresponding cyanate species (HGeCNO) is significantly higher in energy (~79 kcal/mol) than the HGeNCO isomer which is similar to that seen for HNCO/ HCNO[29,30] (0.0/70.1 kcal/mol) and $CH_3NCO/CH_3CNO$[31] (0.0/54.9 kcal/mol). There is a significant jump in energy to the next isomer (S6) which is HGe(O)CN, the germanium analogue to formyl cyanide, and is 28.03 kcal/mol higher in energy than isomer S1. Unlike that seen in the silicon case, the isocyanide analogue HGe(O)NC turns out to be significantly higher in energy and occupies the S11 position with an

energy 37.81 kcal/mol higher in energy than the S1 isomer. The S7 isomer is a cyclic system with the germanium, nitrogen and carbon forming a three-membered ring, with the oxygen double bonded to the carbon and the hydrogen bonded to the nitrogen, and is 30.6 kcal/mol higher in energy than the S1 isomer. The S8 and S9 isomers, which are cyanatogermylene and isocyanatogermylene, are found to be 31.4 and 31.6 kcal/mol, respectively higher in energy than the S1 isomer. Lastly the S10 isomer is another cyclic system, this time with the germanium, oxygen and carbon forming a three-membered ring, with the N-H fragment bound to the carbon with a double bond, and is 37.8 kcal/mol higher in energy than the S1 isomer.

In order to check if the MP2(FC) calculations were giving the correct ordering of the five lowest isomers, further calculations were carried out using different levels of theory. It is worth noting that this is different to the route taken in the analogous silicon system, where the lowest seven isomers were examined at higher levels of theory. The reasons for this are that it is far more computationally demanding to examine these germanium-containing species, and the fact that there is such a large energy gap in between isomers S5 and S6. To look at the effect core electrons have on the relative energies of the proposed isomers the MP2 calculations were re-run with inclusion of the core electrons. Higher level calculations were carried out at the QCISD(T) level of theory as implemented in the G03 package, while to test the reliability of the DFT methods the B3LYP hybrid functional was employed. For each calculation the geometries were re-optimized and where possible the vibrational frequencies calculated. In the case of the QCISD(T) calculations, the geometry was re-optimised at the QCISD level of theory and a single-point calculation at this geometry was carried out, using the aug-cc-pVDZ basis set. Like the analogous silicon system, the QCISD(T) calculations were carried out with the inclusion of core electrons to examine what effect this would have to the energies of the isomers.

Table 7.1 shows the relative energy differences between the lowest five isomers found at each level of theory. The results in Table 7.1 show there is some confusion with regards to the ordering of the lowest lying isomers. All of the calculations show that the S1 isomer is the lowest in energy. The B3LYP result shows that all five of the isomers are lying within ~3 kcal/mol of one another, which seems unlikely given the findings of the analogous silicon system studied previously. The results show that the second and third lowest energy isomers are S3 (the isocyanide form of S1) and

S5, respectively. After this the S2 isomer is only 0.1 kcal/mol higher in energy, and S4 predicted to be the highest in energy. The MP2 (both frozen core and full) calculations show good agreement with the QCISD(T) calculations, predicting the ordering of the isomers as shown in Figure 7.1.

The differences between MP2(FC) and QCISD(T) values are minimal for isomer S2, but after that there is some discrepancy. For isomer S3 the MP2(FC) energy is 3.7 kcal/mol higher in energy relative to S1, while for the QCISD(T) calculation it is only 1.9 kcal/mol. For isomer S4 the MP2(FC) energy is 5.3 kcal/mol higher in energy than isomer S1, while the QCISD(T) value is 3.8 kcal/mol. For isomer S5 there is better agreement between the two methods with the MP2(FC) value being 9.2 kcal/mol and the QCISD(T) value is 10.0 kcal/mol.

The inclusion of the core electrons is important in the case of the MP2 calculations, especially for the lowest four isomers. There is complete agreement, in terms of the ordering of the five lowest isomers with the MP2(FC) calculations. However, in terms of the relative energies there is far better agreement between the MP2(Full) and QCISD(T) values for the lowest four isomers when the core electrons are included in the calculation. The value for the S5 isomer is closer to the QCISD(T) value for the MP2(FC) calculation. The inclusion of core electrons in the QCISD(T) case appears to make little difference to the outcome of the calculations.

The G3MP2 and G3B3 multilevel methods used in the silicon study are not available to systems containing $3^{rd}$ row atoms (such as germanium) as the GTlarge basis set used does not cover $3^{rd}$ row atoms. Therefore, to obtain accurate energies and thermodynamic data a similar, but slightly less accurate method was used. The G2MP2 multilevel method was carried out on the lowest five isomers (in the $\tilde{X}\,^1A'$ electronic state) in order to determine more accurate relative energies.[32-34]

As can be seen from Table 7.1 the G2MP2 results seem to lie somewhere between the MP2(Full) and QCISD(T) results, but the results of the G2MP2 method are indicating that isomer S3 is the second lowest lying isomer and not isomer S2 as found at the other levels of theory.

Table 7.1: The energies of the lowest five [H, Ge, N, C, O] isomers (in kcal/mol). All energies are relative to isomer S1 (as in Figure 7.1). All Energies have been ZPE corrected.

| Isomer | B3LYP | MP2[a] | QCISD(T)[b] | G2MP2 | SAC-CI |
|--------|-------|----------|-------------|-------|--------|
| S1 | 0.0 | 0.0 (0.0) | 0.0 (0.0) | 0.0 | 0.0 |
| S2 | 1.4 | 1.1 (1.0) | 1.3 (1.2) | 1.2 | 0.7 |
| S3 | 0.9 | 3.7 (1.8) | 1.9 (1.8) | 1.1 | 3.7 |
| S4 | 2.7 | 5.3 (3.3) | 3.8 (3.6) | 2.7 | 5.2 |
| S5 | 1.3 | 9.2 (6.1) | 10.0 (9.9) | 6.6 | 8.2 |

[a]Number in parentheses are the MP2 values with inclusion of the core electrons [MP2(Full)]
[b] Zero-point energy calculated at QCISD level of theory with an aug-cc-pVDZ basis set. Number in parentheses are the QCISD(T) values with inclusion of the core electrons.
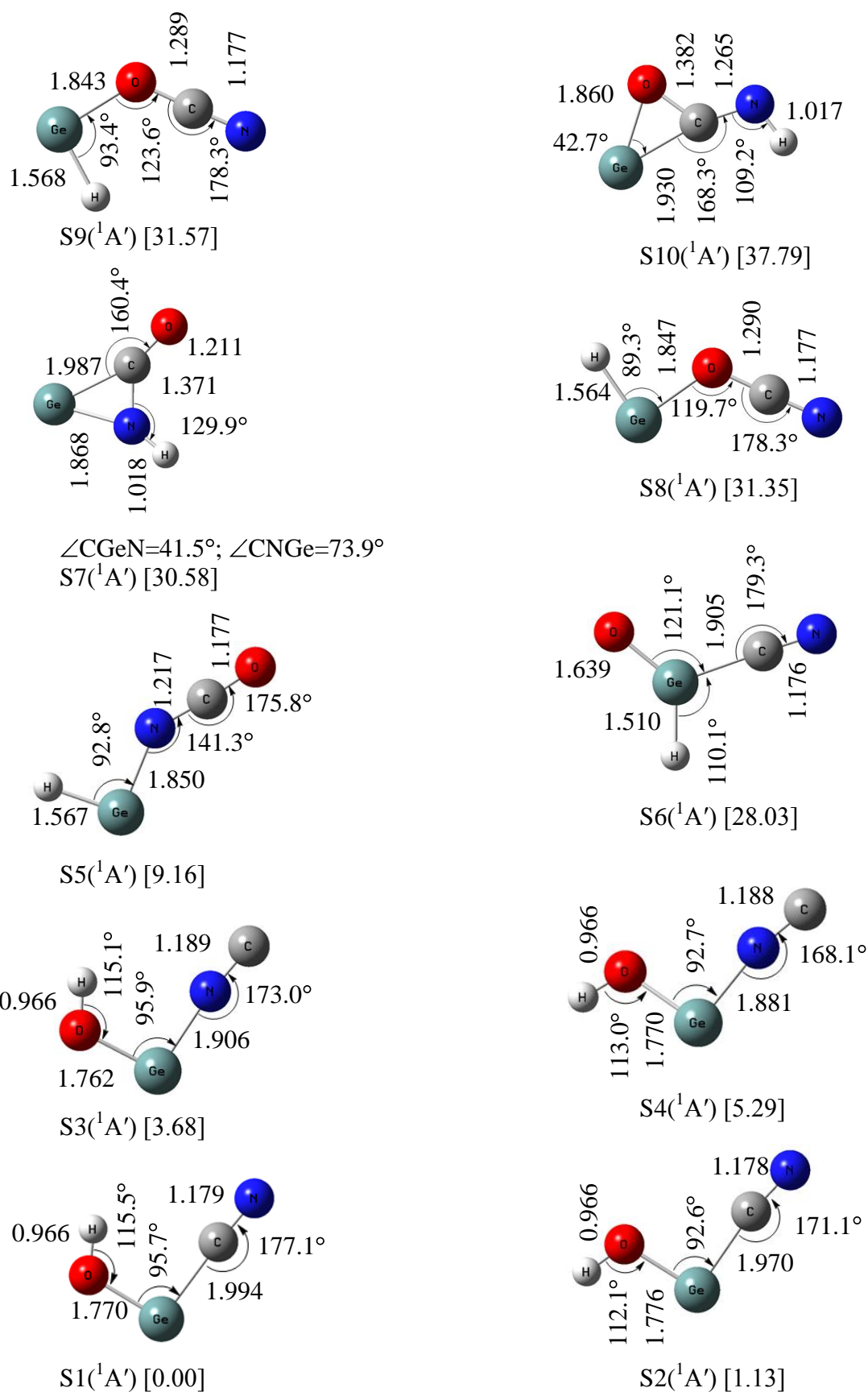
Figure 7.1: Optimized geometries (in Å and degrees) of the lowest singlet states of the [H, Ge, C, N,O] system computed at the MP2(FC)/aug-cc-pVTZ level of theory. Relative energies [in kcal/mol] to the lowest energy isomer.

### 7.3.1 HOGeCN/HOGeNC

As can be seen from Figure 7.1 the geometry of these germanols shows a short O-H bond length, which is analogous to that observed for the silicon case seen in the previous chapter. In fact, the structures of these germanols are in complete agreement with the structures determined for the analogous silicon containing isomers in the previous chapter. The only changes are a lengthening of the Ge-O and Ge-C/N bonds when compared to the Si-O and Si-C/N bonds. This change intuitively makes sense as the Ge atom is larger than the Si atom. The other changes in the structures make less sense as there is a reduction in the H-O-Ge and O-Ge-C/N angles in swapping the Si for a Ge atom. The average Ge-O bond length is 1.782 Å, which is much shorter than the covalent radii sum (1.86 Å). This mirrors what was seen in the silicon system studied in the previous chapter, and is similar to that seen in other germanols.[35] The C-N/N-C bond lengths are similar to that observed in experimental studies of HSiCN/NC, and previous theoretical work on GeCN and HGeCN/NC.[15,16,36] These values are longer than the average CN/NC bond. In the case of the silicon containing isomers studied in Chapter 5, the two most interesting aspects were the O-Si-C/N and Si-O-H angles. In this case, the same features are present with the O-Ge-C/N angle being small, ~93° and is similar to the H-Si-X angle found in HSiNC/CN (~95°) in Chapter 4, while the Ge-O-H angle is inline with that observed for the analogous [H, Si, N, C, O] isomers (Chapter 5) and alkylsilanols (~120°).

*7.3.1.1 Natural Bond Analysis: (cis/trans) HOGeCN*

Natural bond analysis (NBA) on HO-GeCN indicates that C-N bond is triple in nature with the Ge-O bond being a double bond, while the bonding between Ge-C and O-H is single in nature. The bonding of Ge-O is counter-acted slightly by population of anti-bonding MOs and results in the Ge-O bond length being 0.1 Å longer than the diatomic GeO, which is regarded to be double bonded.[37] The NBA also indicates the presence of three lone-pairs situated on the Ge, O and N. The Ge lone pair has *s* character (*cis*: $sp^{0.17}$ (14.2% *p* character), *trans*: $sp^{0.17}$ (14.5% *p* character)). For O and N the lone-pairs are, to a fair extent, hybridised; for O *cis*: $sp^{1.18}$ (54.0% *p* character) and *trans*: $sp^{1.04}$ (50.9% *p* character), while for N *cis*: $sp^{0.93}$ (48.0% *p* character) and *trans*: $sp^{0.92}$ (47.8% *p* character). The bonding between Ge-O is almost pure *p* in character on the germanium atom (*cis*: 89.6% *p* character, *trans*: 90.9% *p* character), while the bonding between Ge-C is again almost pure *p* in

character on the germanium atom (*cis*: 92.9% *p* character, *trans*: 91.8% *p* character). The almost pure *p* character of these MOs explains the relatively small O-Ge-C angle seen in both isomers. No additional resonance structures are thought to contribute to the structural characteristics of these isomers. The NBA also shows excellent agreement with the analogous silicon containing isomers.

*7.3.1.2 Natural Bond Analysis: (cis/trans) HOGeNC*

The NBA on HO-GeNC indicates that N-C bond is triple in nature, the bonding between Ge-N and O-H bonds are single in nature, while like HO-GeCN the Ge-O is considered a double bond. The NBA indicates the presence of three lone-pairs situated on the Ge, O and C. The Ge lone pair has *s* character (*cis*: $sp^{0.16}$ (13.7% *p* character), *trans*: $sp^{0.16}$(13.8% *p* character)), while for O and C the lone-pair are hybridised to a fair extent; for O *cis*: $sp^{1.18}$ (54.0% *p* character) and *trans*: $sp^{1.04}$ (50.8% *p* character), while for C *cis*: $sp^{0.46}$ (31.5% *p* character) and *trans*: $sp^{0.46}$ (31.4% *p* character). The bonding between Ge-O is almost pure *p* in character on germanium atom (*cis*: 86.6% *p* character, *trans*: 91.1% *p* character), while the bonding between Ge-N again is almost pure *p* in character on the germanium atom (*cis*: 93.1% *p* character, *trans*: 91.8% *p* character). As seen for HO-GeCN, the almost pure *p* character of these MOs explains the relatively small O-Ge-N angle as seen in both isomers. Again, there is thought to be no additional resonance structures that will contribute to the structural characteristics for these isomers. Again, there is excellent agreement between the germanium and silicon containing isomers.

*7.3.1.3 Isomerisation*

For the *cis* and *trans* forms of HO-GeCN and HO-GeNC, calculations were performed on both species in order to determine the potential of rotation of the hydrogen about the oxygen atom.

Figure 7.2 shows the potential for both HO-GeCN and HO-GeNC. The potentials were generated by changing the HOGeC/HOGeN dihedral angle, while relaxing the rest of the structure at the B3LYP level of theory using the aug-cc-pVTZ basis set. A total of 35 points were calculated for each species. From Figure 7.2 it can be seen that potential has a double minimum at 0 and 180° corresponding to the *cis* and *trans* forms, respectively. Where $\theta$ is the dihedral angle between H-O-Ge-C/N. In both cases the *trans* form is higher in energy by ~0.3 kcal/mol, which is opposite to that

found for formic, thiolformic, thionformic and dithioformic acids[38]. As before, the potentials have been fitted using the function of Toro-Labbe *et al.*, [38,39]:

$$V(\theta) = \frac{1}{2}\Delta V^\circ (1 - \cos\theta) + \frac{1}{4}(k_t + k_c)(1 - \cos^2\theta) + \frac{1}{4}(k_t - k_c - \Delta V^\circ)(1 - \cos^2\theta)\cos\theta$$

[7.1]

The results from the fits are shown in Table 7.2 and are compared against the results found for HOSiCN and HOSiNC in Chapter 5. It can be seen that the germanium analogues have very similar values for all the parameters as one would expect with such a similar system. The barrier heights are very slightly lower than in the case of the silicon analogues.

As before, the values of $k_c$ and $k_t$ are slightly different from those of thiolformic and dithioformic acids with the $k_c$ force constant larger than $k_t$. These forces constants indicate that for the *trans* form there is a repulsive interaction between the hydrogen and the germanium and oxygen atoms. Delocalisation effects contribute to stabilising the *cis-* form, but these effects are too small to analyse fully. This is similar to what was seen in the silicon system in Chapter 5.

The parameters $\alpha$ and $\Delta V^{\ddagger}$ are the angle in which the potential is at a maximum and the barrier height, respectively. For HOGeCN $\alpha$=95.2° and $\Delta V^{\ddagger}$=3065.4 cm$^{-1}$, while for HOGeNC $\alpha$=95.7 and $\Delta V^{\ddagger}$=2828.8 cm$^{-1}$. On isomerisation the Ge-C/N bond length decreases by ~0.02 Å going from the *trans* to the *cis* forms which is most likely the result of delocalisation between H-O and Ge-C/N.

Table 7.2: Isomerisation Parameters[a] for HOGeCN and HOGeNC

| Parameters | HOGeCN | HOGeNC | HOSiCN | HOSiNC |
|---|---|---|---|---|
| $k_c$ | 17.11 | 14.43 | 18.63 | 15.93 |
| $k_t$ | 15.07 | 14.08 | 15.23 | 13.92 |
| $V_0$ | 1634.63 | 1557.62 | 1661.55 | 1513.67 |
| $V_1$ | -300.88 | -357.91 | -278.17 | -278.60 |
| $V_2$ | -1406.90 | -1246.45 | -1480.45 | -1304.99 |
| $V_3$ | 73.14 | 46.75 | 97.08 | 69.91 |
| $\Delta V_0$ | 455.5 | 622.3 | 362.2 | 417.4 |
| $\alpha_0$ | 95.23 | 95.67 | 95.42 | 95.29 |
| $\Delta V^{\ddagger}$ | 3065.36 | 2828.77 | 3169.04 | 2841.28 |

[a] $k_c$ and $k_t$ (force constants) in kcal mol$^{-1}$ rad$^{-2}$, $V_1, V_2, V_3, \Delta V_0$ and $\Delta V^{\ddagger}$ in cm$^{-1}$ and $\alpha_0$ in degrees.
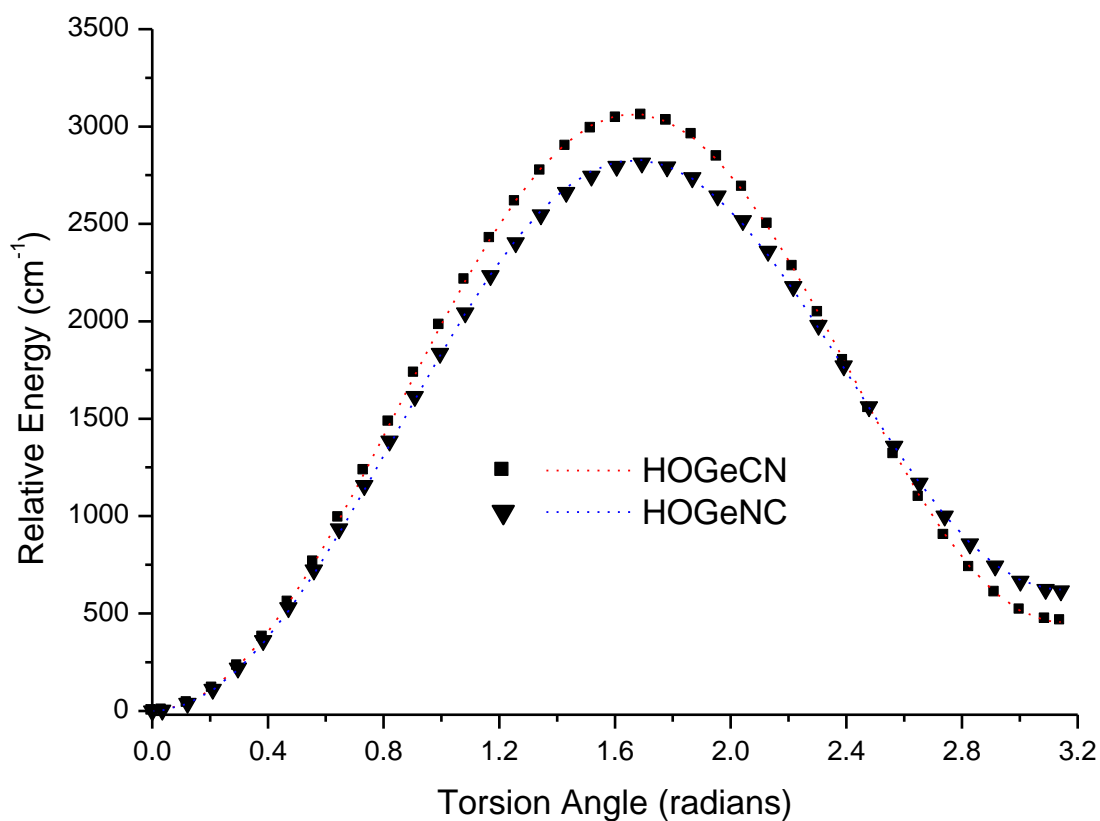


Figure 7.2: *cis* to *trans* isomerisation of HOGeCN and HOGeNC

*7.3.1.4 Vibrational Wavenumbers*

Vibrational wavenumbers have been calculated for all the species at the B3LYP and MP2(FC) levels of theory. Table 7.3 shows the ground electronic state unscaled vibrational wavenumbers for *cis*/*trans* HO-GeCN and *cis*/*trans* HO-GeNC. There is good agreement between the B3LYP and MP2(FC) results except for the C-N stretching mode where there is a 200 cm$^{-1}$ difference. The rotational constants at the equilibrium geometry are also given for each species in Table 7.3. At the MP2(Full) level of theory the dipole moments ($\mu_x/\mu_y$) of *cis* and *trans* HO-GeCN are 1.09/1.97, and 2.14/4.19 Debye, respectively, while for *cis/trans* HO-GeNC they are, 1.26/2.21 and 2.38/4.39 Debye, respectively. As was found with the NBA, there is great similarity between these values and those observed for the analogous silicon containing isomers. The dipole moments for all these species are sufficiently high enough that detection using microwave spectroscopy should be possible.

Table 7.3: Harmonic vibrational wavenumbers[a] [intensities (in km/mole)] and rotational constants (in GHz) of the five lowest [H,Ge,N,C,O] isomers in the $\widetilde{X}\,^1A'$ state at the B3LYP and MP2(FC) levels of theory

| Species | Wavenumbers (infared intensities) | Rotational Constants ($A$, $B$, $C$) |
|---|---|---|
| *cis*-HOGeCN | 114.1 (11), 170.7 (13), 333.2 (11), 404.3 (93), 526.5 (123), 681.4 (116), 846.3 (73), 2254.6 (51), 3814.4 (79) | 11.76590, 3.15376, 2.48711 |
| *cis*-HOGeCN[b] | 116.0 (11), 172.2 (14), 349.6 (7), 427.5 (97), 539.3 (124), 718.1 (119), 854.0 (66), 2072.0 (87), 3814.4 (92) | 11.88213, 3.22368, 2.53572 |
| *trans*-HOGeCN | 130.7 (2), 179.2 (0), 331.5 (3), 437.9 (104), 525.2 (83), 676.9 (99), 879.0 (113), 2261.5 (54), 3816.6 (105) | 12.14846, 3.17178, 2.51512 |
| *trans*-HOGeCN[b] | 130.7 (2), 181.6 (0), 344.1 (0), 461.1 (104), 550.8 (78), 713.7 (102), 887.4 (113), 2084.2 (89), 3816.7 (129) | 12.23606, 3.24024, 2.56184 |
| *cis*-HOGeNC | 104.3 (7), 110.7 (5), 284.0 (15), 445.5 (126), 511.0 (126), 686.5 (129), 831.0 (73), 2111.7 (398) 3805.0 (73) | 12.34270, 3.53288, 2.74669 |
| *cis*-HOGeNC[b] | 113.4 (9), 130.1 (7), 306.6 (15), 461.9 (133), 523.2 (125), 728.2 (134), 835.5 (67), 2039.0 (288), 3805.2 (88) | 12.24563, 3.60749, 2.78658 |
| *trans*-HOGeNC | 117.1 (1), 121.3 (0), 294.0 (0), 478.6 (140), 490.7 (83), 677.4 (103), 851.9 (119), 2116.2 (416), 3818.5 (98) | 12.66914, 3.56604, 2.78276 |
| *trans*-HOGeNC[b] | 122.1 (2), 136.1 (0), 310.5 (1), 495.9 (145), 514.5 (81), 720.7 (105), 855.6 (120), 2046.7 (303), 3820.4 (125) | 12.66914, 3.56604, 2.78276 |
| HGeNCO | 94.8 (3), 149.4 (0), 450.0 (81), 637.7 (22), 651.3 (22), 779.0 (38), 1413.2 (27), 1879.3 (415), 2295.8 (1624) | 77.66454, 1.81310, 1.77174 |
| HGeNCO[b] | 87.6 (3), 155.9 (0), 476.2 (86), 631.4 (22), 637.4 (16), 818.1 (44), 1383.6 (48), 2042.1 (404), 2300.6 (1563) | 72.39905, 1.84439, 1.79857 |

[a] Unscaled wavenumbers
[b] MP2(FC) calculations

*7.3.1.5 Excited States*

Calculations were carried out on the $\tilde{A}^1 A''$ excited state for both species at the MP2 and B3LYP levels of theory. The optimised structures are given in Figure 7.3 (E1 and E2). These calculations indicate that the O-Ge-C/N angle opens up to ~115° as expected with electron density being transferred to an out-of-plane *p* orbital on the germanium. At both the MP2(FC) and B3LYP levels theory, vibrational frequencies calculations gave an imaginary vibration for the H-O-Ge out-of-plane bending mode for both isomers, which probably indicates the optimised structure is a 1$^{st}$ order transition point.

*7.3.1.6 Out-of-Plane Excited States*

As the planar structures for the excited state isomers gave a negative wavenumber corresponding to the Ge-H out-of-plane wagging mode, further investigation was necessary. As with the analogous silicon isomers in Chapter 5, it was found that by allowing the hydrogen atom to bend out of the plane with respect to the rest of the molecule, lower energy isomers were found giving no negative wavenumbers indicating that the true minima had been located. The resulting isomer (labelled E1/E2 in Figure 7.4) has $^1 A$ symmetry and is lower in energy than the planar $^1 A''$ isomers.

This breaking of the symmetry in going from the ground state ($\tilde{X}^1 A'$) to the newly located excited state ($\tilde{A}^1 A$) provides a new problem in determination of the transition energy ($T_0$). It is not possible to carry out MP2 or B3LYP calculations on the out-of-plane structures, and it is not possible to carry out the CIS calculations on the ground state. Therefore it was necessary to carry out SAC-CI calculations similar to those detailed in Chapter 5. In this case, however, it is too computationally demanding to use the augmented cc-pVDZ basis set for optimisation, and indeed to carry out single point calculations using the cc-pVTZ basis set. Given these problems, the best estimate for the energies is obtained through using the cc-pVDZ basis set and optimising the structures for both ground and excited states affording the desired consistency between states.

E5 $\tilde{A}^1A''$ [50.18]
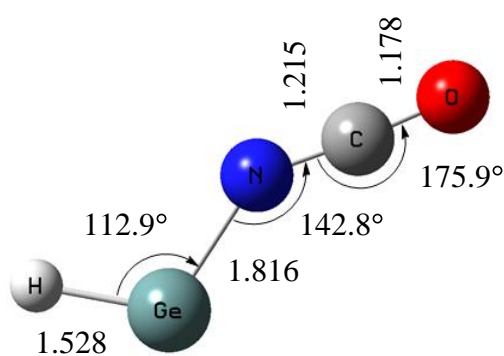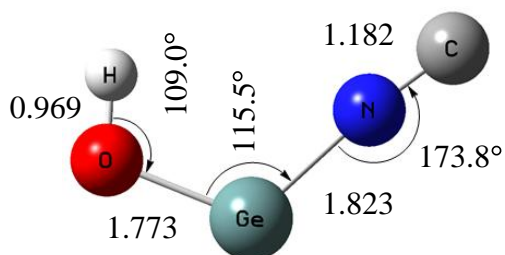


E3 $\tilde{A}^1A''$ [88.86]
Gives a single imaginary vibration
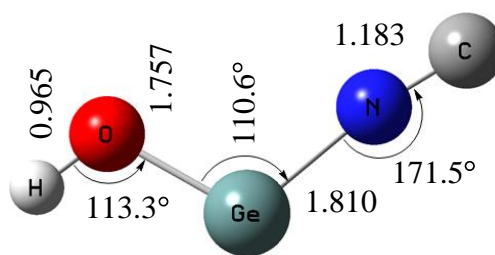


E4 $\tilde{A}^1A''$ [85.24]
Gives a single imaginary vibration
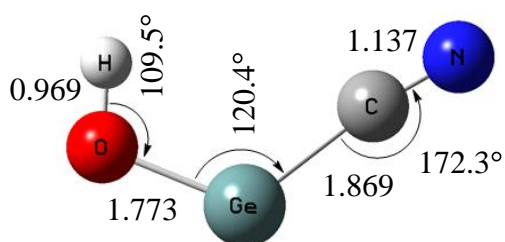


E1 $\tilde{A}^1A''$ [81.57]
Gives a single imaginary vibration
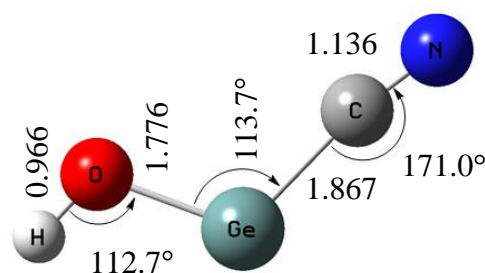


E2 $\tilde{A}^1A''$ [77.97]
Gives a single imaginary vibration

Figure 7.3: Optimized geometries of the excited states $\tilde{A}^1A''$ of the five lowest energy isomers given in Figure 7.1 (bond lengths in Å; bond angles in degrees) computed at the MP2(FC)/aug-cc-pVTZ level of theory. All energies [in kcal/mol] are relative to their corresponding $^1A'$ isomers as in Figure 7.1.
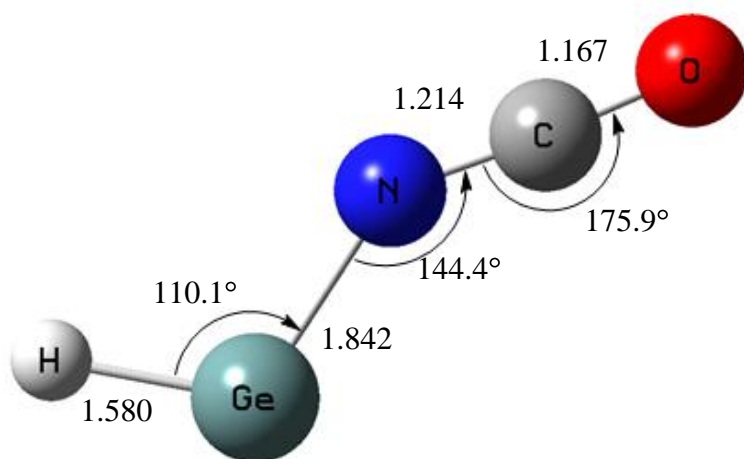
E5 $\tilde{A}^1A''$ [64.20]
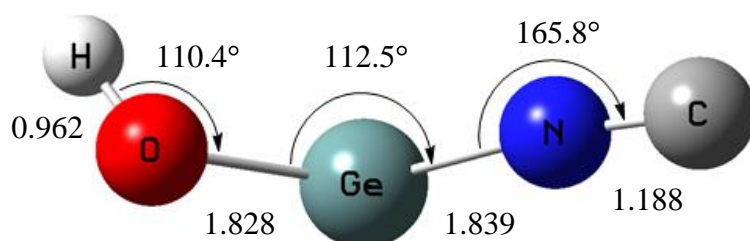
DNGeOH=-114.9°;
DOGeNC=+0.0°
E3/E4 $\tilde{A}^1A$ [26.14/24.61]
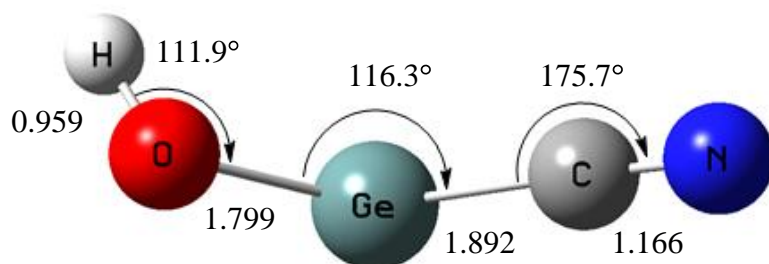
DCGeOH=-116.4°;
DOGeCN=+0.0°
E1/E2 $\tilde{A}^1A$ [34.57/33.90]

Figure 7.4: Optimized geometries of the excited states ($\tilde{A}^1A$ for S1-S4 and $\tilde{A}^1A''$ for S5) of the five lowest energy isomers given in Figure 7.1 (bond lengths in Å; bond angles in degrees) computed at the SAC-CI/cc-pVDZ level of theory. All energies [in kcal/mol] are relative to their corresponding $^1A'$ isomers calculated at the same level.

### 7.3.2  HGeNCO

The ground electronic state structure of HGeNCO is analogous to HSiNCO (see Chapters 5 and 6) with the H-Ge-X angle being ~93°. As in the silicon case, the small H-Ge-X angle is also seen for the analogous halogen species HGeX (X= Cl, Br, I) with the H-Ge-X angle going from 94.3°, 93.9° and 93.5°, respectively.[4,5] The Ge-H bond length of 1.567 Å is ~0.03 Å shorter than that observed for HGeX (X=Cl, Br, I),[4,5] ~0.05 Å longer than that observed in germane (GeH$_4$),[40] but very similar to that found for HGeCN/NC in a previous theoretical study.[16] As in the previous chapter, Table 7.4 compares the N=C and C=O bond distances against other molecules containing an isocyanate group. From Table 7.4 it can seen that in all cases the N=C bond is longer than the C=O bond.

As discussed in Chapter 5, the question of linearity or non-linearity of the N=C=O bond has been of much interest for several decades. As before, the natural bond analysis proposes three resonance structures with the N=C=O being the most probable, while $^+$N≡C-O$^-$ and $^-$N-C≡O$^+$ being the other minor forms. It is therefore possible that the N=C=O group is, in all probability, non-linear based on the proposed resonance structures.

Vibrational wavenumbers and rotational constants for HGeNCO in its ground electronic state were also calculated and are given in Table 7.3.  The dipole moments ($\mu_x/\mu_y$) at the MP2(Full) level of theory were calculated to be -0.75/-2.24 Debye, respectively. As before, there is good agreement between these values and those determined for the analogous silicon containing isomer. Again, the dipole moments are sufficiently high enough that the rotational spectrum of HGeNCO should be observable using standard microwave spectroscopy techniques.

Table 7.4: The distances (in Å) and angles (in degrees) for molecules containing the isocyanate group

| Compound | r(N=C) | r(C=O) | ∠(N=C=O) | ∠(X-N=C) | r(X-N) | Reference |
|---|---|---|---|---|---|---|
| HGeNCO | 1.215 | 1.178 | 175.9 | 142.8 | 1.816 | This Work (MP2(FC)) |
| HGeNCO | 1.205 | 1.171 | 176.9 | 146.0 | 1.840 | This Work (B3LYP) |
| HGeNCO | 1.196 | 1.150 | 177.0 | 139.6 | 1.834 | This Work (MC-SCF) |
| HSiNCO | 1.217 | 1.175 | 176.2 | 145.9 | 1.749 | Chapter 5 (MP2(FC)) |
| HSiNCO | 1.203 | 1.168 | 177.5 | 154.1 | 1.742 | Chapter 5 (B3LYP) |
| HSiNCO | 1.198 | 1.15 | 174.7 | 144.1 | 1.748 | Chapter 5 (MC-SCF) |
| HNCO | 1.214 | 1.166 | 172.6 | 123.9 | 0.995 | Reference[58] |
| CH$_3$NCO | 1.214 | 1.166 | 172.6 | 140.3 | 1.45 | Reference [59] |
| CH$_3$CH$_2$NCO | 1.217 | 1.173 | 174.1 | 138.8 | 1.439 | Reference[60] |
| H$_3$SiNCO | 1.197 | 1.174 | (180)[a,b] | 163.8 | 1.704 | Reference[61] |
| (CH$_3$)$_3$SiNCO | 1.202 | 1.176 | 165.8 | 156.9 | 1.74 | Reference[62] |
| F$_3$SiNCO | 1.19 | 1.168 | (180)[b] | 160.7 | 1.648 | Reference[63] |
| Cl$_3$SiNCO | 1.219 | 1.139 | (180)[b] | 138 | 1.646 | Reference[64] |
| ClNCO | 1.226 | 1.162 | 170.9 | 118.8 | 1.705 | Reference[65] |

[a] Electron diffraction data put this angle at 173.3° [Ref [41]]
[b] Angle is assumed to 180°

*7.3.2.1 Natural Bond Analysis*

The NBA shows the Ge-H and Ge-N bonds are single in nature. On the oxygen the LP is mainly *s* in character with $sp^{0.63}$ (38.5% *p* character), which is different from that seen in the HO-GeCN/NC isomers where the oxygen LP was situated out-of-plane and was mainly *p* in character. The bonding between Ge-H and Ge-N is mainly *p* in character with 91.1% *p* character and 91.1% *p* character, respectively, which as seen in the HO-GeCN/NC isomers, explains the small H-Ge-N bond angle of 95°. As before, there is good agreement with these values and those calculated for the analogous silicon containing isomer.

*7.3.2.2 Excited State*

Table 7.5 shows calculations carried out on the $\tilde{A}^1 A''$ state of HGeNCO. It shows that, just as was seen in the analogous HSiNCO species, on excitation the H-Ge-N angle increases significantly. As before, this is due to electron density being transferred from the hybridised Ge-H molecular orbital to the out-of-plane $p_z$ orbital on the germanium. This can be seen in Figure 7.5 which gives a three dimensional representation of the HOMO orbital (using natural bond analysis) in both the ground electronic state and the $\tilde{A}^1 A''$ excited electronic state of HGeNCO at the MP2 level of theory. On excitation all levels of theory predict the H-Ge-N angle increases from ~94° to ~115°. Similar increases are seen for the analogous halogen species H-Ge-X (X=H, Cl, Br, I) where on excitation the H-Ge-X angle opens up from ~90-95° in the ground state to 123.4°, 114.5°, 116.3° and 116.2°, respectively.[4,5,10,42] It seems therefore highly likely that the HGeNCO species would exhibit axis-switching peaks as discussed in Chapters 4 and 6, if its electronic spectrum was indeed detected in future studies. It is interesting to note that there have been no previous experimental studies of HGeF.

Table 7.5: Bond distances (Å), Bond angles (degrees), Dipole Moments ($D$) and Transition Energy (cm$^{-1}$) for the $\tilde{A}^1A''$ state of HGeNCO

| Parameter | B3LYP | MP2(FC) | MP2(Full) | QCISD[a] | MC-SCF | SAC-CI |
|---|---|---|---|---|---|---|
| r(H-Ge) | 1.573 | 1.528 | 1.519 | 1.561 | 1.532 | 1.580 |
| r(Ge-N) | 1.840 | 1.816 | 1.785 | 1.830 | 1.834 | 1.842 |
| r(N-C) | 1.205 | 1.215 | 1.201 | 1.202 | 1.196 | 1.214 |
| r(C-O) | 1.171 | 1.178 | 1.174 | 1.168 | 1.150 | 1.167 |
| ∠(H-Ge-N) | 109.7 | 112.9 | 112.5 | 112.2 | 116.5 | 110.1 |
| ∠(Ge-N-C) | 146.0 | 142.8 | 161.9 | 146.6 | 139.6 | 144.4 |
| ∠(N-C-O) | 176.9 | 175.9 | 177.4 | 183.2 | 177.0 | 175.9 |
| $\mu_x$ | -1.12 | -1.19 | -0.75 | -1.23 | - | -1.48 |
| $\mu_y$ | -1.81 | -1.82 | -2.24 | -2.01 | - | -1.68 |
| $T_0$ | 17551 | 16402 | 17654 | - | 18267 | 22455 |

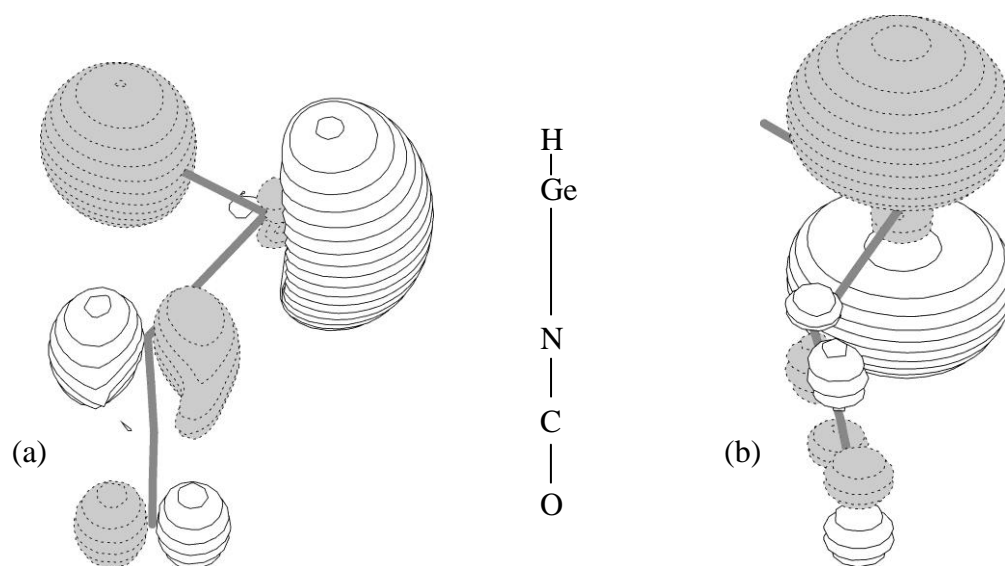[a] ZPE correction taken from a QCISD/aug-cc-pVDZ calculation.
[b] QCISD(T) value.



Figure 7.5: Three dimensional representations of the HOMO of HGeNCO in the (a) ground electronic state ($^1A'$) and (b) the first $\tilde{A}^1A''$ electronic state (contours are in 0.08 steps).

### 7.3.3 Enthalpies of Formation

As in the Chapter 5, to get some understanding of how the chemical structure of the isomers relate to their reactivity the enthalpies of formation for some isomers were calculated. As mentioned earlier, the large basis set requirements of the G3 mutilevel methods meant that it was not possible to follow the same approach used in Chapter 5, and therefore the slightly less accurate G2MP2 method was employed. Table 7.6 shows the enthalpy of formation at 0 and 298 K of the five lowest isomers using the G2MP2 multilevel method. As before, the enthalpies were calculated using the method of Curtiss *et al.* where the theoretical enthalpies were calculated by subtracting the calculated atomization energies from the known enthalpies of formation of the isolated atoms.[33] In this case, previous studies have indicated the it is necessary to include first-order spin-orbit corrections for the Ge atom in order to obtain reliable information, while further corrections to this energy are deemed unecessary.[43] To calculate the enthalpy of formation at 0 K Equation [7.2] was employed:

$$\Delta H^{o}_{f,0}(M) = E(M) + ZPE(M) - \sum_{z}^{atoms} E(X_z) + \sum_{z}^{atoms} \Delta H^{o}_{f,0}(X_z) \qquad [7.2]$$

while for the enthalpy of formation at 298 K Equation [7.3] was used:

$$\Delta H^{o}_{f,298}(M) = E(M) + ZPE(M) + \left[ H_{298}(M) - H_0(M) \right]$$
$$- \sum_{z}^{atoms} \left\{ E(X_z) + \left[ H_{298}(X_z) - H_0(X_z) \right] \right\} \sum_{z}^{atoms} \Delta H^{o}_{f,298}(X_z) \qquad [7.3]$$

In Equation [7.3], $H_{298}(M)$ and $H_0(M)$ are taken from the theoretical calculations, while the values of $H_{298}$-$H_0$ for the atoms where taken from the JANAF tables, as were the values for $\Delta H^{o}_{f,0}$ and $\Delta H^{o}_{f,298}$ for the atoms.[44]

It is very difficult to compare these results with previous data as there is very limited thermodynamic data on species containing H, Ge, C, N, and O, probably due to the fact that there are many Ge isotopes, making this kind of data difficult to obtain. Therefore, to test the reliability of this method in determination of thermodynamic properties, further calculations were carried out on germane ($GeH_4$) and germanium

dicarbide (GeC$_2$), for which accurate thermodynamic data are known.[45,46] In both cases, the calculated thermodynamic values were determined in exactly the same way as for the [H, Ge, N, C, O] isomers and the results are reasonably encouraging. For germane the literature values for the enthalpies of formation at 0 K and 298 K are 24.4 ±2.4 and 21.6 ±2.4 kcal/mol, respectively. The corresponding calculated values for these enthalpies are 18.7 and 20.6 kcal/mol. For germanium dicarbide the literature values for the enthalpies of formation at 0 K and 298 K are 142.7 ±2.4 and 143.6 ±2.4 kcal/mol, respectively. The corresponding calculated values for these enthalpies are 132.3 and 135.2 kcal/mol. This gives an indication that the calculated values are underestimating the enthalpies by up to ~15 kcal/mol. Therefore, the G2MP2 results, while not 100% accurate, appear to be consistent in that they underestimate the thermodynamic properties of these germanium containing species, and the results given in Table 7.6 should be considered to be lower than in reality.

The calculated enthalpies of formation of the [H, Ge, N, C, O] isomers lies in a range similar to, and indeed lower than, those of germane. Therefore, it should be considered that the generation and detection of the [H, Ge, N, C, O] isomers is, from a thermodynamic standpoint at least, highly possible. If the correct generation technique is employed (*i.e.*, photolysis, pyrolysis, laser ablation or electric discharge) in conjunction with the right pre-cursor then the spectroscopic detection of the proposed isomers is highly feasible.

Table 7.6: Enthalpy of formation (kcal/mol) at 0 and 298 K of the five lowest [H, Ge, N, C, O] isomers

| Isomer | $\Delta_f H^o$ [G2MP2] | |
| --- | --- | --- |
| | 0 K | 298 K |
| *cis*-HOGeCN | 5.36 | 7.08 |
| *trans*-HOGeCN | -0.01 | 2.12 |
| *cis*-HOGeNC | 1.65 | 3.61 |
| *trans*-HOGeNC | 1.84 | 4.06 |
| HGeNCO | 16.99 | 18.25 |

### 7.3.4 Triplet States

As was mentioned in Chapter 5 the alkyl isocyanates exhibit phosphorescence. Therefore, it would be interesting to see if any of the isomeric [H, Ge, N, C, O] species also follow this trend (particularly the HGeNCO isomer). To that end, triplet state calculations have been carried out on the five lowest lying isomers as depicted in Figure 7.6. At first calculations were carried out on the $^3A''$ triplet state of the five lowest [H, Ge, C, N, O] isomers at the B3LYP level of theory. The $^3A''$ triplet state was found to be the lowest lying triplet state for each species with the $^3A'$ state being substantially higher in energy. However, as was found in Chapter 5 for the [H, Si, N, C, O] isomers, harmonic vibration calculations for the planar forms of these triplet states gave a single imaginary vibration for all but the HGeNCO (T5) isomer indicating that these structures correspond to a $1^{st}$ order saddle point or transition state on the potential. Further calculations were then carried out investigating the non-planar structures as in Chapter 5.

Calculations were carried out on the $\tilde{a}^3A$ state of the two lowest isomers, and the $\tilde{a}^3A''$ state for the fifth lowest isomer (corresponding to the five lowest ground state isomers in Figure 7.1). Figure 7.6 shows the structures of the $\tilde{a}^3A/\tilde{a}^3A''$ triplet state of each isomer and their energies relative to their $^1A'$ isomer as given in Figure 7.1 at the B3LYP level of theory. The first two isomers (T1-T4 in Figure 7.6) the electronic configuration of the triplet species was $26\alpha28\beta$, and these isomers are those which deviate from the planar geometry having $\tilde{a}^3A$ symmetry. Isomer T5 in Figure 7.6 has the electronic configuration for the triplet state as $20a'^2 21a'^1 6a''^2 7a''^1$, and is the only isomer which does not give any negative frequencies in the planar ($\tilde{a}^3A''$) symmetry.
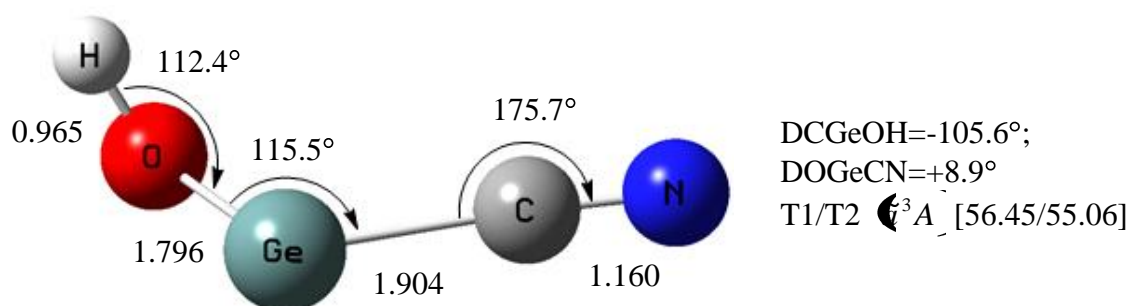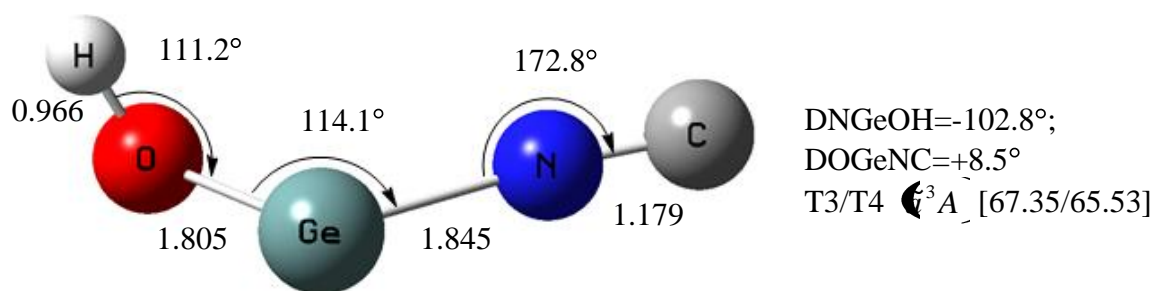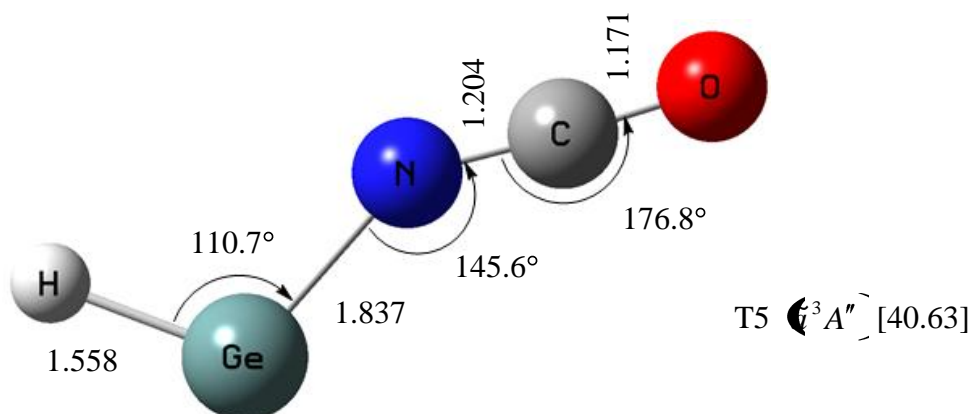
Figure 7.6: Optimized geometries of five lowest energy triplet states of the [H, Ge, C, N,O] system (in Å and degrees) computed at the B3LYP/aug-cc-pVTZ level of theory. All energies [kcal/mol] are relative to their corresponding $^1A'$ isomers also claculated at the B3LYP/aug-cc-pVTZ level of theory.

## 7.4 Concluding Remarks

In this chapter we have looked in detail at the five lowest energy [H, Ge, N, C, O] isomers. This is the first ever study on these isomeric species. We have shown that the identity of the lowest energy isomer is dependent on the level of theory applied to the isomers. In brief, all levels of theory predict the *cis*-HOGeCN (S1) isomer to be lowest in energy, but after that the B3LYP and G2MP2 calculations show a different ordering of the isomers when compared to the MP2 (both frozen core and full) and QCISD(T) calculations which show good agreement. The inclusion of core electrons does have a significant impact on the structure and relative energy of the isomers. Overall, the five lowest energy isomers lie within ~10 kcal/mol of each other, after which there is a significant increase in energy to the next isomer of ~20 kcal/mol. Therefore the remainder of the chapter focuses specifically on these five low lying isomers.

One of main reasons for this study was to collect data to aid in the detection of these species spectroscopically. To do this we have calculated vibrational wavenumbers and rotational constants of each isomer in their ground electronic state. For each of the lowest five isomers we have also determined the structure and transition energy of the first $^1A$ / $^1A''$ electronic state. However, it was found that for the lowest four isomers these excited state calculations gave a single negative frequency, indicating that the obtained structures were saddle points or transition states. Therefore, these isomers were recalculated with non-planar symmetry ($^1A$) to locate the minimum energy structures and it was found that when computed, these structures gave no negative frequencies. For the most part, each isomer shows a significant change in its geometry on excitation resulting mainly from electron density being shifted to an out-of-plane orbital resulting in the X-Si-C/N angle increasing by ~20°.

We have also determined the enthalpy of formation for each of the isomers using the G2MP2 method and have found that the species are relatively thermodynamically stable and are comparable to that of germane. We have also looked at the electronic structure of each isomer using natural bond analysis in its ground electronic state.

Lastly, we have looked at the lowest lying triplet state ($\tilde{A}\,^3A''$ for planar and $\tilde{a}\,^3A$ for non-planar) for each of the five lowest energy isomers and have shown that on excitation there is a substantial change in geometry for the lowest four isomers

where, as with their respective excited states, there is deviation from the planar geometry observed in the ground state isomers together with a significant change in the X-Ge-C/N angle.

Overall it is thought the species investigated in this work should be easily observable using spectroscopic techniques, in particular, microwave spectroscopy. However, there are problems associated with studying these species. Firstly there is the issue of health and safety, as germane ($GeH_4$), which is a likely candidate to be used as a precursor is a particularly unpleasant and hazardous chemical (highly toxic and flammable). However, this problem may be overcome by being very safe and methodical in ones approach to using it. The chief problem associated with studying any germanium containing species is the inherent spectroscopic complications which occur as a result of the existence of five isotopes of germanium in natural abundance ($^{70}$Ge, $^{72}$Ge, $^{73}$Ge, $^{74}$Ge and $^{76}$Ge). This leads to the production of spectra that are often quite congested even at low temperatures, making assignments difficult. In some cases, particularly when more than one atom of germanium is present in the species under study, the spectra produced may be so congested that incorrect assignments of lines occur often and there is a heavy reliance on the limited theoretical data available.

In terms of experimental study of the isomers discussed in this chapter, there is also the issue of how such species may be generated. There is no commercially available precursor analogous to that used to generate HSiNCO covered in Chapter 6, so the only way of generating these species would be to synthesise a precursor. Synthesis of trimethylgermylisocyanate (and its isothiocyanate analogue) has been previously achieved by Durig *et al.*[47] and the synthesis appears fairly straight forward, although there is obviously the issue of toxicity to be considered in production of such compounds. Once production of this precursor has been achieved it could be subjected to pyrolysis or electrical discharge to break down into the desired species of interest. Another possible route of production of the species discussed in this chapter would be to use gas mixtures of germane ($GeH_4$) and isocyanic acid (HNCO), which could then be subjected to electrical discharge to generate the desire species.

Given that the species discussed in this chapter appear fairly thermodynamically stable it is reasonable to assume that they may also be present in the interstellar medium, if and when more astronomical studies on germanium containing species are carried out.

## 7.5 REFERENCES FOR CHAPTER 7

(1)     Osmundsen, J. F.; Abele, C. C.; Eden, J. G. *J. Appl. Phys.* **1985**, *57*, 2921.

(2)     Sterling, N. C.; Dinerstein, H. L.; Bowers, C. W. *Astrophys. J.* **2002**, *578*, L55.

(3)     Klynning, L.; Lindgren, B. *Ark. Fys.* **1966**, *32*, 575.

(4)     Harper, W. W.; Clouthier, D. J. *J. Chem. Phys.* **1998**, *108*, 416.

(5)     Harper, W. W.; Klusek, C. M.; Clouthier, D. J. *J. Chem. Phys.* **1998**, *109*, 9300.

(6)     Ibuki, T. *Chem. Phys. Lett.* **1990**, *169*, 64.

(7)     Ito, H.; Hirota, E.; Kuchitsu, K. *Chem. Phys. Lett.* **1990**, *175*, 384.

(8)     Ito, H.; Hirota, E.; Kuchitsu, K. *Chem. Phys. Lett.* **1991**, *177*, 235.

(9)     Karolczak, J.; Zhuo, Q.; Clouthier, D. J.; Davis, W. M.; Goddard, J. D. *J. Chem. Phys.* **1993**, *98*, 60.

(10)    Saito, K.; Obi, K. *Chem. Phys. Lett.* **1993**, *215*, 193.

(11)    Smith, T. C.; Li, H. Y.; Clouthier, D. J.; Kingston, C. T.; Merer, A. J. *J. Chem. Phys.* **2000**, *112*, 8417.

(12)    Pang, W. X.; Wang, M. S.; Yang, C. L.; Zhang, Y. F. *J. Chem. Phys.* **2007**, *126*,194301.

(13)    Sari, L.; Yamaguchi, Y.; Schaefer, H. F. *J. Chem. Phys.* **2001**, *115*, 5932.

(14)    Tackett, B. S.; Clouthier, D. J. *J. Chem. Phys.* **2006**, *124*, 144308.

(15)    Wang, Q.; Ding, Y.; Sun, C. *J. Chem. Phys.* **2005**, *122*, 204305.

(16)    Wang, Q.; Ding, Y. H.; Xie, H. B.; Sun, C. C. *J. Comput. Chem.* **2006**, *27*, 505.

(17)    Frisch, M. J.; Trucks, G. W.; Schlegel, H. B.; Scuseria, G. E.; Robb, M. A.; Cheeseman, J. R.; Montgomery, J., J. A.; Vreven, T.; Kudin, K. N.; Burant, J. C.; Millam, J. M.; Iyengar, S. S.; Tomasi, J.; Barone, V.; Mennucci, B.; Cossi, M.; Scalmani, G.; Rega, N.; Petersson, G. A.; Nakatsuji, H.; Hada, M.; Ehara, M.; Toyota, K.; Fukuda, R.; Hasegawa, J.; Ishida, M.; Nakajima, T.; Honda, Y.; Kitao, O.; Nakai, H.; Klene, M.; Li, X.; Knox, J. E.; Hratchian, H. P.; Cross, J. B.; Bakken, V.; Adamo, C.; Jaramillo, J.; Gomperts, R.; Stratmann, R. E.; Yazyev, O.; Austin, A. J.; Cammi, R.; Pomelli, C.; Ochterski, J. W.; Ayala, P. Y.; Morokuma, K.; Voth, G. A.; Salvador, P.; Dannenberg, J. J.; Zakrzewski, V. G.; Dapprich, S.; Daniels, A. D.; Strain, M. C.; Farkas, O.; Malick, D. K.; Rabuck, A. D.; Raghavachari, K.; Foresman, J. B.; Ortiz, J. V.; Cui, Q.; Baboul, A. G.; Clifford, S.; Cioslowski, J.; Stefanov, B. B.; Liu, G.; Liashenko, A.; Piskorz, P.; Komaromi, I.; Martin, R. L.; Fox, D. J.; Keith, T.; Al-Laham, M. A.; Peng, C. Y.; Nanayakkara, A.; Challacombe, M.; Gill, P. M. W.; Johnson, B.; Chen, W.; Wong, M. W.; Gonzalez, C.; Pople, J. A. Gaussian 03; Revision D.02 ed.; Gaussian Inc.: Wallington CT, **2004**.

(18)    Dunning, T. H. *J. Chem. Phys.* **1989**, *90*, 1007.

(19)    Kendall, R. A.; Dunning, T. H.; Harrison, R. J. *J. Chem. Phys.* **1992**, *96*, 6796.

(20)    Woon, D. E.; Dunning, T. H. *J. Chem. Phys.* **1993**, *98*, 1358.

(21)    Becke, A. D. *J. Chem. Phys.* **1993**, *98*, 5648.

(22)    Møller, C.; Plesset, M. S. *Phy. Rev.* **1934**, *46*, 618.

(23)    Head-Gordon, M.; Pople, J. A.; Frisch, M. J. *Chem. Phys. Lett.* **1988**, *153*, 503.

(24)    Frisch, M. J.; Head-Gordon, M.; Pople, J. A. *Chem. Phys. Lett.* **1990**, *166*, 275.

(25)    Frisch, M. J.; Head-Gordon, M.; Pople, J. A. *Chem. Phys. Lett.* **1990**, *166*, 281.

(26) Pople, J. A.; Head-Gordon, M.; Raghavachari, K. *J. Chem. Phys.* **1987**, *87*, 5968.

(27) Baboul, A. G.; Curtiss, L. A.; Redfern, P. C.; Raghavachari, K. *J. Chem. Phys.* **1999**, *110*, 7650.

(28) Curtiss, L. A.; Redfern, P. C.; Raghavachari, K.; Rassolov, V.; Pople, J. A. *J. Chem. Phys.* **1999**, *110*, 4703.

(29) East, A. L. L.; Johnson, C. S.; Allen, W. D. *J. Chem. Phys.* **1993**, *98*, 1299.

(30) Shapley, W. A.; Bacskay, G. B. *J. Phys. Chem. A* **1999**, *103*, 6624.

(31) Pasinszki, T.; Westwood, N. P. C. *J. Phys. Chem. A* **2001**, *105*, 1244.

(32) Curtiss, L. A.; Mcgrath, M. P.; Blaudeau, J. P.; Davis, N. E.; Binning, R. C.; Radom, L. *J. Chem. Phys.* **1995**, *103*, 6104.

(33) Curtiss, L. A.; Raghavachari, K.; Redfern, P. C.; Pople, J. A. *J. Chem. Phys.* **1997**, *106*, 1063.

(34) Curtiss, L. A.; Raghavachari, K.; Trucks, G. W.; Pople, J. A. *J. Chem. Phys.* **1991**, *94*, 7221.

(35) Trachtman, M.; Markham, G. D.; Glusker, J. P.; George, P.; Bock, C. W. *Inorg. Chem.* **2001**, *40*, 4230.

(36) Sanz, M. E.; McCarthy, M. C.; Thaddeus, P. *Astrophys. J.* **2002**, *577*, L71.

(37) Ogden, J. S.; Ricks, M. J. *J. Chem. Phys.* **1970**, *52*, 352.

(38) Smeyers, Y. G.; Villa, M.; Cardenas-Jiron, G. I.; Toro-Labbe, A. *THEOCHEM-J. Mol. Struc.* **1998**, *426*, 155.

(39) Toro-Labbe, A. *THEOCHEM-J. Mol. Struc.* **1988**, *49*, 209.

(40) Ohno, K.; Matsuura, H.; Endo, Y.; Hirota, E. *J. Mol. Spectrosc.* **1986**, *118*, 1.

(41) Glidewel.C; M., S. G.; Robiette, A. G. *Chem. Phys. Lett.* **1972**, *16*, 526.

(42) Smith, T. C.; Clouthier, D. J.; Sha, W.; Adam, A. C. *J. Chem. Phys.* **2000**, *113*, 9567.

(43) Mayer, P. M.; Gal, J.-F.; Radom, L. *Int. J. Mass Spectrom. Ion Processes* **1997**, *167/168*, 689.

(44) Chase, M. W., Jr. *J. Phys. Chem. Ref. Data (Monograph 9)* **1998**.

(45) Ruscic, B.; Schwarz, M.; Berkowitz, J. *J. Chem. Phys.* **1990**, *92*, 1865.

(46) Schmude, R. W.; Gingerich, K. A.; Kingcade, J. E. *J. Phys. Chem.* **1995**, *99*, 15294.

(47) Durig, J. R.; Sullivan, J. F.; Cox, A. W.; Turner, J. B. *J. Mol. Struct.* **1978**, *44*, 31.

# Appendices

# Appendix A: Chapter 4:

Correlation matrix for the fitting of the HSiNC constants given in Tables 4.7 and 4.8:

| Parameter | $A''$ | $\Delta_K''$ | $T_0$ | $A'$ | $B'$ | $C'$ | $\Delta_K'$ | $\Delta_{JK}'$ | $\Delta_J'$ |
|---|---|---|---|---|---|---|---|---|---|
| $A''$ | 1.000 | | | | | | | | |
| $\Delta_K''$ | 0.967 | 1.000 | | | | | | | |
| $T_0$ | 0.619 | 0.533 | 1.000 | | | | | | |
| $A'$ | -0.024 | -0.005 | -0.492 | 1.000 | | | | | |
| $B'$ | -0.643 | -0.582 | -0.662 | -0.031 | 1.000 | | | | |
| $C'$ | 0.648 | 0.630 | 0.084 | 0.282 | -0.500 | 1.000 | | | |
| $\Delta_K'$ | -0.093 | -0.024 | -0.446 | 0.898 | 0.012 | 0.134 | 1.000 | | |
| $\Delta_{JK}'$ | 0.170 | 0.147 | -0.279 | 0.713 | -0.230 | 0.631 | 0.464 | 1.000 | |
| $\Delta_J'$ | -0.316 | -0.265 | -0.501 | -0.075 | 0.862 | -0.148 | -0.037 | -0.208 | 1.000 |

## *Appendix B: Chapter 5:*

Table B.1: All [H, Si, N, C, O] isomers calculated at the MP2(FC)/aug-cc-pVTZ level in the $^1A'$ electronic state.

| No. | Isomer | Energy(au) | ZPEC(au) |
|-----|--------|------------|----------|
| 1 | *cis*-HOSiCN | -457.4649223 | 0.0214713 |
| 2 | *trans*-HOSiCN | -457.4635752 | 0.0217564 |
| 3 | *cis*-HOSiNC | -457.4625667 | 0.0211984 |
| 4 | *trans*-HOSiNC | -457.4608962 | 0.0214641 |
| 5 | HSi(O)CN | -457.4529765 | 0.0192415 |
| 6 | HSi(O)NC | -457.4448987 | 0.0191585 |
| 7 | HSiNCO | -457.4401549 | 0.0201224 |
| 8 | Cyclic 1 | -457.4100916 | 0.0231459 |
| 9 | *trans*-HSi-O-CN | -457.4043421 | 0.019399 |
| 10 | *cis*-HSi-O-CN | -457.4041041 | 0.019282 |
| 11 | Cyclic 2 | -457.4026229 | 0.0233347 |
| 12 | Cyclic 3 | -457.401016 | 0.022512 |
| 13 | SiNCOH | -457.3671531 | 0.0226693 |
| 14 | NSiC(O)H | -457.3298665 | 0.0205419 |
| 15 | HSiCNO | -457.3225524 | 0.0194094 |
| 16 | *trans*-HSi-O-NC | -457.3032278 | 0.018421 |
| 17 | *cis*-HSi-O-NC | -457.3023809 | 0.018249 |
| 18 | SiCNOH | -457.2877963 | 0.0222642 |
| 19 | HCSiNO | -457.212235 | 0.0185312 |
| 20 | SiC(H)ON | -457.2034769 | 0.0212867 |

Isomers studied (as listed in Table B.1)
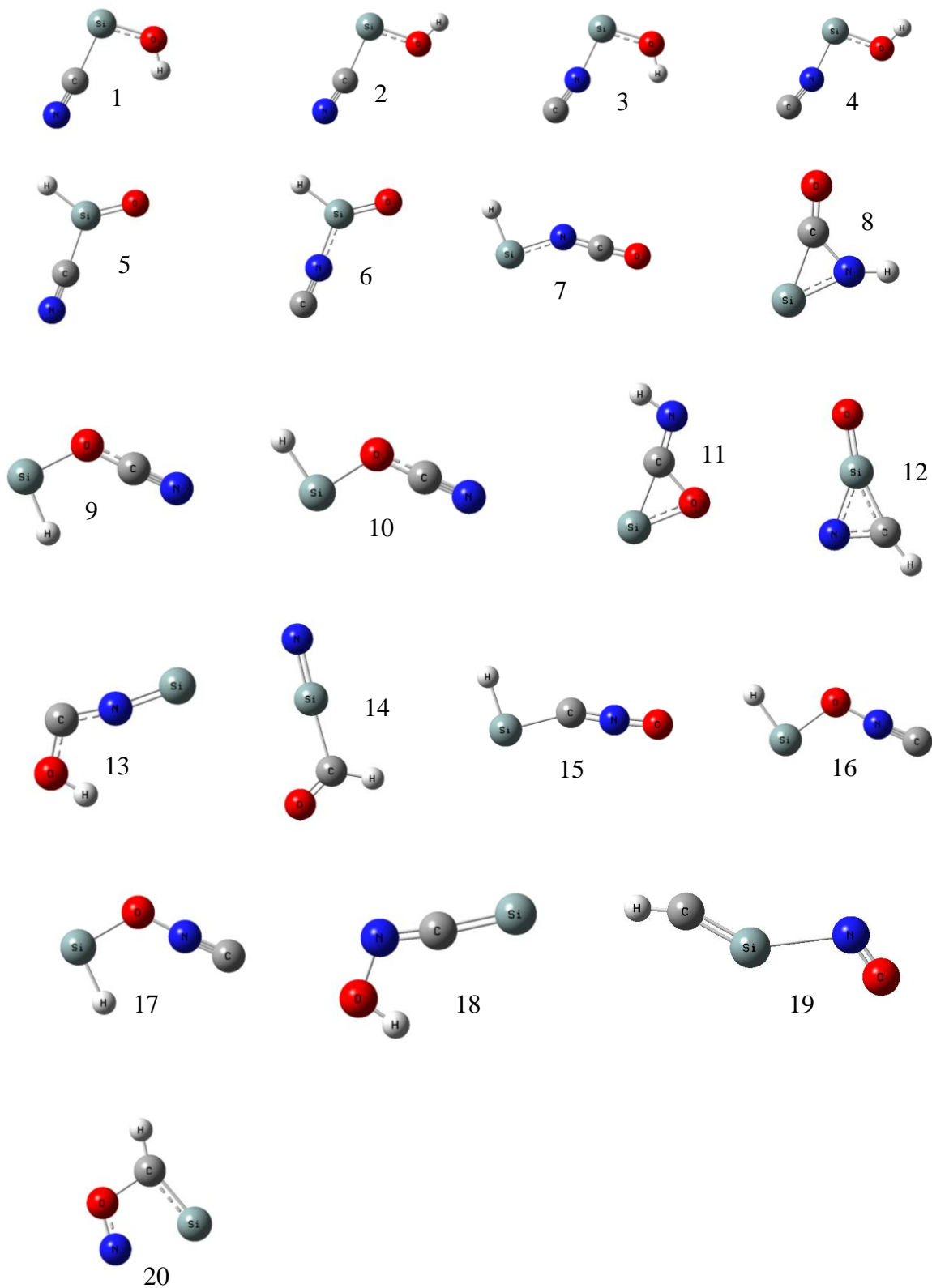
# Appendix C: Chapter 6:

Correlation matrix for the fitting of the HSiNCO constants given in Tables 6.1 and 6.2:

| Parameter | $A''$ | $B''$ | $C''$ | $\Delta_K''$ | $\Delta_{JK}''$ | $\Delta_J''$ | $\delta_K''$ | $T_0$ | $A'$ | $B'$ | $C'$ | $\Delta_K'$ | $\Delta_{JK}'$ | $\Delta_J'$ | $\delta_K'$ |
|---|---|---|---|---|---|---|---|---|---|---|---|---|---|---|---|
| $A''$ | 1.000 | | | | | | | | | | | | | | |
| $B''$ | -0.126 | 1.000 | | | | | | | | | | | | | |
| $C''$ | -0.103 | 0.955 | 1.000 | | | | | | | | | | | | |
| $\Delta_K''$ | 0.908 | -0.108 | -0.086 | 1.000 | | | | | | | | | | | |
| $\Delta_{JK}''$ | 0.742 | -0.064 | -0.039 | 0.510 | 1.000 | | | | | | | | | | |
| $\Delta_J''$ | -0.183 | 0.842 | 0.817 | -0.141 | -0.221 | 1.000 | | | | | | | | | |
| $\delta_K''$ | -0.189 | -0.243 | -0.237 | -0.106 | -0.342 | -0.326 | 1.000 | | | | | | | | |
| $T_0$ | 0.510 | 0.124 | 0.106 | 0.434 | 0.346 | 0.157 | -0.178 | 1.000 | | | | | | | |
| $A'$ | -0.079 | 0.094 | 0.121 | -0.155 | 0.114 | 0.006 | -0.041 | -0.546 | 1.000 | | | | | | |
| $B'$ | -0.174 | 0.925 | 0.927 | -0.129 | -0.131 | 0.703 | -0.077 | -0.100 | 0.159 | 1.000 | | | | | |
| $C'$ | -0.158 | 0.940 | 0.946 | -0.117 | -0.126 | 0.795 | -0.264 | -0.043 | 0.125 | 0.931 | 1.000 | | | | |
| $\Delta_K'$ | -0.304 | 0.271 | 0.265 | -0.302 | -0.133 | 0.288 | -0.085 | -0.404 | 0.796 | 0.253 | 0.280 | 1.000 | | | |
| $\Delta_{JK}'$ | 0.182 | -0.340 | -0.280 | 0.077 | 0.359 | -0.613 | 0.146 | -0.300 | 0.408 | -0.157 | -0.297 | -0.106 | 1.000 | | |
| $\Delta_J'$ | -0.202 | 0.812 | 0.792 | -0.141 | -0.276 | 0.977 | -0.298 | 0.070 | -0.008 | 0.717 | 0.819 | 0.293 | -0.647 | 1.000 | |
| $\delta_K'$ | -0.135 | 0.358 | 0.279 | -0.099 | -0.215 | 0.494 | -0.160 | -0.024 | -0.003 | 0.290 | 0.368 | 0.201 | -0.449 | 0.542 | 1.000 |

# *Appendix D: Chapter 7:*

Table D.1: All [H, Ge, N, C, O] isomers calculated at the B3LYP/aug-cc-pVDZ level in the $^1A'$ electronic state.

| No. | Isomer | Energy (au) | ZPEC (au) |
|-----|--------|-------------|-----------|
| 1 | *cis*-HOGeCN | -2245.728021 | 0.0207331 |
| 2 | *trans*-HOGeCN | -2245.726073 | 0.0209647 |
| 3 | *cis*-HOGeNC-cis | -2245.72534 | 0.021718 |
| 4 | *trans*-HOGeNC | -2245.722425 | 0.0203487 |
| 5 | HGe(O)CN | -2245.660347 | 0.0175551 |
| 6 | HGe(O)NC | -2245.649275 | 0.0169074 |
| 7 | HGeNCO | -2245.724032 | 0.0189173 |
| 8 | Cyclic1 | -2245.691624 | 0.0223411 |
| 9 | *cis*-HGe-O-CN | -2245.685584 | 0.0182956 |
| 10 | *trans*-HGe-O-CN | -2245.686141 | 0.0184007 |
| 11 | Cyclic 2 | -2245.68016 | 0.0228531 |
| 12 | GeNCOH | -2245.650762 | 0.0215973 |
| 13 | HGeCNO | -2245.612244 | 0.0178922 |
| 14 | *trans*-HGe-O-NC | -2245.593043 | 0.0170094 |
| 15 | *cis*-HGe-O-NC | -2245.591857 | 0.0168837 |
| 16 | GeCNOH | -2245.591149 | 0.0216267 |
| 17 | GeC(H)ON | -2245.515903 | 0.0206453 |

Isomers studied (as listed in Table D.2):
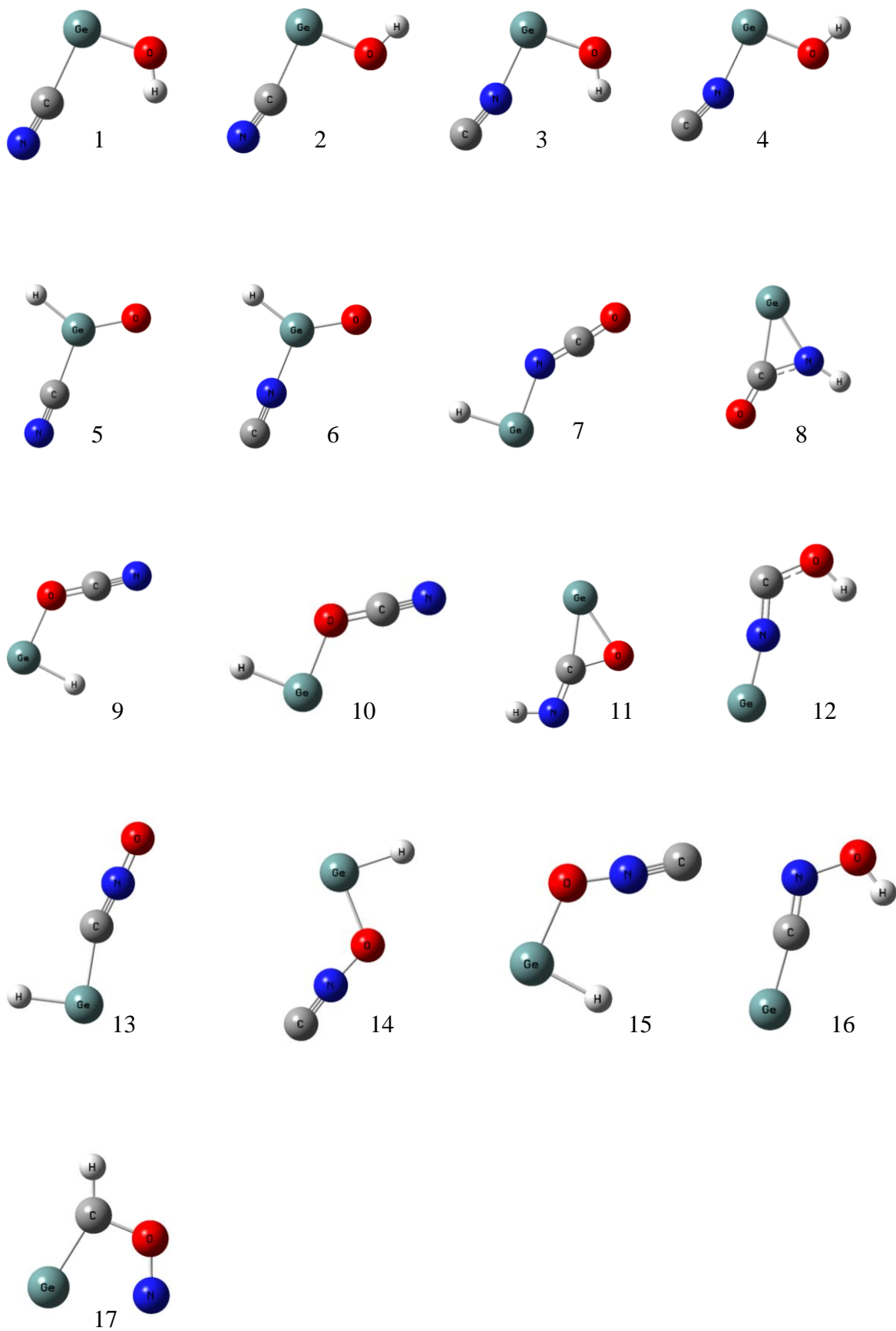
## *Addendum contents (consisting of one compact disc)*

- **Calculations** – Contains input and output files for all Gaussian 03 calculations.
    - .com and .out files may be accessed with a standard text editor (e.g., WordPad).
    - .out files may also be opened with GaussView or Molden to access structural data.
- **LabVIEW programs** – contains all versions of the data acquisition software.
- **Matlab programs** – Contains all Matlab programs used ofr the various fitting procedures.

## *Record of Achievement*

### Publications:

Computational study on the structures of the [H, Si, N, C, O] isomers: possible species of interstellar interest, Dover M. R.; Evans C. J., *J. Phys. Chem. A.*, **2007**, 111(50), 13148-56.

### Conferences and Meetings Attended:

| | |
|---|---|
| 19/12/04 – 21/12/04 | Spectroscopy and Dynamics group, University of Leicester |
| April '05 | Annual Southern Universities Meeting of Chemical Physics |
| 29/06/05 | Annual Northern Universities Meeting of Chemical Physics |
| 26/10/05 | Leic/War/Bham Tri-University Gas Phase Chem. Phys. meeting – Oral presentation (20 min) |
| 05/07/06 | Annual Northern Universities Meeting of Chemical Physics |
| 21/09/06 | Astrochemistry Young Researchers Meeting – Poster presentation |
| 04/10/06 | Leic/War/Bham Tri-University Gas Phase Chem. Phys. meeting – Oral presentation (20 min) |
| 18/12/06 – 20/12/06 | Spectroscopy and Dynamics group, University of Oxford – Oral presentation (15 min) and poster presentation |